

Lifetime Prediction and Durability of Elastomeric Seals for Fuel Cell Applications

Hitendra K. Singh

Dissertation Submitted to the Faculty of the Virginia Polytechnic Institute and State University in
Partial Fulfillment of the Requirements for the Degree of

Doctor of Philosophy
in
Engineering Mechanics

David A. Dillard - Chair

John G. Dillard

Michael W. Hyer

Scott W. Case

Surot Thangjitham

April 29th, 2009
Blacksburg, Virginia

Keywords: Polymer Electrolyte Membrane Fuel Cell (PEMFC), Elastomeric Seals, Degradation, Viscoelastic, Stick-slip, Strain Energy Release Rate, Stress Relaxation, Durability, Lifetime Prediction.

Lifetime Prediction and Durability of Elastomeric Seals for Fuel Cell Applications

Hitendra K. Singh

(Abstract)

Polymer electrolyte membrane (PEM) fuel cell (FC) stacks require elastomeric gaskets for each cell to keep the reactant gases within their respective regions[1]. If any gasket degrades or fails, the reactant gases can leak or mix with each other directly during operation or standby, affecting the overall operation and performance of the FC. The elastomeric gaskets used as FC seals are exposed to a range of environmental conditions, and concurrently, subjected to mechanical compression between the bipolar plates forming the cell. The combination of mechanical stress and environmental exposure may result in degradation of the seal material[2] over a period of time. In order to address the durability and make reliability predictions, the long-term stability of the gaskets in FC assemblies is critical. The aim of this study is to investigate the performance of elastomeric seals in a simulated FC environment in the presence of mechanical stresses. The overall scope of the study includes mechanical and viscoelastic properties characterization, and lifetime durability predictions based on an accelerated characterization approach.

With the help of finite element analysis software, ABAQUS, a fixture was designed to perform strain-based accelerated characterization of seal material in air, deionized (DI) water, 50v/50v ethylene glycol/water solution, and 0.1M sulfuric acid solution. Dogbone samples were strained to different levels in the custom fixture and submerged in liquid solutions at 90°C and in air at 90°C and 120°C. It was observed that mechanical properties such as tensile strength, strain to break, 100% modulus, crosslink density, and tensile set degrade due to aging and the extent of change (increase or decrease) depends significantly on the strain level on the specimen.

Trouser tear tests were conducted on reinforced specimens in air and deionized water (DI) to evaluate the tear resistance of an elastomeric seal material intended for proton exchange membrane fuel cells. Plots relating the crack growth rate with tearing energy were obtained at various temperatures and provided significant insight into the rate and temperature dependence of the tearing strength of the seal material. Stick-slip crack propagation was observed at all temperatures and loading rates, although the behavior was suppressed significantly at low loading rates and high temperatures. Crack growth rate versus tearing energy data at different temperatures was shifted to construct a master curve and an estimate on the threshold value of tear energy was obtained which may be helpful in designing components where material tear is of concern. Strain energy release rate (SERR) value, calculated using the J-integral approach for a pre-existing crack in ABAQUS, was used to estimate the crack growth rate in a given seal cross-section to predict lifetime.

In order to assess the viscoelastic behavior and to investigate the long term stress relaxation behavior of the seal material, compression stress relaxation (CSR) tests were performed on molded seals, called as SMORS, over a range of environmental conditions using a custom-designed fixture. The effect of temperature and environment was evident on material property changes and presented in terms of momentary properties and stress relaxation behavior. Various mechanisms involved in material degradation, chain scission and crosslinking, were suggested and insights were gained into how cure state and level of antidegradants in a material dictate the material behavior during the first phase of environmental exposure leading to change in material properties. Ring samples made of silicone were also tested using the fixture to obtain insight additional into material degradation due to aging. Results presented from testing on SMORS

showed a lot more variation in data as compared to neat silicone rings due to the complexity involved in making SMORS.

For understanding the deformation behavior of an elastomeric seal and its sealing performance, finite element characterization of seal cross-section was carried out on O-ring and SMORS cross-section. The effect of a seal's layout on distribution and magnitude of contact stresses and contact width was investigated for the O-ring and the information obtained thereby helped to analyze a complex assembly such as SMORS, where several interfaces and boundary conditions are involved. Stress/strain profiles were generated to visualize their concentration and distribution in the seal cross-section. Frictionless and rough interfacial conditions between seal material and platens were assumed and it was found that its effect on contact width and peak contact pressure was insignificant. Results obtained from FEA on SMORS were validated through comparison with contact mechanics approach and experimental data and it was found that Lindley's equation correlates well with experimental data whereas ABAQUS overestimates the load values at a given compression. Lindley's approach may be used to develop contact pressure profiles that may help estimate peak contact pressure at a given time so leaking can be avoided.

Acknowledgements

I wish to express my sincere appreciation to my advisor, Dr. David Dillard for his patience, guidance, and support through my time at Virginia Tech providing me with tremendous opportunities to learn and grow.

I also wish to acknowledge my other committee members Dr. John Dillard, Dr. Michael Hyer, Dr. Scott Case, and Dr. Surot Thangjitham for taking the time to serve on my advisory committee, as well as for useful suggestions and guidance on my research work.

I would like to thank Dr. Robert West for teaching me ABAQUS and providing guidance relevant to various finite element analysis aspects involved in this research. Thanks are also due to Derek Slaughter for his help during ABAUS modeling.

I would like to thank Dr. Robert Moore and Dr. Wonho Kim for useful discussions and great help in this work.

I would like to thank the UTC Power for sponsoring this research in coordination with the Department of Energy, under cooperative agreement number DE-FG36-07GO17005. I wish to thank Jason Parsons and Bhavana Bommarajapeta at UTC Power, Dr. Matthew Burdzy, Dr. Yanbing Wang and Dr. Yonghui Zhang at Henkel Corporation, and Mark Belchuk and Dr. Oon Hock Yeoh at Freudenberg-NOK for their assistance and advice during the project.

I would like to thank Abhijit Chakraborty, Harpreet Chadha, David Pohlit, Edoardo Nicoli, Kshitish Patankar, Jake Grohs, Geoffrey Tizard, Lei Yan, and Timothy Gray for making my time as a part of the Adhesion Science Lab incredibly enjoyable and fulfilling.

I would like to thank the Engineering Science and Mechanics at Virginia Tech for providing research facilities. Thanks are also due to Joyce Smith, Beverly Williams, Lisa Smith, Pat Baker, Paul Siburt, Dave Simmons, Darrell Link, Marshall McCord, and Robert Simonds along with all of the ESM staff.

I would like to especially thank Melissa Nipper for her support and help during my research.

I would like to extend my appreciation to my aunt Dr. Kusum Singh and Uncle Dr. Mahendra P. Singh for their blessings over the years.

Finally, I extend my profound appreciation to my mother, Mithlesh Singh, my father-in-law, Malkhan Singh, my mother-in-law, Usha Singh, my brothers, Dhruv, Raj, and Rahul, my sister, Diksha, my wife, Anu, and the person I love the most, my daughter Riya, for their love, care, inspiration, support, and blessings over the years.

Table of Contents

1	Introduction	1
1.1	Background	1
1.1.1	Degradation of seal material properties such as tensile strength, modulus etc.....	4
1.1.2	Characterization of tear properties.....	5
1.1.3	Stress relaxation of the seal material under compression	5
1.2	Motivation	6
1.3	Dissertation Organization.....	8
2	Literature Review	13
2.1	Seal Failure Modes.....	14
2.2	Seal Material Characterization: Test Protocols.....	16
2.2.1	Bulk Material Properties	17
2.2.2	Stress Relaxation - Loss of Sealing Force	18
2.2.3	Lifetime Prediction Methodologies	21
2.3	Constitutive Modeling of Elastomeric Materials	23
2.3.1	Background on Hyperelasticity.....	23
2.3.2	Hyperelastic Material Modeling	36
2.4	Conclusion.....	40
3	Uniaxial Tension Test.....	66
3.1	Introduction	66
3.1.1	Experimental	69
3.1.2	Results& Discussion	72
3.1.3	Conclusions.....	76
4	Trouser Tear Test.....	97
4.1	Abstract	97
4.2	Introduction	97
4.2.1	Available Tearing Energy	99
4.3	Experimental	100
4.3.1	Material & Sample Preparation	100
4.3.2	Test Procedure	101
4.4	Results & Discussion	101

4.4.1	Lifetime Prediction Approach using Finite Element Analysis	105
4.5	Conclusion.....	108
5	Viscoelastic Characterization of the Seal Material.....	124
5.1	Abstract	124
5.2	Background	125
5.3	Compression Stress Relaxation Fixture Design	128
5.4	Experimental	130
5.4.1	Material & Sample Preparation	130
5.4.2	Environments and Specimen Conditioning	131
5.4.3	Test Procedure	131
5.5	Results & Discussion	132
5.5.1	SMORS.....	132
5.5.2	Silicone rings	138
5.6	Conclusion.....	141
6	Finite Element Characterization of Seal Design.....	169
6.1	Seal Stress Analysis	169
6.1.1	O-ring Analysis.....	171
6.1.2	SMORS Analysis.....	172
6.2	Contact Mechanics of Elastomeric Seals	174
6.3	Theoretical & Experimental Validation of Finite Element Results for SMORS	176
6.3.1	No-slippage between seal and GDL	177
6.3.2	Single GDL with Fixed Boundary Conditions.....	178
6.4	Development of Peak Contact Pressure Profile	178
6.5	Conclusion.....	179
7	Summary.....	209
7.1	Observations.....	209
7.2	Future Work	213
7.2.1	Characterization of Bulk Material Properties	213
7.2.2	SMORS Characterization.....	215

List of Figures

Figure 1.1 Illustration of a fuel cell unit showing membrane electrode assembly, anode, cathode, gas diffusion layer, seal, and bipolar plates.	12
Figure 2.1 Evaluation of U and X from instantaneous and stress relaxation curve.	52
Figure 2.2 Illustration of Arrhenius approach. (a) Change in property with time at three temperatures, (b) Arrhenius plot.	53
Figure 2.3 Illustration of constructing a master curve using WLF approach.	54
Figure 2.4 Typical true stress-true strain response of an elastomer under uniaxial tension, shear and biaxial extension.	55
Figure 2.5 Sketch of part of a typical elastomeric network. The crosslinks are indicated by filled circles[120].	56
Figure 2.6 The statistically kinked chain. Specification of probability that the end should fall in the volume element $d\tau (=dx dy dz)$	57
Figure 2.7 The tension on a chain whose ends are fixed in position is proportional to the distance r.	58
Figure 2.8 Pure homogenous strain: (a) the unstrained state; (b) the strained state.	59
Figure 2.9 Illustration of an individual chain having an end-to-end distance represented by the vector r_0 in the unstrained state of the network. The vector r represents the end-to-end distance after deformation.	60
Figure 2.10 Hyperelastic material diagram for (a) unit cube in unstrained state, (b) unit cube subjected to uniaxial tension, (c) Mohr's diagram for stress, and (d)) Mohr's diagram for strain.	61
Figure 2.11 Hyperelastic material diagram for (a)unit cube in unstrained state, (b) unit cube subjected to uniaxial compression, (c) Mohr's diagram for stress, and (d)) Mohr's diagram for strain.	62
Figure 2.12 Hyperelastic material diagram for (a)unit cube in unstrained state, (b) unit cube subjected to equi-biaxial extension, (c) Mohr's diagram for stress, and (d)) Mohr's diagram for strain.	63
Figure 2.13 Hyperelastic material diagram for (a)unit cube in unstrained state, (b) unit cube subjected to simple shear, (c) Mohr's diagram for stress, and (d)) Mohr's diagram for strain. .	64

Figure 2.14 Hyperelastic material diagram for (a) unit cube in unstrained state, (b) unit cube subjected to pure shear, (c) Mohr’s diagram for stress, and (d) Mohr’s diagram for strain.	65
Figure 3.1 Illustration of dogbone specimen used for tensile testing, shown with nominal dimensions. Holes drilled in the grip region are reinforced with PSA tape to avoid deformation around holes.	80
Figure 3.2 Plot of experimental data and predicted uniaxial behavior using various material models.	82
Figure 3.3 Hyperelastic material model evaluation results from ABAQUS for silicone seal material.	85
Figure 3.4 Illustration of dogbone samples under uniaxial tension loading configuration in ABAQUS.	86
Figure 3.5 Illustration of screening tests performed on dogbone samples strained to different levels in various environments at different temperatures to evaluate their aggressiveness to the seal material.	87
Figure 3.6 Illustration of procedure for measuring experimental strain in a dogbone sample stretched in the custom fixture.	88
Figure 3.7 Uniaxial tension test set up showing the laser extensometer, Instron load frame and dogbone specimen in the pneumatic grips. White benchmarks on the specimen for the measurement of strain are also shown in the picture.	90
Figure 3.8 Typical stress strain plot and test results obtained from the uniaxial tension test performed on silicone elastomer at 500 mm/min at room temperature.	91
Figure 3.9 Effect of aging on tensile strength of silicone seal material.	92
Figure 3.10 Effect of aging on strain to failure of silicone seal material.	93
Figure 3.11 Effect of aging on modulus at 100% strain for silicone seal material.	94
Figure 3.12 Effect of aging on crosslink density of silicone seal material.	95
Figure 3.13 Tensile set in the silicone seal material as a result of aging.	96
Figure 4.1 Illustration of the sample preparation method for trouser tear testing. (a) illustrates reinforcing fiber cloth strips in seal material slab, (b) illustrates the trouser tear sample with dimensions, and (c) illustrates the sample configuration during loading in an Instron load frame.	113

Figure 4.2 Load displacement plot obtained from trouser tear tests conducted at 100 mm/min in air at RT on hydrocarbon based seal material.....	114
Figure 4.3 Load displacement plot obtained from trouser tear tests performed in air at rates from 2 mm/min to 500 mm/min at RT on hydrocarbon based seal material.....	115
Figure 4.4 Rate dependence of tearing energy, G_{cr} in air at RT.	116
Figure 4.5 Plot of tearing energy versus test temperatures at different loading rates on hydrocarbon based seal material.....	117
Figure 4.6 Plot of tearing energy versus crack growth rate at different temperatures on hydrocarbon based seal material.....	118
Figure 4.7 Master curve of tearing energy versus crack growth rate ($T_{reference} = 80^{\circ}C$, $T_g = -55^{\circ}C$) for hydrocarbon based seal material. Shift factor, a_T , versus temperature is shown in inset.....	119
Figure 4.8 Load versus displacement behavior in DI water and air at various rate and temperatures for hydrocarbon based seal material.....	120
Figure 4.9 Finite element simulation of an O-ring under compression with a surface crack.	121
Figure 4.10 J-integral contour along with quantities used to calculate SERR around a crack tip.	122
Figure 4.11 Contours around a crack tip and corresponding SERR values.....	123
Figure 5.1 Evaluation of U and X from instantaneous and stress relaxation curve. At a given time t, U is the value of the relaxed load and U + X is the load obtained from compressing unstrained samples.....	148
Figure 5.2 Illustration of quarter-section view of the CSR fixture and other components.....	149
Figure 5.3 Illustration of the fixture placed on a polycarbonate support and immersed in the liquid for aging. Also showing the fixture placed between compression platens in an Instron load frame.	150
Figure 5.4 Illustration of molded seal (SMORS) and silicone rings with dimensions.	151
Figure 5.5 Typical load versus displacement behavior of seals obtained from compressing the upper stack.	152
Figure 5.6 Typical load versus displacement behavior of seals obtained from compressing the lower stack. The value of relaxed load, due to stress relaxation, as well momentary properties of the seal can be obtained as a function of time.	153

Figure 5.7 Load-displacement data from (a) upper and (b) lower SMORSs stack obtained after different aging times in air at 120°C. Normalized value of momentary and relaxed loads at different aging time is shown in (c).	154
Figure 5.8 Load-displacement data from (a) upper and (b) lower SMORSs stack obtained after different aging times in air at 90°C. Normalized value of momentary and relaxed loads at different aging time is shown in (c).	155
Figure 5.9 Load-displacement data from (a) upper and (b) lower SMORSs stack obtained after different aging times in air at 60°C. Normalized value of momentary and relaxed loads at different aging time is shown in (c).	156
Figure 5.10 Load-displacement data from (a) upper and (b) lower SMORSs stack obtained after different aging times in DI Water at 90°C. Normalized value of momentary and relaxed loads at different aging time is shown in (c).	157
Figure 5.11 Load-displacement data from (a) upper and (b) lower SMORSs stack obtained after different aging times in 50/50 v/v ethylene glycol solution at 90°C. Normalized value of momentary and relaxed loads at different aging time is shown in (c).	158
Figure 5.12 Load-displacement data from (a) upper and (b) lower SMORSs stack obtained after different aging times in 0.1M sulfuric acid solution at 90°C. Normalized value of momentary and relaxed loads at different aging time is shown in (c).	159
Figure 5.13 Mass uptake results at 90°C for seal material used for SMORS. DI Water and 0.1M sulfuric acid solution show significantly higher mass uptake as compared to ethylene glycol solution.	160
Figure 5.14 (a) Restoring force decay with time at different temperatures, and (b) shows typical Arrhenius approach to predict seal life at a desired temperature for a 50% drop in restoring force.	161
Figure 5.15 Compression stress relaxation behavior of SMORS at 120°C, 90°C and 60°C in air.	162
Figure 5.16 Illustration of SMORS failure either due to (a) seal material degradation or (b) poor impregnation of seal material into GDL fibers.	163
Figure 5.17 Load-displacement data from (a) upper and (b) lower silicone rings stack obtained after different aging times in air at 120°C. Normalized value of momentary and relaxed loads at different aging time is shown in (c).	164

Figure 5.18 Load-displacement data from (a) upper and (b) lower silicone rings stack obtained after different aging times in air at 90°C. Normalized value of momentary and relaxed loads at different aging time is shown in (c).	165
Figure 5.19 Load-displacement data from (a) upper and (b) lower silicone rings stack obtained after different aging times in air at 60°C. Normalized value of momentary and relaxed loads at different aging time is shown in (c).	166
Figure 5.20 Load-displacement data from (a) upper and (b) lower silicone rings stack obtained after different aging times in DI water at 90°C. Normalized value of momentary and relaxed loads at different aging time is shown in (c).	167
Figure 5.21 Difference in stress relaxation behavior for silicone rings tested in forced and gravity convection ovens at 90°C. Also shown is the result obtained from CSR fixture tested periodically.	168
Figure 6.1 Illustration of the O-ring under compression shown with original and deformed configurations in ABAQUS.	184
Figure 6.2 Plot of experimental data and predicted uniaxial behavior in tension and compression using various material models.	185
Figure 6.3 Material Parameters and stability limit information on (a) Mooney Rivlin, (b) two-parameter Ogden, (c) Neo-Hookean, (d) Yeoh, and (e) Van der Waals hyperelastic material models.	188
Figure 6.4 FEA simulation of seals subjected to 25% compression for $R/r = 1$. The interfacial friction is given by $\mu = 0.1$. Note the asymmetric nature (with respect to 2-direction) of (a) stresses and (b) strains in 1-2-3 directions for O-ring cross-section.	189
Figure 6.5 FEA simulation of seals subjected to 25% compression for $R/r = 10$. The interfacial friction is given by $\mu = 0.1$. The stresses (a) and strains (b) are more symmetrically distributed in 1-2-3 directions for O-ring cross-section.	190
Figure 6.6 FEA simulation of seals subjected to 25% compression for $R/r = 100$. The interfacial friction is given by $\mu = 0.1$. The symmetry in stresses (a) and strains (b) is more pronounced in 1-2-3 directions for O-ring cross-section.	191
Figure 6.7 Illustration of concept for contact stress and width for O-ring seal.	192

Figure 6.8 Contact pressure profile for O-ring for (a) $R/r = 1$, (b) $R/r = 10$ & (c) $R/r = 100$ with rough ($\mu = 0.1$) interfacial condition. The symmetry of pressure is more evident as the ratio of R/r increases.....	193
Figure 6.9 Contact width and peak contact stress profiles for O-ring under compression for different R/r ratios.....	194
Figure 6.10 Illustration of the SMORS under compression showing (a) full cross-section with original and deformed shape, and (b) half section used for analysis in ABAQUS.	195
Figure 6.11 FEA simulation of SMORS subjected to 25% compression for $R/r = 20$. The interfacial friction is given by $\mu = 0$. The stresses (a) and strains (b) are symmetrically distributed in 1-2-3 directions for O-ring cross-section.....	196
Figure 6.12 Contact stress profile for frictionless and rough conditions from 10 to 40% compression of SMORS. Note the higher peak contact stress for the case where friction is present between seal and compression platen.....	197
Figure 6.13 Effect of interfacial friction (frictionless $\mu = 0$ and Rough $\mu = 0.3$) between compression platens and seal on (a) peak contact pressure and (b) contact width.	198
Figure 6.14 Shape factor for some common geometries.	199
Figure 6.15 Contact width and contact pressure data on O-ring compression from FEA analysis and Lindley and Dragoni equations.	201
Figure 6.16 Calculation of total load from contact width and contact pressure profile obtained from FEA of SMORS under compression.	202
Figure 6.17 Comparison of load versus % compression behavior obtained from finite element analysis in ABAQUS, theoretical approach based on Lindley's empirical relationship and experimental data from SMORS.....	203
Figure 6.18 Cross-section of SMORS to illustrate various components of a unitized electrode assembly (UEA) (membrane electrode assembly (MEA) consisting of cathode-membrane-anode assembly + two GDL layers).	204
Figure 6.19 (a) Simplified SMORS tested in compression stress relaxation tests, and (b) delamination at seal/GDL interface due to poor impregnation of seal material into fibers (Courtesy of Henkel Corporation).	205
Figure 6.20 Sliding at seal/GDL interface and lifting of seal web observed in ABAQUS.	206
Figure 6.21 Bending & rotation of GDL on compression of SMORS.	207

Figure 6.22 Illustration of Lindley’s approach used to develop peak contact stress profile to predict seal leakage.	208
Figure 7.1 New compression stress relaxation fixture design containing a load cell for continuous data collection via a data acquisition system and LabVIEW code.	217
Figure 7.2 Continuous compression stress relaxation test set-up showing (a) fixtures loaded with SMORS in various liquid solutions arranged in the water bath 90°C, (b) close-up of the fixtures showing polypropylene balls and glass wool to minimize liquid evaporation.	218

List of Tables

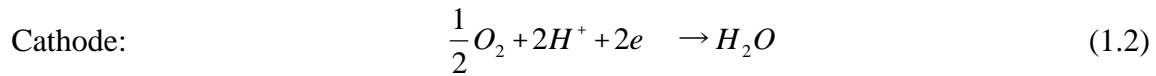
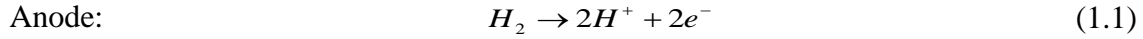
Table 3.1-1 Hyperelastic material models used in finite element analysis for material evaluation	81
Table 3.1-2 Experimental validation of ABAQUS simulation results.	89
Table 6-1 Test matrix developed to analyze the seal cross-sections using ABAQUS.	183
Table 6-2 Contact width and contact pressure data on O-ring obtained from FEA analysis and Lindley and Dragoni approach.....	200

1 Introduction

1.1 Background

Due to rising oil prices and increasing environmental concerns, the demand for alternative sources of energy and environmentally friendly fuels has increased over the years. One such alternative is the proton exchange membrane (PEM) fuel cell, which is an electrochemical device that combines hydrogen and oxygen to produce electricity, with water and heat as the by-product[1]. The PEM fuel cell offers a combination of benefits including low or zero emissions, high energy conversion efficiency and reliability, multi-fuel capability, scalability and ease of maintenance[2, 3]. Apart from this, they also exhibit rapid response to varying loads and rapid startup due to relatively low operating temperatures[3]. Fuel cells operate silently, so they reduce noise pollution as well as air pollution. The key components of a PEM fuel cell are the membrane electrode assembly (MEA), gas diffusion layers, bipolar plates, and sealing gaskets, as illustrated in Figure 1.1.

The membrane electrode assembly (MEA) consists of a proton-conducting polymer electrolyte membrane, typically a perfluorinated sulfonic acid polymer membrane sandwiched between two porous carbon electrodes (anode and cathode) [4]. The polymer membranes employed in PEM fuel cells are typically thin (18-100 μm) and flexible. The anode is supplied with fuel (hydrogen gas) while the cathode, the positive side of the fuel cell, is supplied with an oxidant, which is typically air. The electrodes are made porous to ensure good gas access, increased reaction surface area, and effective water removal. The polymer electrolyte membrane spatially separates the anode and cathode and ensures that the two individual half reactions, given in equations 1.1 and 1.2, occur in isolation from one another.



The anode conducts the electrons that are freed from the hydrogen molecules so that they can be used in an external circuit. The cathode conducts the electrons back from the external circuit, where they can recombine with the hydrogen ions and oxygen to form water. The MEA is typically less than 1mm thick[5].

A conductive diffusion material (backing layer or gas diffusion layer), usually made of a porous carbon paper or carbon cloth, is typically provided on both anode and cathode sides of MEA. The gas diffusion layer (GDL) is made of a stable material (like carbon) to conduct the electrons that leave the anode and after passing through the external load enter the cathode. The porous nature of the backing material ensures effective diffusion (flow of gas molecules from a region of high concentration to a region of low concentration) of each reactant gas to the catalyst on the MEA. The gas spreads out as it diffuses so that when it penetrates the backing, it will be in contact with the entire surface area of the catalyzed membrane. Assembly consisting of MEA and gas diffusion layers on anode and cathode is called unitized electrode assembly (UEA) which serves as a repeating unit in a fuel cell stack.

Pressed against the outer surface of each GDL is a component called a bipolar plate that typically serves as both flow field and current collector. Channels in the bipolar plate carry the reactant gas from the place where it enters the fuel cell to the place where it exits. The pattern of the flow field in the plate (as well as the width and depth of the channels) has a large impact on how evenly the reactant gases are spread across the active area of the MEA[6]. Flow field design also affects water supply to the anode side of the membrane and water removal from the cathode.

The current collector plates contain flow channels for effective distribution of reactant gases along the surface of the electrodes. The conductive collector plates are made of a lightweight, strong, gas-impermeable, electron-conducting material- graphite, metallic or composite plates are commonly used[7, 8]. For feeding the reaction media, distributor plates having integrated gas or liquid feeding ducts are used. In order to prevent an uncontrolled escape of the reaction media, PEM fuel cell stacks typically require a liquid and gas-tight seal between UEA and bipolar plates to keep the reactant gases within their respective regions, preventing them from reacting directly. The long term stability and durability of the elastomeric seal are critical to the lifetime and commercial viability of the PEM fuel cells. In order to meet DOE requirements, PEM fuel cell seals are required to demonstrate durability of about 40,000 h under normal operating conditions (-40°C to 90°C)[9].

The elastomeric seals in a PEM stack are compressed to a desired level in order to generate required sealing force to prevent any leakage. Due to material aging, the sealing force decays owing to physical or chemical relaxation of the material. Thus, leakage can occur as a result of loss of sealing force or seal failure. Air that leaks through the seal chemically interacts with hydrogen and the Pt-based catalysts, generating hydrogen peroxide, which in turn attacks the catalysts and the electrolyte membrane and causes gradual loss of electrode catalytic activity and degradation of the membrane electrolyte[10]. Also, an elastomeric seal under compression typically has high concentration of opening tensile stresses on the surface and in the bulk (comparatively much higher in the bulk than on the outside surface), as shown in Figure 1.1, which may lead to propagation of an already present crack on the surface. A crack on the surface and in the bulk of the seal may be introduced during molding or handling the seals during post-molding operations. These cracks or voids may appear to be insignificantly small/minor flaws at

first but may lead to slow tearing of the material over a period of time as material degrades due to aging and ultimately affecting the durability target. Also, as the seal under compression is simultaneously exposed to a hot, humid and acidic environment[11], where the temperature may reach as high as 90°C depending on the load requirement, temperature cycling in the presence of environment may introduce hygrothermal fatigue in the material resulting in crack nucleation and growth over a period of time. Since the long-term performance of fuel cell stacks depends heavily on the durability of the seals, the resistance of the seal material to the above mentioned failure modes is one of the functional requirements for improved lifetime of fuel cells.

For lifetime prediction and durability of the seal material and to address issues discussed above, several aspects must be taken into consideration for mechanical characterization of the seal material in environmental conditions relevant to fuel cells:

1.1.1 Degradation of seal material properties such as tensile strength, modulus etc

As mentioned before, a seal material under stress is exposed to a variety of environments at elevated temperature. Exposure to environments results in mass uptake due to diffusion of liquid media into the material matrix and/or mass loss due to the evaporation of volatile components of seal material in air or degradation of seal material in a liquid environment. The presence of stresses may even accelerate the mass uptake or loss process, leading to faster degradation of material properties to an extent that hygrothermal fatigue in the fuel cell eventually gives rise to crack nucleation and growth. To understand how the combination of stress and environments result in material degradation, a test fixture was designed so that specimens can be subjected to strain in the presence of environment. High values of strain (120% in tension) were used so that degradation process in the seal material could be accelerated to obtain meaningful results in a comparatively short time. Aged specimens can be taken out of the conditioning media and tested

to evaluate how material properties have changed with respect to neat material properties. Such accelerated testing may also provide information on aggressiveness of various environments on seal material so attention during further testing can be focused on environments that degrade the material faster.

1.1.2 Characterization of tear properties

Tear strength is an important property of elastomeric materials for many applications because it influences the lifetime of a component. Trouser tear tests are typically performed on elastomeric samples to estimate the tear energy, which depends on rate of testing (loading rate) and temperature. Data obtained from trouser tear tests conducted at various loading rates and temperatures is often used to develop master curves. Development of such master curves may provide an estimate on threshold value of the tear strength. Trouser tear samples can also be aged in environments and a master curve generated to compare how the threshold value is affected due to aging. The lowest possible threshold value of tear strength may then be considered during component design.

1.1.3 Stress relaxation of the seal material under compression

Seal material relaxation may be addressed by performing typical compression stress relaxation (CSR) in commercially available fixtures designed to test disk or ring samples according to the procedure outlined in ASTM D-6147-97[12]. Data obtained from such testing is helpful to characterize the bulk material alone. For the case where a seal material is molded onto a UEA, various interfaces, such as the seal/GDL interface and seal/bipolar plate interface, adds to the complexity and therefore data obtained from bulk material testing may not be reliably used to predict relaxation behavior of a molded seal assembly. To effectively characterize the molded seal assembly during long-term environmental aging, custom designed fixtures were designed for

this study and will be discussed in detail later in the dissertation. Relaxation studies thus conducted will provide more relevant data that can be used for lifetime predictions

1.2 Motivation

The primary goal of this research was to characterize the mechanical and viscoelastic properties of elastomeric seals used for fuel cell applications, along with a durability assessment based on constitutive properties, chemical resistance, and degradation mechanisms. In order to establish the baseline characterization of the seal material and to obtain bulk material properties, uniaxial tension (ASTMD412C[13]) and trouser tear (ASTMD624T[14]) tests were conducted on samples prepared from as-received material. For the purpose of accelerated characterization, a fixture was designed so that dogbone samples, cut from seal material slabs using ASTM D412 Die C, could be subjected to high levels of strain during aging in various environments. Samples were taken out of the conditioning media after the desired aging time was reached and tested in a uniaxial tension test configuration. Useful insights into material property degradation due to the various combinations of stress and environments were obtained, and aging environments could then be arranged in increasing order of their aggressiveness to the seal material. With this information, further testing to explore stress relaxation behavior of molded seal assembly could be focused on most aggressive environments. Trouser tear tests were conducted on reinforced samples, prepared using specifications provided in ASTM D624 Type T, at various loading rates and temperature so that rate and temperature dependence of the fracture energy of the seal material could be explored, obtained from a tear energy master curve generated on the basis of time-temperature superposition principle (TTSP).

Besides obtaining material property data on bulk material and studying aging effects on these properties, the primary concern of this project was to study stress relaxation of molded seal

assembly or SMORS under compression in various environments. A dual-chamber fixture was designed so that a material can be evaluated based on a two-network model in rubber elasticity theory where permanent set of a material could be estimated from stress relaxation and unstressed material behavior in an environment. SMORS arranged in series between stainless steel washers were placed in two chambers of the fixture and aged in a given environment. Load versus displacement data on SMORS from both upper and lower chambers were periodically obtained by using a high-precision Instron 5848 (Norwood, MA) MicroTester and analyzed to obtain momentary as well as relaxed properties of SMORS respectively. Data obtained in various environments were compared and provided significant insight not only to improve seal material properties, as to the amount and distribution of antidegradants in seal material matrix, but also mixing and molding parameters to make SMORS. Tests were also carried out on ring samples cut from silicone slabs and data obtained on relaxed and momentary properties of silicone provided insight into fixture's sensitivity to small load variations leading to change in fixture design. The change included adding a load cell and a micrometer in the fixture which along with the data acquisition system provided automatic data collection for long-term studies. Additionally, finite element characterization of the seal design provided significant insights into stress/strain, contact pressure, and contact width distribution as well as the role of friction at various interfaces. Load required to achieve a given compression of SMORS were calculated using FEA tools and an analytical approach using Lindley's equation. Good correlation between analytical and experimental results was obtained up to 25% compression of SMORS whereas FEA overestimated the load values at a given compression. Assumptions used in the FEA are discussed to explain possible reasons behind the discrepancy in load values.

1.3 Dissertation Organization

This dissertation will begin with an in-depth literature review in an attempt to provide sufficient background to support the topics that will be addressed throughout the remainder of this dissertation. Various tests were conducted to characterize the seal material, the details of which will be presented. Finally, this dissertation concludes with the presentation of the analysis methods used, test results obtained, and conclusions drawn from the work conducted for the purpose of this research. This dissertation is organized into the following chapters:

- *Chapter 1:* Provides a brief description of background information related to this research and presents the objective and significance of this study along with the organization of this dissertation.
- *Chapter 2:* Reviews relevant literature with regards to the following key topics: Fuel cell sealing, seal failure modes, stress relaxation, lifetime prediction methodologies, and hyperelastic material modeling.
- *Chapter 3:* In this chapter, mechanical characterization of properties such as tensile strength, modulus, strain to break etc. is presented and also how these properties are affected in the presence of a test environment. Accelerated characterization techniques were employed to study the combined effect of stress and environment on material properties and also identify the most detrimental environments to the seal material. A review of the material studied, specimen preparation, method followed, and test methods utilized will be discussed.
- *Chapter 4:* In this chapter, tear property characterization of the seal material in terms of rate and temperature effect on tear strength is presented. A preliminary estimate of seal

lifetime utilizing finite element analysis tools and tear energy master curve is also presented.

- *Chapter 5:* This chapter investigates the stress relaxation behavior of sub-scale molded seals. Behavior of molded seals as well as bulk material samples were investigated in various environments and momentary, as well as relaxed properties, were determined to understand the seal failure mechanism.
- *Chapter 6:* This chapter presents a finite element characterization of the seal design. Finite element analysis of several seal cross-sections was carried out and the results generated were compared against experimental and analytical data.
- *Chapter 7:* This chapter provides a summary of the research project including relevant conclusions and recommendations for future work.

References:

1. L.J. Blomen and M.N. Mugerwa, *Fuel Cell Systems*. 1993, New York: Plenum Press.
2. K.A. Mauritz and R.B. Moore, "State of Understanding of Nafion," *Chemical Reviews*, **104**(10), 4535-4585, 2004.
3. S. Gottesfeld and T. Zawodzinski, "Polymer Electrolyte Fuel Cells," *Advances in Electrochemical Science and Engineering*, **5**, 195–301, 1997.
4. K.D. Kreuer, S.J. Paddison, E. Spohr, and M. Schuster, "Transport in Proton Conductors: Reactions and Phenomenology," *Chemical Reviews*, **104**, 4637-4678, 2004.
5. R. O'Hayre, S.-W. Cha, W. Colella, and F.B. Prinz, *Fuel Cell Fundamentals*. 2006, Hoboken, New Jersey: John Wiley & Sons.
6. S. Thomas and M. Zalbowitz, *Fuel Cell-Green Power*. 2006, U. S. Department of Energy : Energy Efficiency and Renewable Energy.
7. V. Mehta and J.S. Cooper, "Review and Analysis of Pem Fuel Cell Design and Manufacturing," *Journal of Power Sources*, **114**, 32-53, 2003.
8. A. Herman, T. Chaudhuri, and P. Spagnol, "Bipolar Plates for Pem Fuel Cells: A Review," *International Journal of Hydrogen Energy*, **30**, 1297-1302, 2005.
9. M.T. Hicks, K. Epping, and T. Benjamin, *Mea and Stack Durability for Pem Fuel Cells*, in *2006 Hydrogen Program Review*. 2006, DOE Saint Paul, MN.
10. T.J. Schmidt, U.A. Paulus, H.A. Gasteiger, and R.J. Behm, "The Oxygen Reduction Reaction on a Pt/Carbon Fuel Cell Catalyst in the Presence of Chloride Anions," *Journal of Electroanalytical Chemistry*, **508**, 41- 47, 2001.
11. J. Tan, Y.J. Chao, J.W.V. Zee, X. Li, X. Wang, and M. Yang, "Assessment of Mechanical Properties of Fluoroelastomer and Epdm in a Simulated Pem Fuel Cell Environment by Microindentation Test," *Material Science and Engineering A*, **In Print**2008.
12. ASTM-D6147-97, *Standard Test Method for Vulcanized Rubber and Thermoplastic Elastomer-Determination of Force Decay (Stress Relaxation) in Compression*, in *Annual Book of ASTMStandards*. 2008, ASTMInternational: West Conshohocken, PA, 19428-2959.

13. ASTM-D412-06a, *Standard Test Methods for Vulcanized Rubber and Thermoplastic Elastomers-Tension*, in *Annual Book of ASTM Standards*. 2002, ASTM International: West Conshohocken, PA, 19428-2959.
14. ASTM-D624-00, *Standard Test Method for Tear Strength of Conventional Vulcanized Rubber and Thermoplastic Elastomers*, in *Annual Book of ASTM Standards*. 2007, ASTM International: West Conshohocken, PA, 19428.

2 Literature Review

A fuel cell is an electrochemical energy converter that includes two electrodes placed on opposite surfaces of an electrolyte[1]. Polymer electrolyte membrane (PEM) fuel cell (FC) stack contain 100 or more individual cells connected in series and require elastomeric gaskets on both sides of each cell to keep the reactant gases within their respective regions. Seals not only prevent leakages but also function as electrical insulation and stack height control[2]. If any gasket degrades or fails, the reactant gases can leak overboard or mix with each other directly during operation or standby, affecting the overall operation and performance of the FC. The performance of elastomeric materials in various applications was studied extensively [3-7]. Nakajima[4] studied polyacrylate rubber in comparison with fluoro-rubber for automotive engine sealing application. Dillard et. al.[5] discussed the durability of elastomeric seal in a PEM fuel cells. Youn and Huh [6] reported the surface degradation of high temperature vulcanizing HTV silicone and ethylene propylene diene monomer EPDM rubber under accelerated ultraviolet weathering conditions. Mitra et al. [7] studied the time-dependent chemical degradation of a fluoro-elastomer in an alkaline environment. Although substantial literature exists regarding degradation of the elastomeric gasket materials, few results were reported for the degradation and its mechanisms in PEM FC environments [5, 8-13]. Typical sealing materials utilized in PEM fuel cells include fluorinated elastomers, EPDM, silicone[14, 15], and glass-reinforced PTFE[16]. All of these materials offer good chemical resistance; however, there are problems associated with each system. Fluoroelastomers offer excellent sealing properties, but are poor when it comes to gasketing and disassembly of the cell. Silicone offers good thermal and chemical resistance but has a high value of compression set. PTFE-based systems are only suited for one-time use applications due to poor compressive compression set. Tan et. al. studied

the degradation characteristics of silicone[8, 11, 13], fluoroelastomers [8, 9], and EPDM[8, 9] in a simulated fuel cell environment consisting of solutions containing hydrogen fluoride and sulfuric acid and found significant leaching of fillers from seal material that contaminated the gas diffusion layer and the MEA. Cleghorn et. al. [17] and St-Pierre [18] observed the complete degradation of the glass reinforced silicone seal in the fuel cell stack where silicon from the seal could be detected throughout the MEA. Schulze et. al.[15] investigated the degradation of silicone and found that silicone in direct contact with a perfluorosulphonic membrane degraded at the anode as well as at the cathode, leading to coloration of the membrane and detectable amounts of silicon on the electrodes. Ahn et al.[19] observed a significant decay in fuel cell performance due to migration of silicone seal decomposition products at the catalyst layer on both anode and cathode sides.

Results from these few studies of PEM sealing systems suggest that a systematic approach needs to be adopted by which a given seal material, exposed to chemical, thermal, and mechanical environments in a fuel cell, can be effectively characterized so that high performance sealing systems could be developed. In order to quantify the performance and durability of a sealing system so that the long term performance can be accurately predicted, seal failure modes must be understood.

2.1 Seal Failure Modes

There may be a variety of failure modes in PEMFC stack [5, 20-24] that may result in leakage and reduced fuel cell performance but the study only focuses on failure modes specific to elastomeric seals. A review by de Bruijn [25] covers the durability issues associated with several fuel cell components. During the operation of a fuel cell, the seal material is subjected to mechanical stress in the presence of cyclic temperature and chemical environments. The chemical and

changing thermal environments pose a significant durability concerns for polymeric materials in terms of enhanced degradation. Thermal cycling alone may result in enhanced stress relaxation and compression set leading to reduced stack pressure affecting the performance of fuel cell[26]. Compression of a simple seal geometry, such as an O-ring, results in a direction-dependent stress state where compressive as well as tensile stresses are present. Residual stresses induced during seal material curing or due to shrinkage against the bipolar plate may be tensile in nature and lead to failure over time. The presence of tensile stresses and corrosive environment may lead to the formation of a crack or growth of a pre-existing crack which may lead to seal failure. The above mentioned failure modes, each of which is affected by a complex interaction of physical and chemical processes[27-29], may be grouped as follows:

1. Seal cracking/fracture due to material degradation in environments, and
2. Reduction in sealing contact stress due to stress relaxation.

These can both depend on diffusion of fluid into the rubber leading to swelling, changes in the internal rubber structure, and modification of physical properties. The process causing stress relaxation may be physical or chemical in nature and under normal conditions both processes can occur simultaneously. Physical relaxation involves the motion of molecular chains towards new configurations in equilibrium at the new strained state, and may involve the movement of entanglements and dangling ends [30]. The whole process of chain flow and entanglement motion is generally believed to be reversible in crosslinked systems, upon removing the strain from the system. Chemical relaxation[7, 31-35] involves primarily scission and crosslinking events resulting from the breakage and formation of covalent bonds, respectively[36]. Chemical processes may occur, either in the absence (thermal degradation [37-41]) or presence of oxygen (oxidative degradation), both leading primarily to chain scission reactions. The chemical

component of relaxation is typically irreversible. At normal to low temperatures and/or short periods of time, stress relaxation is dominated by the physical processes, whilst at high temperatures and/or long time periods, the chemical processes are often dominant[42]. Both physical and chemical relaxation processes cause a reduction in the counterforce when conducting relaxation experiments. Cracks may be present on the surface of the seal as a result of manufacturing or handling and may also develop during service due to seal material degradation. During the course of fuel cell operation, the seal is subjected to temperature cycling (depending on the fuel cell usage and load) in the presence of various aggressive environments. A pre-existing crack on the seal surface may grow and reach a critical size leading to seal failure. Also, the presence of a liquid environment may significantly reduce the energy required for the crack to propagate[43].

2.2 Seal Material Characterization: Test Protocols

The degradation of the seal material due to the aging in the presence of a corrosive environment, temperatures as high as 90°C, and mechanical stress may result in the loss of sealing force leading external leaks of coolant, gas crossover, or plate electrical shorting. It is, therefore, very important to develop and fabricate durable seals that could last the desired lifetime of a fuel cell unit. To be able to choose the best-suited sealing material or to reliably judge whether a given material is suited for sealing applications, seal material characterization must be conducted and an accelerated means to degrade seal material must be adopted so that the performance of such gaskets or seals under service conditions can be accurately predicted. This study involves developing an approach for seal life prediction that considers the different factors limiting seal life, and also performs direct measurements of changes in sealing force under relevant conditions. When an elastomeric seal is exposed to chemical environments at high temperature,

there is an interaction between liquid diffusion, chemical aging, and other changes in physical properties (such as modulus change and stress relaxation). These changes in the properties of the seal with time, and the effect of these changes on the sealing ability of the seal, can be measured on relevant test specimens, provided the means exist to interpret the consequences for actual seals.

2.2.1 Bulk Material Properties

Elastomers are normally amorphous polymers above the glass transition temperature. They exhibit the ability to elongate to a large extent under an applied force and subsequently return to their original shape. To obtain material properties of the bulk specimens, standard tests such as uniaxial tension and trouser tear are conducted. These tests are typically performed according to the procedure outlined in ASTM standards such as ASTM D412 [44] for tensile and ASTM D624 [45] for tear properties and provide baseline properties of the neat material. A typical result of a tensile test of an elastomer is a stress-strain curve of S-shape, for which Hooke's law is not valid. For characterization of tensile properties of an elastomer, tensile strength, strain to break, tension set, and modulus at 100% strain are typically used[46, 47]. In measurement of tensile stress-strain properties, a test piece is stretched to the breaking point, and the force and elongation are measured at regular intervals. Modulus is relevant where stiffness of the product is important [46]. Tensile strength can be used to evaluate aging performance, though tensile strength decreases more slowly than elongation to break[48]. Owing to the differences in aging characteristics of tensile strength and elongation to break, the most important property criterion for lifetime prediction must be selected based on the particular application[49].

In measuring tensile strength, the material has to completely break through the cross-section in the absence of a defect, whereas measurement of the tear strength indicates the material resistance

to the propagation of a defect. Tear properties are commonly determined at a constant rate, but such properties can also be determined at various rates due to the rate-dependent behavior of elastomeric materials. The tear strength of noncrystallizing elastomers depends on the rate of tearing and temperature [50, 51]. These variations parallel closely the variation of viscoelastic properties with rate and temperature, i.e. the tear strength increasing with increasing viscoelastic energy dissipation. Tearing in noncrystallizing elastomers often proceeds in a steady, time-dependent manner whereby the force in a trouser tear test carried out at a constant rate remains relatively constant. In strain-crystallizing elastomers, time-dependent growth is often absent and tearing generally proceeds in a stick-slip manner (also referred to as knotty tear). In this case, experimental determination of the critical tearing energy becomes complicated because of the unstable tearing, where the crack does not propagate at a steady rate but is arrested and re-initiated at somewhat regular intervals resulting in stick-slip tearing. The force necessary to drive the crack varies widely from a maximum at crack initiation to a minimum at crack arrest. In some cases, the crack deviates sideways from a linear path resulting in specimen failure. To suppress unstable crack growth and crack path deviation, Gent and Henry[52] developed a constrained trouser specimen by attaching thin fiber reinforced tape on opposite sides of the specimen legs. The use of this specimen helped to control the crack-path deviation phenomena. Such an approach was used in this study to characterize tear behavior of the seal material.

2.2.2 Stress Relaxation - Loss of Sealing Force

Elastomers are widely used for a number of engineering, scientific and industrial applications due to their broad range of tailorable viscoelastic properties[53-55]. Developing lifetime estimates for these materials, particularly in harsh environments while under physical stress, requires detailed knowledge of the degradation processes and the resulting effects on service

properties. For example, elastomeric materials subjected to physical stress while undergoing crosslinking reactions are known to exhibit permanent set [56, 57]. Elastomeric seals, when used in compression, generate a restoring force that not only depends on the compressive strain but also on the aging with time and with exposure to elevated temperature and/or to a chemical environment. Aging affects thermal rheological properties, and the ability of the samples to keep their initial dimensions. When stress is removed after a long loading time, a seal only slowly reaches its initial dimensions or may even show permanent distortion[58]. This phenomenon is known as “compression set” and is of utmost importance for fuel cell applications [59, 60]. The long-term mechanical behavior of seals is typically studied by compression stress relaxation tests in which a cylindrical disk sample with dimensions 13.0mm (diameter) \times 6.3mm (thickness) or 29.0mm (diameter) \times 12.5mm (thickness) or a washer sample with the dimensions 12.5mm(inside diameter) \times 19.0mm(outside diameter) \times 2.0mm (thickness) per ASTM D 6147 [61] is sandwiched between two solid parallel surfaces that compress the sample. The resulting stress in the sample produces a restoring force which decreases with time. A typical compression stress relaxation experiment imposes a constant strain while measuring the resulting force, $F(t)$. The average normal stress, $\sigma(t)$, is calculated by dividing the restoring force, $F(t)$, by the cross-sectional area, A , of the sample.

Long-term relaxation experiments generally require the development of dedicated instruments that hold the seal in compression while measuring the restoring force periodically without unloading the sample. Numerous methods have been developed to measure stress relaxation in compression and the advantages and disadvantages of continuous versus intermittent test methods have been elucidated[62-64]. These methods differ in fixture design and in the measurement of the sealing force. Hardware or fixture design influences the stress relaxation

response and overall sensitivity of the measurement. Sample geometry (large or small compression set buttons, o-ring, die cut washer, micro-pellets, molded part) also has an impact on the extent of diffusion-limited oxidation anomalies, as well as test-to-test variability. Continuous monitoring of fixtures (e.g. Elastocon[65] & modified Jamak) allows for continuous force measurement via a force transducer permanently connected to the fixture, whereas in the intermittent type (Jamak, Jones-Odom, Shawbury-Wallace[66], Wykeham-Farrance[67]), large strain is initially induced in the sample by sandwiching it in the compression cell and relaxed force measurements are obtained over time by adding an incremental strain. Such superposition of small deformations onto a dominant large strain has been shown to be useful for exploring the time dependence of viscoelastic properties (relaxation behavior) [68, 69].

Stress relaxation and aging in strained polymer networks can be attributed to two distinct processes. At short times, relaxation is dominated by viscoelastic effects, in which chains approach a new equilibrium state through sliding, rotation etc. The dominant effect at long times is stress relaxation occurring as a result of chemical changes, such as chain scission, that affect the physical properties of an elastomeric material [70-72]. Generally, physical relaxation proceeds approximately linearly with logarithmic time and is often overtaken by chemical relaxation which proceeds approximately linearly with time[73]. Tobolsky [27, 57, 74] and co-workers systematically studied these chemical relaxation effects and developed a molecular theory based on which a material postcured in a strained state could be analyzed with a two-network model consisting of distinct networks crosslinked in the unstrained and strained states. According to the two-network model, intermittent measurements of the properties of elastomers maintained in a relaxed state during exposure to elevated temperature provide a method of measuring the net rate of chain scission and crosslinking. On the other hand, it is possible to isolate the chain scission

reaction by measuring the decay of stress in a sample maintained at constant extension at elevated temperatures. The decay of stress is a direct measure of scission of the molecular chains of the network because the crosslinking of the chains, occurring simultaneously, does not cause any increase of stress. Based on this approach, Andrews, et al. [57] developed the relationship to calculate the permanent set for an elastomeric sample:

$$\% \text{ Permanent Set} = \left\{ \left[\frac{C_1}{(U/X)C_2 + 1} + 1 \right]^{\frac{1}{2}} - 1 \right\} C_3 \quad (2.1)$$

where $C_1 = \left(\frac{l_x}{l_u}\right)^3 - 1$, $C_2 = \left(\frac{l_x}{l_u}\right)^2$, $C_3 = \frac{100}{(l_x/l_u) - 1}$, l_u is the length of the sample before extension, l_x is the length of the sample after compression, U is the value of the relaxed load obtained from the strained samples in lower stack at a desired strain and $U + X$ can be defined as the load obtained from unstrained samples in upper stack at a desired strain, as shown in Figure 2.1. In other words, U is a measure of the rate of chain scission and $U + X$ is a measure of the net rate of chain scission and crosslinking occurring in the material at an elevated temperature so the difference between the two will provide the net rate of crosslinking and its effect on the seal behavior in terms of permanent set. For this part of the study, measurement of U and $U+X$, as described above, was conducted using a custom-designed fixture. The details on fixture design are provided in chapter 4.

2.2.3 Lifetime Prediction Methodologies

Owing to the degradation of a seal material due to aging in environments[75], as-received seal material properties may change over time and it is very important to estimate the extent to which a material has degraded in a given environment. Material property changes are usually estimated by conducting tests on samples aged in relevant environmental conditions for a desired time.

Since aging of a material at operating conditions may take very long to show observable change, degradation is typically accelerated. The accelerated aging method consists of increasing the reaction speeds of the material without modifying the degradation mechanisms that are liable to occur with the long term use of the material. This usually involves increasing the exposure temperatures, stress levels, or concentration of the liquid solutions in which the material is aging. Failure times or degradation rates are determined at accelerated aging conditions and are used to extrapolate material performance to ambient conditions. In order to predict the failure point in the future, Arrhenius and WLF (Williams-Landel-Ferry transform) [76] methods are often used. The Arrhenius model is often used where physico-chemical mechanisms are dominant, e.g. thermo-oxidative aging[48], whereas a WLF approach is employed to predict viscoelastic effects (creep, relaxation etc.). Arrhenius extrapolations assume that a chemical degradation process is controlled by a reaction rate k proportional to $\exp(-E_a/RT)$, where E_a is the Arrhenius activation energy, R the gas constant (8.314 J/mol-K), T the absolute temperature, and A the pre-exponential factor, as shown in Equation 2.3.

$$k = A \times \exp\left(\frac{-E_a}{RT}\right) \quad (2.2)$$

Therefore, a log-plot of reaction rates (k) or degradation times ($1/k$) versus inverse temperature ($1/T$) is expected to result in a straight line, allowing simple extrapolations to lower temperatures, as illustrated in Figure 2.2. The main assumption made here is that the chemical kinetics of material degradation remain the same at elevated and service temperatures.

The WLF model is based on the physical change of the polymer, i.e. the progressive disentangling of the macromolecules under the effect of stress (creep) or permanent deformation (relaxation). These viscoelastic processes can be modeled using concepts derived from molecular

dynamics[28]. This approach is based on the time-temperature superposition principle (TTSP) [77] and involves shifting the plots of property versus time determined at different temperatures to the plot at a selected reference temperature until the property-time curves overlap. Such construction is illustrated in Figure 2.3. Hence, by successive shifts, a master curve at the reference temperature is obtained. Use is made of the WLF equation to perform a time-temperature superposition:

$$\text{Log}(a_T) = \frac{C_1(T - T_o)}{C_2 + (T - T_o)} \quad (2.3)$$

where a_T is the shift factor of an isotherm determined at temperature T , in relation to the isotherm at the reference temperature T_o , and C_1 and C_2 are two adjustable coefficients which are dependent upon the material. The WLF technique has the advantage that no particular measure of the reaction rate has to be chosen nor any form assumed for the change of parameter with time, but it can only be used if the curves at different temperatures have essentially the same form [46]. Although both Arrhenius [78-82] and WLF[83-86] forms have been used for lifetime prediction of elastomeric material, results obtained from both may be compared to obtain more conservative lifetime estimates[87].

2.3 Constitutive Modeling of Elastomeric Materials

2.3.1 Background on Hyperelasticity

An elastomer is a polymer that exhibits rubber elastic properties, i.e. a material that can be stretched to several times its original length without breaking (very high deformability) and which, upon release of the stress, immediately returns to its original length (complete recoverability). A typical true stress-strain curve for vulcanized natural rubber is shown in Figure

2.4. In order for a material to exhibit rubber-like properties, three molecular requirements must be satisfied[88]:

1. the presence of long-chain molecules, with freely rotating links;
2. weak secondary forces between the molecules i.e. the chains must have a high degree of flexibility and mobility; and
3. an interlocking of the molecules at a few places along their length to form a three-dimensional network.

The first requirement is associated with the very high deformability. It arises from the fact that the molecules in an elastomeric material must be able to alter their arrangements and extensions in space dramatically in response to an imposed stress, and only a long-chain molecule possess very large number of spatial arrangements of very different extensions. The second characteristic required for rubberlike elasticity also relates to the high deformability. It specifies that the chains be flexible and mobile enough that the different spatial arrangements of the chains are accessible. That is, changes in these arrangements should not be hindered by such constraints as might result from inherent rigidity of the chains, or by decreased mobility as would result from extensive chain crystallization, or from the very high viscosity characteristic of the glassy state[88-90]. The last characteristic cited is required to obtain the recoverability part of the definition. The network structure is obtained by joining together, or crosslinking, pairs of segments, approximately 1 out of every 100, thereby preventing stretched polymer chains from irreversibly sliding by one another. The structure obtained in this way is illustrated in Figure 2.5, in which the crosslinks may be either chemical bonds or physical aggregates, like the small crystallites in a partially crystalline polymer or the glassy domains in a multiphase triblock copolymer[89].

The early molecular-based statistical mechanical theory was developed by Wall & Flory[91] and Flory & Rehner[92], with the simple assumption that chain segments of the network deform independently and on a microscopic scale in the same way as the whole sample (affine deformation). The crosslinks are assumed to be fixed in space at positions exactly defined by the specimen deformation ratio. This model is referred to as the ‘affine network model’. The affine network model assumes that the junction points (i.e. the crosslinks) have a specified fixed position defined by the specimen deformation ratio (λ). The chains between the junction points are, however, free to take any of the many possible conformations. The stress and strain relations in a rubber are derived on the basis of the affine network model with the following assumptions[88]:

1. The chains between crosslinks can be represented by Gaussian statistics of phantom chains.
2. The free energy of the network is the sum of the free energies of the individual chains.
3. The positions of the crosslinks are changed precisely according to the macroscopic deformation, i.e. deformation is affine.
4. The unstressed network is isotropic.
5. The volume remains constant during deformation.

The derivation of the stress-strain equation goes through some elementary steps. The Gaussian distribution function for the end-to-end distance expresses the probability of finding the end of a chain at a certain position (x,y,z) with respect to the other chain end found at $(0,0,0)$, as shown in Figure 2.6. This equation expresses, to phrase it differently, the number of conformations a chain can take provided that the chain ends are in $(0, 0, 0)$ and (x, y, z) . It is then possible to calculate the Helmholtz free energy (the free energy associated with constant volume) for a single chain

and by adding the contributions from all individual chains of the network, also for the network. The stress-strain equation is finally obtained by taking the derivative of the Helmholtz free energy with respect to length. The Gaussian function describing the distribution of the chain end position[88] is given as:

$$p(r)dx dy dz = \frac{b^3}{\pi^{\frac{3}{2}}} \exp(-b^2 r^2) dx dy dz \quad (2.4)$$

where $b^3 = \frac{3}{2nl^2}$. The Helmholtz free energy, A (the free energy associated with constant volume) for a single chain is given as:

$$A = U - TS \quad (2.5)$$

where U is the internal energy, T is the temperature, and S is the entropy of a single chain. For a change taking place at constant temperature,

$$dA = dU - TdS \quad (2.6)$$

From the first law of thermodynamics, the change in internal energy in any process is given by:

$$dU = dQ + dW \quad (2.7)$$

where dQ and dW are respectively the heat absorbed by the system and the work done on it by the external forces. From equations 2.7 and 2.8,

$$dA = dQ + dW - TdS \quad (2.8)$$

The second law defines the entropy change dS in a reversible process by the relation:

$$TdS = dQ \quad (2.9)$$

Combining equations 2.9 and 2.10 yields (at constant T)

$$dW = dA = dU - TdS \quad (2.10)$$

which signifies that in a reversible isothermal process, the change in Helmholtz free energy is equal to the work done on the system by the applied forces. According to the basic concept of the kinetic theory, the deformation of a rubber (at constant temperature) is associated with a reduction of entropy, with no change in the internal energy i.e. $dU = 0$. Therefore,

$$dW = dA = -TdS \quad (2.11)$$

For gases and solids, the work done on the system in a small displacement is written as:

$$dW = -pdV \quad (2.12)$$

For problems related to the elasticity of solids, the work done by a tensile force, for example, on a specimen of length l in a small displacement is give by:

$$dW = -fdl \quad (2.13)$$

When, in addition, a hydrostatic pressure (e.g. atmospheric pressure) is also present, the total work done by the applied forces becomes:

$$dW = fdl - pdV \quad (2.14)$$

In the case of rubbers, the volume change is usually very small, so as a first approximation can be neglected. Combining equations 2.12 and 2.15, it can be written that:

$$f = -T \frac{ds}{dr} \quad (2.15)$$

According to the general principles of statistical thermodynamics, as developed by Boltzmann, the entropy will be proportional to the logarithm of the number of configurations available to the system i.e. to the logarithm of the number of possible configurations corresponding to any specified state. The entropy s of the chain is therefore given by:

$$s = k \cdot \ln\{p(r)d\tau\} \quad (2.16)$$

where $d\tau$ is the infinitesimal small volume. Using equations 2.5 and 2.6 along with 2.16 yields,

$$s = k \cdot \ln\left(\frac{b^3}{\pi^2}\right) - kb^2r^2 + k \cdot \ln d\tau \quad (2.17)$$

Since the volume element $d\tau$ is assumed constant, equation 2.18 can also be written as:

$$s = c - kb^2r^2 \quad (2.18)$$

Where $c = k \cdot \ln\left(\frac{b^3}{\pi^2}\right) + k \cdot \ln d\tau$ and is of no physical significance when the difference of entropy

between any two states is of concern. Combining equations 2.16 and 2.19 yields:

$$f = 2kTb^2r \quad (2.19)$$

Thus, a molecule with its ends fixed at specified points is acted upon by a tensile force, f , in the direction of the line joining its ends and proportional to the length of the line r , as shown in Figure 2.7. Also, because of continuous fluctuations in a molecular chain, f is an average quantity.

In order to define stress-strain relationships for a rubber specimen, Let's take a unit cube subjected to strains in three perpendicular directions and transformed into a rectangular parallelepiped having three unequal edge lengths λ_1 , λ_2 , and λ_3 , as shown in Figure 2.8. These extension ratios may be greater than unity, corresponding to a stretch, or less than unity, corresponding to a compression, provided that the assumption for constancy of volume, namely,

$$\lambda_1\lambda_2\lambda_3 = 1 \quad (2.20)$$

is satisfied. For an individual chain, shown in Figure 2.9, having an end-to-end distance represented by the vector r_o , with components (x_o, y_o, z_o) , in the unstrained state of the network,

and let (x, y, z) be the components of the vector length r of the same chain after deformation.

Then,

$$x = \lambda_1 x_o, y = \lambda_1 y_o, z = \lambda_1 z_o \quad (2.21)$$

The entropy of chain in the original state, as given by equation 2.19, will be

$$s_o = c - kb^2 r_o^2 = c - kb^2 (x_o^2 + y_o^2 + z_o^2) \quad (2.22)$$

Similarly, the entropy of the same chain in a strained state will be

$$s = c - kb^2 r^2 = c - kb^2 (\lambda_1^2 x_o^2 + \lambda_2^2 y_o^2 + \lambda_3^2 z_o^2) \quad (2.23)$$

The contribution to the total entropy of deformation for the network due to this chain will be

$$\Delta S = s - s_o = -kb^2 \{(\lambda_1^2 - 1)x_o^2 + (\lambda_2^2 - 1)y_o^2 + (\lambda_3^2 - 1)z_o^2\} \quad (2.24)$$

The total entropy of deformation for all the N chains contained in unit volume of the network will be:

$$\Delta S = s - s_o = -kb^2 \{(\lambda_1^2 - 1)\Sigma x_o^2 + (\lambda_2^2 - 1)\Sigma y_o^2 + (\lambda_3^2 - 1)\Sigma z_o^2\} \quad (2.25)$$

Σx_o^2 is the sum of the squares of the x_o components, in the unstrained state of the network, for the assembly of N chains. Since the direction of chain vectors r_o in the unstrained state are entirely random, there will be no preference for the x, y, or z directions and hence we may write

$$\Sigma x_o^2 = \Sigma y_o^2 = \Sigma z_o^2 = \frac{1}{3} \Sigma r_o^2 \quad (2.26)$$

But $\Sigma r_o^2 = N \overline{r_o^2}$ where $\overline{r_o^2}$ is the mean-square length of the chains in the unstrained state and

equal to $\frac{3}{2} b^2$. Hence from equation 2.26,

$$\Delta S = -\frac{1}{2}Nk(\lambda_1^2 + \lambda_2^2 + \lambda_3^2 - 3) \quad (2.27)$$

The work of deformation or elastically stored free energy per unit volume (also referred to as strain-energy function) can be obtained using equation 2.12 and is given by:

$$W = -TdS = \frac{1}{2}NkT(\lambda_1^2 + \lambda_2^2 + \lambda_3^2 - 3) \quad (2.28)$$

$$W = \frac{1}{2}G(\lambda_1^2 + \lambda_2^2 + \lambda_3^2 - 3) \quad (2.29)$$

It is of particular interest to observe that equation 2.30 involves only a single physical parameter or elastic constant, G , which is related to the number of chains per unit volume, N , which is itself determined by the degree of crosslinking. It follows that the elastic properties of a rubber are independent of the chemical nature of the molecules of which it is composed. The elastic constant G may be expressed alternatively as:

$$G = NkT \quad (2.30)$$

where G is the shear modulus, N is elastically effective network strands per unit volume, k is the Boltzmann's constant ($k = 1.381 \times 10^{-23}$ J/K), and T is absolute temperature. The derivation of general stress-strain relations is based on the expression in equation 2.28 for the elastically stored energy, and makes use of the condition for constancy of volume, equation 2.21. The principal stresses, σ_1 , σ_2 , and σ_3 can be calculated as:

$$\sigma_1 = \frac{f_1}{\lambda_2 \lambda_3} = \lambda_1 f_1 \quad (2.31)$$

$$\sigma_2 = \frac{f_2}{\lambda_1 \lambda_3} = \lambda_2 f_2 \quad (2.32)$$

$$\sigma_3 = \frac{f_3}{\lambda_1 \lambda_2} = \lambda_3 f_3 \quad (2.33)$$

To determine the forces f_1, f_2 and f_3 , equation 2.14 can be used. Since λ_1, λ_2 and λ_3 are not independent of each other and are connected by the constant volume relation, any two of these are chosen as independent variables to determine the third one. If λ_1 and λ_2 are chosen as independent variables, then

$$\lambda_3 = \frac{1}{\lambda_1 \lambda_2} \quad (2.34)$$

Such a condition may be realized for the case where only two forces, f_1 and f_2 , are applied so that $f_3 = 0$. Therefore, the strain energy function in equation 2.29 can be written as:

$$W = \frac{1}{2} G (\lambda_1^2 + \lambda_2^2 + \frac{1}{\lambda_1^2 \lambda_2^2} - 3) \quad (2.35)$$

Using equation 2.14,

$$f_1 = \frac{dW}{d\lambda_1} = G (\lambda_1 - \frac{1}{\lambda_1^3 \lambda_2^2}) \quad (2.36)$$

The corresponding principal stress σ_1 is:

$$\sigma_1 = \lambda_1 f_1 = G (\lambda_1^2 - \lambda_3^2) \quad (2.37)$$

Similarly,

$$\sigma_2 = \lambda_2 f_2 = G (\lambda_2^2 - \lambda_3^2) \quad (2.38)$$

2.3.1.1 Several Common Stress Strain Relationship

2.3.1.1.1 Simple Extension

For the case of simple extension, a cube of unit length is increased in the ratio λ in one direction while the other two dimensions are correspondingly reduced. The strain state along with Mohr's diagram is shown in Figure 2.10. From the incompressibility assumption

$$\lambda_1 = \lambda, \lambda_2 = \lambda_3 = \lambda^{-\frac{1}{2}} \quad (2.39)$$

The corresponding strain energy function is therefore;

$$W = \frac{1}{2}G\left(\lambda^2 + \frac{2}{\lambda} - 3\right) \quad (2.40)$$

The only force is the tensile force in the direction of extension. If f is the force per unit cross-sectional area measured in the unstrained state, then

$$f = \frac{dW}{d\lambda} = G\left(\lambda - \frac{1}{\lambda^2}\right) \quad (2.41)$$

The quantity f is the nominal stress. Since the new cross sectional area is $\frac{1}{\lambda}$, the true stress σ is given by:

$$\sigma = \lambda f = G\left(\lambda^2 - \frac{1}{\lambda}\right) \quad (2.42)$$

2.3.1.1.2 Uniaxial Compression

The uniaxial compression strain state is obtained by the application of inwardly directed forces to a pair of opposite surfaces of a cubical block, the lateral surfaces being free of stress. This strain

state is identical to simple extensions where λ is less than unity. The strain state along with Mohr's diagram is shown in Figure 2.11. From the incompressibility assumption:

$$\lambda_1 = \lambda, \lambda_2 = \lambda_3 = \lambda^{-\frac{1}{2}} \quad (2.43)$$

The corresponding strain energy, the force per unit unstrained area, f , (negative in this case for compressive stresses) and the true stress relations are similar to the case of uniaxial tension (and are given as:

$$W = \frac{1}{2}G(\lambda^2 + \frac{2}{\lambda} - 3) \quad (2.44)$$

$$f = \frac{dW}{d\lambda} = G(\lambda - \frac{1}{\lambda^2}) \quad (2.45)$$

$$\sigma = \lambda f = G(\lambda^2 - \frac{1}{\lambda}) \quad (2.46)$$

2.3.1.1.3 Equi-biaxial Extension

In this type of strain, the rubber is stretched by equal amounts in two directions at right angles. The state of strain corresponds exactly with that produced by uniaxial compression, the only difference being in the nature of applied stress. The strain state along with Mohr's diagram is shown in Figure 2.12. If $\lambda_1 = \lambda_2 = \lambda$ is the stretch ratio in the plane of the sheet, then

$$\lambda_3 = \frac{1}{\lambda^2} \quad (2.47)$$

Since the stress σ_3 normal to the plane of the sheet is zero, the stress σ_1 (or σ_2) can be written as:

$$\sigma_1 = \sigma_2 = G(\lambda^2 - \frac{1}{\lambda^4}) \quad (2.48)$$

Equation 2.49 represents the true stress in the sheet as a function of stretch ratio in the two-dimensional extension. If d_o is the original thickness of the sheet, then force, P , acting on a section of unit length (in the strained state) cut at right angles to the plane of sheet can be calculated as:

$$P = \sigma_1 \lambda_3 d_o = G \left(\lambda^2 - \frac{1}{\lambda^4} \right) \times \frac{1}{\lambda^2} d_o = G d_o \left(1 - \frac{1}{\lambda^6} \right) \quad (2.49)$$

For thin sheet, force P per unit length may be thought of as a surface tension. For extensions exceeding $\lambda = 2$, tension P becomes substantially independent of the extension and is analogous to the surface tension of a liquid.

2.3.1.1.4 Simple Shear

Simple shear is a type of strain which may be represented by the sliding of planes which are parallel to a given plane through a distance proportional to their distance from the given plane. It is a constant volume deformation, whether the material is incompressible or not. The lateral faces of a cube are transformed by simple shear into parallelograms, and the amount of shear is measured by the tangent of angle ϕ through which a vertical edge is tilted. There is no strain in the plane normal to the plane of shear; the extension ratio corresponding to this direction is therefore unity. Since the volume is constant, the three principal extension ratios may therefore be expressed as,

$$\lambda_1 = \lambda, \lambda_3 = 1, \lambda_2 = \frac{1}{\lambda} \quad (2.50)$$

The strain state along with Mohr's diagram is shown in Figure 2.13. The amount of the shear γ may be related either to the angle ϕ or to the principal extensions ratio[93] thus

$$\gamma = \tan \phi = \lambda - \frac{1}{\lambda} \quad (2.51)$$

The strain energy W , can then be written as

$$W = \frac{1}{2}G\left(\lambda^2 + \frac{1}{\lambda^2} - 2\right) = \frac{1}{2}G\gamma^2 \quad (2.52)$$

The shearing stress, τ_{xy} , may be given as:

$$\tau_{xy} = \frac{dW}{d\gamma} = G\gamma \quad (2.53)$$

which means that the shearing stress is proportional to the shear strain and therefore Hooke's law is obeyed in simple shear, and the quantity G corresponds to the modulus of rigidity in classical elasticity. The statistical theory thus leads to the interesting result that a rubber should obey Hooke's law in shear, though not in extension or compression.

2.3.1.1.5 Pure Shear

For some purposes, a less familiar type of deformation known as pure shear is more convenient than simple shear. In general, a pure strain is one which involves extensions in three perpendicular directions, without rotation of the principal axes of strain, the most general homogeneous strain involves both extension and rotations. In pure shear, the extensions ratios are represented as before for simple shear but the axes of strain do not rotate. A simple shear is thus equivalent to a pure shear together with a rotation. The state corresponding to pure shear, in the case of an incompressible material, may be maintained by principal stresses σ_1 and σ_2 only, with $\sigma_3 = 0$. The three principal extension ratios may therefore be expressed as,

$$\lambda_1 = \lambda, \lambda_2 = 1, \lambda_3 = \frac{1}{\lambda} \quad (2.54)$$

The strain state along with Mohr's diagram is shown in Figure 2.14. True stress values can be written as:

$$\sigma_1 = G\left(\lambda^2 - \frac{1}{\lambda^2}\right) \quad (2.55)$$

$$\sigma_2 = G\left(1 - \frac{1}{\lambda^2}\right) \quad (2.56)$$

2.3.2 Hyperelastic Material Modeling

The application of rubber-like materials (called as hyperelastic materials) in different industrial areas is enormous. The modeling and design of hyperelastic materials consists of the selection of an appropriate strain energy function W , and accurate determination of material constants for such a function. Due to the complexity of rubber components, an important problem in nonlinear elasticity theory is to derive a reasonable and applicable elastic law, which is the key to the development of reliable analysis tools. Many phenomenological[88, 94-97] and physically motivated[98, 99] material models have been developed to describe the stress–strain relation for hyperelastic materials. This section describes several of the most commonly used hyperelastic materials models.

Hyperelasticity is the capability of a material to undergo large elastic strain on application of forces, without losing its original properties. A hyperelastic material has nonlinear behavior, which means that its deformation is not directly proportional to the load applied. In the finite element analysis of elastomers, material models are characterized by different forms of their strain energy (density) functions. Implicit in the use of these functions (usually denoted by W) is the assumption that the material is isotropic and elastic. The derivative of W with respect to strain, ε , yields the stress. The commonly available strain energy functions have been represented either in

terms of the strain invariants which are functions of the stretch ratios or directly in terms of the stretch ratios themselves. The three strain invariants, I_1 , I_2 and I_3 can be expressed as:

$$I_1 = \lambda_1^2 + \lambda_2^2 + \lambda_3^2 \quad (2.57)$$

$$I_2 = \lambda_1^2 \lambda_2^2 + \lambda_2^2 \lambda_3^2 + \lambda_3^2 \lambda_1^2 \quad (2.58)$$

$$I_3 = \lambda_1^2 \lambda_2^2 \lambda_3^2 \quad (2.59)$$

The symbols λ_1 , λ_2 and λ_3 represent the principal stretch ratios given by the ratio of stretched to the unstretched length of the material. In the case of a perfectly incompressible material, the strain invariant $I_3 = \lambda_1^2 \lambda_2^2 \lambda_3^2 = I$. In this case, the strain energy potential is a function of I_1 and I_2 , i.e. $U = f(I_1, I_2)$. The most common available strain energy functions are as follows.

2.3.2.1 *Mooney-Rivlin model*

The earliest phenomenological theory of nonlinear elasticity was proposed by Mooney and Rivlin[94, 95] where strain energy function W is an infinite series in powers of $(I_1 - 3)$ and $(I_2 - 3)$ of the form:

$$W(I_1, I_2) = \sum_{i,j=0}^{\infty} C_{ij} (I_1 - 3)^i (I_2 - 3)^j \quad (2.60)$$

where C_{ij} are constants. For example, the Mooney-Rivlin form with two parameters is:

$$W = C_{10}(I_1 - 3) + C_{01}(I_2 - 3) \quad (2.61)$$

Although Mooney-Rivlin model shows good agreement with tensile test data up to 100% strains, it has been found inadequate in describing the compression mode of deformation[100]. Moreover, the Mooney-Rivlin model fails to account for the stiffening of the material at large strains[100, 101]. Tschoegl [102] underscored the fact that the retention of higher order terms in the

generalized Mooney-Rivlin polynomial function of strain energy led to a better agreement with test data for both unfilled as well as filled rubbers.

2.3.2.2 *Neo-Hookean model*

This simplest model of rubber elasticity is obtained by taking only the first term of equation 2.62 and is given by Treloar[88]:

$$W = C_{10}(I_1 - 3) \quad (2.62)$$

This model exhibits a constant shear modulus, and gives good correlation with the experimental data up to 40% strain in uniaxial tension and up to 90% strains in simple shear[100].

2.3.2.3 *Ogden model*

Ogden [96] deduced a hyperelastic constitutive model for large deformations of incompressible rubber-like solids. The strain energy is expressed as a function of principal stretches as:

$$W(\lambda_1, \lambda_2, \lambda_3) = \sum_{r=0}^{n \rightarrow \infty} \frac{\mu_r}{\alpha_r} (\lambda_1^{\alpha_r} + \lambda_2^{\alpha_r} + \lambda_3^{\alpha_r} - 3) \quad (2.63)$$

with μ_r and α_r as material constants, which can be determined by experimental tests. The Neo-Hookean[88] and Mooney-Rivlin[94, 95] material models are special cases of the Ogden model. The model gives good correlation with test data in simple tension up to 700%[100]. The model accommodates non-constant shear modulus and slightly compressible material behavior. Also, for $\alpha < 2$ or > 2 , the material softens or stiffens respectively with increasing strain.

2.3.2.4 *Yeoh model*

The Yeoh [103] model depends only on the first strain invariant I_1 . The strain energy function W is obtained by:

$$W(I_1) = \sum_{n=1}^i C_{i0} (I_1 - 3)^i \quad (2.64)$$

It applies to the characterization of elastic properties of carbon-black filled rubber vulcanizates. This model is more versatile than the others since it has been demonstrated to fit various modes of deformation using the data obtained from a uniaxial tension test only. This leads to reduced requirements on material testing. However, caution needs to be exercised when applying this model for deformations involving low strains[104].

2.3.2.5 *Van der Waals Model*

This model is based on physical quantities such as the maximum stretching of a polymer chain and the global interaction between the network chains. The energy function of the Van der Waals equation formulated by Killian [99, 105, 106] is given by:

$$W = \mu \left[-(\lambda_m^2 - 3) \times (\ln(1 - \eta) + \eta) - \frac{2}{3} a \cdot \left(\frac{\bar{I} - 3}{2} \right)^{\frac{3}{2}} \right] + \frac{1}{D} \left(\frac{J_{el}^2 - 1}{2} - \ln J_{el} \right) \quad (2.65)$$

where $\bar{I} = (1 - \beta)I_1 + \beta \cdot I_2$ and $\eta = \sqrt{\frac{\bar{I} - 3}{\lambda_m^2 - 3}}$ with β representing the linear mixture parameter, λ

is the stretch ratio, a is the global interaction parameter between chains.

The Mooney and neo-Hookean strain energy function have played an important role in the development of the nonlinear hyperelastic theory and its applications [107, 108]. It has been shown by Bogert [109] that the Mooney model performs well for moderately large deformation in uniaxial elongation and shear deformation. But, it cannot describe the typical S-curvature of the force–stretch relation in the uniaxial elongation experiment. Rivlin[110, 111] modified the Mooney model to obtain a general expression of the strain energy function expressed in terms of strain invariants. An alternative high-order polynomial model of the first invariant has been

proposed by Gent [112] and has the form of a natural logarithm. Besides these purely phenomenological models, micro-mechanics based idealized network models have also been proposed. The first explicit expression for the configurational entropy of a single chain was given by Kuhn and Grun [113]. James and Guth [114] proposed a model based on the assumption that the possible configurations of links in a chain are described by using a Gaussian distribution. This network model is frequently referred to as the three-Gaussian-chain model, which is available for small strains. For the large strain range, James and Guth [115] and Wang and Guth [116] proposed a non-Gaussian network model consisting of three independent sets of chains (each set contains $n/3$ chains per unit volume), a so-called three-chain model. Treloar [117] and Flory and Rehner [92] simplified the complex polymer network by a four-chain model, in which four non-Gaussian chains are connected to the corners of a tetrahedron. Later on, Arruda and Boyce [118] developed an eight-chain model and Wu and van der Giessen [119] proposed the so-called full-network model.

The Mooney-Rivlin, Ogden, Neo-Hookean, Yeoh, and Van der Waals models were evaluated for best fit analysis with the experimental data from uniaxial tension tests. Attention was later restricted to the Ogden/Neo-Hookean model for computational analysis of the static behavior of the seal for this study.

2.4 Conclusion

Elastomeric materials are used in a number of applications where properties of interest are characterized and used for lifetime prediction of a component. Depending on the end application of a product, failure modes for a component must carefully be defined and studied in detail so that material durability can be estimated. In order to make reliability and durability predictions, test methods in relevant environmental conditions for material aging can be selected to address

failure modes. Means to accelerate the degradation process can be employed so that data are generated during the research and development cycle and are extrapolated to predict component lifetime at operating conditions.

Based on the reviews on various test methods and procedures for characterizing the elastomeric materials and failure modes that are most relevant to address seal failure in a fuel cell, tests such as uniaxial tension, trouser tear, and compression stress relaxation were performed. Accelerated characterization based on thermal and mechanical means were used. Based on the fundamentals of hyperelasticity theory, several material models were explored to understand and define seal behavior under compression. With the help of finite element analysis, the distribution of stress strain and other relevant parameters for the seal were presented.

References:

1. R. O'Hayre, S.-W. Cha, W. Colella, and F.B. Prinz, *Fuel Cell Fundamentals*. 2006, Hoboken, New Jersey: John Wiley & Sons.
2. L. Frisch, "PEM Fuel Cell Stack Sealing Using Silicone Elastomers," *Sealing Technology*, **93**, 7-9, 2001.
3. R.J. Pazur, J. Bielby, and U. Dinges, "Continuous Compressive Stress Relaxation of Elastomers Used in Engine Sealing Applications," *Rubber World*, **229**(5), 24-29, 2004.
4. N. Nakajima and R.D. DeMarco, "Application of Polyacrylate Rubber for High Performance Automotive Gaskets and Seals," *Journal of Elastomers and Plastics*, **33**(2), 114-120, 2001.
5. D.A. Dillard, S. Guo, M.W. Ellis, J.J. Lesko, J.G. Dillard, J. Sayre, and B. Vijayendra, *Seals and Sealants in PEM Fuel Cell Environments: Material, Design, and Durability Challenges*, in *ASME Second International Conference on Fuel Cell Science Engineering and Technology*. 2004: Rochester, New York. p. 553-560.
6. B.H. Youn and C.S. Huh, "Surface Degradation of HTV Silicone Rubber and EPDM Used for Outdoor Insulators under Accelerated Ultraviolet Weathering Conditions," *IEEE Transactions on Dielectrics and Electrical Insulation*, **12**(5), 1015-1024, 2005.
7. S. Mitra, A. Ghanbari-Siahkali, P. Kingshott, K. Almdal, H.K. Rehmeier, and A.G. Christensen, "Chemical Degradation of Fluoroelastomer in an Alkaline Environment," *Polymer Degradation and Stability*, **83**(2), 195-206, 2004.
8. J. Tan, Y.J. Chao, J. W. Van Zee, and W.k. Lee, "Degradation of Elastomeric Gasket Materials in PEM Fuel Cells," *Materials Science and Engineering: A*, **445**, 669-675, 2007.
9. J. Tan, Y.J. Chao, J.W.V. Zee, X. Li, X. Wang, and M. Yang, "Assessment of Mechanical Properties of Fluoroelastomer and EPDM in a Simulated PEM Fuel Cell Environment by Microindentation Test," *Material Science and Engineering A*, **In Print**2008.
10. M. Schulze, T. Knori, A. Schneider, and E. Gulzow, "Degradation of Sealings for PEMFC Test Cells During Fuel Cell Operation," *Journal of Power Sources*, **127**, 222-229, 2004.

11. J. Tan, Y.J. Chao, X. Li, and J.W.V. Zee, "Degradation of Silicone Rubber under Compression in a Simulated PEM Fuel Cell Environment," *Journal of Power Sources*, **172**, 782-789, 2007.
12. A. Husar, M. Serra, and C. Kunusch, "Description of Gasket Failure in a 7 Cell PEMFC Stack," *Journal of Power Sources*, **169**(1), 85-91, 2007.
13. J. Tan, Y.J. Chao, M. yang, C.T. Williams, and J.W.V. Zee, "Degradation Characteristics of Elastomeric Gasket Materials in a Simulated PEM Fuel Cell Environment," *Journal of Materials Engineering and Performance*, **17**(6), 785-792, 2008.
14. N. Meguriya and Y. Taira, *Polymer Electrolyte Fuel-Cell Separator Sealing Rubber Composition*, in *US Patent 7087338*. 2006, Shin-Etsu Chemical Co., Ltd. (Tokyo, JP) US.
15. M. Schulze, T. Knori, A. Schneider, and E. Gulzow, "Degradation of Sealings for PEFC Test Cells During Fuel Cell Operation," *Journal of Power Sources*, **127**(1-2), 222-229, 2004.
16. M. Mikkola, *Modifications to a PEM Fuel Cell Stack*, in *Department of Engineering Physics and Mathematics*. 2000, Helsinki University of Technology.
17. S.J.C. Cleghorn, D.K. Mayfield, D.A. Moore, J.C. Moore, G. Rusch, T.W. Sherman, N.T. Sisofo, and U. Beuscher, "A Polymer Electrolyte Fuel Cell Life Test: 3 Years of Continuous Operation " *Journal of Power Sources*, **158**(1), 446-454, 2006.
18. J. St-Pierre and N. Jia, "Successful Demonstration of Ballard PEMFCs for Space Shuttle Applications," *Journal of New Materials for Electrochemical Systems*, **5**(4), 263-271, 2002.
19. S.Y. Ahn, S.J. Shih, H.Y. Ha, S.A. Hong, Y.C. Lee, T.W. Lim, and I.H. Oh, "Performance and Lifetime Analysis of the KW-Class PEMFC Stack " *Journal of Power Sources*, **106**(1-2), 295-303, 2002.
20. M.S. Wilson, F.H. Garzon, K.E. Sickafus, and S. Gottesfeld, "Surface Area Loss of Supported Platinum in Polymer Electrolyte Fuel Cells," *Journal of the Electrochemical Society*, **140**(10), 2872-2877, 1993.
21. F. Barbir and S. Yazici, "Status and Development of PEM Fuel Cell Technology," *International Journal of Energy Research*, **32**(5), 369-378, 2007.

22. H. Tawfik, Y. Hung, and D. Mahajan, "Metal Bipolar Plates for PEM Fuel Cell-a Review," *Journal of Power sources*, **163**(2), 755-767, 2006.
23. S. Stucki, G.G. Sherer, S. Schlagowski, and E. Fischer, "PEM Water Electrolysers: Evidence for Membrane Failure in 100kw Demonstration Plants " *Journal of Applied Electrochemistry*, **28**(10), 1041-1049, 1998.
24. R. Borup, J. Meyers, B. Pivovar, Y.S. Kim, R. Mukundan, N. Garland, D. Meyers, M. Wilson, F. Garzon, D. Wood, P. Zelenay, K. More, K. Stroh, T. Zawodzinski, J. Boncella, J.E. McGrath, M. Inaba, K. Miyatake, M. Hori, K. ota, Z. Ogumi, S. Miyata, A. Nishikata, Z. Siroma, Y. Uchimoto, K. Yasuda, K. Kimijima, and N. Iwashita, "Scientific Aspects of Polymer Electrolyte Fuel Cell Durability and Degradation," *Chemical Reviews*, **107**(10), 3904-3951, 2007.
25. F.A. Bruijn, V.A.T. Dam, and G.J.M. Janssen, "Review: Durability and Degradation Issues of PEM Fuel Cell Components," *Fuel Cells*, **2008**(1), 3-22, 2007.
26. T.J. Schmidt, M. Inaba, and F.N. Büchi, *Polymer Electrolyte Fuel Cell Durability*. 2009, New York, NY: Springer.
27. A.V. Tobolsky, *Properties and Structure of Polymers*. 1960, New York: Wiley.
28. J.D. Ferry, *Viscoelastic Properties of Polymers*. 3 ed. 1980, New York: John Wiley & Sons Inc.
29. K. Murakami and K. Ono, *Chemorheology of Polymers*. 1979, Amsterdam and New York: Elsevier Scientific Publishing Company.
30. J.G. Curro and P. Pincus, "A Theoretical Basis for Viscoelastic Relaxation of Elastomers in the Long-Term Limit," *Macromolecules*, **16**, 559-562, 1983.
31. X. Wang, H. Zhang, Z. Wang, and B. Jiang, "In Situ Epoxidation of Epdm Rubber by Performic Acid," *Polymer*, **38**, 5407-5410, 1997.
32. S. Mitra, A. Ghanbari-Siahkali, P. Kingshott, H.K. Rehmeier, H. Abildgaard, and K. Almdal, "Chemical Degradation of Crosslinked Epdm Rubber in an Acidic Environment. Part II. Effect of Peroxide Crosslinking in the Presence of a Coagent," *Polymer Degradation and Stability*, **91**(1), 81-93, 2006.
33. S. Mitra, S. Ghanbari-Siahkali, P. Kingshott, H.K. Rehmeier, H. Abildgaard, and K. Almdal, "Chemical Degradation of Crosslinked Epdm Rubber in an Acidic Environment.

- Part I. Effect on Accelerated Sulphur Crosslinks," *Polymer Degradation and Stability*, **91**(1), 69-80, 2006.
34. T. Sugama, "Surface Analyses of Fluoroelastomer Bearings Exposed to Geothermal Environments," *Materials Letters*, **50**(2-3), 66-72, 2001.
 35. J. Tan, Y.J. Chao, M. Yang, W.K. Lee, and J.W.V. Zee. in *Proceedings of the 2nd Annual Korea-USA Joint Symposium on Hydrogen & Fuel Cell Technologies*. 2007. Columbia, SC.
 36. K.T. Gillen, R. Bernstein, and M.H. Wilson, "Predicting and Confirming the Lifetime of O Rings," *Polymer Degradation and Stability*, **87**, 257-270, 2005.
 37. T. Zaharescu, M. Giurginca, and S. Jipa, "Radiochemical Oxidation of Ethylene-Propylene Elastomers in the Presence of Some Phenolic Antioxidants," *Polymer Degradation and Stability*, **63**(2), 245-251, 1999.
 38. A.K. Bhowmick, J. Konar, S. Kole, and S. Narayanan, "Surface-Properties of Epdm, Silicone-Rubber, and Their Blend During Aging," *Journal of Applied Polymer Science*, **57**(5), 631-637, 1995.
 39. B.H. Youn and C.S. Huh, "Surface Degradation of Htv Silicone Rubber and Epdm Used for Outdoor Insulators under Accelerated Ultraviolet Weathering Condition," *IEEE Transactions on Dielectrics and Electrical Insulation*, **12**(5), 1015-1024, 2005.
 40. T. Zaharescu, E. Feraru, and C. Podina, "Thermal Stability of Gamma Irradiated Ethylene-Propylene-Diene Monomer Divinyl Benzene Systems," *Polymer Degradation and Stability*, **87**(1), 11-16, 2005.
 41. V. Deniz, B. Karaagac, and N. Ceyhan, "Thermal Stability of Butyl/Epdm/Neoprene Based Rubber Compounds," *Journal of Applied Polymer Science*, **103**(1), 557-563, 2007.
 42. L.H. Sperling, *Introduction to Physical Polymer Science*. 4 ed. 2005, New York: Wiley-Interscience.
 43. H.F. Mark, *Encyclopedia of Polymers Science and Technology*. 3rd ed. Vol. 12. 2004, Malden, MA: John Wiley & Sons Inc.
 44. ASTM-D412-06a, *Standard Test Methods for Vulcanized Rubber and Thermoplastic Elastomers-Tension*, in *Annual Book of Astm Standards*. 2002, ASTM International: West Conshohocken, PA, 19428-2959.

45. ASTM-D624-00, *Standard Test Method for Tear Strength of Conventional Vulcanized Rubber and Thermoplastic Elastomers*, in *Annual Book of Astm Standards*. 2007, ASTM International: West Conshohocken, PA, 19428.
46. R.P. Brown, *Practical Guide to the Assessment of the Useful Life of Rubbers*. 2001, Shawbury, UK: Rapra Technology Ltd.
47. R.P. Brown, *Physical Testing of Rubber*. 3 ed. 1996, London, UK: Chapman and Hall. 342.
48. P. Albiñ, *The 5-Year Accelerated Ageing Project for Thermoset and Thermoplastic Elastomeric Materials: A Service Life Prediction Tool*, in *Elastomers & Components: Service Life Prediction- Progress & Challenges*, V.A. Coveney, Editor. 2006, Woodhead Publishing Ltd.: Cambridge, UK. p. 3-26.
49. E.W. Bergstrom, "Environmental Aging of Elastomers," *Elastomerics*, **109**(3), 21-30, 1977.
50. A. Kadir and A.G. Thomas, "Tearing of Unvulcanized Natural Rubber," *Journal of Polymer Science: Polymer Physics Edition*, **22**(9), 1623-1634, 2003.
51. G.J. Lake and A.G. Thomas, *Strength*, in *Engineering with Rubber: How to Design Rubber Components*, A.N. Gent, Editor. 2001, HanserGardner Publications, Inc.: Cincinnati.
52. A.N. Gent and A.W. Henry. *On the Tear Strength of Rubbers*. in *Proceedings of the International Rubber Conference*. 1968. Brighton.
53. S.J. Clarson and J.A. Semlyen, *Siloxane Polymers*. 1993, New Jersey: Prentice Hall.
54. J.M. Zeigher and F.W.G. Fearon, *Silicon Based Polymer Science: A Comprehensive Resource*. Advances in Chemistry. Vol. 224. 1990, Washington, DC: ACS Press.
55. B. MA, *Silicon in Organic, Organometallic, and Polymer Chemistry*. 2000, New York: Wiley.
56. D.R. Rottach, J.G. Curro, G.S. Grest, and A.P. Thompson, "Effect of Strain History on Stress and Permanent Set in Cross-Linking Networks: A Molecular Dynamics Study," *Macromolecules*, **37**(14), 5468-5473, 2004.
57. R.D. Andrews, A.V. Tobolsky, and E.E. Hanson, "The Theory of Permanent Set at Elevated Temperatures in Natural and Synthetic Rubber," *Journal of Applied Physics*, **17**, 352-361, 1946.

58. P.C.M. Tate and S. Talal, "Compressive Properties of Rigid Polyurethane Foams," *Polymers & Polymer Composites*, **7**(2), 117-124, 1999.
59. J.W. Schneider, "Stress-Relaxation of Cellular Silicone," *Industrial & Engineering Chemistry Product Research and Development*, **20**(4), 684-688, 1981.
60. J.C. Phillips, "Creep/Recovery Behavior of Open-Cell Foams," *Journal of Applied Polymer Science*, **55**(3), 527-536, 1995.
61. ASTM-D6147-97, *Standard Test Method for Vulcanized Rubber and Thermoplastic Elastomer-Determination of Force Decay (Stress Relaxation) in Compression*, in *Annual Book of Astm Standards*. 2008, ASTM International: West Conshohocken, PA, 19428-2959.
62. F.J. Walker. *Csr Testing of Elastomers*. in *Advanced Elastomers Conference*. 2002. Dearborn, MI.
63. P.F. Tuckner. *Compression Stress Relaxation Testing: Comparison, Methods, and Correlations*. in *SAE World Congress*. 2001. Detroit, MI.
64. A. Pannikottu, R. Samples, and S.J. Sadon, *Performance Prediction of Elastomeric Gasket Materials by Compression Stress Relaxation*, in *American Society of Mechanical Engineers, Design Engineering Division (Publication) DE*. 1998, ASME, Fairfield, NJ: Anaheim, CA. p. 9-11.
65. G. Spetz, *Stress Relaxation-Test Methods, Instruments, Test Results and Lifetime Estimation*, in *Lifetime estimation of rubber materials by ageing and stress relaxation tests*. 2000: Boras, Sweden.
66. D. Chirhart, "Obtaining Consistent, Reliable Results in Elastomer Seal Testing," *NASA Tech Briefs*, 2001.
67. A.R.D. Laboratory, *Compression Stress Relaxation (Csr)*. 2007.
68. G.B. Mckenna and L.J. Zapas, "The Superposition of Small Deformations on Large Deformations - Measurements of the Incremental Relaxation Modulus for a Polyisobutylene Solution," *Journal of Polymer Science Part B-Polymer Physics*, **23**(8), 1647-1656, 1985.
69. G.B. Mckenna and L.J. Zapas, "Superposition of Small Strains on Large Deformations as a Probe of Nonlinear Response in Polymers," *Polymer Engineering and Science*, **26**(11), 725-729, 1986.

70. J.G. Curro and E.A. Salazar, "Physical and Chemical Stress Relaxation of Elastomers," *Journal of Applied Polymer Science*, **19**(9), 2571-2581, 1975.
71. J.G. Curro and E.A. Salazar, "Physical and Chemical Stress Relaxation of Elastomers," *Rubber Chemistry and Technology*, **50**(5), 895-905, 1977.
72. E.A. Salazar, J.G. Curro, and K.T. Gillen, "Physical and Chemical Stress Relaxation of a Fluoroelastomer," *Journal of Applied Polymer Science*, **21**(6), 1597-1605, 1977.
73. A. Stevenson and R.P. Campion, *Durability*, in *Engineering with Rubber: How to Design Rubber Components*, A.N. Gent, Editor. 2001, Hanser Gardner Publications: Cincinnati. p. 179-220.
74. A.V. Tobolsky, I.B. Prettymann, and J.H. Dillon, *Journal of Applied Physics*, **15**, 380-387, 1944.
75. H.W. Greensmith and A.G. Thomas, "Rupture of Rubber. Iii. Determination of Tear Properties," *Journal of Polymer Science Part B-Polymer Physics*, **18**(88), 189-200, 1955.
76. M.L. Williams, R.F. Landel, and J.D. Ferry, "The Temperature Dependence of Relaxation Mechanisms in Amorphous Polymers and Other Glass-Forming Liquids," *Journal of the American Chemical Society*, **77**, 3701-3706, 1955.
77. M.T. Shaw and W.J. MacKnight, *Introduction to Polymer Viscoelasticity*. 2005, Hoboken: John Wiley & Sons Inc.
78. K.T. Gillen, M. Celina, R.L. Clough, and J. Wise, "Extrapolation of Accelerated Aging Data - Arrhenius or Erroneous?," *Trends in Polymer Science*, **5**(8), 250-257, 1997.
79. J. Wise, K.T. Gillen, and R.L. Clough, "An Ultrasensitive Technique for Testing the Arrhenius Extrapolation Assumption for Thermally Aged Elastomers," *Polymer Degradation and Stability*, **49**(3), 403-418, 1995.
80. K.T. Gillen, M. Celina, and M.R. Keenan, "Methods for Predicting More Confident Lifetimes of Seals in Air Environments," *Rubber Chemistry and Technology*, **73**(2), 265-283, 2000.
81. K.T. Gillen, M. Celina, and R. Bernstein, "Validation of Improved Methods for Predicting Long-Term Elastomeric Seal Lifetimes from Compression Stress-Relaxation and Oxygen Consumption Techniques," *Polymer Degradation and Stability*, **82**(1), 25-35, 2003.

82. K.T. Gillen, M. Celina, and R. Bernstein. *Review of the Ultrasensitive Oxygen Consumption Method for Making More Reliable Extrapolated Predictions of Polymer Lifetimes.* in *Ann Tech Conf Soc Plast Eng.* 2004.
83. N. Ruddock, P.W. James, and T.E.R. Jones, "Modeling the Linear Viscoelasticity of Unfilled and Carbon Black Loaded Elastomers," *Rheologica Acta*, **32**(3), 286-292, 1993.
84. S. Ertong, H. Eggers, and P. Schummer, "Steady-State Shear Flow Properties of Carbon-Black Filled Rubber Compounds," *Rubber Chemistry and Technology*, **67**(2), 207-216, 1994.
85. M.H. Klopffer, L. Bokobza, and L. Monnerie, "Effect of Vinyl Content on the Viscoelastic Properties of Polybutadienes and Polyisoprenes : Monomeric Friction Coefficient," *Polymer*, **39**(15), 3445-3449, 1998.
86. A. Hotta, S.M. Clarke, and E.M. Terentjev, "Stress Relaxation in Transient Networks of Symmetric Triblock Styrene-Isoprene-Styrene Copolymer," *Macromolecules*, **35**(1), 271-277, 2002.
87. S. Ronan, T. Alshuth, S. Jerrams, and N. Murphy, "Long-Term Stress Relaxation Prediction for Elastomers Using the Time-Temperature Superposition Method," *Materials & Design*, **28**(5), 1513-1523, 2007.
88. L.R.G. Treloar, *The Physics of Rubber Elasticity.* 2 ed. 1975, Glasgow: Oxford University Press.
89. J.E. Mark and B. Erman, *Rubberlike Elasticity: A Molecular Primer.* 1988, New York: Wiley-Interscience.
90. P.J. Flory, *Principles of Polymer Chemistry.* 1953, Ithaca, NY: Cornell University Press.
91. F.T. Wall and P.J. Flory, "Statistical Thermodynamics of Rubber Elasticity," *Journal of Chemical Physics*, **19**(12)1951.
92. P.J. Flory and J. Rehner Jr., "Statistical Mechanics of Cross-Linked Polymer Networks: I. Rubberlike Elasticity," *Journal of Chemical Physics*, **11**, 512-520, 1943.
93. A.E.H. Love, *A Treatise on the Mathematical Theory of Elasticity.* 4th ed. 1906: Cambridge University Press.
94. M.A. Mooney, "A Theory of Large Elastic Deformation.," *Journal of Applied Physics*, **11**, 582-592, 1940.

95. R.S. Rivlin. *Large Elastic Deformations of Isotropic Materials. I. Fundamental Concepts.* in *Philosophical Transactions of the Royal Society of London. Series A, Mathematical and Physical Sciences.* 1948.
96. R.W. Ogden. *Large Deformation Isotropic Elasticity-on the Correlation of Theory and Experiment for the Incompressible Rubber-Like Solids.* in *Proceedings of the Royal Society of London.* 1972.
97. O.H. Yeoh, "Characterization of Elastic Properties of Carbon-Black-Filled Rubber Vulcanizates," *Rubber Chemistry and Technology*, **63**(5), 792-805, 1990.
98. E.M. Arruda and M.C. Boyce, "A Three-Dimensional Constitutive Model for the Large Stretch Behavior of Rubber Elastic Materials," *Journal of the Mechanics and Physics of Solids*, **41**(2), 389-412, 1993.
99. H.G. Kilian, "Equation of State of Real Networks," *Polymer*, **22**(2), 209-217, 1981.
100. W.D. Kim, W.S. kim, C.S. Woo, and H.J. Lee, "Some Considerations on Mechanical Testing Methods of Rubbery Materials Using Nonlinear Finite Element Analysis," *Polymer International*, **53**(7), 850-856, 2004.
101. P. Xu and J.E. Mark, "Strain-Induced Crystallization in Elongated Polyisobutylene Elastomers," *Polymer Gels and Networks*, **3**(3), 255-266, 1995.
102. N.W. Tschoegl, "Constitutive Equations for Elastomers," *Journal of Polymer Science Part a-Polymer Chemistry*, **9**(7), 1959-1970, 1971.
103. O.H. Yeoh, "Some Forms of the Strain-Energy Function for Rubber," *Rubber Chemistry and Technology*, **66**(5), 754-771, 1993.
104. O.H. Yeoh, *Phenomenological Theory of Rubber Elasticity.* 2nd ed. Comprehensive Polymer Science, ed. S.L. Aggarwal. 1995: Pergamon Press.
105. H.G. Kilian and T. Vilgis, "Thermodynamical Description of Deformation Phenomena in Rubbers," *Makromolekulare Chemie-Macromolecular Chemistry and Physics*, **185**(1), 193-203, 1984.
106. H.G. Kilian and T. Vilgis, "Fundamental-Aspects of Rubber-Elasticity in Real Networks," *Colloid and Polymer Science*, **262**(1), 15-21, 1984.
107. R.W. Ogden, *Non-Linear Elastic Deformation.* 1984, Mineola, New York.: Dover Publications, Inc.
108. R.W. Ogden, *Nonlinear Elasticity.* 2001, Cambridge: Cambridge University Press.

109. P.A.J. van den Bogert, *Computational Modelling of Rubberlike Materials*. 1991, Delft University of Technology.
110. R.S. Rivlin. *Large Elastic Deformations of Isotropic Materials Iv-Further Developments of the General Theory*. in *Philosophical Transactions of the Royal Society of London. Series A, Mathematical and Physical Sciences*. 1948.
111. R.S. Rivlin. *A Note on the Torsion of Incompressible Highly-Elastic Cylinder*. in *Proceedings of the Cambridge Philosophical Society*. 1949.
112. A.N. Gent, "A New Constitutive Relation for Rubber," *Rubber Chemistry and Technology*, **69**(1), 59-61, 1996.
113. W. Kuhn and F. Grun, "Beziehungen Zwischen Elastischen Konstanten Und Dehnungsdoppelbrechung Hochelastischer Stoffe.," *Kolloidn Zhurnal* **101**, 248-271, 1942.
114. H.M. James and E. Guth, "Elastic and Thermoelastic Properties of Rubber Like Materials," *Industrial and Engineering Chemistry* **33**, 624-629, 1941.
115. H.M. James and E. Guth, "Theory of Elastic Properties of Rubber," *Rubber Chemistry and Technology*, **11**, 455-481, 1943.
116. M.C. Wang and E. Guth, "Statistical Theory of Networks of Non-Gaussian Flexible Chains.," *Journal of Chemical Physics*, **20**, 1144-1157, 1952.
117. L.R.G. Treloar, "The Elasticity of a Network of Long-Chain Molecules," *Transactions of Faraday Society*, **42**, 83-94, 1946.
118. E.M. Arruda and M.C. Boyce, "A 3-Dimensional Constitutive Model for the Large Stretch Behavior of Rubber Elastic-Materials," *Journal of the Mechanics and Physics of Solids*, **41**(2), 389-412, 1993.
119. P.D. Wu and E. van der Giessen, "On Improved Network Models for Rubber Elasticity and Their Applications to Orientation Hardening in Glassy Polymers," *Journal of the Mechanics and Physics of Solids*, **41**, 427-456, 1993.
120. J.E. Mark, "Rubber Elasticity," *Journal of Chemical Education*, **58**(11), 898-903, 1981.

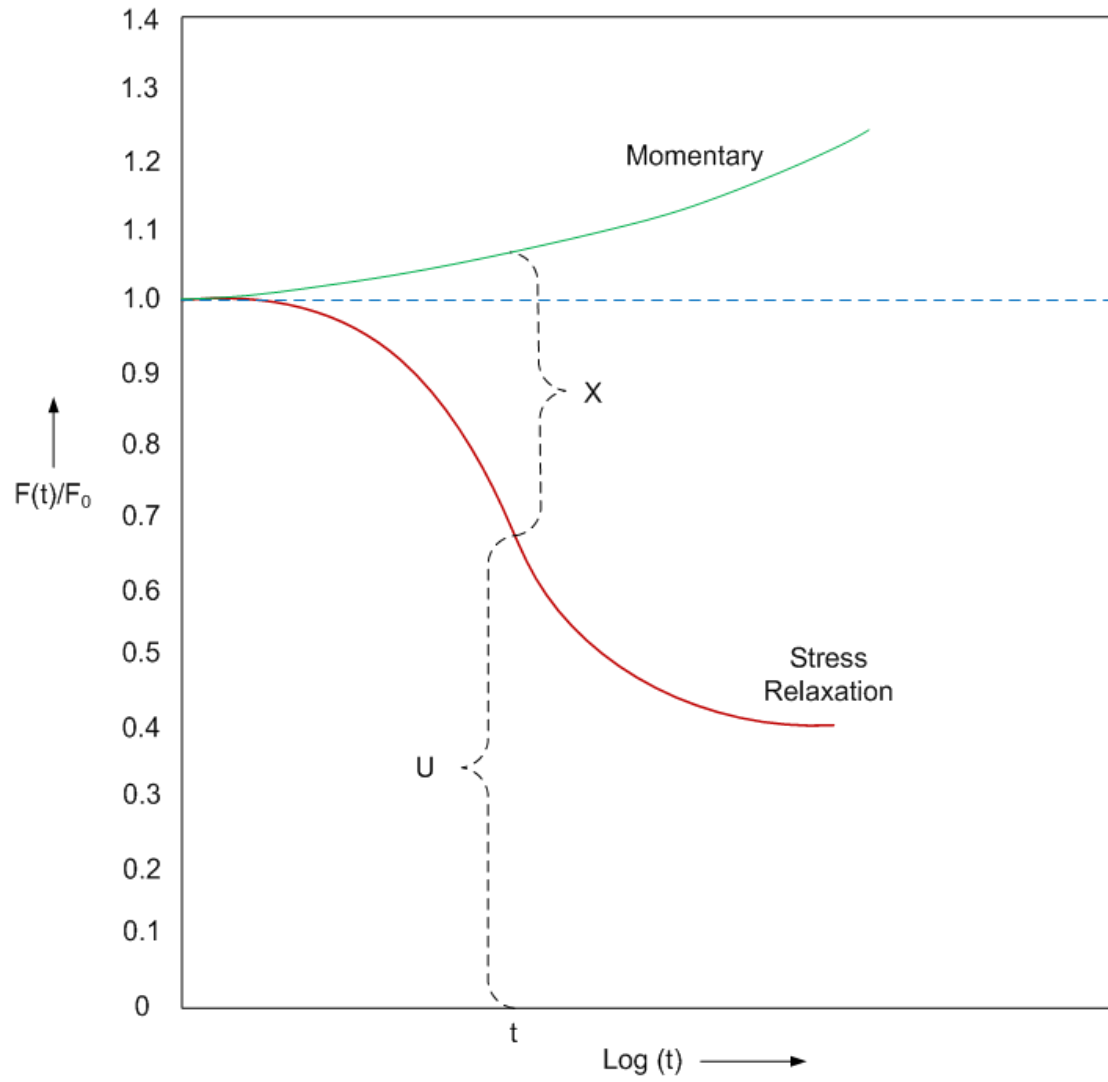


Figure 2.1 Evaluation of U and X from instantaneous and stress relaxation curve.

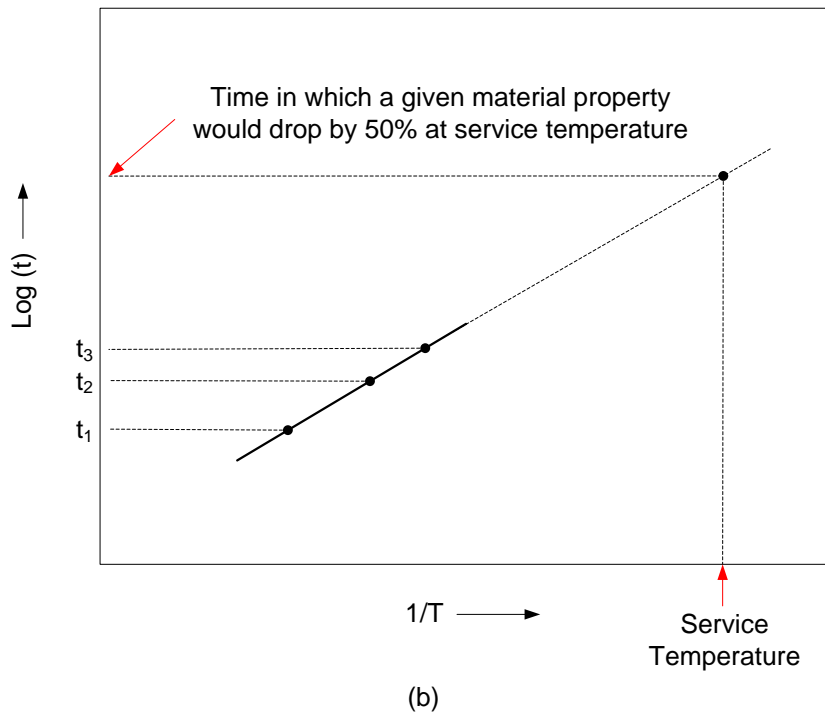
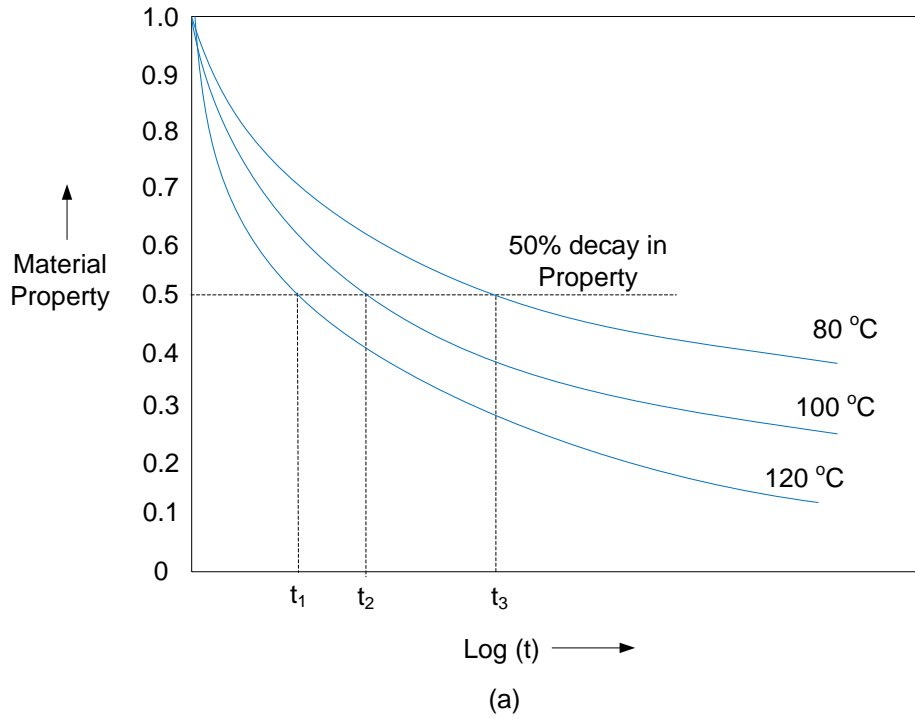


Figure 2.2 Illustration of Arrhenius approach. (a) Change in property with time at three temperatures, (b) Arrhenius plot.

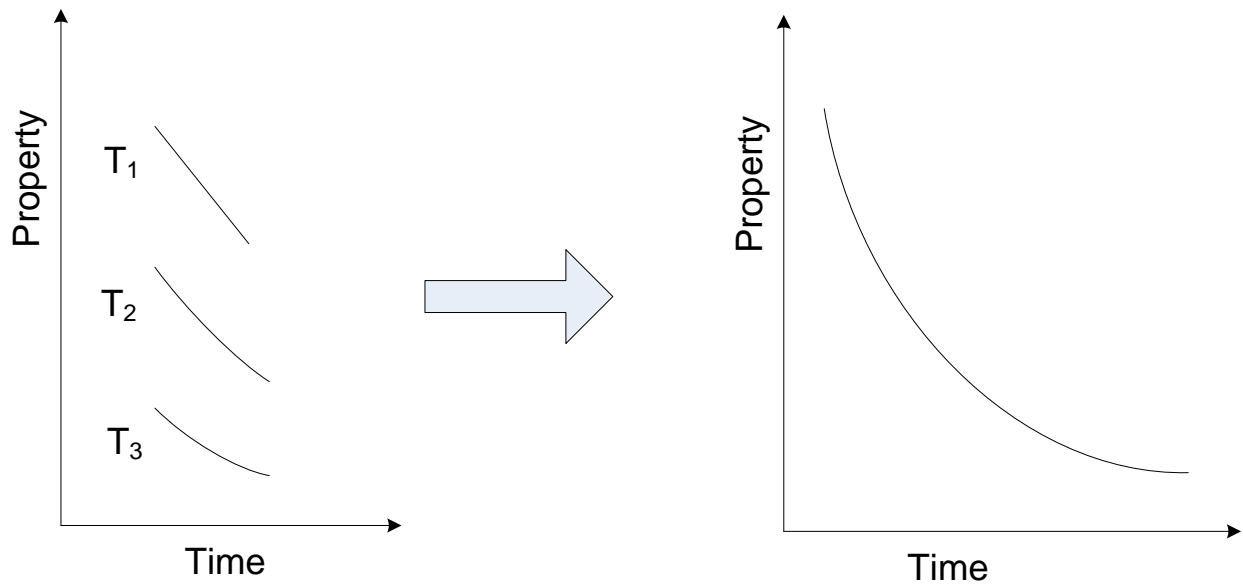


Figure 2.3 Illustration of constructing a master curve using WLF approach.

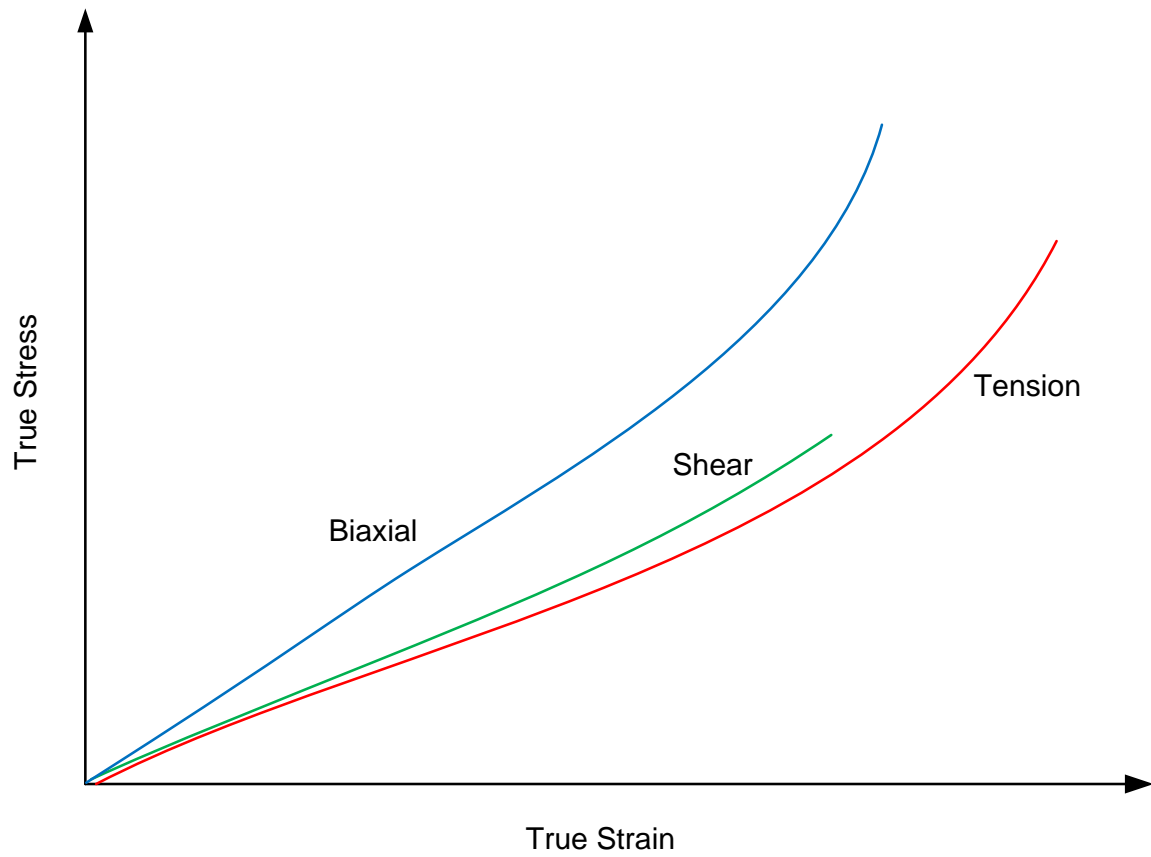


Figure 2.4 Typical true stress-true strain response of an elastomer under uniaxial tension, shear and biaxial extension [88].

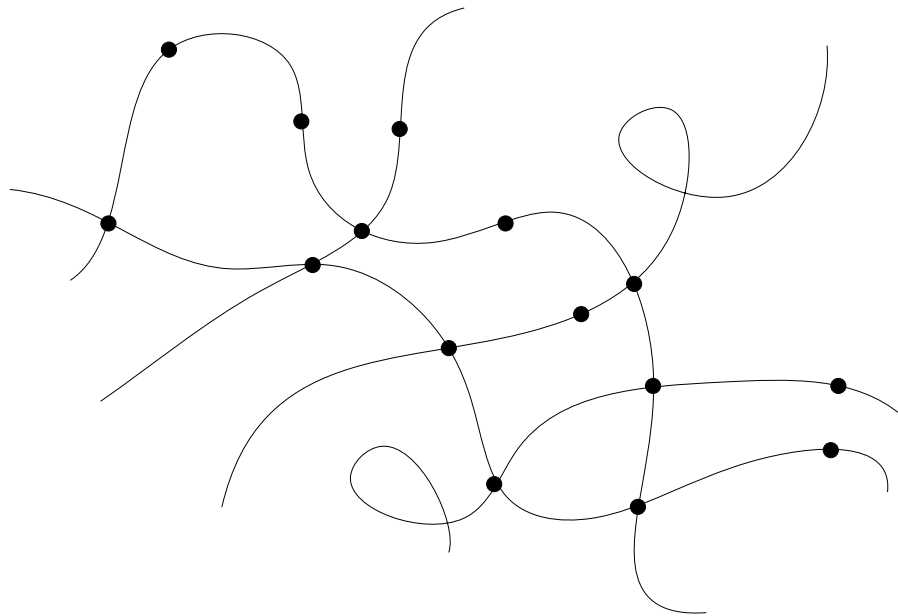


Figure 2.5 Sketch of part of a typical elastomeric network. The crosslinks are indicated by filled circles[120].

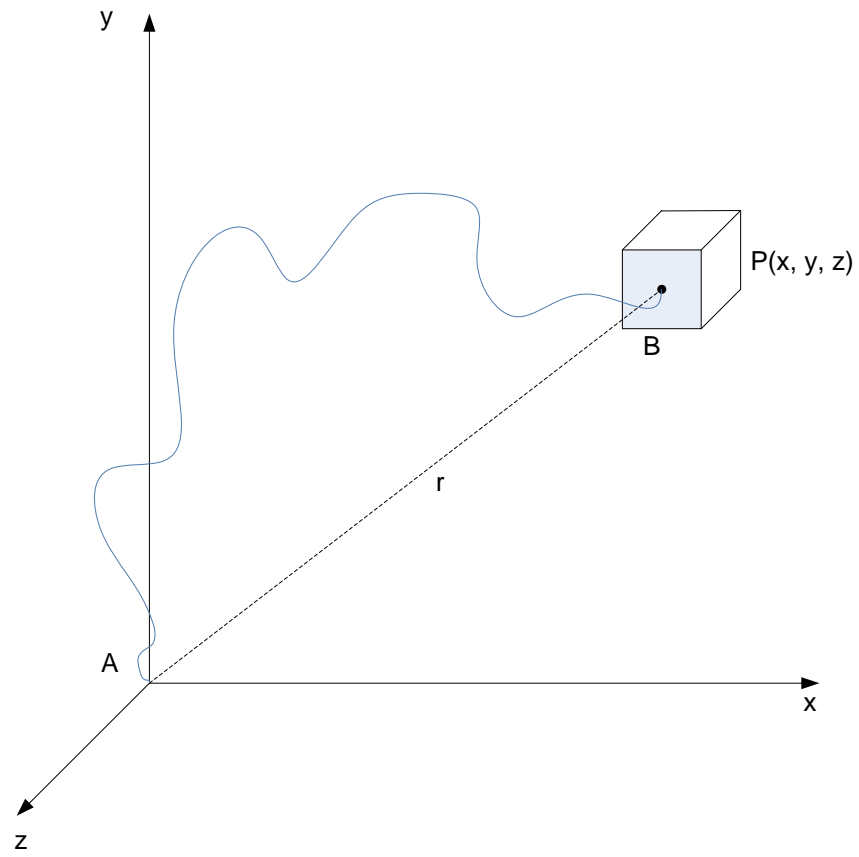


Figure 2.6 The statistically kinked chain. Specification of probability that the end should fall in the volume element $d\tau (=dx dy dz)$ [88].

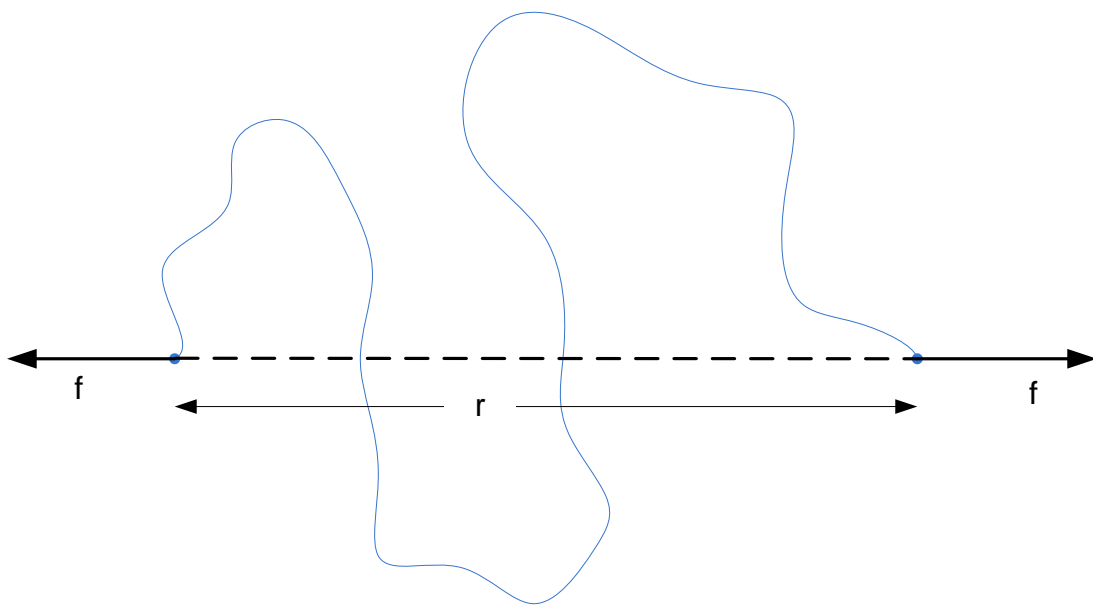


Figure 2.7 The tension on a chain whose ends are fixed in position is proportional to the distance r [88].

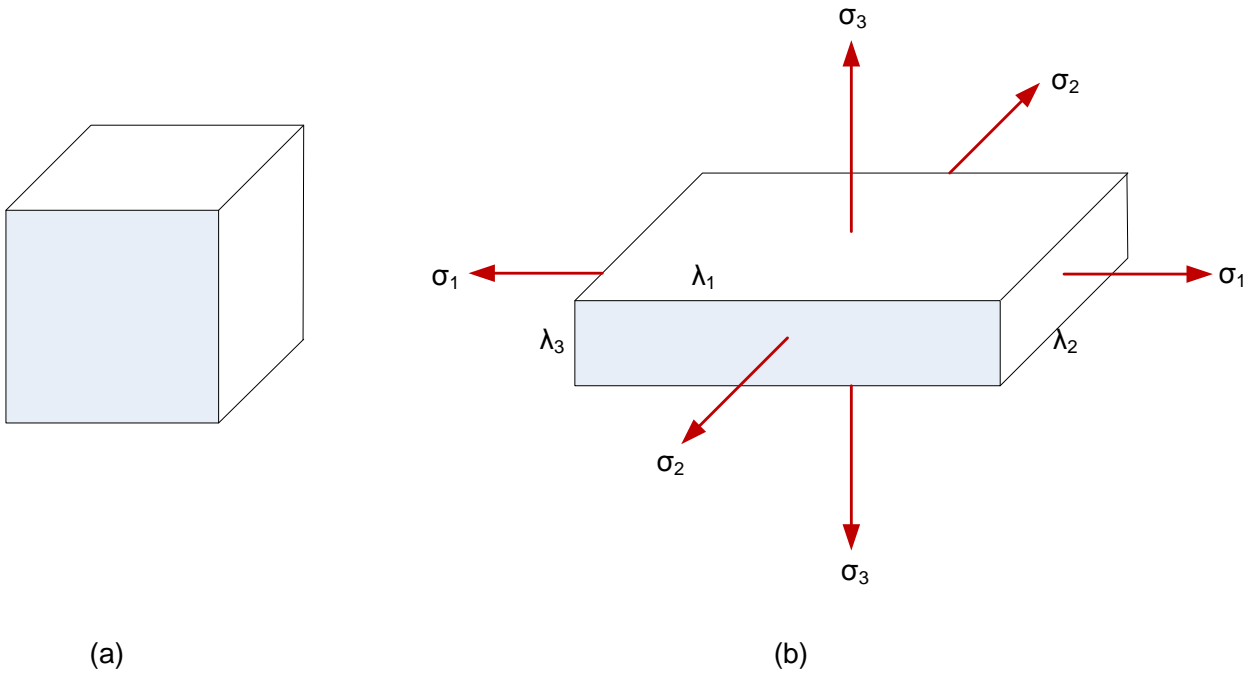


Figure 2.8 Pure homogenous strain: (a) the unstrained state; (b) the strained state.

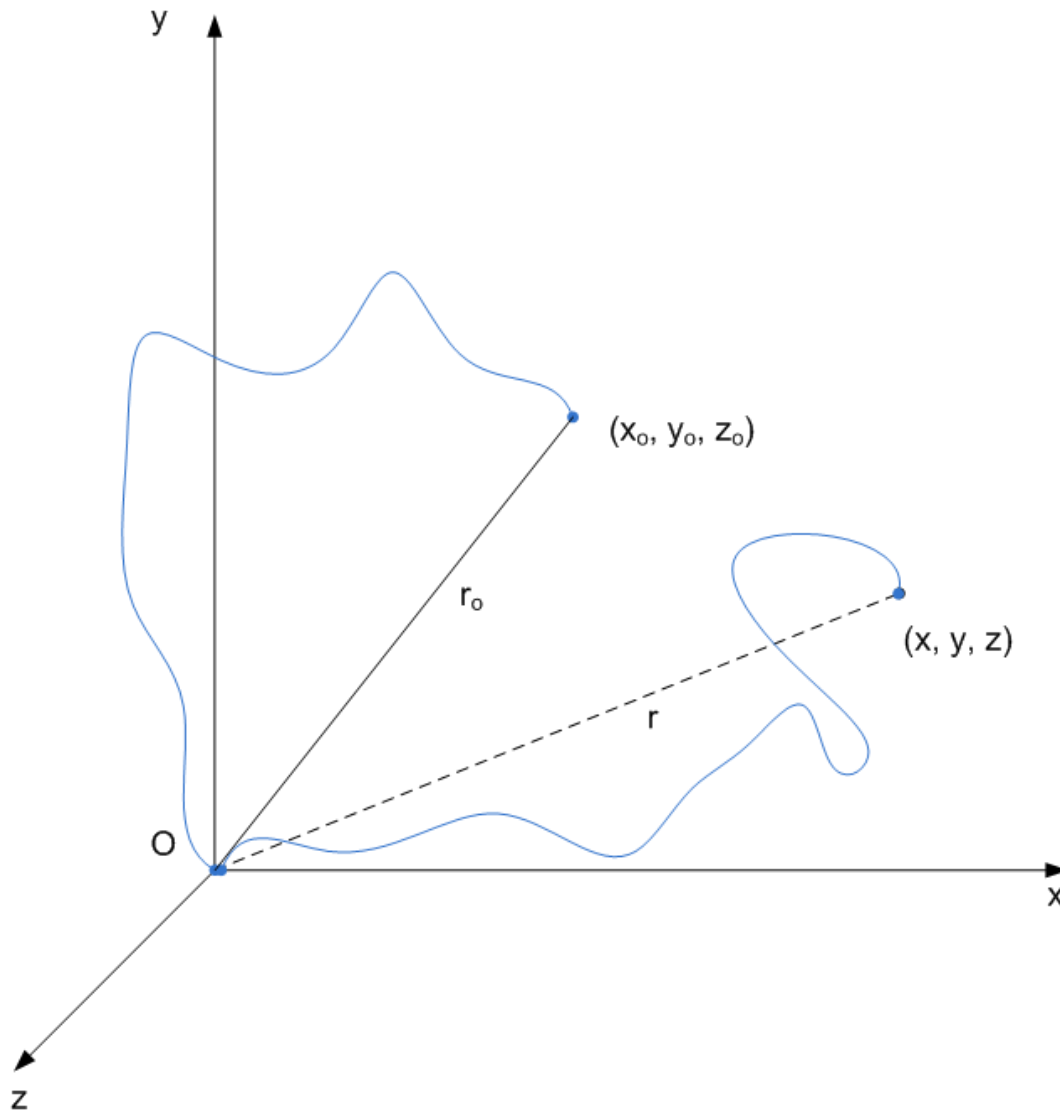


Figure 2.9 Illustration of an individual chain having an end-to-end distance represented by the vector r_0 in the unstrained state of the network. The vector r represents the end-to-end distance after deformation [88].

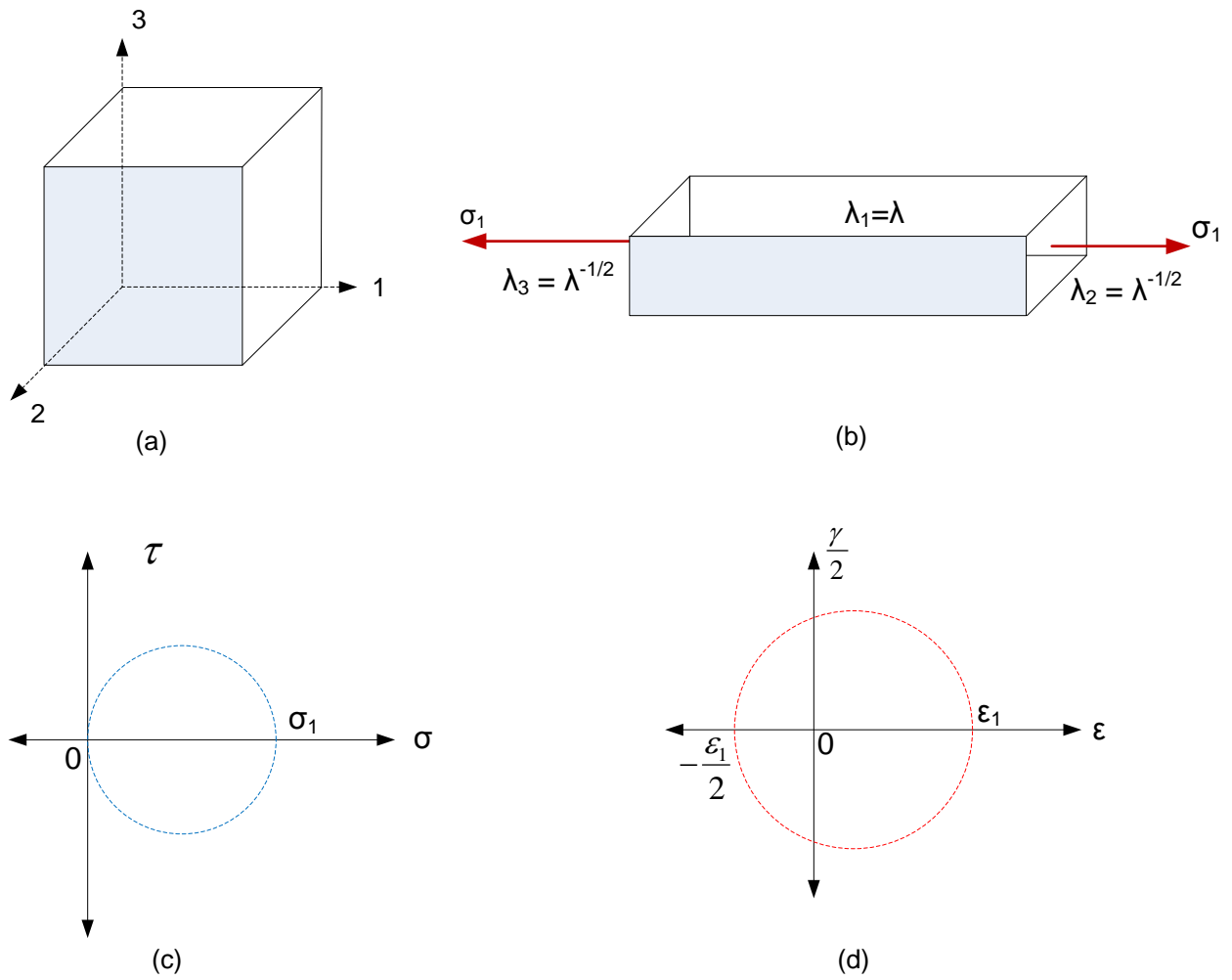


Figure 2.10 Hyperelastic material diagram for (a) unit cube in unstrained state, (b) unit cube subjected to uniaxial tension, (c) Mohr's diagram for stress, and (d) Mohr's diagram for strain.

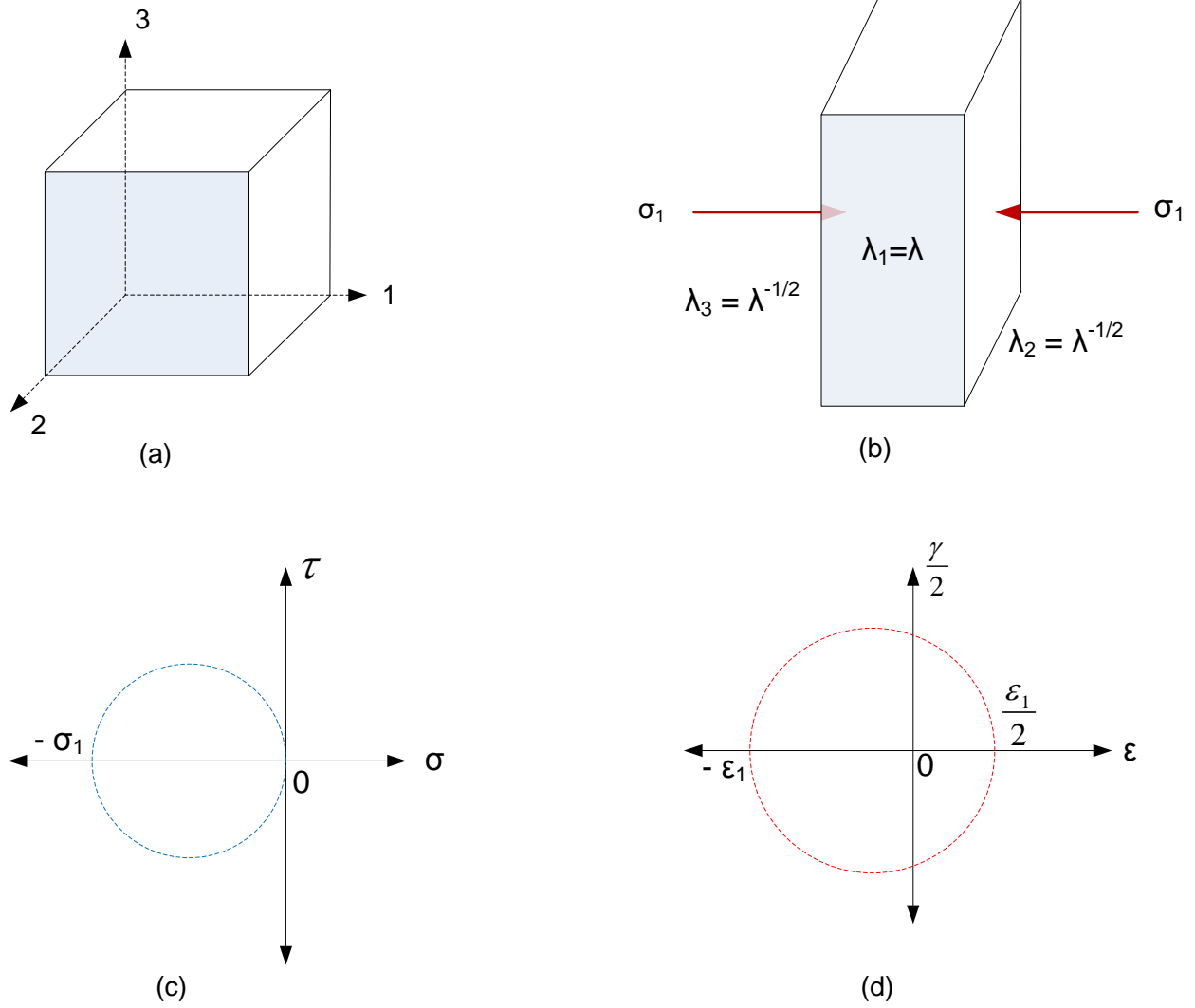


Figure 2.11 Hyperelastic material diagram for (a) unit cube in unstrained state, (b) unit cube subjected to uniaxial compression, (c) Mohr's diagram for stress, and (d) Mohr's diagram for strain.

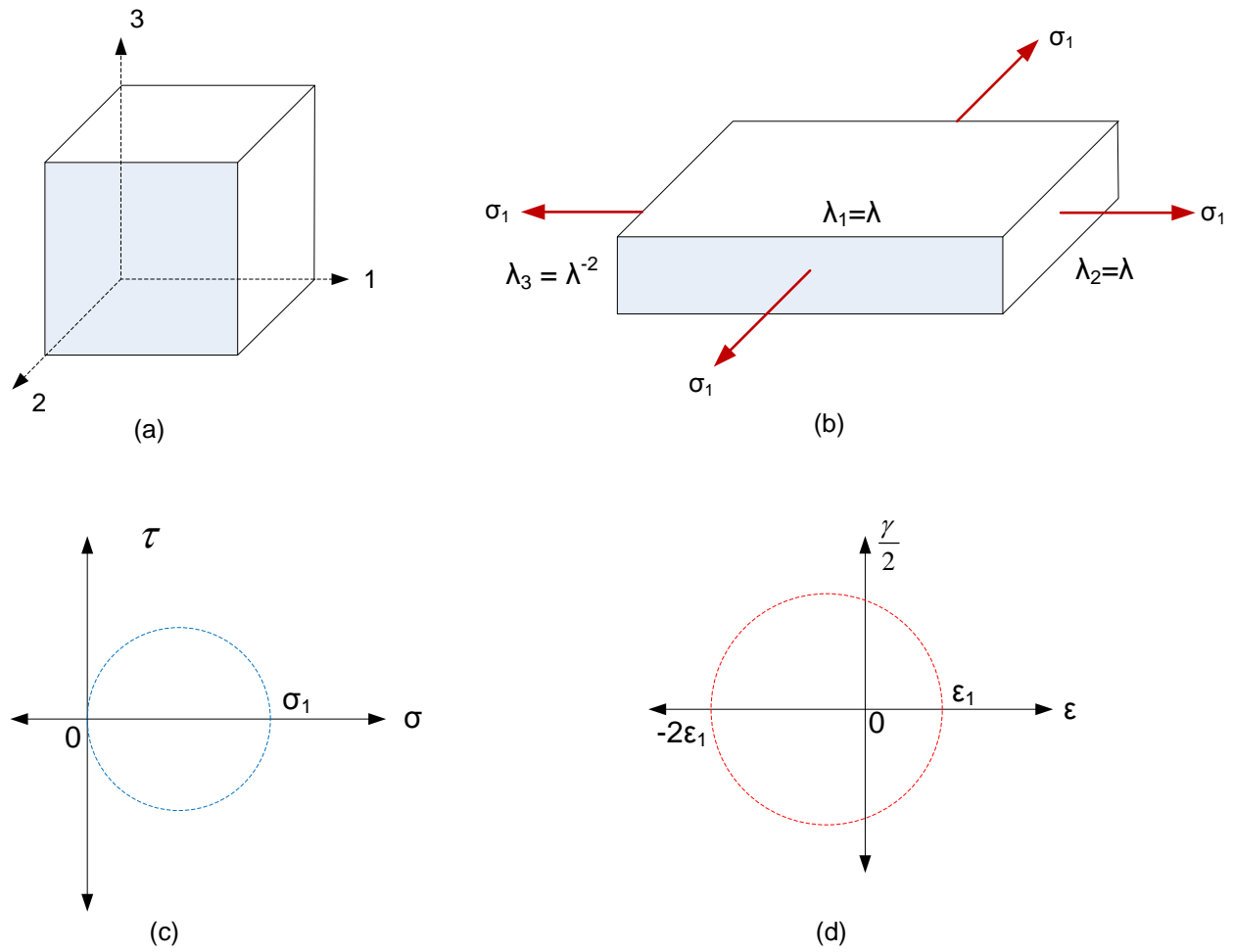


Figure 2.12 Hyperelastic material diagram for (a) unit cube in unstrained state, (b) unit cube subjected to equi-biaxial extension, (c) Mohr's diagram for stress, and (d) Mohr's diagram for strain.

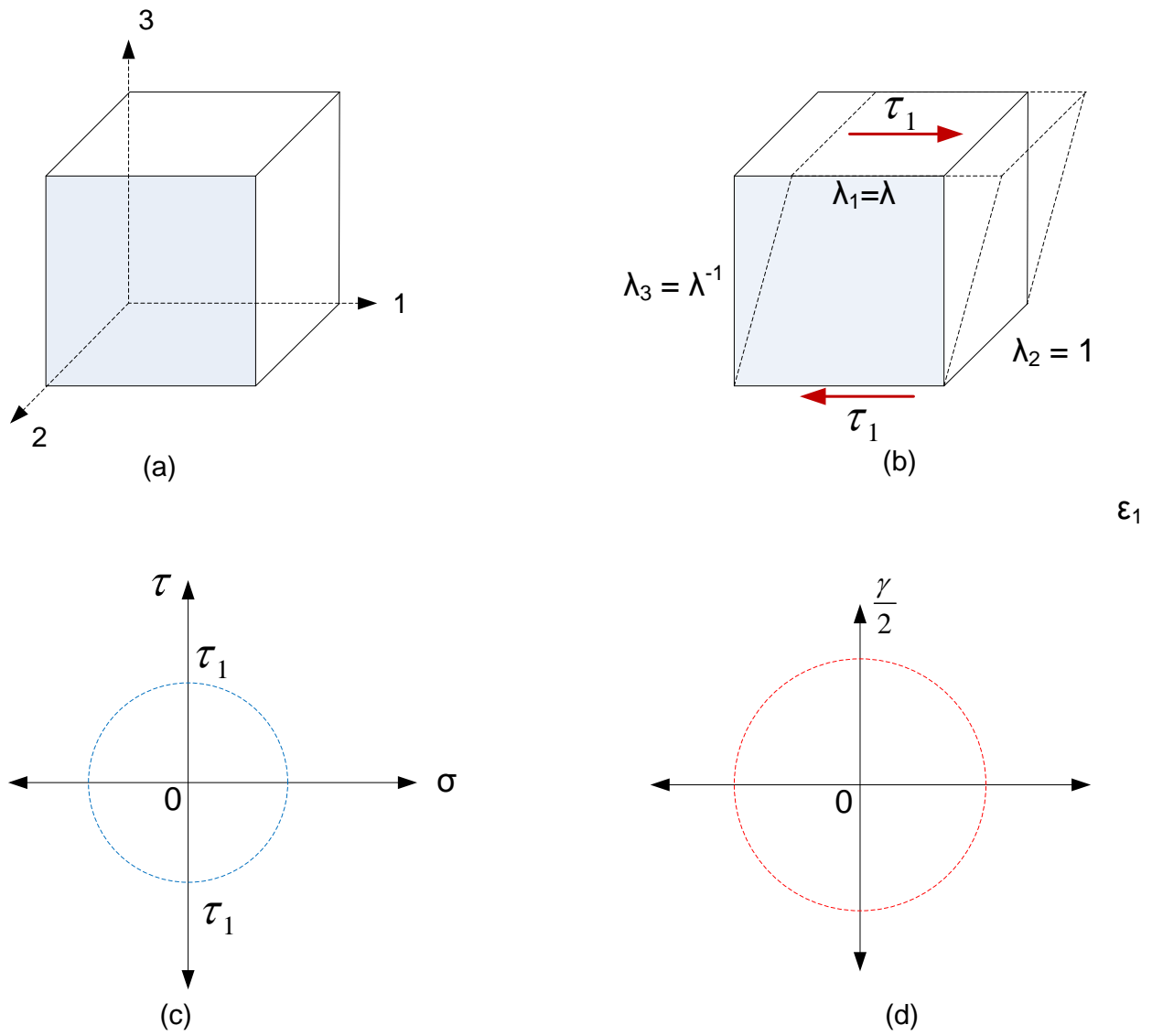


Figure 2.13 Hyperelastic material diagram for (a) unit cube in unstrained state, (b) unit cube subjected to simple shear, (c) Mohr's diagram for stress, and (d) Mohr's diagram for strain.

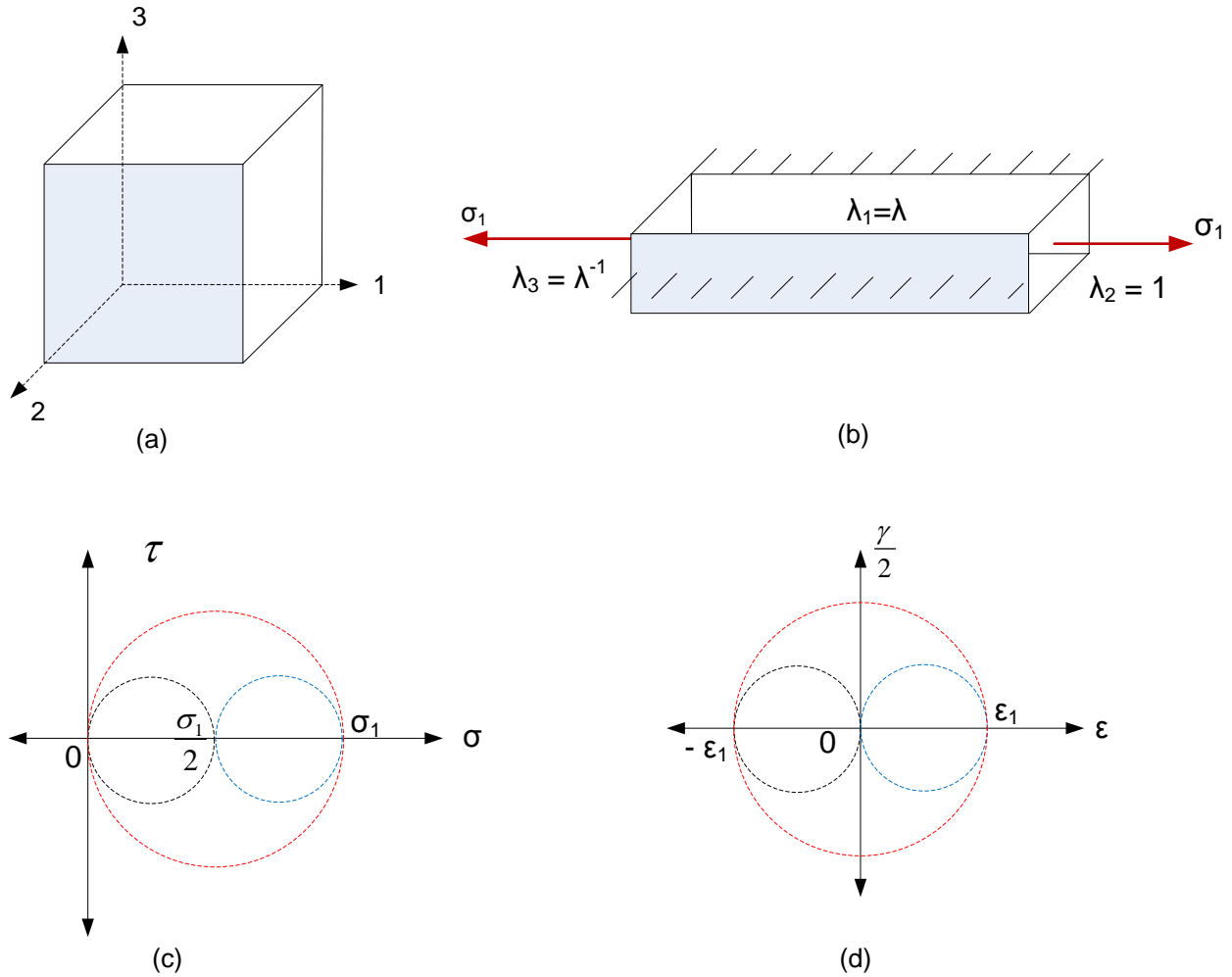


Figure 2.14 Hyperelastic material diagram for (a) unit cube in unstrained state, (b) unit cube subjected to pure shear, (c) Mohr's diagram for stress, and (d) Mohr's diagram for strain.

3 Uniaxial Tension Test

3.1 Introduction

Accurate predictions of component properties require both suitable material models and accurate material property data. Accurate modeling and analysis of elastomers in finite element analysis often require the use of hyperelastic material models. These models require that specimens of the subject material be stretched and stress-strain data collected. The uniaxial tension test is one of the most widely performed tests to determine the mechanical properties of an elastomer, including Young's modulus, tensile strength, and elongation to break in accordance with ASTM D412[1], which involves dumbbells, parallel-sided strips, or rings as test pieces.

Elastomers often exhibit large strains and usually have nonlinear stress-strain characteristics. There have been numerous attempts to characterize the large-strain tensile behavior of elastomers, the most successful of which have used some type of video system to capture images of the specimen at various stages of extension [2-7]. The laser scanning extensometer used in this study (Fiedler Optoelektronik, GmbH) enables non-contact measurement of strain within the specimen during uniaxial tensile testing with a spatial resolution of about 0.25 microns. It utilizes a laser beam to measure the spacing between reflective tape strips (markers) placed on the specimen to be tested. The reference length between the markers on the unstrained specimen is recorded automatically at the beginning of the experiment. Strain introduced in the specimen by the tensile load changes the distance between the markers, which is continuously recorded throughout the experiment.

Tensile properties of elastomers are typically reported based on the initial dimensions of the test piece due to the difficulty associated with calculation of actual dimensions of the deformed

specimen during testing. For this reason, engineering stress or engineering strain is reported in this study and these properties are defined as follows:

Young's modulus of elasticity:

The modulus (E) of a material is typically defined as the ratio of tensile stress to tensile strain in a quasi-static test. Due to the non-linear nature of a typical stress-strain curve for rubber, modulus is typically reported at a given strain, commonly at 100% strain[8]. An estimate for Young's modulus is typically obtained from the slope of the stress-strain curve in the very early part (small tensile strain) of the characteristic S curve.

Tensile Strength:

Tensile strength is defined as the amount of force required per unit original cross-sectional area to cause failure after elongation. Tensile strength is an important property because it relates to cohesive strength of a material against fracture.

Elastic Deformation

Elongation is the length of stretched material relative to its original dimensions. A property of interest for elastomers is the maximum elongation at failure. Elastomers inherently have good elongation properties, but they can vary significantly in the presence of an aggressive environment. Elongation per unit length, also referred to as engineering strain, is expressed in terms of percent of original dimensions as follows:

$$\text{Strain, } \varepsilon = \frac{L - L_o}{L_o} \quad (3.1)$$

where L is the final length after extension and L_o is the original length.

Tensile Set

Tensile set is defined as the tensile elongation remaining after a specimen has been stretched and allowed to relax. A standard test piece of known length is stretched by a stated percentage for a period of time and is then released. After recovery the length is measured and the change in length (i.e. unrecovered length) is expressed as a percentage of the original length as:

$$Set(\%) = \frac{L_f - L_o}{L_o} \times 100 \quad (3.2)$$

where L_f is the length of the specimen after aging.

Corrosive environments and temperature during fuel cell operation may possibly result in the degradation of the seal material properties (tensile strength, 100% modulus etc.). At operating conditions, the degradation process may be slow to show any significant change in material properties within the experimental time frame. Therefore, an accelerated degradation approach is usually adopted to predict material behavior at operating conditions. Temperature is a well-accepted accelerating parameter but may not exceed a certain level in the presence of liquid environments. Increasing the concentration of liquid solution is another approach, but because of the issues associated with handling highly concentrated acidic and/or basic solutions, using higher stress or strain levels seems more appropriate and suitable. Besides accelerating the degradation process of the seal material, this test will also help arrange a combination of temperature and liquid solutions in increasing order of their aggressiveness to the seal material. Based on the information obtained from accelerated testing, future mechanical/viscoelastic tests can be focused on studies in the most detrimental environments.

3.1.1 **Experimental**

3.1.1.1 *Sample Preparation*

For accelerated testing, dogbone samples were cut from a 200mm×200mm×0.5mm thick silicone LO305 seal material slab using ASTM D412 Die C and a clicker press (Qualitest Inc., Buffalo New York). Thin samples were chosen to enable faster diffusion of environment into the material. Holes were then punched in the grip regions of the samples using a custom designed steel rule die to help loading in the custom fixture. Thin dogbone samples tend to deform excessively at the holes in the grip region, so all samples were reinforced with a plastic tape bonded to the samples. Figure 3.1 shows the dimensions of the reinforced dogbone sample.

3.1.1.2 *Fixture Design*

In order to perform strain-based accelerated characterization, a fixture was designed using a stainless steel tube of rectangular cross section. Type 316 stainless steel was used because of its ability to withstand highly corrosive environments. The tube was cut to the desired length and holes were drilled on four sides of the tube wall. Stainless steel pins were then inserted in all the holes for loading samples. To achieve desired strain in the gage region of the sample loaded in the custom fixture, the location of the drilled holes was calculated using finite element analysis (FEA).

Successful modeling and design of elastomeric components using FEA depends on the selection of an appropriate strain energy function and an accurate determination of material constants in the function. Elastomeric materials are usually modeled in FEA using hyperelastic material models, which are based on the assumption of complete incompressibility. In order to characterize the material response and to satisfy the input requirements of the hyperelastic material models that exist in ABAQUS® (SIMULIA Incorporated, Forest Hill, MD), stress-strain

data obtained from multiple loading states such as uniaxial tension, pure shear, uniaxial compression, etc. are usually desired. For the purpose of this study, data from uniaxial tension and pure shear test were provided as material input into ABAQUS. Various hyperelastic material models, given in Table 3.1, were then evaluated in ABAQUS by fitting the material models with the experimental data from a uniaxial tension test. A least-square fitting procedure was used to determine the coefficients of the selected model. An improper fit between the model and test data indicates an unsuitable material model. Figure 3.2 shows the plot of experimental data and predicted uniaxial behavior and Figure 3.3 provides information on stability of material models and constants generated from the ABAQUS evaluation. It was observed that a two-parameter Ogden model and neo-Hookean model correlates very closely with the uniaxial test data. The two-parameter Ogden model was used in this study to further analyze the seals discussed later in this dissertation and also to calculate properties such as initial modulus. After the selection of a desired material model for further analysis, the dogbone sample was modeled in ABAQUS under uniaxial tension loading configuration, as shown in Figure 3.4, and the value of strain in the gage region was recorded. The sample was meshed with four-node reduced-integration axisymmetric quadrilateral elements, CAX4R, with hybrid formulation. Pin separation distance with corresponding strain in the gage region is also provided in Figure 3.4. Holes were then drilled on four sides of stainless steel tube and stainless steel pins were inserted to make the fixture ready for loading the samples. Figure 3.5 shows the dogbone samples strained to different levels using the custom fixture and submerged in various liquid solutions at a desired temperature. These strained dogbone samples were monitored regularly and any observations related to the failure/visual degradation of these samples was recorded. After the desired aging time was

reached, all samples were taken out of the containers and tested according to the procedure given below.

3.1.1.3 *Experimental Validation*

Experimental validation of the ABAQUS simulation for calculating strain in the gage region was also conducted. For that purpose, two white electrical tape strips were placed on the both sides of the samples prior to loading in the screening fixture. Initial and final lengths between two white markers were recorded for each sample, as shown in Figure 3.6, for calculation of engineering strain, according to Equation 3.1. Experimental strains obtained were compared to results from FEA simulation and good correlation between ABAQUS and experimental data was obtained, as shown in Table 3.2.

3.1.1.4 *Environments and Specimen Conditioning*

For aging in a desired environment, silicone dogbone samples were loaded in the fixture and placed in a glass container. For the case of aging in air, the glass containers with fixtures and strained samples were placed in gravity convection ovens at 120°C and 90°C. For the case of aging in liquid solutions, glass containers were filled with the desired liquid solution, viz. deionized (DI) water, 50v/50v ethylene glycol/water, and 0.1M sulfuric acid solutions, as illustrated in Figure 3.5, and placed in an oven at 90°C. To prevent any unwanted evaporation of the liquid from the glass containers during aging, they were sealed with an O-ring and glass lid clamped with the help of binder clips. Samples were aged for two months prior to testing.

3.1.1.5 *Mechanical Testing Procedure*

After the desired aging time, samples were taken out of the ovens and cooled to RT. Uniaxial tension tests were then conducted, according to the procedure outlined in ASTM standard D412[9], using an Instron (Norwood, MA) MicroTester 5848 series test frame outfitted with a

2kN strain-gage-based load cell and operated under displacement control mode at 500mm/min. Specimens were gripped in the tensile testing machine using pneumatic compression grips. As load was applied to the specimen, the elongation of the material was measured by a laser extensometer. Figure 3.7 shows a picture of the laser scanning extensometer and a dogbone specimen mounted in position for testing. Load–extension curves were recorded for all specimens by a host computer through a data acquisition (DAQ) card (PCI-6229, National Instruments Inc.). All tests were conducted at room temperature (about 23°C).

3.1.2 Results & Discussion

Figure 3.8 to Figure 3.13 show the results obtained from this part of the study. Typical stress-strain behavior with other relevant data obtained from testing as-received samples are shown in Figure 3.8. Properties such as tensile strength, strain to failure, 100% modulus, and initial modulus are typically reported in the literature and data obtained from as-received material can be used as a reference point when comparing results with aged samples. Such a comparison may provide insight into the effect of aging (combination of environment and stress) on material behavior and may also be useful to identify more aggressive environments for further long term testing such as compression stress relaxation etc. For example, on comparing tensile strength between as-received and aged samples, as shown in

Figure 3.9, and if the effect of environment alone is compared (i.e. 0% strain in various environments) tensile strength certainly reduces but not significantly. However, if the effect of strain on tensile strength in a given environment is compared, it is evident that reduction in strength depends on the environment. As an example, increasing the strain from 0% to 120% in air, DI water, and sulfuric acid solution, results in tensile strength reductions of 43%, 50%, and 58%, respectively, whereas increasing the strain from 0% to 120% in an ethylene glycol solution

reduces the tensile strength by 35%. Also interesting to note in Figure 3.10 is the reduction in strain to failure and as evident from the graph, strain to failure reduces by approximately 47% due to aging, but the effect is not distinguishable among different environments and strain levels. Figure 3.11 shows the change in 100% modulus of the material as compared to as-received behavior and an increase in modulus was evident for almost all aging conditions except at 120% strain in air and DI water at 90°C where the value is decreasing. The increase in modulus is highest for 120°C air and 90°C DI water at 0% strain and lowest for air and sulfuric acid solution at 90°C at 120% strain. If the modulus change in air is compared at 120°C and 90°C, it is interesting to note that the modulus increase is higher at 120°C than at 90°C for all strain levels except 120% strain at 90°C in air, where a decrease in modulus value is observed.

It is evident from the results and discussion on the effect of aging on mechanical properties that aging certainly affects material properties leading to degradation of the material with time. It appears that the extent of material degradation not only depends on environment but also on the level of stress or strain in the material and may even be accelerated by it (as evident for 120% strain where tensile strength and strain to break significantly reduced). Stress is known to increase the rate of diffusion of environment solution components into the material[10] affecting the crosslink density leading to change in mechanical properties of the material.

The crosslink density of an elastomer can be determined from swelling measurements, using the Flory-Rehner [11] relationship, or by a mechanical method involving stress-strain measurement. Numerous studies[12-18] have been conducted where both these methods of crosslink density calculation have been compared and results depend significantly on the material investigated, cure state, filler content, type etc. The discrepancy in the results obtained from two methods may also be attributed in part to network defects, such as loops and

entanglements, which behave as crosslinks but play a minor role in the stress-strain behavior of the elastomers[12, 18]. On the other hand, the swelling behavior of networks is more sensitive to network irregularities[16], the presence of elastically ineffective chain ends, and presence of flaws in the materials. The calculation of crosslink density of the seal material used in this study was conducted based on the statistical theory of rubber elasticity[19], where the initial modulus, E , can be defined as:

$$E = 3\nu R T \quad (3.3)$$

where E is obtained from the slope of initial region of a stress-strain plot, ν is the crosslink density, R is universal gas constant ($R = 8.314 \text{ J/K.mol}$) and T is absolute temperature. The calculation of crosslink density based on equation 1.3 is based on the assumption that surface degradation or other defects play no role in reducing the modulus of the material. Although the value of crosslink density calculated using equation 3.3 may not be accurate, it may help us provide insight into the material behavior by studying the trends in change of crosslink density with aging. The value of initial modulus, E , at a given temperature can be determined from uniaxial tension test data for aged and as-received samples, and the value of crosslink density can therefore be calculated by using Equation 3.3. To determine the elastic modulus, coefficients obtained above from one of the hyperelastic material models can be used. Both two-parameter Ogden and neo-Hookean models correlate very well with experimental data. Any of these models can be used for further data analysis. For this part of the study, elastic modulus, E was calculated from neo-Hookean material constants using the relationship:

$$E = 6 C_{10} \quad (3.4)$$

where the value of constant C_{10} was generated using stress-strain data in ABAQUS. Since three samples were tested for each aging conditions, an average value of E was used to determine the

average value of crosslink density. Figure 3.12 shows the change in crosslink density of the material in various aging conditions. It is interesting to note that crosslink density increases in aging conditions where samples were not strained i.e. 0% strain samples in all environments show an increase in crosslink density compared to as-received material, with the highest increase in DI water followed by sulfuric acid solution. However, in a given environmental condition, for example, air at 120°C, the crosslink density decreases monotonically as the strain level increases and a similar trend is also evident in all other environments. Crosslink density is defined as the number of elastically effective network chains per unit volume and may change as the material ages. In most applications, materials age in the presence of a degrading environment as well as stresses, and observation described above may help explain how stress alone contributes to material property degradation. In an unstrained molecular network, such as 0% strain samples in an environment, molecular chains have a lot of mobility and freedom to move around in the network and have a higher probability of finding new sites for crosslink formation though the degree of crosslink may depend on environment, as evident in Figure 3.12 where unstrained seal material has different crosslink density in different environments after aging. Since the molecular chains are not stressed, the process of chain scission is perhaps very slow compared to crosslinking. Therefore, net result of crosslink formation and chain scission is increase in crosslink density. On the other hand, if these molecular chains are strained, molecular chains are extended and have less mobility and therefore the probability of finding new sites for crosslink formation decreases. At the same time, chain scission is also taking place and the net rate of these two competing processes will decide change in crosslink density, which again depends on the aging environment. As evident from the samples strained by 25%, crosslink formation is the dominant process, leading to an increase in crosslink density compared to the neat material. As

the strain increases, chain scissioning dominates, leading to a decrease in crosslink density. This observation is evident in all environments, where increasing strain leads to decreasing crosslink density and therefore degradation of material properties such as tensile strength, shown in Figure 3.9, and 100% modulus in Figure 3.11. From this observation, it may be concluded that the crosslink density, and therefore the mechanical properties of a material, are influenced not only by environment but also the level of stress or strain the material is subjected to during service.

After the desired aging times, samples were removed from conditioning media and cooled to RT. Sample lengths were measured and compared with as-received sample lengths for calculating the tensile set using equation 3.2. Figure 3.13 shows the tensile set data in various environments, which can be summarized as follows:

1. In a given environment, set is higher at higher temperature. For example, set at 120°C is higher than at 90°C for a given value of strain.
2. In a given environment, set is higher at higher strain levels, i.e. 120% strained samples have higher set values than samples strained by 25%, 50%, or 80%.
3. Tensile set is highest and approximately the same at 120% strain in all liquid solutions.

3.1.3 Conclusions

Dogbone samples were punched out of PEM fuel cell grade silicone and aged in environments under stress by using a custom built fixture. Finite element analysis was carried out to design a fixture that enabled stretching the specimens to different strain levels on loading. Samples mounted in the fixture were then aged for two months in various environments to study the simultaneous effect of stress and environment on mechanical properties. The mechanical properties such as tensile strength, strain to break, 100% modulus, crosslink density, and tensile set all degrade due to aging and the extent of change (increase or decrease) depends significantly

on the strain level on the specimen. A drop in tensile strength and strain to break and an increase in 100% modulus were observed. Change in the material properties was explained by means of change in crosslink density of the material due to aging which in itself was largely affected by the imposed strain state of the material. Tensile set was observed in the material in all aging conditions and found to be higher in liquid solutions than air for a corresponding value of strain. Also, in given environment, higher the imposed strain higher is the tensile set. Also, observations on changes in material properties lead to the conclusion that at 120% strain, sulfuric acid is the most detrimental to silicone seal material. However, depending on the end application of the seal material, attention may be restricted to one or two important properties in an environment most relevant to application. For example, O-rings are typically used for sealing applications and permanent set is an important parameter in evaluating seal material candidates during screening.

References:

1. ASTM-D412-06a, *Standard Test Methods for Vulcanized Rubber and Thermoplastic Elastomers-Tension*, in *Annual Book of ASTM Standards*. 2002, ASTM International: West Conshohocken, PA, 19428-2959.
2. G. Buisson and K. Ravi-Chandar, "On the Constitutive Behavior of Polycarbonate under Large Deformation," *Polymer*, **31**, 2071-2076, 1989.
3. C. G'Sell, J.M. Hiver, A. Dahoun, and A. Souahi., "Video-Controlled Tensile Testing of Polymers and Metals Beyond the Necking Point," *Journal of Materials Science*, **27**(18), 5031-5039, 1992.
4. S. Nazarenko, S. Bensason, A. Hiltner, and E. Baer, "The Effect of Temperature and Pressure on Necking of Polycarbonate," *Polymer*, **35**(18), 3883-3892, 1994.
5. A.R. Haynes and P.D. Coates, "Semi-Automated Image Analysis of the True Tensile Drawing Behaviour of Polymers to Large Strains," *Journal of Materials Science*, **31**(7), 1843-1855, 1996.
6. J.M. Gloaguen and J.M. Lefebvre, "Plastic Deformation Behaviour of Thermoplastic/Clay Nanocomposites," *Polymer*, **42**(13), 5841-5847, 2001.
7. C. G'Sell, J.M. Hiver, and A. Dahoun, "Experimental Characterization of Deformation Damage in Solid Polymers under Tension and Its Interrelation with Necking," *International Journal of Solids and Structures*, **39**(13-14), 3857-3872, 2002.
8. O.H. Yeoh, "On Hardness and Young's Modulus of Rubber," *Plastics and Rubber Processing and Applications*, **4**(2), 141-144, 1984.
9. ASTM-D412-98a, *Standard Test Methods for Vulcanized Rubber and Thermoplastic Rubbers and Thermoplastic Elastomers-Tension*, in *Annual Book of ASTM Standards*. 1998, ASTM: West Conshohocken.
10. G.J. Morgan, R.P. Champion, and C.J. Derham, *Stress-Induced Phenomenon in Elastomers, and Their Influence on Design and Performance of O-Rings*, in *Elastomers and Components: Service Life Prediction- Progress & Challenges*, V.A. Coveney, Editor. 2006, Woodhead Publishing Ltd.: Cambridge, UK.
11. P.J. Flory and J. Rehner, "Statistical Mechanics of Cross-Linked Polymer Networks. II. Swelling," *Journal of Chemical Physics*, **11**, 521-526, 1943.

12. M.T. Ramesana, R. Alexa, and N.V. Khanhb, "Studies on the Cure and Mechanical Properties of Blends of Natural Rubber with Dichlorocarbene Modified Styrene–Butadiene Rubber and Chloroprene Rubber," *Reactive and Functional Polymers*, **62**(1), 41-50, 2005.
13. K. Ogura and M. Takahashi, "Uniaxial and Biaxial Extension Behavior of Lightly Crosslinked PMMA Melt at Constant Strain Rates," *Journal of the Society of Rheology*, **31**(2), 79-83, 2003.
14. V. Sekkar, K. NARAYANASWAMY, K.J. SCARIAH, P.R. NAIR, K.S. SASTRI, and H.G. ANG, "Evaluation by Various Experimental Approaches of the Crosslink Density of Urethane Networks Based on Hydroxyl-Terminated Polybutadiene," *Journal of applied polymer science*, **103**(5), 3129-3133, 2007.
15. N. Sombatsompop, "Practical Use of the Mooney-Rivlin Equation for Determination of Degree of Crosslinking of Swollen NR Vulcanizates," *Journal of The Science Society of Thailand*, **24**, 199-204, 1998.
16. M.S. Eroglu and O. Guven, "Network Characterization of Energetic Poly (Glycidyl Azide)," *Turkish Journal of Chemistry*, **21**, 256-261, 1997.
17. M.T. Ramesan, T.K.M. Kumar, R. Alex, and B. Kurikose, "Investigations on the Addition of Styrene Butadiene Rubber in Natural Rubber and Dichlorocarbene Modifies Styrene Butadiene Rubber Blends," *Journal of Materials Science*, **37**, 109-116, 2002.
18. J.P. Baker, L.H. Hong, H.W. Blanch, and J.M. Prausnitz, "Effect of Initial Total Monomer Concentration on the Swelling Behavior of Cationic Acrylamide-Based Hydrogels," *Macromolecules*, **27**(6), 1446-1454, 1994.
19. L.R.G. Treloar, *The Physics of Rubber Elasticity*. 2 ed. 1975, Glasgow: Oxford University Press.

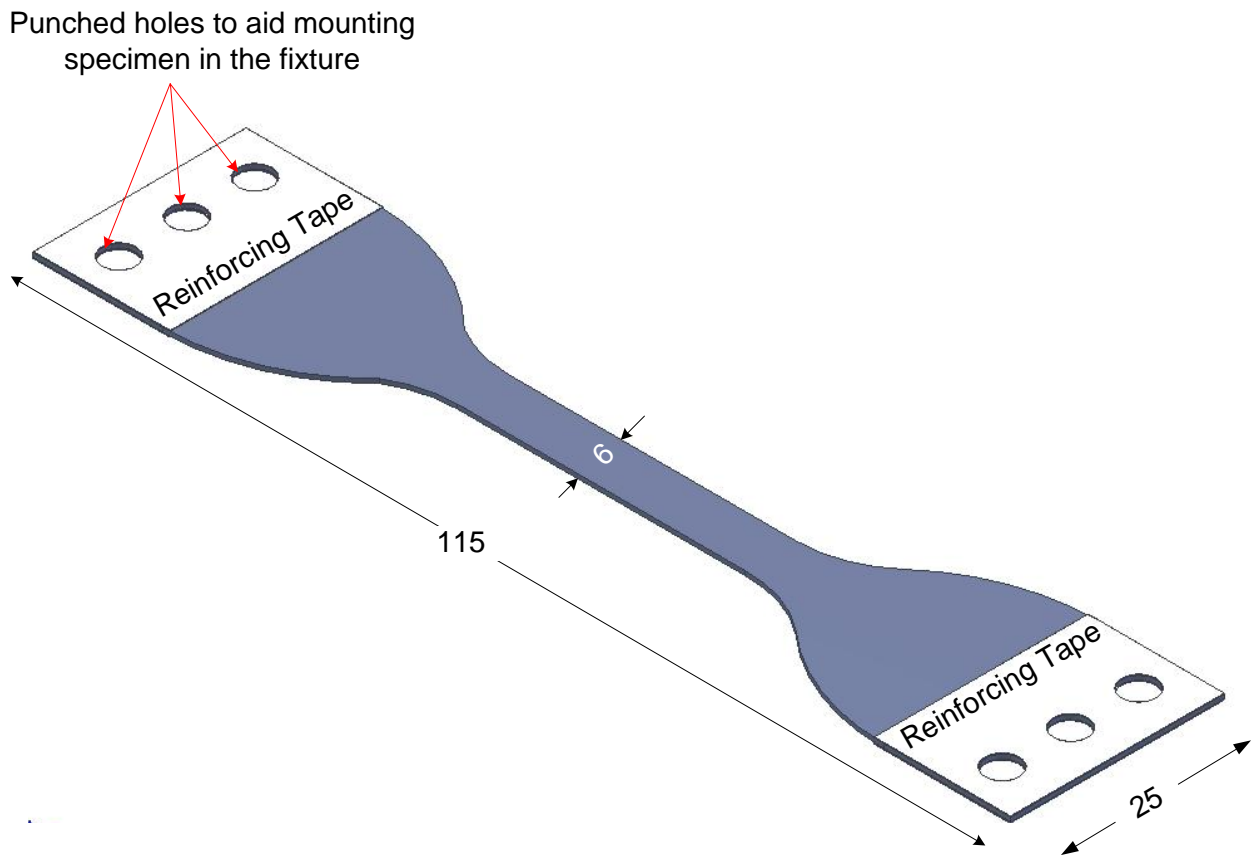


Figure 3.1 Illustration of dogbone specimen used for tensile testing, shown with nominal dimensions. Holes drilled in the grip region are reinforced with PSA tape to avoid deformation around holes. All dimensions shown are in mm.

Table 3.1 Hyperelastic material models used in finite element analysis for material evaluation.

Basis	Models	Material Parameters
Physically Motivated	Van Der Waals	4
Phenomenological	Mooney Rivlin	2
	Ogden (Order N = 1)	2
	Ogden (Order N = 2)	4
	neo-Hookean	2
	Yeoh	3

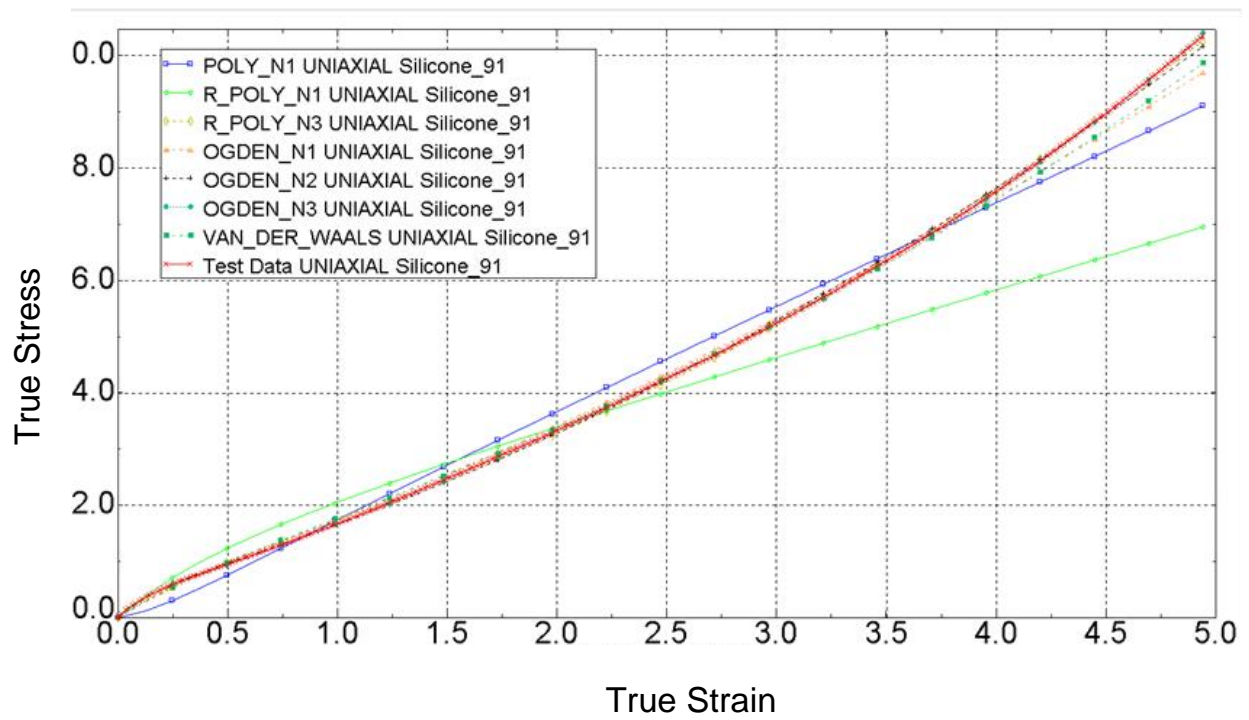


Figure 3.2 Plot of experimental data and predicted uniaxial behavior using various material models.

HYPERELASTICITY - MOONEY-RIVLIN STRAIN ENERGY

D1	C10	C01
0.00000000	0.907709891	-0.817744643

STABILITY LIMIT INFORMATION

WARNING: UNSTABLE HYPERELASTIC MATERIAL

UNIAXIAL TENSION:	UNSTABLE AT A NOMINAL STRAIN LARGER THAN	0.0600
UNIAXIAL COMPRESSION:	UNSTABLE AT A NOMINAL STRAIN LESS THAN	-0.0574
BIAXIAL TENSION:	UNSTABLE AT A NOMINAL STRAIN LARGER THAN	0.0300
BIAXIAL COMPRESSION:	UNSTABLE AT A NOMINAL STRAIN LESS THAN	-0.0287
PLANAR TENSION:	UNSTABLE AT A NOMINAL STRAIN LARGER THAN	0.0500
PLANAR COMPRESSION:	UNSTABLE AT A NOMINAL STRAIN LESS THAN	-0.0476
VOLUMETRIC TENSION:	STABLE FOR ALL VOLUME RATIOS	
VOLUMETRIC COMPRESSION:	STABLE FOR ALL VOLUME RATIOS	

HYPERELASTICITY - OGDEN STRAIN ENERGY FUNCTION WITH N = 1

I	MU_I	ALPHA_I	D_I
1	0.836417438	2.50158477	0.00000000

STABILITY LIMIT INFORMATION

UNIAXIAL TENSION:	STABLE FOR ALL STRAINS
UNIAXIAL COMPRESSION:	STABLE FOR ALL STRAINS
BIAXIAL TENSION:	STABLE FOR ALL STRAINS
BIAXIAL COMPRESSION:	STABLE FOR ALL STRAINS
PLANAR TENSION:	STABLE FOR ALL STRAINS
PLANAR COMPRESSION:	STABLE FOR ALL STRAINS
VOLUMETRIC TENSION:	STABLE FOR ALL VOLUME RATIOS
VOLUMETRIC COMPRESSION:	STABLE FOR ALL VOLUME RATIOS

HYPERELASTICITY - OGDEN STRAIN ENERGY FUNCTION WITH N = 2

I	MU_I	ALPHA_I	D_I
1	0.172957761	2.43121874	0.00000000
2	1.09117431	-5.39657088	0.00000000

STABILITY LIMIT INFORMATION

UNIAXIAL TENSION: STABLE FOR ALL STRAINS
 UNIAXIAL COMPRESSION: STABLE FOR ALL STRAINS
 BIAXIAL TENSION: STABLE FOR ALL STRAINS
 BIAXIAL COMPRESSION: STABLE FOR ALL STRAINS
 PLANAR TENSION: STABLE FOR ALL STRAINS
 PLANAR COMPRESSION: STABLE FOR ALL STRAINS
 VOLUMETRIC TENSION: STABLE FOR ALL VOLUME RATIOS
 VOLUMETRIC COMPRESSION: STABLE FOR ALL VOLUME RATIOS

HYPERELASTICITY - NEO-HOOKEAN STRAIN ENERGY

D1	C10	C01
0.00000000	0.587778936	0.00000000

STABILITY LIMIT INFORMATION

UNIAXIAL TENSION: STABLE FOR ALL STRAINS
 UNIAXIAL COMPRESSION: STABLE FOR ALL STRAINS
 BIAXIAL TENSION: STABLE FOR ALL STRAINS
 BIAXIAL COMPRESSION: STABLE FOR ALL STRAINS
 PLANAR TENSION: STABLE FOR ALL STRAINS
 PLANAR COMPRESSION: STABLE FOR ALL STRAINS
 VOLUMETRIC TENSION: STABLE FOR ALL VOLUME RATIOS
 VOLUMETRIC COMPRESSION: STABLE FOR ALL VOLUME RATIOS

```

HYPERELASTICITY - POLYNOMIAL STRAIN ENERGY FUNCTION WITH N = 3

      D1          C10          C01          C02          C03
      D2          C20          C11          C12
      D3          C30          C21

0.00000000      0.464378911      0.00000000
0.00000000      8.172441640E-03      0.00000000      0.00000000
0.00000000      -4.104576397E-05      0.00000000      0.00000000      0.00000000

      STABILITY LIMIT INFORMATION

WARNING: UNSTABLE HYPERELASTIC MATERIAL

UNIAXIAL TENSION:      UNSTABLE AT A NOMINAL STRAIN LARGER THAN      9.1700
UNIAXIAL COMPRESSION: UNSTABLE AT A NOMINAL STRAIN LESS THAN      -0.9807
BIAXIAL TENSION:      UNSTABLE AT A NOMINAL STRAIN LARGER THAN      6.1900
BIAXIAL COMPRESSION: UNSTABLE AT A NOMINAL STRAIN LESS THAN      -0.6864
PLANAR TENSION:      UNSTABLE AT A NOMINAL STRAIN LARGER THAN      9.1200
PLANAR COMPRESSION: UNSTABLE AT A NOMINAL STRAIN LESS THAN      -0.9012
VOLUMETRIC TENSION:  STABLE FOR ALL VOLUME RATIOS
VOLUMETRIC COMPRESSION: STABLE FOR ALL VOLUME RATIOS

```

```

HYPERELASTICITY - VAN DER WAALS STRAIN ENERGY FUNCTION

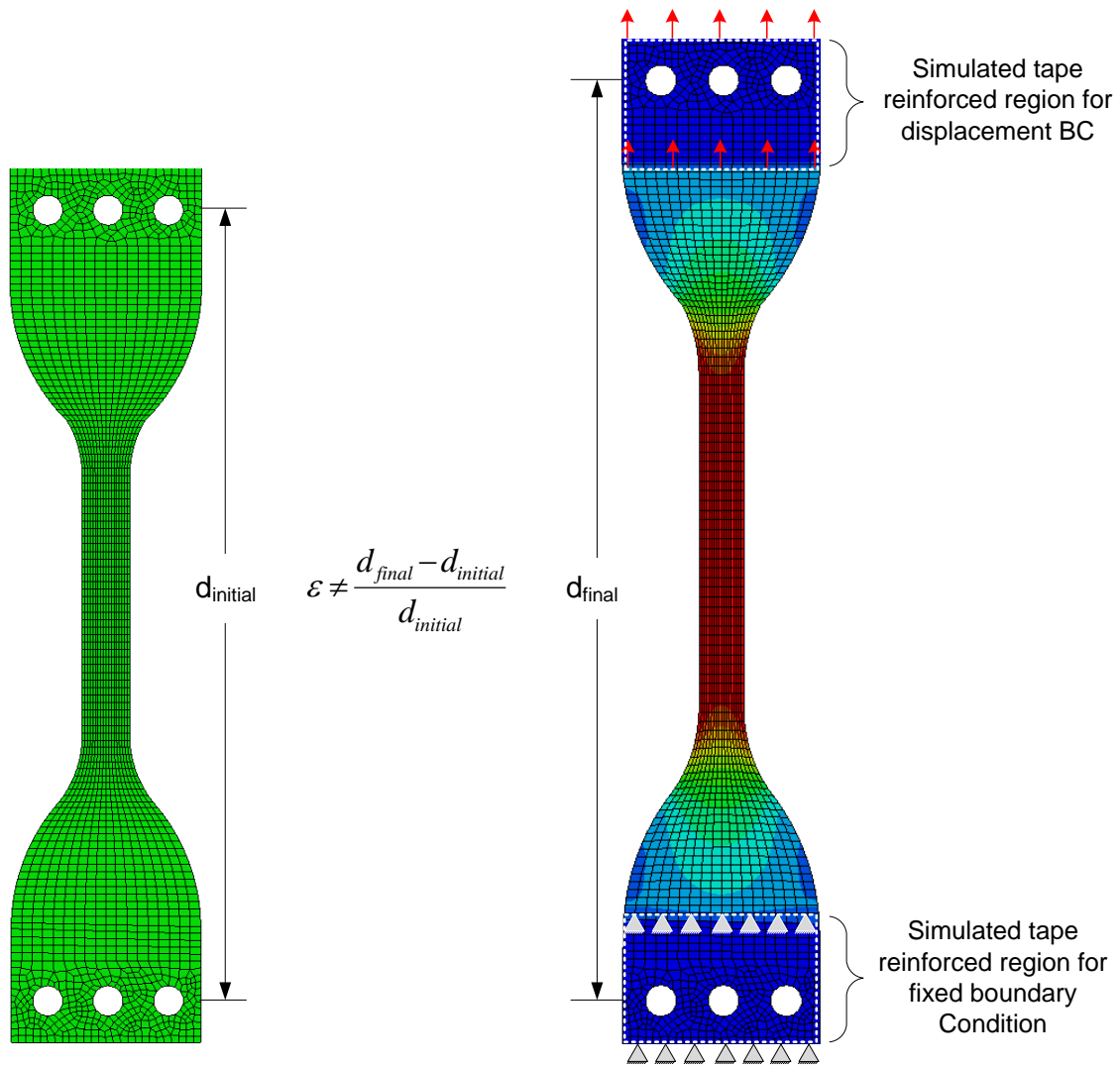
      MU          LAMBDA_M          A          BETA          D
0.859509460      16.6195025      -0.276253384      0.254239240      0.000000000

      STABILITY LIMIT INFORMATION

UNIAXIAL TENSION:      STABLE FOR ALL STRAINS
UNIAXIAL COMPRESSION: UNSTABLE AT A NOMINAL STRAIN LESS THAN      -0.9669
BIAXIAL TENSION:      UNSTABLE AT A NOMINAL STRAIN LARGER THAN      4.5000
BIAXIAL COMPRESSION:  STABLE FOR ALL STRAINS
PLANAR TENSION:      STABLE FOR ALL STRAINS
PLANAR COMPRESSION:  STABLE FOR ALL STRAINS
VOLUMETRIC TENSION:  STABLE FOR ALL VOLUME RATIOS
VOLUMETRIC COMPRESSION: STABLE FOR ALL VOLUME RATIOS

```

Figure 3.3 Hyperelastic material model evaluation results from ABAQUS for silicone seal material.



Pin Separation, d_{final} (mm)	ABAQUS Logarithmic Strain, LE (%)	Engineering Strain, $\epsilon_{engineering} = e^{LE} - 1$ (%)
116.08	20	22.14
130.58	40	49.18
148.58	60	82.21
173.58	80	122.55

Figure 3.4 Illustration of dogbone samples under uniaxial tension loading configuration in ABAQUS.

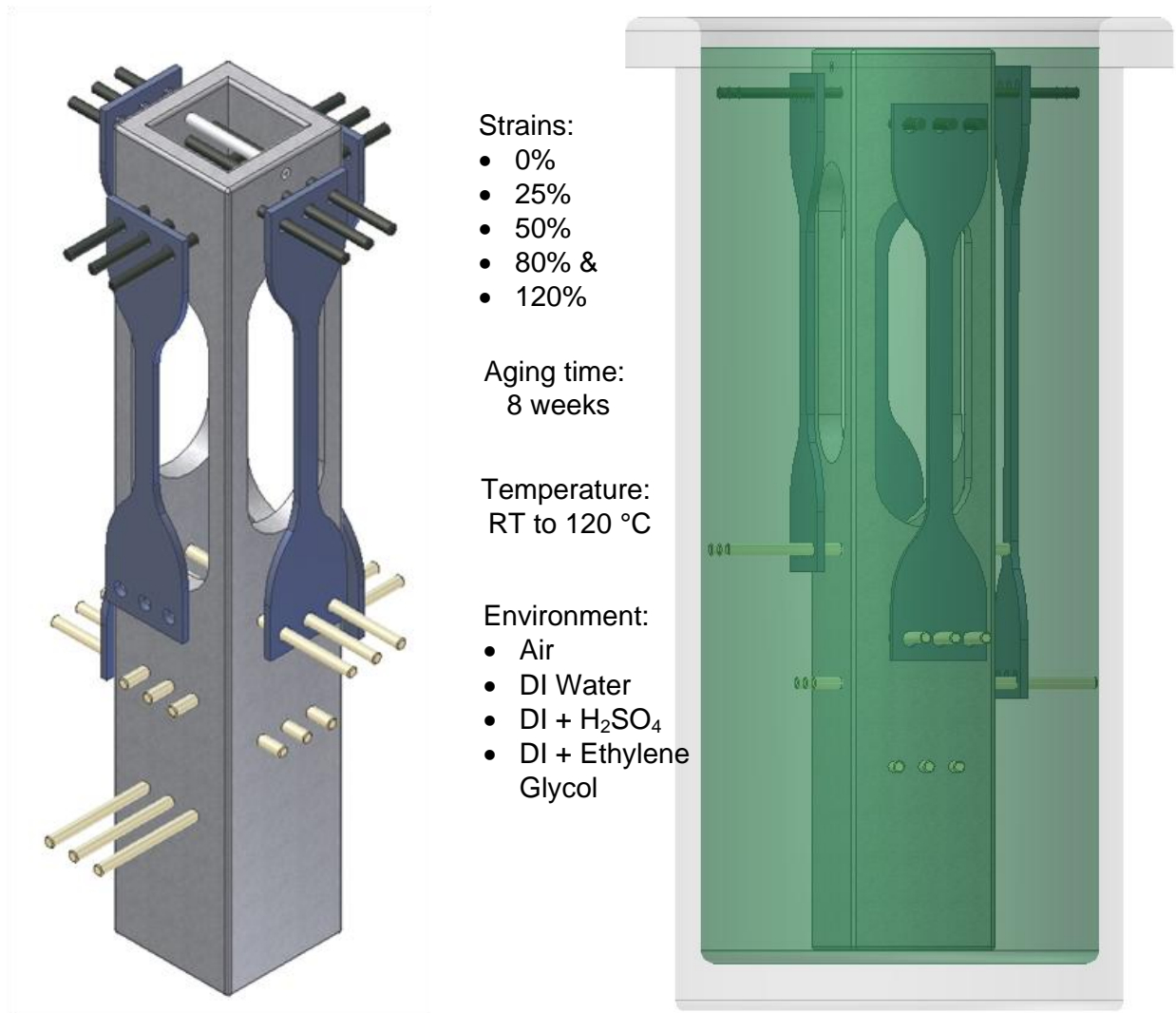


Figure 3.5 Illustration of screening tests performed on dogbone samples strained to different levels in various environments at different temperatures to evaluate their aggressiveness to the seal material.

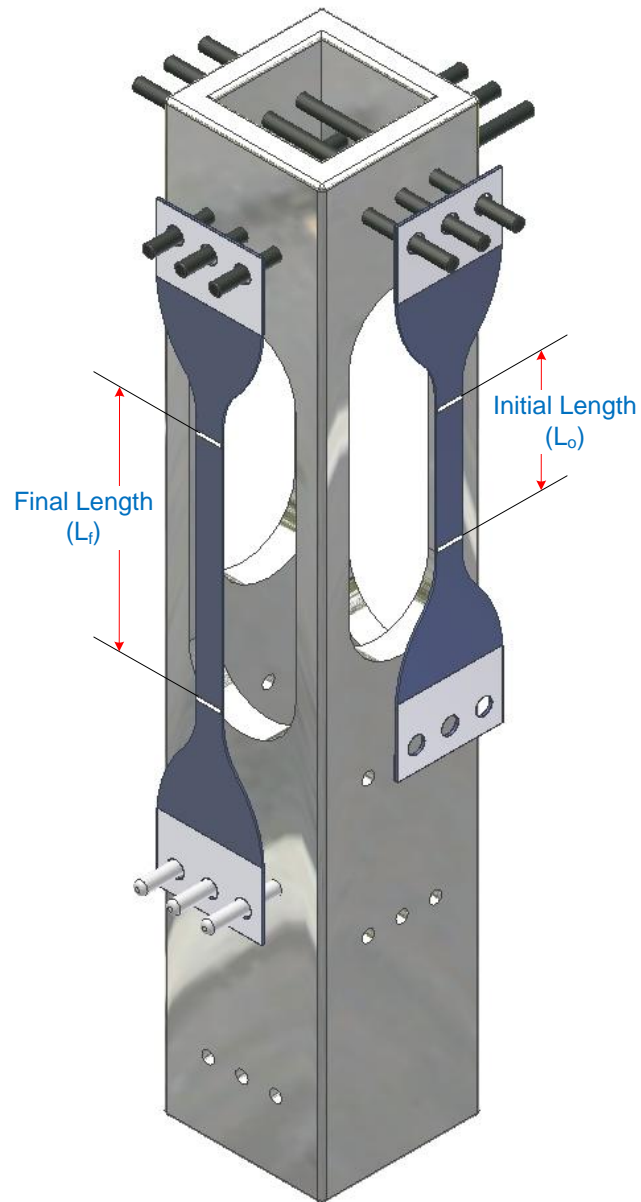


Figure 3.6 Illustration of procedure for measuring experimental strain in a dogbone sample stretched in the custom fixture.

Table 3.2 Experimental validation of ABAQUS simulation results.

ABAQUS		Experimental		
Logarithmic Strain, LE (%)	Engineering Strain, $\varepsilon_{ABAQUS} = e^{LE} - 1$ (%)	Initial Length, L_o (mm)	Final length, L_f (mm)	Engineering Strain, $\varepsilon_{exp} = \frac{L_f - L_o}{L_o} \times 100$ (%)
20	22.14	30	37.1	23.67
40	49.18	30	44.8	49.33
60	82.21	30	54.8	82.67
80	122.55	30	66.3	121

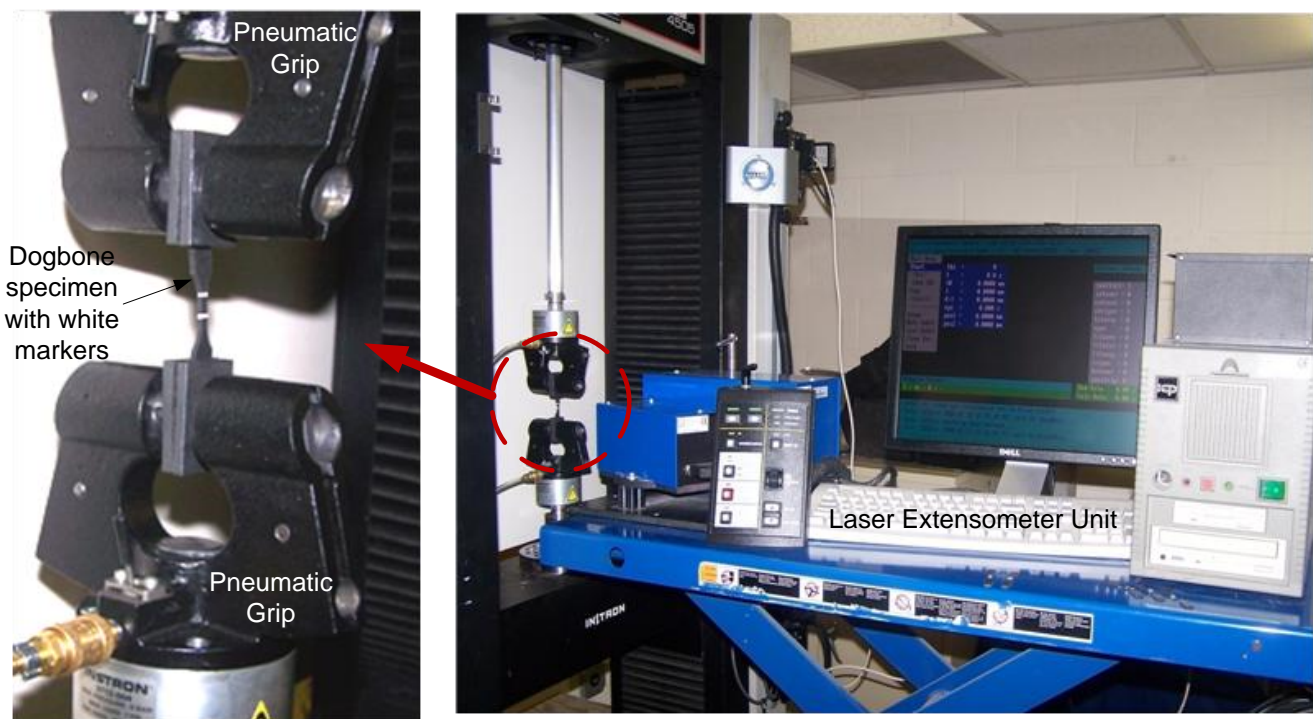
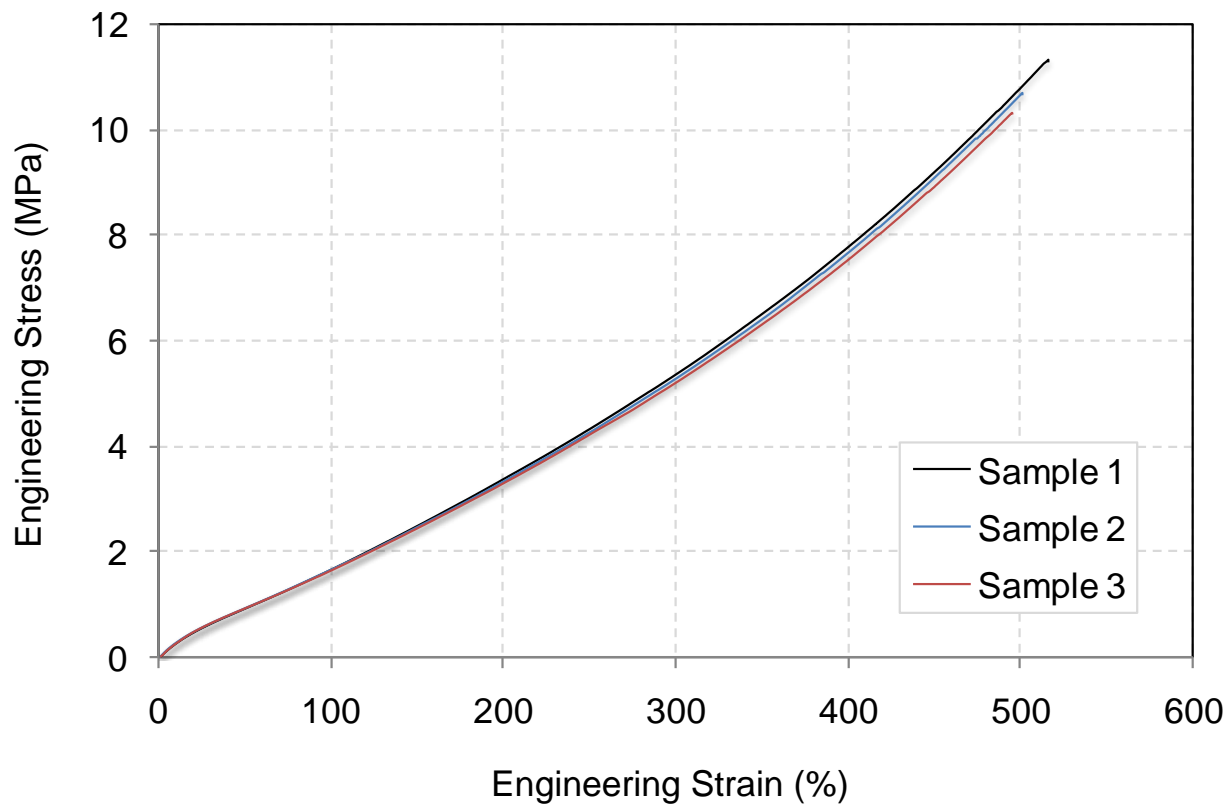


Figure 3.7 Uniaxial tension test set up showing the laser extensometer, Instron load frame and dogbone specimen in the pneumatic grips. White benchmarks on the specimen for the measurement of strain are also shown in the picture.



Sample Number	Tensile Strength (MPa)	Strain to Failure (%)	100% Modulus (MPa)	Initial Modulus (MPa)	Crosslink Density, ν (mol/m ³)
1	11.4	516	1.7	3.6	488
2	10.7	500	1.7	3.6	481
3	10.3	494	1.6	3.5	478
Mean \pm SD	10.8 \pm 0.6	503 \pm 11	1.65 \pm 0.1	3.6 \pm 0.1	482 \pm 5

Figure 3.8 Typical stress strain plot and test results obtained from the uniaxial tension test performed on a silicone elastomer at 500 mm/min at room temperature.

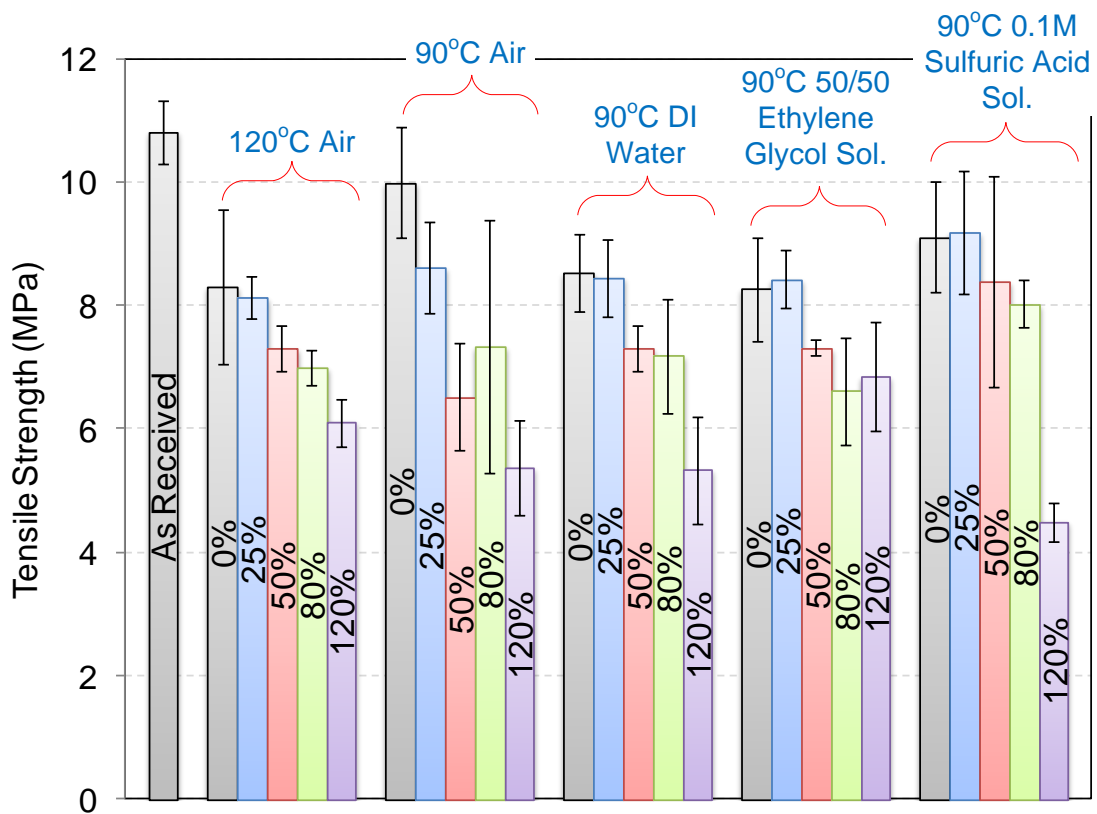


Figure 3.9 Effect of 8 weeks aging on tensile strength of silicone seal material. 50/50 ethylene glycol sol. represents 50v/50v ethylene glycol/DI water solution. Each data point represents an average of 3 samples and error bars indicate \pm one standard deviation.

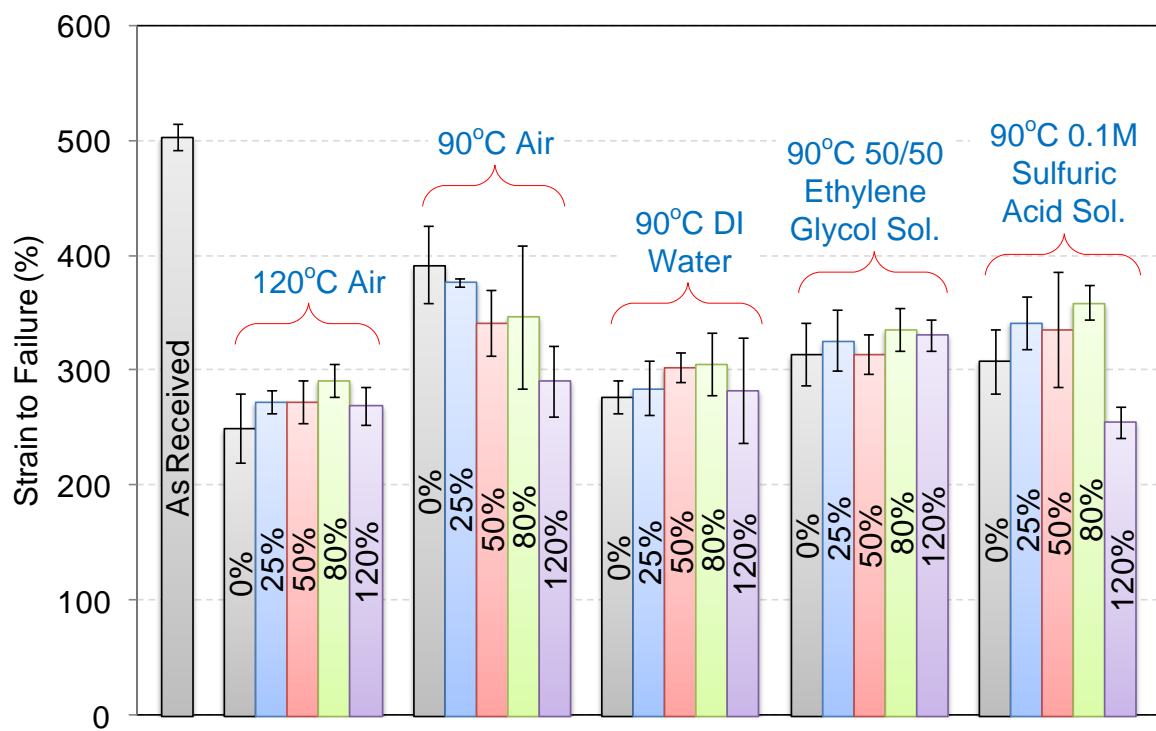


Figure 3.10 Effect of 8 weeks aging on strain to failure of silicone seal material. 50/50 ethylene glycol sol. represents 50v/50v ethylene glycol/DI water solution. Each data point represents an average of 3 samples and error bars indicate \pm one standard deviation.

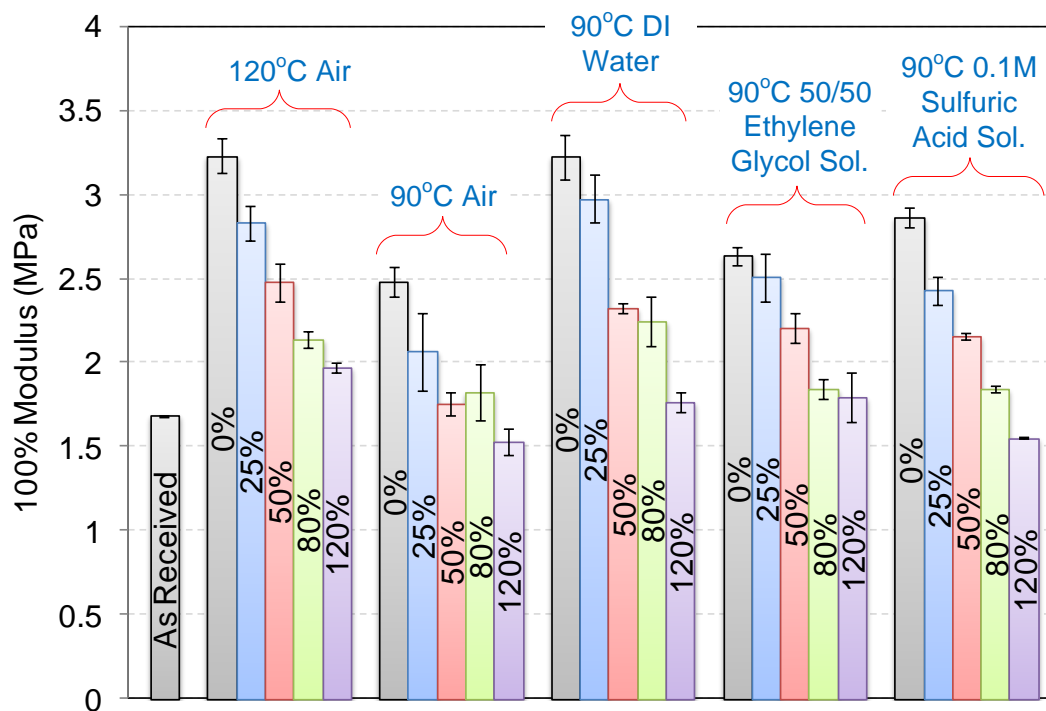


Figure 3.11 Effect of 8 weeks aging on modulus at 100% strain for silicone seal material. 50/50 ethylene glycol sol. represents 50v/50v ethylene glycol/DI water solution. Each data point represents an average of 3 samples and error bars indicate \pm one standard deviation.

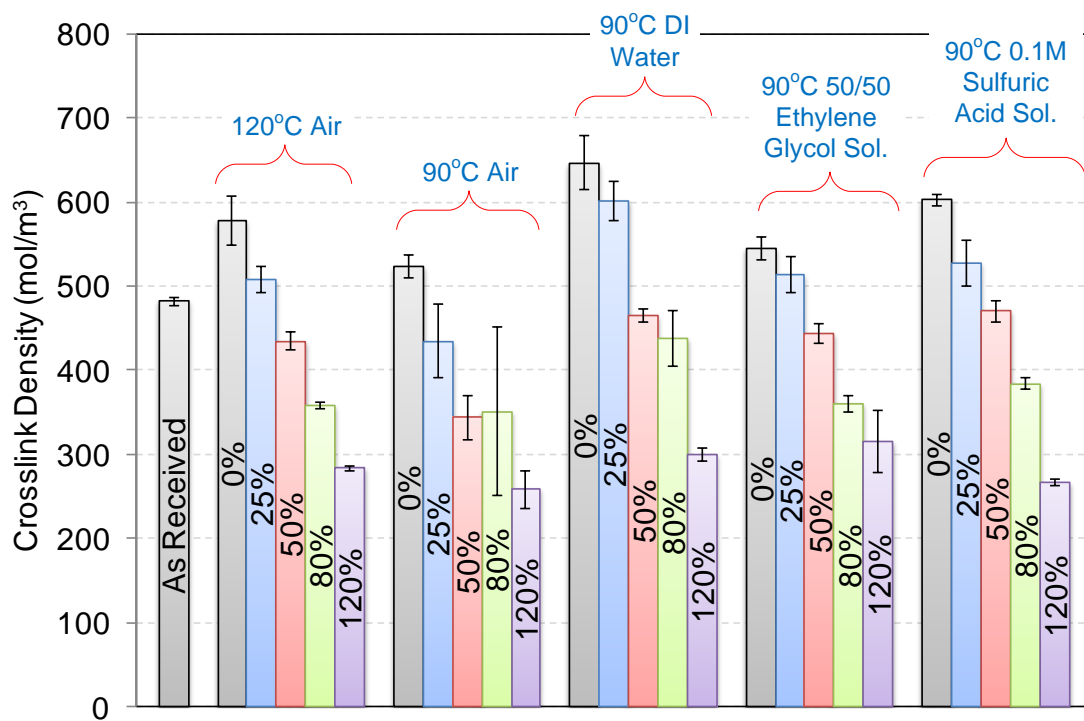


Figure 3.12 Effect of 8 weeks aging on crosslink density of silicone seal material. 50/50 ethylene glycol sol. represents 50v/50v ethylene glycol/DI water solution. Each data point represents an average of 3 samples and error bars indicate \pm one standard deviation.

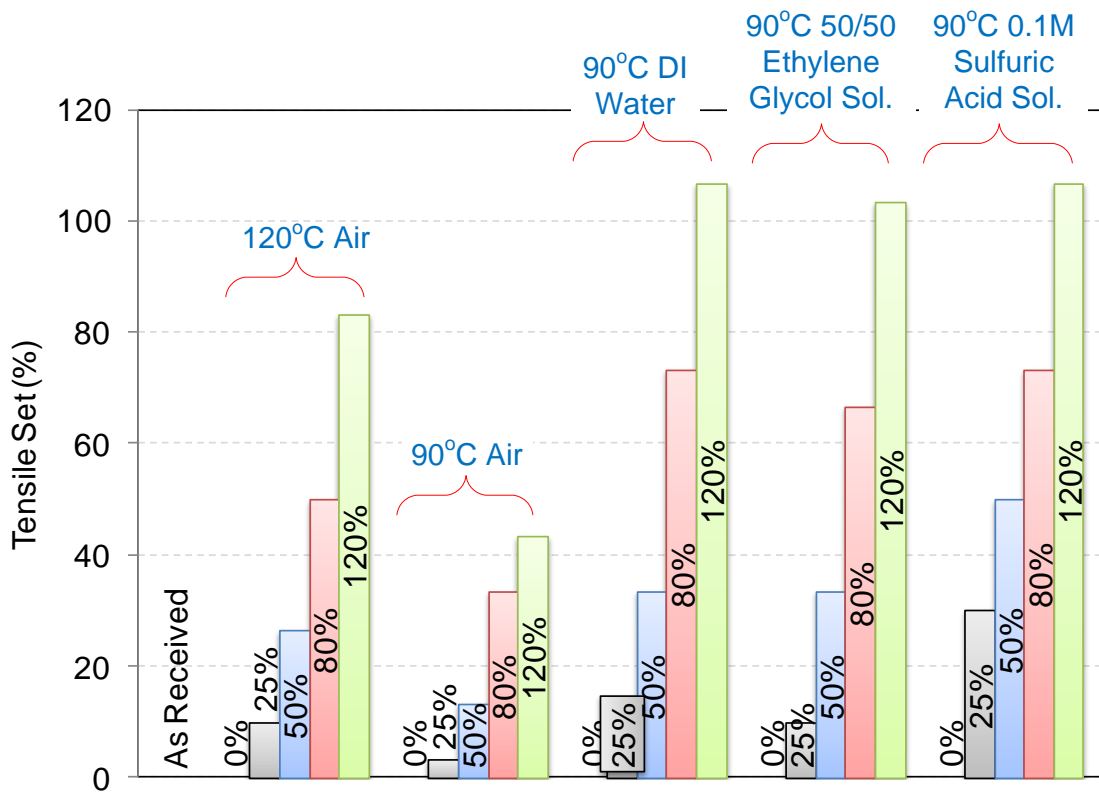


Figure 3.13 Tensile set in the silicone seal material as a result of 8 weeks aging. 50/50 ethylene glycol sol. represents 50v/50v ethylene glycol/DI water solution.

4 Trouser Tear Test

4.1 Abstract

Trouser tear tests were conducted on reinforced specimens in air and deionized water (DI) water to evaluate the tear resistance of an elastomeric seal material intended for proton exchange membrane fuel cells. Rectangular samples were cut from reinforced seal material slabs and split centrally along its length so that two legs were formed. The legs of the specimen were pulled in opposite directions, out-of-plane to the test piece, by using an Instron load frame. Moving the grips at a desired separation rate propagated the crack along the length of the specimen. Tear force was recorded against crosshead displacement and the critical strain energy release rate (SERR), G_{cr} , was calculated and plotted against crack growth rate, $\frac{da}{dt}$. More tests were conducted at increasing crosshead rates and several temperatures to gain an understanding of the effect of environmental conditions on crack growth characteristics during tearing. Data obtained at different temperatures were then used to generate a fracture energy master curve which was used with strain energy release rate predictions for a given crack to obtain a preliminary estimate of seal lifetime.

4.2 Introduction

Resistance to tearing is one of more important mechanical properties of flexible materials such as elastomers, films, etc. The trouser tear test has been widely used to characterize the fracture properties of elastomeric materials, papers, films etc. The Griffith criterion for crack growth in brittle material materials was extended by Rivlin and Thomas[1] to study crack growth phenomena in vulcanized rubber and established a criterion for steady-state tearing based on a characteristic fracture energy, a material property independent of the type and geometry of test

piece. The energy necessary for crack growth is supplied either from the strain energy in the deformed rubber, or the applied forces, or both. When the loaded boundaries do not move, the available tearing energy, G , is the rate of decrease of the elastically stored energy in the cracked body per unit virtual increment of crack area. A number of test pieces were used by Rivlin and Thomas[1] to calculate G for elastic materials undergoing large deformations, from which they were able to determine a critical value of the tearing energy, G_{cr} , which is characteristic of the elastomer, analogous to the Griffith characteristic energy. When the tearing energy exceeds the critical value, G_{cr} , crack growth will occur. Many investigators [2-4] have demonstrated that G_{cr} is independent of the geometry and dimensions of the test piece and can be considered to be a material property. For component design, the available energy release rate, G , is calculated for a hypothetical crack and is compared with G_{cr} to determine if a crack will propagate. Greensmith and Thomas[3] developed a method to evaluate the tear resistance of a rubber vulcanizate, involving the determination of energy required for tearing and its dependence on the rate of propagation. Sawyers and Rivlin[5] studied the development of tear force for both linear elastic (small deformation) and Mooney-Rivlin type (large deformation) materials.

Experimental determination of critical tearing energy may become tedious when unstable or stick-slip tearing occurs which has been reported in the literature for a variety of elastomers [6-8]. In stick-slip crack propagation, the crack does not propagate at a steady rate but arrests and re-initiates at somewhat regular intervals. The force necessary to drive unstable tearing varies widely from a maximum at crack initiation to a minimum at crack arrest. In some cases, the crack deviates sideways from a linear path, resulting in breakage of a specimen leg[9, 10]. In order to suppress unstable crack growth, control the crack-path deviation phenomenon, and minimize the effect of large nonlinear deformation of legs, specimen legs are sometimes

reinforced by a fabric cloth either embedded in the mid plane or bonded to the tension side of the specimen legs[7, 11, 12]. Such reinforced samples, with fabric cloth embedded in specimen legs during molding of seal materials slabs, were used in this study.

4.2.1 Available Tearing Energy

For a test piece held under constant displacement conditions such that the forces do not do work, the energy release rate, \mathcal{G} , available for the propagation of a crack is defined as [13]:

$$\mathcal{G} = -\frac{\partial u}{\partial A} \quad (4.1)$$

where \mathcal{G} is the tearing energy (or strain energy release rate), u the elastic energy stored in specimen, and A the area of one face of the crack. The available energy release rate can be considered as the driving force for crack propagation. Experimental results indicate that the value of tearing energy at crack initiation, \mathcal{G}_{cr} , is a characteristic property of the material[7]. Determination of tearing energy according to equation 4.1 requires measuring the force-deflection relation in specimens with different crack lengths, calculating the energy stored, and differentiating with respect to crack length. Determination of tearing energy in terms of applied forces or deformations for an arbitrarily shaped specimen is difficult because of the nonlinear behavior and large deformations of rubber. However, the trouser tear specimen geometry simplifies the calculation of the strain energy release rate (SERR), \mathcal{G} , and has become the method of choice for fracture characterization of elastomeric materials.

The specimen is a thin rectangular piece cut centrally along its length so that two legs are formed (Figure 4.1). The legs are pulled in opposite directions out of the plane of the test piece by equal and opposite forces. The expression for SERR, \mathcal{G} , is given as[1]:

$$G = \frac{2\lambda P - u_o A_o}{h} \quad (4.2)$$

where λ the extension ratio in the legs (ratio of length of deformed to undeformed leg), P is the force on the legs of the specimen, u_o is the strain energy density in the legs of the specimen, A_o is the cross-sectional area of one of the specimen legs, and h the specimen thickness. When the specimen legs can be considered inextensible compared with the tearing (i.e. $u_o \approx 0$ & $\lambda \approx 1$), Equation (4.2) simplifies to:

$$G = \frac{2P}{h} \quad (4.3)$$

The rate of crack propagation, $\frac{da}{dt}$, when the specimen legs are inextensible ($\lambda \approx 1$) is half the crosshead speed of the testing machine. The average value of the force along the torn path during crack propagation is measured and used with equation 4.3 to determine the critical SERR, G_{cr} .

4.3 Experimental

4.3.1 Material & Sample Preparation

The seal material used in this study is a hydrocarbon elastomer provided by Henkel Corporation (Rocky Hill, CT). More information on the material can be found in [14]. The 200mm×200mm×2mm thick slabs, with fiber cloth strips embedded at the midplane of the sheet during molding as shown in Figure 4.1, were prepared at Freudenberg-NOK (Plymouth, MI). Rectangular pieces with a length of 200 mm and width of 25 mm were cut from 2mm thick reinforced slabs. Fiber cloth strips (≈ 10 mm in width) embedded in specimen legs left a non-reinforced test area 5 mm wide along the center of the strip, as illustrated in Figure 4.1. A notch about 40 mm in length was cut with a razor blade at one end of the test sample.

4.3.2 Test Procedure

The procedure described in ASTM standard D412 [15] was followed for all the tests conducted in this study. The legs of the trouser specimen were gripped using binder clips in an Instron (Norwood, MA) 5848 series test frame outfitted with a $\pm 100\text{N}$ strain-gage-based load cell. Testing at temperatures higher than 90°C precluded the use of available pneumatic grips and, since the forces during testing are low, binder clips were able to provide slip-free gripping of the specimen legs. Separating the grips at a desired rate propagated the crack along the length of the reinforced tear specimen and the tear force was recorded against crosshead displacement. Each specimen was tested at several discrete crosshead rates ranging from 2mm/min to 500mm/min at a given temperature. This yields rate dependent data from a single specimen reducing specimen to specimen variability. Tests were conducted in air at temperatures ranging from -32°C to 100°C . Since the seal material is subjected to humid conditions at high temperature during fuel cell operation, tests were also conducted in DI water at RT and 90°C to compare the tear characteristics of the seal material with those obtained in air. In all the tests, specimens were equilibrated in a forced convection oven at the desired test temperature for a period of one hour prior to testing. Three replicates were typically tested at each environmental conditions and the effect of temperature and crack growth rate, $\frac{da}{dt}$, on G_{cr} was studied.

4.4 Results & Discussion

Figure 4.2 shows a typical load–displacement graph during crack growth for a specimen tested in air at RT at a 100mm/min crosshead rate. Initial results revealed a stick–slip tearing mechanism (also referred to as “knotty” tear) during crack growth, characterized by periodic load fluctuations due to unstable crack propagation and arrest. Tests were conducted at multiple crosshead rates i.e. 2mm/min , 5mm/min , 10mm/min , 20mm/min , 50mm/min , 100mm/min ,

200mm/min, and 500mm/min, on a single specimen and typical load-displacement behavior is shown in Figure 4.3. There are two important observations in Figure 4.3:

1. Tearing load increases with increase in loading rate, and
2. The stick-slip behavior and resulting fluctuation of the force from a maximum value at crack initiation to a minimum value at crack arrest becomes more pronounced as the loading rate increases.

Stick-slip behavior is commonly observed during fracture testing of elastomeric materials [1, 2, 6, 7] and may be attributed to a reinforcing effect of strain-induced crystallization at higher loading rates[16]. Formation of crystallites has a pronounced reinforcing effect within the network resulting in an increase in mechanical properties[17]. Figure 4.4 shows G_{cr} versus $\frac{da}{dt}$ on a log-log plot for tests conducted at 2mm/min, 5mm/min, 10mm/min, 20mm/min, 50mm/min, 100mm/min, 200mm/min, and 500mm/min in air at RT, which indicates an increase in G_{cr} with $\frac{da}{dt}$ described by a power-law relationship. If more tests could be conducted at higher and lower temperatures, and if crack growth rate versus tearing energy curves have the same trend at all temperatures, a master curve may be generated, which can be used to predict the crack growth rate at a given SERR. In an attempt to generate such a master curve, tests were conducted from -32°C to 100°C and values of G_{cr} were calculated at each loading rate and temperature and results are shown as G_{cr} versus temperature plot in Figure 4.5. There are two main aspects:

1. Rate dependence of G_{cr} at a given temperature

At a given temperature, an increase in the loading rate results in an increase in G_{cr} . However, such effect of loading rate diminishes as temperature increases. This may be related to the time-

dependent mechanical characteristics of a viscoelastic material where it exhibits stiff behavior at fast loading or low temperature and soft behavior at slow loading and high temperature.

2. *Temperature dependence of G_{cr} at a given loading rate*

At a given loading rate, G_{cr} showed a steady decrease with increasing test temperature. This behavior is much more pronounced at higher loading rates than at slow tearing of samples. When a vulcanizate is deformed slowly at elevated temperatures, it exhibits equilibrium or time-independent behavior because of negligibly small viscous resistive forces opposing chain rearrangement[18] i.e. decrease in the viscoelastic work done by the elastomer when stretched at the elevated temperatures[19].

A log-log plot of tear energy, G_{cr} , versus crack growth rate, $\frac{da}{dt}$, at various temperatures is shown in Figure 4.6. The values of G_{cr} are seen to change by two orders of magnitude, as the test conditions change from low tear speeds (2 mm/min) at high temperature (100°C) to high tear speeds (500 mm/min) at low temperature (-32°C). The data in Figure 4.6 were shifted using a shift factor, a_T , and the results are shown as a master curve in Figure 4.7 for a reference temperature of 80°C. As shown in Figure 4.7, all data are well superimposed on a single curve. If more data points at slow tearing rates and high temperatures could be used in the master curve, an estimate of a threshold value of SERR may be obtained. A threshold value for the fracture energy of elastomers was first pointed out by Lake and Lindley [20] from fatigue crack growth. Mueller and Knauss[21] and Gent[22, 23] measured extremely low tearing energies directly by employing low tear rates, elevated temperatures, and swollen elastomers.

Often found in the literature is the tear characterization of a seal material in the presence of air, where the effect of temperature and rate is mostly discussed. Literature is rife with such work

for a variety of elastomeric materials and some of the most cited references are [3, 7, 11, 24-28]. Seals are often required to perform in environments such as liquid solutions (acidic or basic), oils etc., where swelling, due to mass uptake, and formation of cracks/crazes occurs. Gent [29] showed the effect of swelling on SERR but, to the best of this author's knowledge, very limited work[30] has been done to evaluate the effect of the presence of a liquid at the crack tip, which may significantly lower the SERR value required for a crack to propagate. Part of the reason for limited research in this area may be due to the unavailability of techniques and instruments to conduct fracture test in controlled environments with good repeatability. In order to investigate how the presence of a liquid affects the tear characteristics of a material and SERR, tests were also conducted in DI water at RT and 90°C and compared with the same temperature behavior in air. Figure 4.8 shows a comparison on a load versus displacement plot, where only the crack propagation region of the curve is plotted. The results can be summarized as follows:

1. At a given temperature and loading rate, no significant difference in load required for crack propagation is observed between air and DI water.
2. At a given loading rate, increasing the temperature results in a typical decrease in load and smoother crack propagation but the presence of water at the crack tip does not contribute to any additional changes in the load values.

These observations indicate that, for the hydrocarbon-based seal material studied here, the presence of DI water at the crack tip does not lead to an immediate weakening of the material. It could be possible that environmental aging over a period of time could lead to reduced critical value of SERR. As seen in Chapter 3, aging affects mechanical properties significantly and to address aging effects on fracture resistance of the material, trouser tear specimens may be aged

in various environments over a period of time. Such a test matrix is proposed in the future work section of this dissertation.

4.4.1 Lifetime Prediction Approach using Finite Element Analysis

Most seals are intended to be used under compression (static or dynamic applications) and when a certain amount of compressive strain is applied, finite element simulation (details are provided in next chapter) shows several critical regions where tensile stresses are present. An example is shown in Figure 4.9 for an O-ring cross-section, where tensile stresses are present not only on the outside surface of the seal but also to a greater extent in the bulk of the material. The opening nature of tensile stresses may cause an initial flaw, a crack or scratch on the outside surface or a void present in the bulk of the material, to propagate. In the static application of the seals used in compression, crack on the surface may grow initially but not through the seal due to closing compressive region ahead. In dynamic applications where the seal material is subjected to fatigue, even in the absence of a flaw to start with, cracks may initiate due to repeated cycling and grow, resulting in failure of the seal[31, 32]. Since aging in environment (high temperature and liquid solution) leads to a decrease in the value of the critical tearing energy, the seal may fail sooner than expected. If an estimate of the available SERR for a given cross-section may be obtained, it can be used with the fracture energy master curve to estimate the crack growth rate in the seal material providing a preliminary estimate on seal lifetime. Besides seals, there are many applications where elastomers are used in form of films/membranes etc., such as silicone hydrogels for contact lenses, silicone dielectric elastomers[33], synthetic heart valves[34], subjected to stretching. For such cases also, knowledge of the tear energy master curve and an estimation of available SERR may be very helpful in predicting lifetime.

The Finite element method (FEM) has been widely used to determine energy release rate (G)[35, 36] that is one of the most important parameters in fracture mechanics. FEM has the advantage in its adaptability to the analysis of crack growth in structures that are with complicated geometry or multiple irregular cracks, especially when subject to complex loading. Existing FEM-based techniques, such as the virtual crack closure technique (VCCT)[37-41], J-integral[38, 42-44], and global energy change (GEC) method[44, 45] have been successfully used for determining the SERR. Busfield [46] showed that all three techniques produced equivalent results. In this section, an attempt is made to use the fracture mechanical parameter J-integral and master curve obtained above to predict lifetime of a given seal cross-section. The J-integral, a path-independent line integral representing the strain energy release rate of non-linear elastic materials[47], is a standard tool provided in ABAQUS to compute the energy release rate. It is applicable to large strain elasticity and hence can be applied to the analysis of elastomeric materials. The expression for the J-integral is given as:

$$J = \int_{\Gamma} w \cdot dy - T_i \frac{\partial u_i}{\partial x} ds \quad (4.4)$$

where $w = \int_0^{\varepsilon_{ij}} \sigma_{ij} d\varepsilon_{ij}$ is the strain energy density, $T_i = \sigma_{ij} n_j$ is the traction vector, Γ is a counter-clockwise contour around the tip of the crack, ds is a small element on Γ , n is the unit vector normal to Γ , σ is the stress, ε is the strain, and u is the displacement vector, as illustrated for a crack in Figure 4.10. This integral represents the balance of energy flow through any contour surrounding the notch tip. Although J-integral is path-independent, it is widely accepted that the first few contours do not provide good results because of numerical singularities. Therefore, J-integral value is typically obtained at contours away from crack tip in order to get a convergent

value. To check the accuracy of these contours, more contours are typically requested and the value of the contour integral that appears approximately constant from one contour to the next is determined. The contour integral values that are not approximately equal to this constant are discarded. For a given crack on the seal surface, the energy available at the crack tip can be calculated based on J-integral approach, and when used in conjunction with master curve, may provide an approximate value of crack propagation rate at a given temperature.

Finite element analysis was carried out by using a four-node, reduced-integration, axisymmetric quadrilateral elements mesh, CAX4R, with hybrid formulation in ABAQUS [48]. In this study, a 2-D unrestrained axisymmetric model of O-ring with a surface crack (for SERR calculation) was compressed between two rigid plates, as shown in Figure 4.9. During FEA simulation, the top surface moves down by a fixed distance in the axial direction, compressing the O-ring against the opposite contact surface to achieve the desired strain. The friction coefficient between the compression platens and O-ring was assumed to be $\mu = 0$ (frictionless). Since two-parameter Ogden material model correlates closely with experimental data obtained from uniaxial tension tests on the seal material, as discussed in chapter 3, the analysis was carried out using this model. For the crack configuration shown in Figure 4.9, a total of five crack-tip contours were utilized to obtain accurate results, as recommended in the software manual[49], with the final contour being used for determining the associated energy release rate for each test, as the final contour always showed convergence amongst the calculated results. ABQUS automatically generated contours around the crack tip to carry out the energetic analysis and value of SERR around each contour was obtained using J-integral. J-integral value around contour five was used here and found to be approximately 175 J/m^2 , and the corresponding value of crack growth rate, obtained from the fracture energy master curve in

Figure 4.7, was approximately 10^{-6} m/s. It should be noted that the SERR value obtained using the J-integral is specific to the particular specimen geometry containing a crack of a specific size and orientation subjected to specific loading conditions. Also, due to the compressive region ahead of the crack tip in compressed seals, the crack may not grow further in this particular case. For applications where tensile stresses are present all through the cross-section, such as elastomeric films or membranes under stretching, estimation of available SERR and crack growth rate may help predict the lifetime of a component.

4.5 Conclusion

Trouser tear tests were conducted on reinforced samples to evaluate the tear strength of a seal material proposed for use in PEM fuel cells. Plots relating the crack growth rate with tearing energy were obtained at various temperatures and provided significant insight into the rate and temperature dependence of the tearing strength of the seal material. Stick-slip crack propagation was observed at all temperatures and loading rates, although the behavior was suppressed significantly at low loading rates and high temperatures. Tests were also conducted in DI water and compared with tear characteristics in air at the same temperatures (RT and 90°C). No significant difference in either crack propagation behavior or tearing energy was observed, leading to the conclusion that presence of media at the crack tip for hydrocarbon elastomer used in this study may not cause change in tearing energy required for crack propagation. Crack growth rate versus tearing energy data at different temperatures were shifted to construct a master curve. Finite element analysis is a useful tool that can be used to characterize the fracture behavior of elastomers using a fracture mechanics approach, where a measure of the crack growth rate can be estimated at specific level of available SERR using fracture energy master curve to predict component lifetime.

References:

1. R.S. Rivlin and A.G. Thomas, "Rupture of Rubber. Part 1: Characteristic Energy for Tearing," *Journal of Polymer Science*, **10**, 291-318, 1953.
2. A.G. Thomas, "Rupture of Rubber. Ii. The Strain Concentration at an Incision," *Journal of Polymer Science Part A-Polymer Chemistry*, **18**, 177-188, 1955.
3. H.W. Greensmith and A.G. Thomas, "Rupture of Rubber. Iii. Determination of Tear Properties," *Journal of Polymer Science Part B-Polymer Physics*, **18**(88), 189-200, 1955.
4. A.G. Thomas, "The Development of Fracture Mechanics for Elastomers," *Rubber Chemistry and Technology* **67**, G50–G60, 1994.
5. K.N. Sawyers and R.S. Rivlin, "The Trouser Test for Rupture," *Engineering Fracture Mechanics*, **6**, 557-562, 1974.
6. T.W. Webb and E.C. Aifantis, "Loading Rate Dependence of Stick-Slip Fracture in Polymer," *Mechanics Research Communications*, **24**, 115-121, 1995.
7. E.E. Gdoutos, P.M. Schubel, and I.M. Daniel, "Determination of Critical Tearing Energy of Tire Rubber," *Strain*, **40**(3), 119-125, 2004.
8. C. Kumudinie and J.E. Mark, "Tear Strengths of Poly(Dimethylsiloxane) Networks Reinforced with in Situ Precipitated Silica," *Materials Science and Engineering B-Solid State Materials for Advanced Technology*, **11**(10), 61-66, 2000.
9. E.E. Gdoutos, I.M. Daniel, and P. Schubel, "Fracture Mechanics of Rubber," *Mechanics, Automation Control and Robotics*, **13**(13), 497-510, 2003.
10. R.P. Brown, *Physical Testing of Rubber*. 3 ed. 1996, London, UK: Chapman and Hall. 342.
11. A.N. Gent and A.W. Henry. *On the Tear Strength of Rubbers*. in *Proceedings of the International Rubber Conference*. 1968. Brighton.
12. D. Gibala, D. Thomas, and G.R. Hamed, "Cure and Mechanical Behavior of Rubber Compounds Containing Ground Vulcanizates, Part Iii: Tensile and Tear Strength," *Rubber Chemistry & Technology*, **72**, 357-360 1999.
13. E.E. Gdoutos, *Fracture Mechanics—an Introduction*. 1993, Dordrecht, The Netherlands: Kluwer Academic Publishers.

14. M.P. Burdzy, B.R. Einsla, K.J. Welsh, A.F. Jacobine, J.G. Woods, and S.T. Nakos, *Bonded Fuel Cell Assembly, Methods, Systems, and Sealant Compositions for Producing the Same*, W.I.P. Organization, Editor. 2007: USA.
15. ASTM-D412-98a, *Standard Test Methods for Vulcanized Rubber and Thermoplastic Rubbers and Thermoplastic Elastomers-Tension*, in *Annual Book of Astm Standards*. 1998, ASTM: West Conshohocken.
16. A.N. Gent, S. Kawahara, and J. Zhao, "Crystallization and Strength of Natural Rubber and Synthetic Cis-1,4-Polyisoprene," *Rubber Chemistry and Technology*, **71**(4), 668-678, 1998.
17. J.E. Mark, "The Effect of Strain-Induced Crystallization on the Ultimate Properties of an Elastomeric Polymer Network," *Polymer Engineering & Science*, **19**(6), 409-413, 2004.
18. T.L. Smith. *Relations between Ultimate Tensile Properties of Elastomers and Their Structure*. in *Proceedings of the Royal Society of London. Series A, Mathematical and Physical Sciences*. 1964: The Royal Society.
19. K. Tsunoda, J.J.C. Busfield, C.K.L. Davies, and A.G. Thomas, "Effect of Materials Variables on the Tear Behavior of a Non-Crystallizing Elastomer," *Journal of Materials Science*, **35**, 5187-5198, 2000.
20. G.J. Lake and P.B. Lindley, "Ozone Cracking, Flex Cracking and Fatigue of Rubber," *Rubber Journal*, **146**, 30-39, 1964.
21. H.K. Mueller and W.G. Knauss, "The Fracture Energy and Some Mechanical Properties of a Polyurethane Elastomer," *Journal of Rheology*, **15**(2), 217-233, 1971.
22. A.N. Gent and R.H. Tobias, "Threshold Tear Strength of Elastomers," *Journal of Polymer Science Part B-Polymer Physics*, **20**(11), 2051-2058, 2003.
23. A. Ahagon and A.N. Gent, "Threshold Fracture Energy for Elastomers," *Journal of Polymer Science: Polymer Physics Edition*, **13**(10), 1903-1911, 2003.
24. D.P. Isherwood and J.G. Williams, "Some Observations on the Tearing of Ductile Materials," *Engineering Fracture Mechanics*, **10**, 887-895, 1978.
25. A.K. Bhowmick, "Tear Strength of Elastomers over a Range of Rates, Temperatures and Crosslinking: Tearing Energy Spectra " *Journal of Materials Science*, **21**(11), 3927-3932, 1986.

26. A. Kadir and A.G. Thomas, "Tearing of Unvulcanized Natural Rubber," *Journal of Polymer Science: Polymer Physics Edition*, **22**(9), 1623-1634, 2003.
27. A.N. Gent and H.J. Kim, "Tear Strength of Stretched Rubber," *Elastomerics*, **109**(9), 37-37, 1977.
28. A.N. Gent and M. Hindi, "Effect of Oxygen on the Tear Strength of Elastomers," *Rubber Chemistry and Technology*, **63**(1), 123-134, 1990.
29. A.N. Gent and R.H. Tobias, "Threshold Tear Strength of Elastomers," *Journal of Polymer Science Part B-Polymer Physics*, **20**(11), 2051-2058, 1982.
30. D.A. Dillard, S. Guo, M.W. Ellis, J.J. Lesko, J.G. Dillard, J. Sayre, and B. Vijayendra, *Seals and Sealants in Pem Fuel Cell Environments: Material, Design, and Durability Challenges*, in *ASME Second International Conference on Fuel Cell Science Engineering and Technology*. 2004: Rochester, New York. 553-560.
31. S.M. Cadwell, R.A. Merrill, C.M. Sloman, and F.L. Yost, "Rubber in Automotive Industry," *Industrial & Engineering Chemistry*, **33**(3), 370-374, 1941.
32. A. Stevenson, "A Fracture Mechanics Study of the Fatigue of Rubber in Compression," *International Journal of Fracture*, **23**(1), 47-59, 1983.
33. R. Pelrine, R. Kornbluh, Q. Pei, and J. Joseph, "High-Speed Electrically Actuated Elastomers with Strain Greater Than 100%," *Science*, **287**(5454), 836-839, 2000.
34. G. Cacciola, *Design, Simulation and Manufacturing of Fiber Reinforced Polymers Heart Valves*. 1998, Eindhoven University of Technology.
35. O.H. Yeoh, *Strain Energy Release Rates for Some Classical Rubber Test Pieces by Finite Element Analysis*, in *Elastomers and Components*, V.A. Coveney, Editor. 2006, Woodhead Publishing Limited: Cambridge, UK. 75-90.
36. A.N. Gent and C. Wang, "Strain-Energy Release Rates for Crack-Growth in an Elastic Cylinder Subjected to Axial Shear," *Rubber Chemistry and Technology*, **66**(5), 712-732, 1993.
37. E.F. Rybicki and M.F. Kanninen, "A Finite Element Calculation of Stress Intensity Factors by a Modified Crack Closure Integral," *Engineering Fracture Mechanics*, **9**(4), 931-938, 1977.
38. Y. Wang and J.G. Williams, "Corrections for Mode-Ii Fracture-Toughness Specimens of Composites Materials," *Composites Science and Technology*, **43**(3), 251-256, 1992.

39. S.A. Salpekar, I.S. Raju, and T.K. O'Brien, "Strain Energy Release Rate Analysis of the End-Notched Flexure Specimen Using the Finite-Element Method," *Journal of Composites Technology & Research* **10**(4), 133-139, 1988.
40. D. Xie, A.M. Waas, K.W. Shahwan, J.A. Schroeder, and R.G. Boeman, "Computation of Energy Release Rates for Kinking Cracks Based on Virtual Crack Closure Technique," *Cmes-Computer Modeling in Engineering & Sciences*, **6**(6), 515-524, 2004.
41. D. Xie, A.M. Waas, K.W. Shahwan, J.A. Schroeder, and R.G. Boeman, "Fracture Criterion for Kinking Cracks in a Tri-Material Adhesively Bonded Joint under Mixed Mode Loading," *Engineering Fracture Mechanics*, **72**(16), 2487-2504, 2005.
42. C.F. Shih and A. Needleman, "Fully Plastic Crack Problems. I. Solutions by a Penalty Method," *Journal of Applied Mechanics*, **51**(1), 48-56, 1984.
43. C.F. Shih and A. Needleman, "Fully Plastic Crack Problems. II. Application of Consistency Checks," *Journal of Applied Mechanics*, **51**(1), 57-64, 1984.
44. P.B. Lindley, "Energy for Crack Growth in Model Rubber Components," *Journal of Strain Analysis for Engineering Design*, **7**(2), 132-140, 1972.
45. E.F. Rybicki and M.F. Kanninen, "Finite-Element Calculation of Stress Intensity Factors by a Modified Crack Closure Integral," *Engineering Fracture Mechanics*, **9**(4), 931-938, 1977.
46. J.J.C. Busfield, C.K.L. Davies, and A.G. Thomas, "Aspects of Fracture in Rubber Components," *Progress in Rubber and Plastic Technology*, **12**, 191-207, 1996.
47. J.R. Rice, "A Path Independent Integral and the Approximate Analysis of Strain Concentration by Notches and Cracks," *Journal of Applied Mechanics-Transactions of the ASME*, **35**(2), 379-386, 1968.
48. I. Green and C. English, "Analysis of Elastomeric O-Ring Seals in Compression Using the Finite Element Method," *Society of Tribologists and Lubrication Engineers-Tribology Transactions*, **35**(1), 83-88, 1992.
49. Hibbitt, Karlsson, and Sorensen, *Abaqus User's Manual, Verison 6.8-2*. 2008, HKS Inc: Providence, RI, USA.

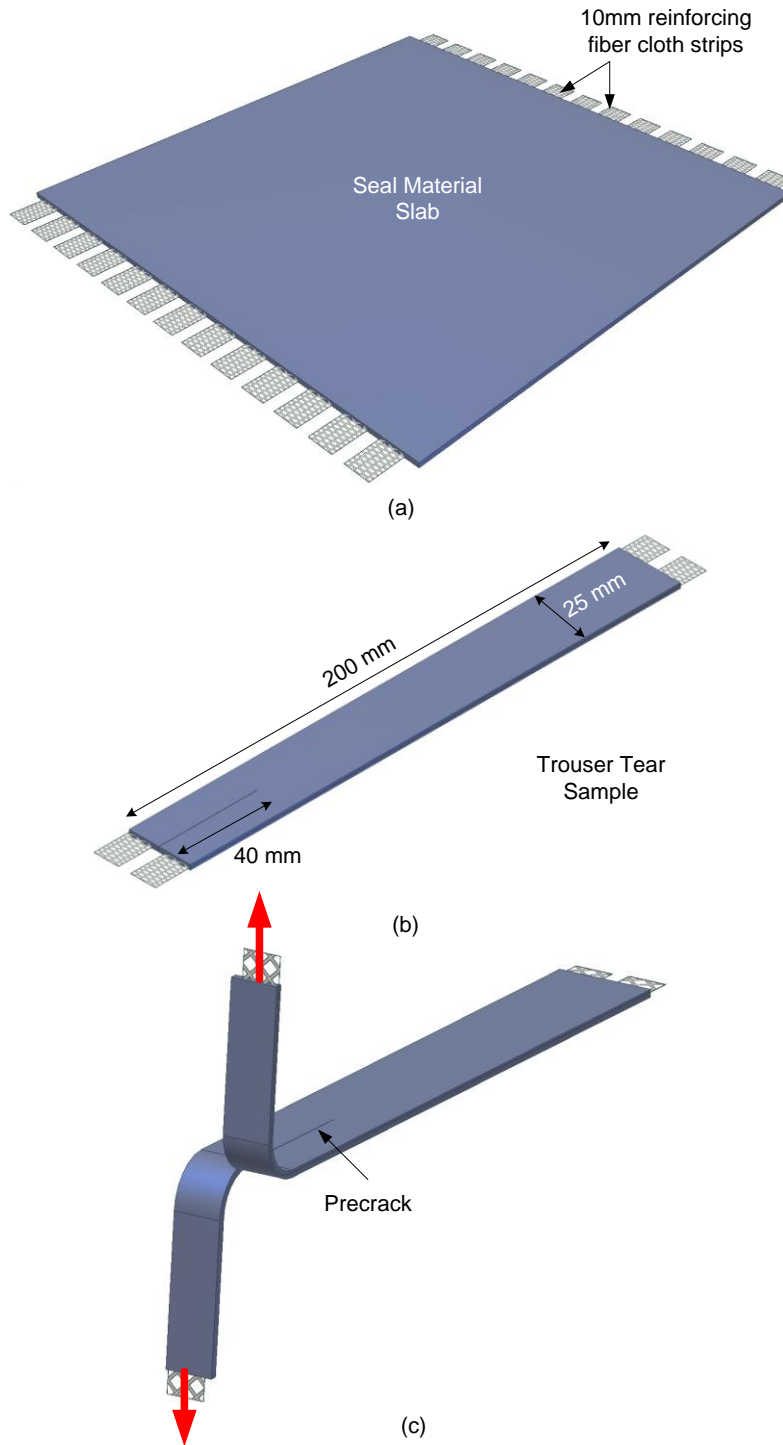


Figure 4.1 Illustration of the sample preparation method for trouser tear testing. (a) illustrates reinforcing fiber cloth strips in seal material slab, (b) illustrates the trouser tear sample with dimensions, and (c) illustrates the sample configuration during loading in an Instron load frame.

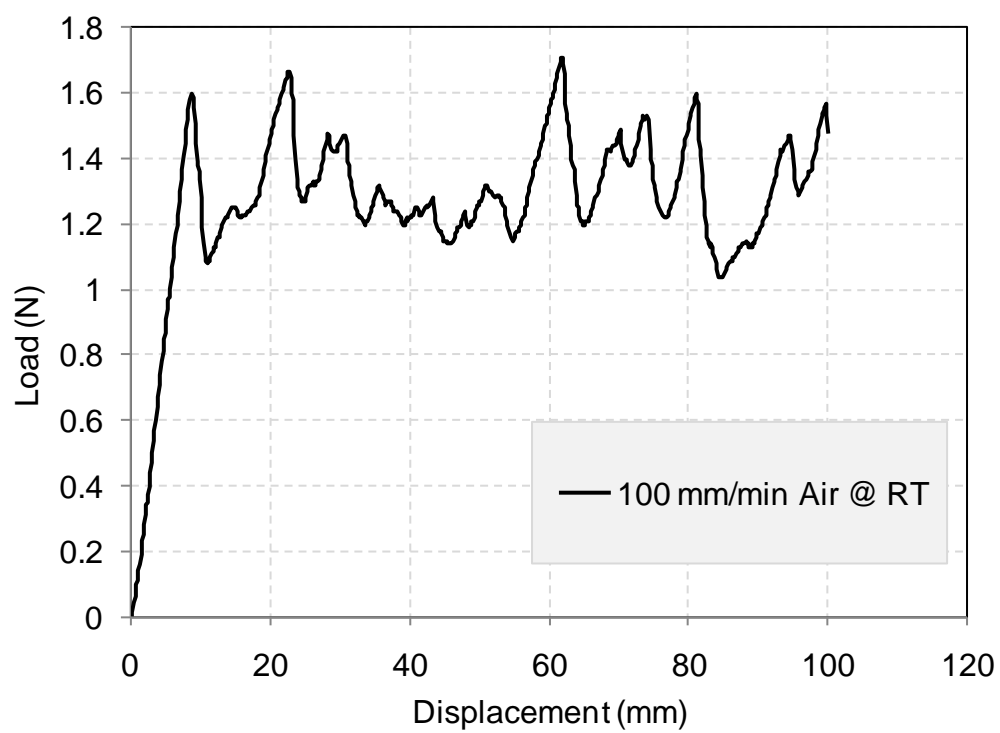


Figure 4.2 Load displacement plot obtained from trouser tear tests conducted at 100 mm/min in air at RT on hydrocarbon seal material.

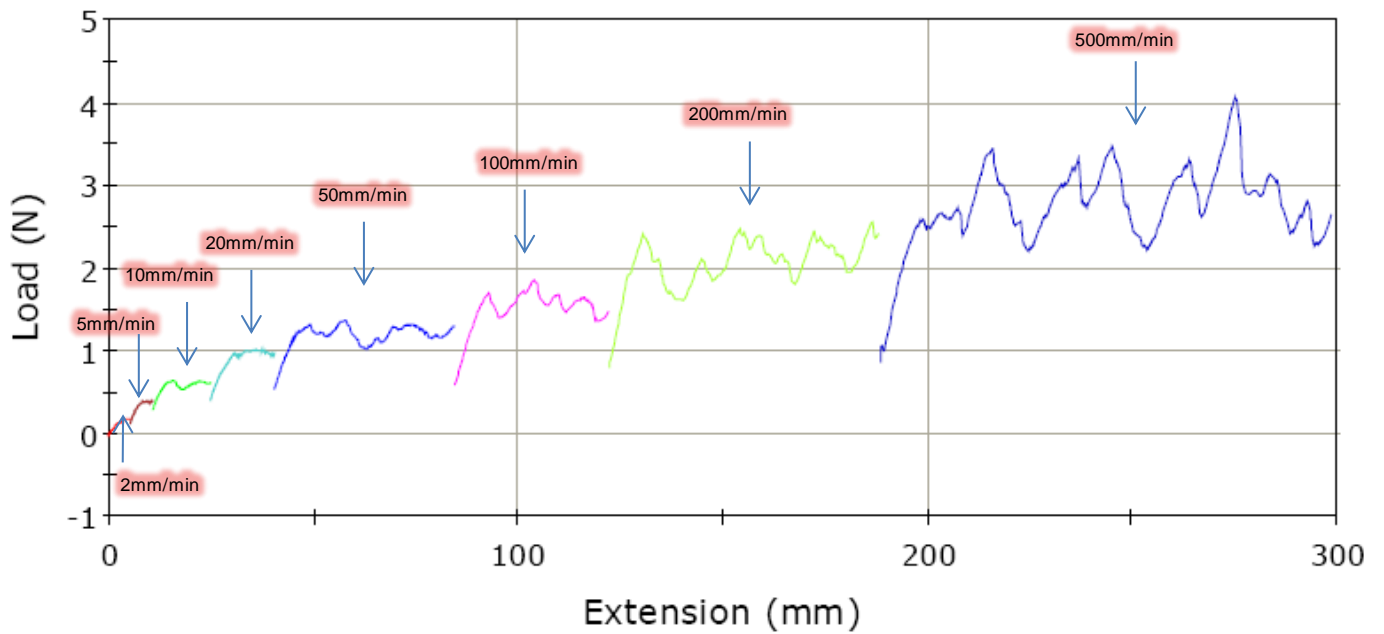


Figure 4.3 Load displacement plot obtained from trouser tear tests performed in air at rates from 2 mm/min to 500 mm/min at RT on hydrocarbon seal material.

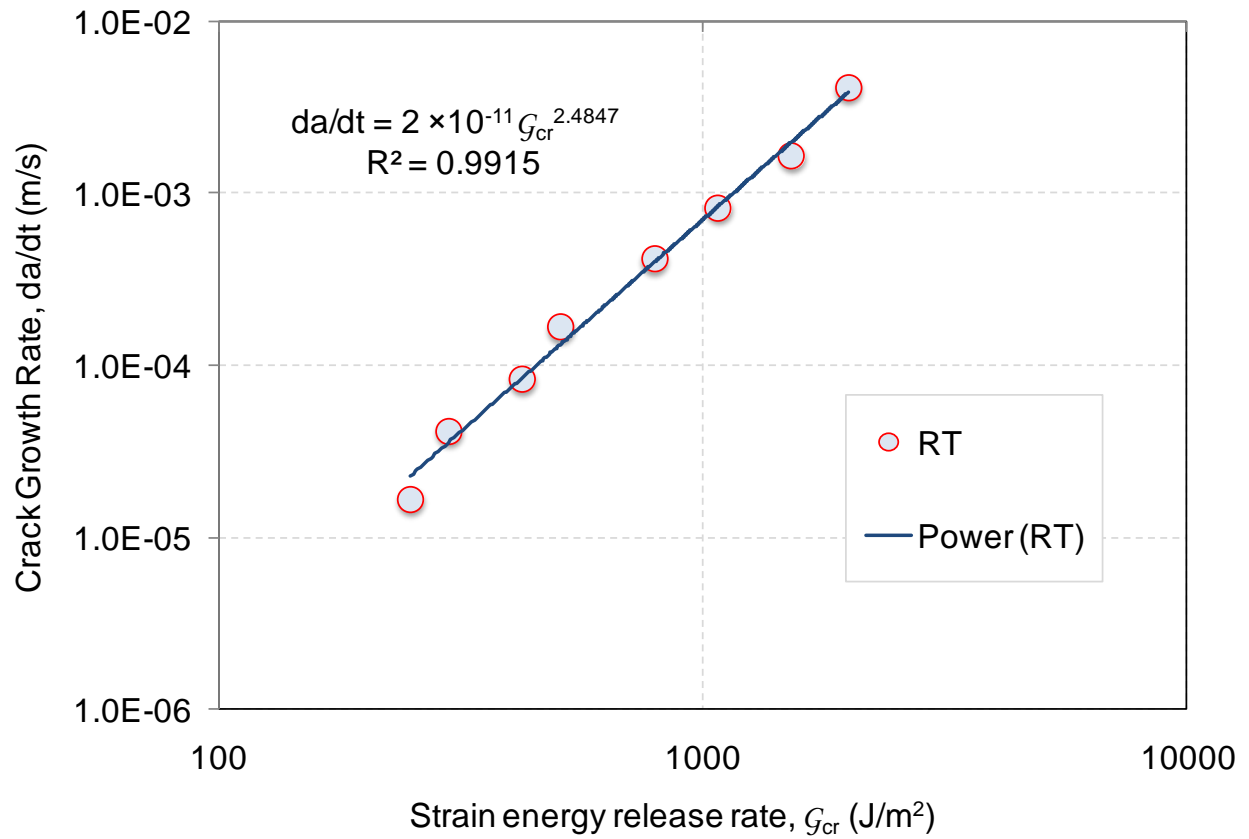


Figure 4.4 Rate dependence of tearing energy, G_{cr} in air at RT on hydrocarbon seal material.

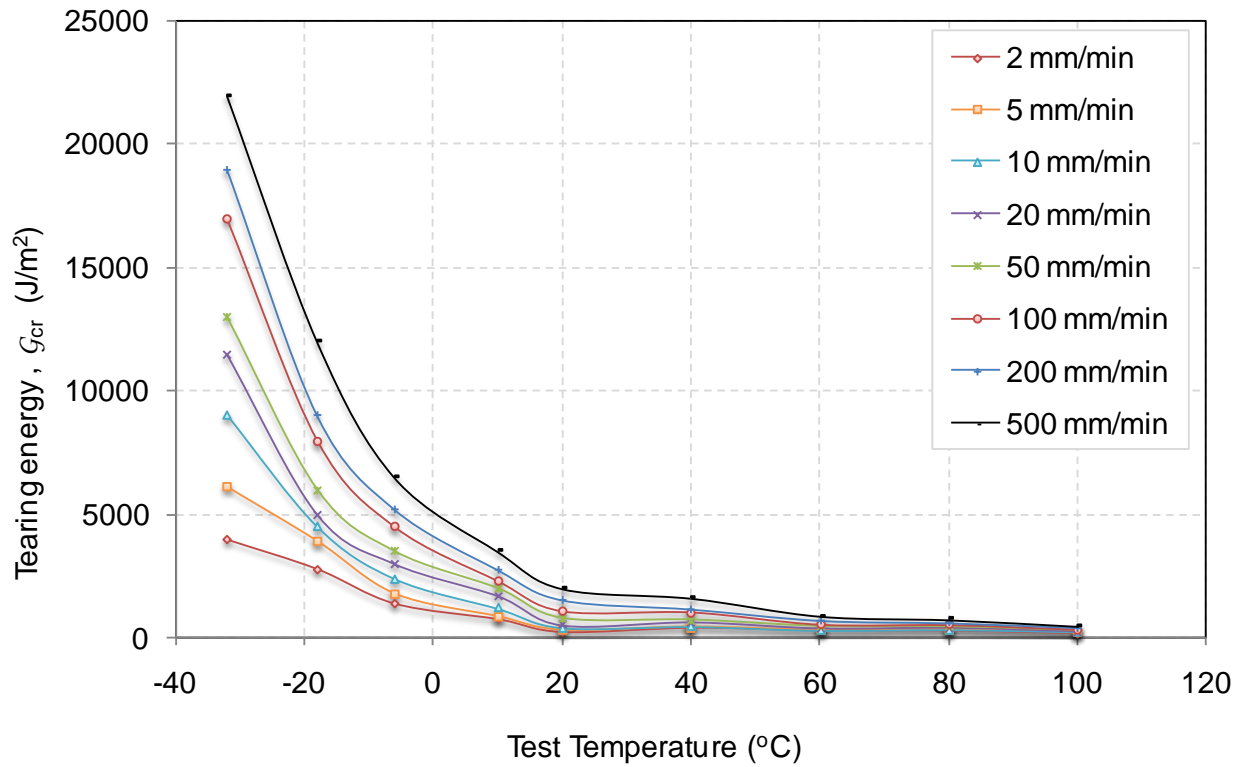


Figure 4.5 Plot of tearing energy versus test temperatures at different loading rates on hydrocarbon seal material.

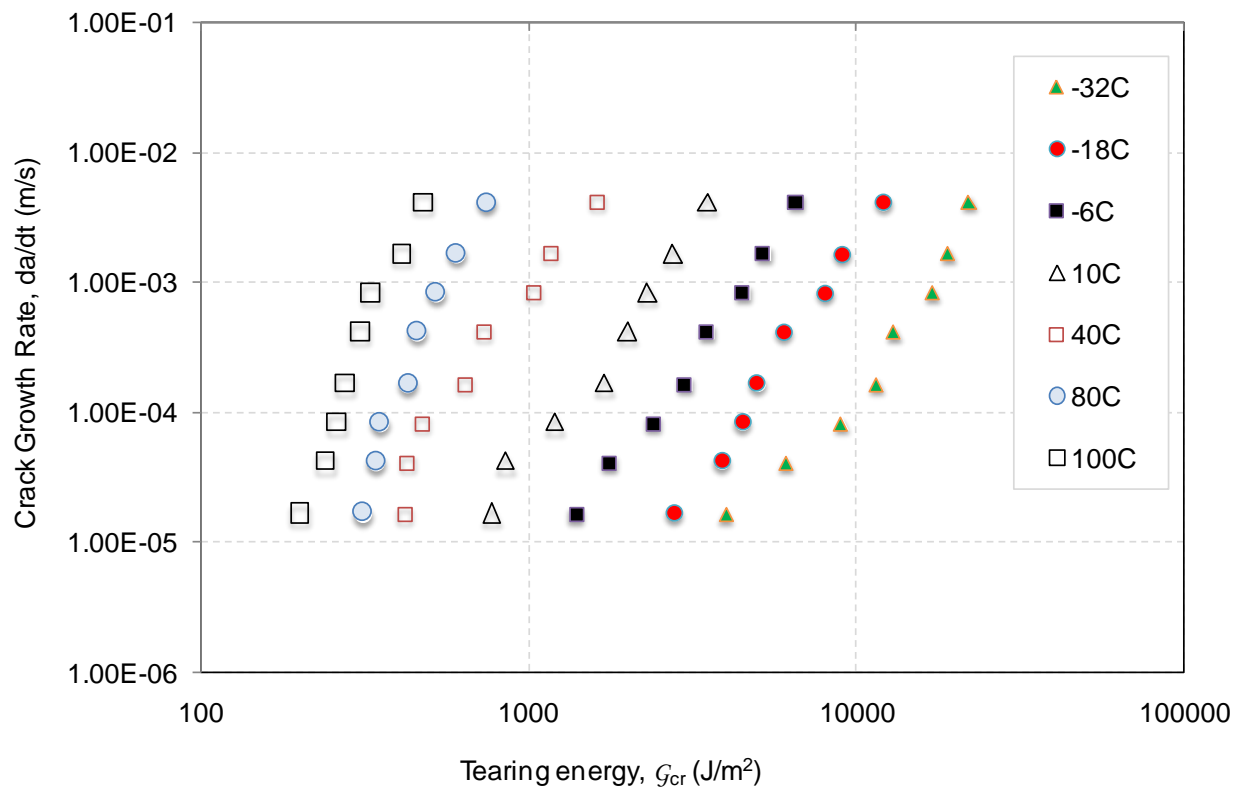


Figure 4.6 Plot of tearing energy versus crack growth rate at different temperatures on hydrocarbon seal material.

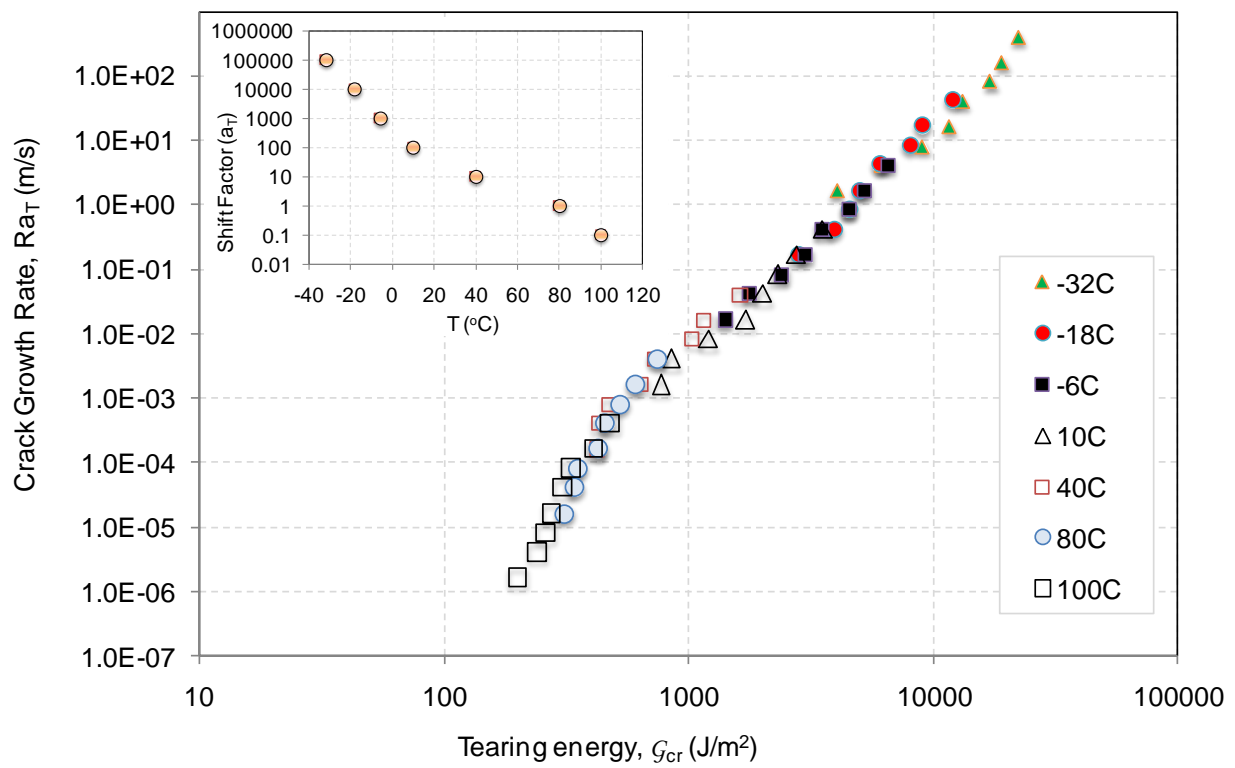


Figure 4.7 Master curve of tearing energy versus crack growth rate ($T_{reference} = 80^{\circ}C$, $T_g = -55^{\circ}C$) for hydrocarbon seal material. Shift factor, a_T , versus temperature is shown in inset.

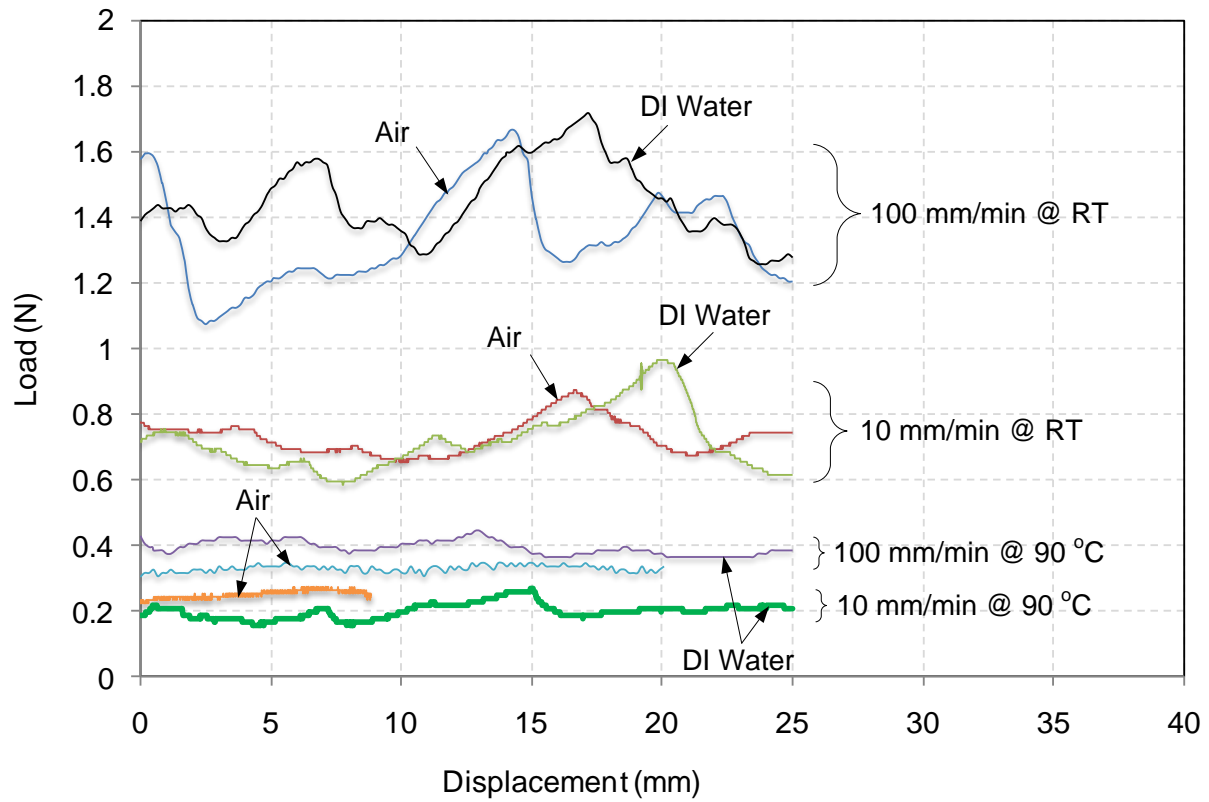


Figure 4.8 Load versus displacement behavior in DI water and air at various rates and temperatures for hydrocarbon seal material.

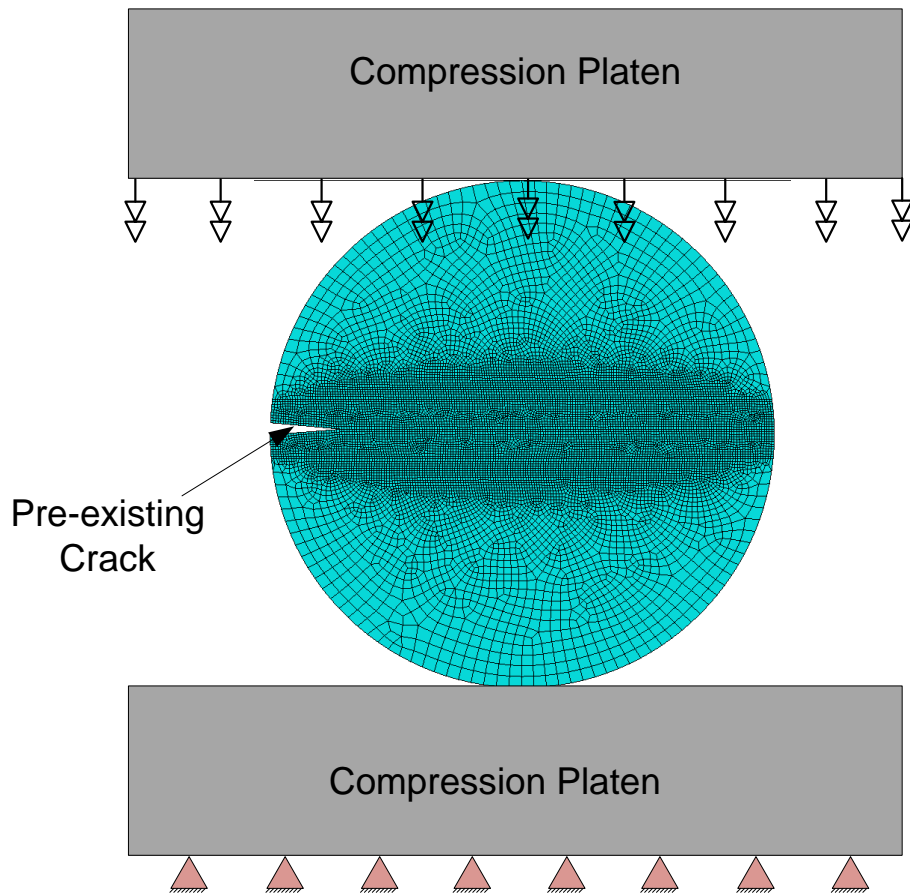


Figure 4.9 Finite element simulation of an O-ring under compression with a surface crack.

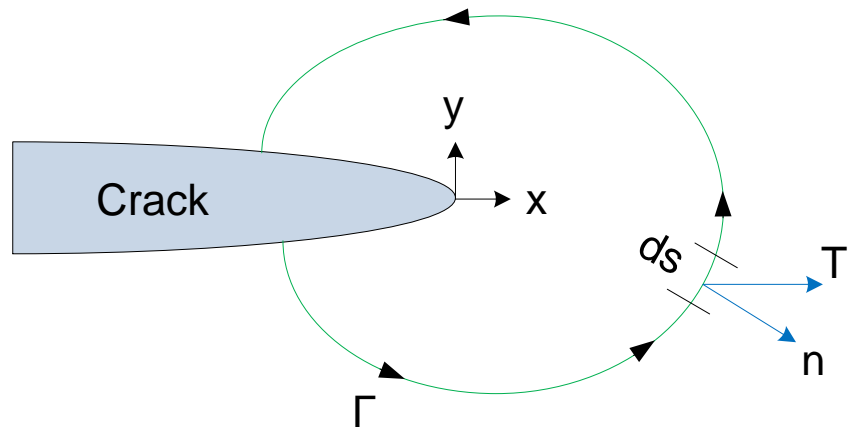


Figure 4.10 J-integral contour along with quantities used to calculate SERR around a crack tip.

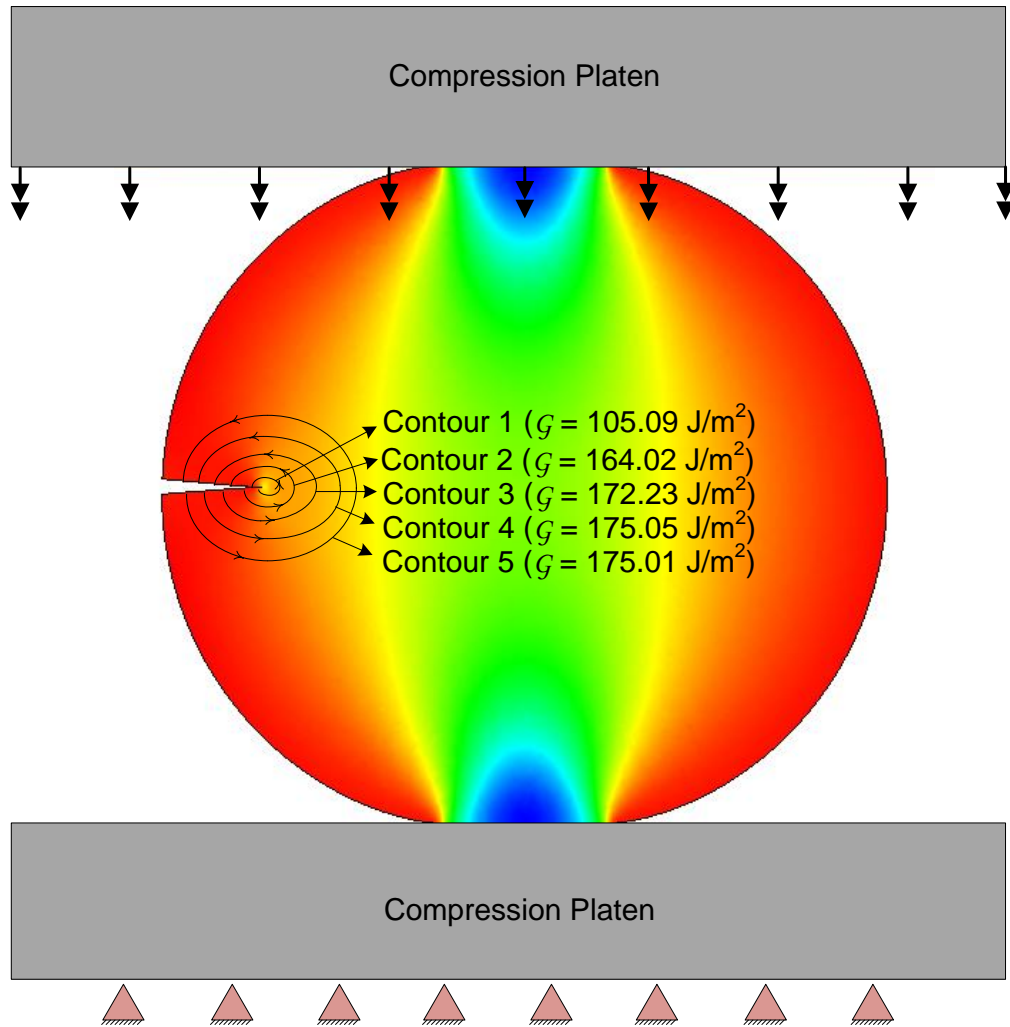


Figure 4.11 Contours around a crack tip and corresponding SERR values.

5 Viscoelastic Characterization of the Seal Material

5.1 Abstract

This chapter addresses the scientific and technological needs in understanding the viscoelastic behavior of an elastomeric seal under compression in a polymer electrolyte membrane (PEM) fuel cell assembly through the use of a unique apparatus. This apparatus consists of two sample chambers, a lower and upper one, in which samples to be studied can be arranged for measurement of several properties, such as compression stress relaxation, instantaneous modulus, modulus under strain, and compression set over a period of time. Although the fixture was developed to test a molded seal, a sub-scale elastomeric seal molded onto gas diffusion media (GDM) to simulate actual polymer electrolyte membrane (PEM) fuel cell sealing, it can also be used to test other seal geometries such as O-rings, disks or rings. If seal dimensions, such as cross-section diameter or thickness, are very small, then 10 to 12 such seal-washer assembly (an assembly of a seal arranged between two parallel stainless steel washers) can be arranged in series to form a stack, which provides better strain resolution during compression in a load frame. Since test samples (ring samples cut from a 2mm thick silicon sheet and SMORS) are small in dimensions (< 2mm in thickness), four seal-washer assemblies were arranged in series to form a stack. These stacks were then arranged in the lower and upper chambers of the apparatus. The stack in the lower chamber was compressed and held at a constant strain for long-term stress relaxation studies. The relaxed load in the seals was measured periodically by inserting the apparatus in a high precision load frame. The stack in the upper chamber was left unstrained and was used to obtain data on instantaneous properties of the seals. Together, these two sets of data allow one to measure changes in seal properties in both compressed and free states, providing valuable insights into the nature of chemical changes that take place.

A test matrix consisting of test temperatures and environments (relevant to PEM fuel cells) was developed, and fixtures loaded with seal stacks were placed in these environments and after the desired aging time, stress relaxation and instantaneous properties the seal material were measured by generation of load versus displacement plots. The capability to study the stress relaxation behavior of seals subjected to aggressive environments at high temperature, such as in fuel cells, makes this apparatus a useful apparatus to characterize long term behavior of seals.

5.2 Background

Elastomers are widely used for a number of engineering, scientific and industrial applications due to their broad range of tailorable viscoelastic properties[1-3]. Developing lifetime estimates for these materials, particularly in harsh environments while under physical stress, is often desired prior to their usage. For example, elastomeric materials subject to physical stress while undergoing crosslinking reactions are known to be subject to permanent set [4, 5]. This degradation can limit component lifetime assessment of field aged materials. The performance of elastomeric materials in various applications was studied extensively [6-10]. Nakajima[7] studied polyacrylate rubber in comparison with fluoro-rubber for automotive engine sealing application. Dillard et. al.[8] discussed the durability of elastomeric seal in PEM fuel cells. Youn and Huh [9] reported the surface degradation of high temperature vulcanizing HTV silicone and ethylene propylene diene monomer EPDM rubber under accelerated ultraviolet weathering conditions. Mitra et al. [10] studied the time-dependent chemical degradation of a fluoro-elastomer in an alkaline environment. Although substantial literature exists regarding degradation of the elastomeric gasket materials, few results were reported for the degradation and its mechanisms in PEM FC environments [8, 11-16]. Tan et. al. studied the degradation characteristics of silicone[11, 14, 16], fluoroelastomer[11, 12], and EPDM[11, 12] in a simulated

fuel cell environment. Schulze et. al.[17] investigated the degradation of silicone and resulting effect of leachants on fuel cell performance.

Stress relaxation and aging in strained polymer networks can be attributed to two distinct processes. The process causing stress relaxation may be physical or chemical in nature, and under normal conditions, both processes can occur simultaneously. Physical relaxation involves the motion of molecular chains towards new configurations in equilibrium at the new strained state, and may involve the movement of entanglements and dangling ends [18]. Upon removing the strain, the process of chain flow and entanglement motion is generally believed to be reversible in crosslinked systems. Chemical relaxation[10, 19-23] involves primarily scission and crosslinking events, resulting from the breakage and formation of covalent bonds[24]. Chemical processes may occur, either in the absence (thermal degradation [25-29]) or presence of oxygen (oxidative degradation), both leading primarily to chain scission reactions. The chemical component of relaxation is typically irreversible. At normal to low temperatures and/or short periods of time, stress relaxation is dominated by the physical processes, whilst at high temperatures and/or long time periods, the chemical processes are dominant[30]. Both physical and chemical relaxation processes cause a reduction in the counterforce when conducting relaxation experiments.

Tobolsky [5, 31, 32] and co-workers systematically studied these chemical relaxation effects and developed a theory based on two-network model consisting of distinct networks crosslinked in the unstrained and strained states. According to the two-network model, intermittent measurements of the properties of elastomers maintained in a relaxed state during exposure to elevated temperature provide a method of measuring the net rate of chain scission and crosslinking. On the other hand, it is possible to isolate the chain scission reaction by measuring

the decay of stress in a sample maintained at constant extension at elevated temperatures. The decay of stress is a direct measure of breaking of the molecular chains of the network (chain scission) because the crosslinking of the chains, occurring simultaneously, does not cause any increase of stress. Based on this approach, Tobolsky [5] developed a relationship to calculate the permanent set for an elastomeric sample:

$$\% \text{ Permanent Set} = \left\{ \left[\frac{C_1}{(U/X)C_2 + 1} + 1 \right]^{\frac{1}{2}} - 1 \right\} C_3 \quad (5.1)$$

where $C_1 = \left(\frac{l_x}{l_u}\right)^3 - 1$, $C_2 = \left(\frac{l_x}{l_u}\right)^2$, $C_3 = \frac{100}{(l_x/l_u) - 1}$, l_u is the thickness of the sample before compression, l_x is the thickness of the sample after compression, U is the value of the relaxed load obtained from the strained samples in lower stack at a desired strain, and $U + X$ can be defined as the load obtained from unstrained samples in upper stack at a desired strain, as shown in Figure 5.1. In other words, U is a measure of the rate of chain scission and $U + X$ is a measure of the net rate of chain scission and crosslinking occurring in the material at an elevated temperature, so the difference between the two will provide the net rate of crosslinking and its effect on the seal behavior in terms of permanent set. Based on a two-network model approach, if tests are conducted at several temperatures, possibly elevated temperatures for accelerated thermal aging exposures, data obtained may be used to evaluate material performance at ambient conditions. The most important methodology for such extrapolations is based on the Arrhenius relationship. Arrhenius extrapolations assume that a chemical degradation process is controlled by a reaction rate k proportional to $\exp(-E_a/RT)$, where E_a is the Arrhenius activation energy, R the gas constant (8.314 J/mol-K), T the absolute temperature, and A the pre-exponential factor, as shown in Equation 5.2.

$$k = A \times \exp\left(\frac{-E_a}{RT}\right) \quad (5.2)$$

Therefore, a log-plot of reaction rates (k) or degradation times ($1/k$) versus inverse temperature ($1/T$) is expected to result in a straight line, allowing simple extrapolations to lower temperatures. The main assumption made here is that the chemical kinetics of material degradation remain the same at elevated and service temperatures. Many studies [33-37] have clearly demonstrated that some degradation processes can be well described by a simple linear Arrhenius relationship. In order to estimate seal material lifetime based on accelerated characterization technique mentioned above, measurement of momentary properties, $U+X$, and relaxed behavior, U , was conducted in several environments and temperatures by using a dual-chamber fixture, the details of which are provided in the following section.

5.3 Compression Stress Relaxation Fixture Design

The fixture used in this study is made entirely of Type 316 stainless steel to enable aging studies in corrosive environments at elevated temperatures. Since the fixture does not contain any measuring device, such as a load cell or other transducer, the entire fixture can be immersed in liquid media at high temperatures for accelerated characterization. The main intention of the design is to provide the long-term measurements of the mechanical properties of elastomers. A quarter-section view of the fixture can be seen in Figure 5.2. The fixture consists of a top flange with a center hole, an upper chamber and a lower chamber mounted vertically and connected by means of a threaded connector, a bottom flange with a center hole, and two pistons, upper and lower, one for each chamber to compress the seal stack. Sample, such as an O-ring, can be placed in the upper and lower chambers under the pistons. If the sample is very small in thickness, it may be difficult to obtain desired precision during compression. In that case, a

sample can be placed concentrically between two stainless steel washers and 10 to 12 such seal-washer assemblies can be arranged in series to form a stack, as shown in bottom left corner of Figure 5.2. Since the seal studied here is only a few mm thick ($\approx 1.5\text{mm}$), 4-5 such washers-seal assembly were arranged in series to form a stack, so as to obtain better resolution during compression of seals. Such seal stacks prepared in this manner can be placed in the upper and lower chambers of the fixture. The seal stack in upper and lower chambers are centered and arranged concentrically with the help of the piston rod attached to the lower piston. The upper piston compresses the upper seal stack to obtain the instantaneous properties of the seal material at a given time. The lower seal stack is compressed by pushing the lower piston and locked to a desired value of compressive strain by means of a spacer. Spacers of different thickness enable a range of compressive strains. The spacers are attached to the rod, as shown in the bottom right corner of Figure 5.2, by means of a screw. Simple turning of the rod moves the spacer in and out, allowing measurement of compression set. After samples were arranged in the two chambers, the fixture is placed on a polycarbonate base. Since the rod attached to the fixture protrudes out of the lower flange, the polycarbonate base was used to facilitate placing the fixture on a flat surface as well as provide room for accommodating the spacer and locking nuts attached, as shown in Figure 5.3. For aging in desired environmental conditions, the fixture can be placed in a glass container filled with liquid media and placed in an oven to maintain the desired temperature. In order to prevent unwanted evaporation of the liquid from glass container, the glass container can be sealed with an O-ring and glass lid clamped with the help of binder clips as shown in Figure 5.3.

5.4 Experimental

5.4.1 Material & Sample Preparation

The seal material used for the SMORS is a hydrocarbon elastomer provided by Henkel Corporation (Rocky Hill, CT). More information on the material can be found in [38]. Custom designed seals (elastomeric seal material molded onto gas diffusion media), called sub-scale molded O-ring seal or SMORS, were prepared by Freudenberg-NOK (Plymouth, MI), as shown in Figure 5.4. The thickness of SMORS was determined using a Mitutoyo thickness measurement gage (Mitutoyo Corporation, Aurora, IL). Before measuring the thickness, the sample was arranged between two glass plates and placed on the instrument plate. After zeroing the gage, the probe was lowered until it touched the glass surface to determine the total thickness of two glass and sample. Four readings of total thickness were taken around the perimeter at equally spaced intervals and an average value of total thickness was obtained. The thickness of each glass plate was then measured separately and subtracted from total thickness to obtain thickness of the sample. The SMORS cross-section with dimensions is shown in Figure 5.4. Four SMORS were then arranged between type 316 stainless steel washers in series to form a stack, as shown in Figure 5.2.

The seal material used for preparing the ring samples is a low-viscosity fuel cell grade silicone rubber (LO305) provided by Freudenberg-NOK. Ring samples (dimensions of a ring sample are also shown in Figure 5.4) were punched out of 2mm thick silicone rubber sheets and the.. Silicones are attractive because of low cost and ease of fabrication. They are widely used as sealing materials, including in fuel cells[13, 39]. Three rings were then arranged between type 316 stainless steel washers in series to form a stack.

5.4.2 Environments and Specimen Conditioning

Mechanical property characterization of SMORS and silicone rings were conducted in air, as well as immersed in deionized (DI) water, 50v/50v DI water and ethylene glycol, 0.1M DI water and sulfuric acid solutions for this study. In air, tests were conducted at 120°C, 90°C, and 60°C whereas tests in the liquid solutions were conducted at 90°C in gravity convection ovens. For aging in a desired environment, the fixture is placed in a glass container filled with the desired liquid solution and placed in an oven to maintain the temperature. In order to prevent unwanted evaporation of the liquid from glass container, the glass containers were sealed with an O-ring and glass lid clamped with binder clips as shown in Figure 5.3.

5.4.3 Test Procedure

For measurements of seal properties, a high precision Instron MicroTester 5848 load frame equipped with an auto-calibrated 2000 N capacity tension/compression load cell was used. The load cell measures the force and a linear LVDT measures the displacement. The measured force was corrected for the weight of the pistons, approximately 1.5N. For measurement of seal properties, the fixture was periodically removed from the aging oven and placed between compression platens, as shown in Figure 5.3, for momentary and sealing force measurements and then returned to the oven for further aging. During the measurement, the piston pushes against the seal stacks from above. The compression of the upper stack provides information on momentary seal properties. A superposition of small strain onto a large dominating strain in the lower stack provides the value of relaxed value of restoring load in the seal stack as well as stiffness of the seals that were held under constant strain. The rate of loading was 10 mm/min.

For measurement of momentary properties, the seal stack in the upper chamber was compressed in the fixture. The stress starts to rise when increasing the compression strain and

typical behavior is shown in Figure 5.5 (plotted in first quadrant). The experiment is stopped when the desired compression of the seals is achieved. For measuring the relaxed force (restoring force) and stiffness in a compressed sample in the lower seal stack, an incremental strain is applied by pushing the lower piston. A typical curve, as shown in Figure 5.6, shows two distinct regions. In region 1, when the compression platen starts to touch the lower piston, the load cell registers an abrupt increase in compressive force. The slope of this region indicates the stiffness of the load train in the fixture-test material assembly. In region 2, as a small amount of strain is superimposed on a dominating large strain, the seals get compressed by an incremental amount, causing a comparatively slight increase of force with displacement. Further piston movement results in the typical compression curve for an elastomeric material. The stiffness of the seals held under strain for a given aging time can be calculated from the slope of force versus displacement plot in region 2. Comparison of slope obtained from stress free samples with the value obtained from seals held under strain can provide insight into how stresses in a compressed seal affect material properties due to aging in an environment. The value of the force, measured at the intersection of linear extrapolations of region 1 and 2, as shown in Figure 5.6, is the relaxed value of the force in the compressed seal samples.

5.5 Results & Discussion

5.5.1 SMORS

Results obtained from the testing performed on SMORS are shown in Figure 5.7 to Figure 5.9 for air at 120°C, 90°C, and 60°C, respectively and in Figure 5.10 to Figure 5.12 for DI water, 50v/50v DI water/ethylene glycol solution, and 0.1M sulfuric acid solution at 90°C, respectively. The spacer provided 25% compression of each seal in the stack. For a given aging environment, load versus strain plots were generated to determine momentary and compression stress

relaxation behavior of SMORS from the upper and lower stack, respectively. Plots of decay in normalized relaxed force, represented by $\frac{F(t)}{F_o}$ where F_o is the initial force at the desired compression, against time were also generated for both momentary as well as relaxed values of force.

5.5.1.1 *Momentary Properties from Top Stack: SMORS Behavior in Environment without Stress*

In this case, the measured load depends on the net difference between crosslinking and chain scission during aging. As observed in plots of $\frac{F(t)}{F_o}$ versus time from Figure 5.7 to Figure 5.12, an initial increase and then decrease in the value of force at desired compression was observed. The initial increase in load was different for different environmental conditions the SMORS was exposed to. For example, SMORS in air at 120°C, 90°C and 60°C show approximately 80% (Figure 5.7), 25% (Figure 5.8), and 10% (Figure 5.9) increases, respectively and SMORS in ethylene glycol solution (Figure 5.11) show approximately a 30% increase in load. On the other hand, SMORS in DI water and sulfuric acid solution at 90°C did not show a significant increase in load value. This behavior may be attributed to aging, which is common to a wide variety of natural and synthetic elastomers[40], leading to changes in properties. For instance, in oxygen-containing environments, the mechanical strength of rubber can be greatly affected by oxidation, especially at high temperatures[41]. Based on the statistical theory of rubber elasticity, one can define shear modulus of an elastomer as:

$$G = NkT \tag{5.3}$$

where G is the shear modulus, N is elastically effective network strands per unit volume, k is the Boltzmann's constant ($k = 1.381 \times 10^{-23}$ J/K), and T is absolute temperature. Equation 5.3 can also be written in terms of the elastic modulus, E , as:

$$E = 3NkT \quad (5.4)$$

At constant temperature, Equation 5.4 indicates that stiffness or elastic modulus of an elastomer is linearly related to crosslink density of the material. Crosslink type and density of a rubber vulcanizate determine physical properties such as modulus, hardness, elongation to break, etc. By increasing crosslink density, modulus, hardness, and abrasion resistance increase[42]. During thermal aging, chain scission and crosslinking may occur, leading to changes in mechanical properties [41, 43-47]. The greater the degree of crosslinking, the greater the elastic modulus becomes and initial increase in load discussed above may be attributed to this behavior. During the initial phase of environmental exposure, new crosslink formation is the dominating process leading to increase in modulus of the material. After this initial increase, chain scissioning may dominate the degradation process, leading to decrease in stiffness of the material.

Also, the degree of crosslinking or change in stiffness of the material seems to depend on how a given material reacts to a certain environment. For example, higher temperatures lead to higher degrees of crosslinking, as observed in air at 120°C, 90°C, and 60°C. On the other hand, at a given temperature, the higher the mass uptake, the lower the degree of crosslinking because the presence of liquid solution in the network may interfere with the process of crosslink formation and contribute more towards chain scission. Hence the presence of a liquid environment may lead to decay in material properties if a seal material has high mass uptake in a given solution. This is clearly evident in Figure 5.10 and Figure 5.12 for DI water and sulfuric acid solutions, respectively, where higher mass uptake in these solutions compared to ethylene glycol, as shown

in Figure 5.13, seems to mitigate the crosslinking process to a great extent, resulting in an insignificant increase in load.

5.5.1.2 *CSR from Bottom Stack: SMORS Behavior under stress in Environment*

Figure 5.7 to Figure 5.12 show results for stress relaxation tests performed in different environments. For a typical compression stress relaxation process, the restoring force decays with time owing to both physical and chemical relaxation taking place in the seal material. There is an immediate physical relaxation of molecular chains and fillers due to the deformation. The whole process of chain flow and resulting movement of their entanglements is reversible upon removing the strain from the system. A continuous stress relaxation test apparatus, such as developed by Elastocon [48], is usually better equipped to capture initial physical relaxation of the material. Since the fixture was mainly designed for long term testing of seal material through intermittent data collection, physical relaxation is not evident in the results presented here. Physical relaxation is often followed by chemical relaxation process, either in the absence (thermal degradation) or presence of oxygen (oxidative degradation), both leading primarily to chain scission type reactions and loss of polymer molecular weight. The chemical component of relaxation is irreversible.

Although the decay was observed in all the cases studied here, an increase in restoring force was initially observed except in DI water and the 0.1M sulfuric acid solution. As mentioned earlier, specimens in DI water or the sulfuric acid solution exhibited significantly higher mass uptake values compared to the aqueous ethylene glycol solution, as shown in Figure 5.13. The increase in restoring force may be attributed to thermal expansion of the seal material, and depending on coefficient of thermal expansion of the seal material, may give rise to a significant increase in restoring force[49]. The decay in restoring force provides a measure of the

degradative reaction in the network because any new networks/crosslinks formed are considered to be in equilibrium with the main network and do not impose new stress[50]. Only scission of the original network chains causes reduced restoring load. Since thermal expansion leads to increase and chain scission results in decay in relaxed load, the effect of these competing mechanisms is discussed in the next section.

When such CSR tests are performed over a wide range of strains and environmental conditions, life prediction charts can be compiled as a predictive guide. One common method of using such data is to select an arbitrary degradation criterion and find the time at each temperature required to reach this criterion. These times are then plotted versus reciprocal temperature on an Arrhenius graph to see whether linear (e.g., Arrhenius) behavior is indicated. For example, $\frac{F(t)}{F_0} = 0.2$ can be chosen as the degradation criterion and pick off the times required to reach this value at each temperature. This approach is illustrated in an Arrhenius graph in Figure 5.14. The principle of the Arrhenius approach is based on accelerating the physico-chemical change of the material by raising the temperature to simulate its long-term state, and then measuring the relevant properties in this thermo-activated state. This method assumes that the same state of the material is attained after both a long period of exposure to the working temperature and a shorter period of exposure to a higher temperature. The resulting property values can then be estimated far in excess of the experimentally accessible time scale.

The seal material studied here is expected to have a lifetime of 40,000 hours (≈ 10 years) at 70°C in the PEM fuel cell. To make lifetime predictions using the Arrhenius approach, CSR data obtained at temperatures higher than 70°C can be used. Figure 5.15 shows the normalized relaxed value of the force in SMORS at three different temperatures and as evident from the

figure, the erratic nature of the data and the absence of distinguishable temperature-dependent behavior makes it impossible to use an Arrhenius approach. The erratic behavior may result from one or combination of factors listed below:

5.5.1.2.1 Effect of Antidegradants

Oxidative aging of rubber is one of the most important problems in rubber technology because the absorption of a small amount of oxygen causes a considerable change in physical and mechanical properties[51, 52]. Oxidation is usually accelerated by heat and stress and oxygen can react with elastomers and alter network structure by causing chain scission and/or crosslinking [53]. If chain scission dominates during aging, the elastomer softens and becomes sticky, eventually resulting in complete loss of seal bead, as evident in Figure 5.16 (a). An antioxidant, derivatives of amines and phenols[54], is usually added to inhibit oxidation but inadequate amounts may lead to failure of an elastomeric component.

5.5.1.2.2 State of Cure

Differences in the state of cure may result in poor predictability of test results.

5.5.1.2.3 Friction

Due to change in seal material properties with time, the friction between seal and surrounding steel washers in a stack may change between each loading/unloading cycle.

5.5.1.2.4 Compatibility of seal material with unitized electrode assembly (UEA)

As mentioned before, the seal material is molded onto a UEA where porous gas diffusion layers are assembled on either side of membrane electrode assembly (MEA), as shown in Figure 5.16 (b). In an ideal situation, seal material, when injected in the mold, penetrates the porous gas diffusion layer and forms mechanical interlocking with the porous media, so that there is no

relative slippage between the seal and gas diffusion layer. Such interlocking is very critical to seal performance in fuel cell assembly because any slippage at the seal-GDL interface, due to either partial or no impregnation of seal material into GDL, may result in the leakage at seal-GDL interface.

5.5.2 Silicone rings

The purpose behind conducting compression stress relaxation tests on bulk material samples was to investigate the root cause of erratic nature in the results obtained for SMORS. As mentioned above, error in the data may come from frictional sliding at interfaces, level and performance of antioxidants in the seal material, and when seal material is molded onto UEA forming an assembly. Silicone was selected as bulk material because silicone is a well understood material and known for its excellent properties at high temperature ($\approx 250^{\circ}\text{C}$) in oxygen containing environments[55].

Results obtained from the testing performed on silicone rings are shown in Figure 5.17 to Figure 5.19 for air at 120°C , 90°C and 60°C , respectively and Figure 5.20 for DI water at 90°C . For a given aging environment, load versus strain plots were generated to determine momentary and compression stress relaxation behavior of silicone rings from upper and lower stack respectively. The specific set of silicone rings stack and spacer provided an average compression of 25% in each ring sample. Plots of $\frac{F(t)}{F_o}$ against time were also generated for both momentary as well as relaxed value of the force.

5.5.2.1 *Momentary Properties from Top Stack: Silicone Behavior in Environment without Stress*

Initial increase in modulus of silicone, as shown in (a) in Figure 5.17 to Figure 5.20, is similar to what was observed for SMORS. This observation from silicone and SMORS confirms the

material properties changes due to aging in the environment. However, weakening of the material followed by initial stiffening was not observed for silicone and this may be attributed to silicone's excellent resistance against oxidation and also indicates towards the unstable nature of the seal material used to make SMORS. .

5.5.2.2 *CSR from Bottom Stack: Silicone Behavior under Stress in Environment*

Normalized decay in relaxed load, as shown in Figure 5.17 (c) to Figure 5.20, is comparatively much smoother compared to erratic behavior from SMORS although some amount of roughness in the data is still observed and this could be due to CSR fixture resolution. Comparatively better results obtained from bulk silicone samples indicate the complexity associated with testing seal/GDL assembly or SMORS. Because the elastomer does not impregnate the GDL, relative slippage at seal/GDL interface during compression is possible. Also, friction present at seal/GDL and seal/washer interface, measured by the coefficient of static friction (which depends on test environment i.e. either air or liquid solutions); may contribute to the error in measuring the relaxed load.

Also important to consider is an initial increase in relaxed load, as shown in (c) in Figure 5.17 to Figure 5.20. Since newly formed crosslinks are not contributing to any increase in load, swelling of the material seems to be a viable alternative. In order to define this process of initial increase and then decay, investigation must be conducted into physical or chemical processes occurring in the seal material immediately followed by compression. As discussed earlier, processes that may be present are:

- (a) Physical relaxation
- (b) Chemical relaxation

(c) Swelling

Physical relaxation is dominant during the first moments of CSR leading to an instantaneous drop in relaxed load. Chemical relaxation involves chain scission and crosslink formation where chain scission leads to drop in relaxed load over time. Swelling of the material will lead to increase in relaxed load. Hence, there are a few competing mechanisms, especially chemical relaxation and swelling, going on at the same time and depending on the rate of these processes, an increase or decrease may be observed. For example, if chain scissioning is a dominant process and occurs at a rate faster than thermal expansion of the material, the net effect of these phenomena should not result in any increase in load. On the other hand, if chemical relaxation is slower than thermal expansion, an increase in load should be observed. High temperature or the presence of a liquid environment (due to diffusion of liquid media into material) or both may decide the rate of chain scission as chemical relaxation is an environment-dependent process[56].

In order to distinguish between these two competing processes, two continuous CSR experiments were additionally performed in air at 90°C on silicone rings where the fixture, loaded with silicone ring stacks in the bottom chamber, was placed in an Instron load frame fitted with a convection oven for temperature control. Ring stacks were compressed to 25% and relaxed load in silicone rings was continuously measured by load cell for two environmental conditions as follows:

- (a) The fixture was placed in the oven so that the seal stack is completely exposed to air circulating in the oven due to fan.
- (b) The fixture was placed in a glass container and covered with a lid so that no circulation of air is available. The air in the container will move around due to gravity convection only.

Figure 5.21 shows the results for cases (a) and case (b) as well as results obtained from the CSR fixture. Plenty of air circulation in the forced convection oven leads to faster chain scission rate so the effect of thermal expansion is not evident. In the absence of good air circulation around the seal material in the gravity convection oven, the chain scissioning process is slower compared to swelling and hence an increase in the load was initially observed. Therefore, chain scission or chemical relaxation is an environment dependent process and different environments show different behavior during CSR. Because all CSR tests on SMORS and silicone rings were conducted in gravity convection ovens, the observation above may explain the initial increase in relaxed load in all tests conducted in air but lacking the reason for significant difference between continuous relaxation and relaxation data from the CSR fixture. This may indicate the poor sensitivity of the fixture in measuring the load. If changes in material properties are significant, the CSR fixture is good to capture the increasing or decreasing trend in material behavior. However, if a material does not degrade much, and load change is very minor, error in the data is inevitable. In order to minimize error in future tests, the fixture was redesigned using a load cell to for automatic data collection using a data acquisition board and custom designed LabVIEW[®] code.

5.6 Conclusion

Viscoelastic property characterization of a proprietary molded seal material (FCS1 molded into SMORS) and a silicone system used in PEM fuel cells was conducted using a novel fixture which enables a comparison of material properties of strained and unstrained samples in a given environment. Based on a two-network model and rubber elasticity theory, a comparison of material properties obtained through these tests provided significant scientific insight and understanding of material behavior over a range of environmental conditions. The effects of

temperature and environment were evident on material property changes and could be understood in terms of momentary properties and stress relaxation behavior. Various mechanisms involved in material degradation, chain scissioning and crosslinking, were discussed and insights were gained into how the cure state and level of antidegradants in a material dictates the material behavior during the first phase of environmental exposure leading to modulus change in the material tested here. Also discussed was the effect of competition between several mechanisms such as chain scissioning, crosslinking, and thermal expansion on stress relaxation behavior initially although chain scission dominated the long term relaxation behavior.

Results presented from testing on SMORS showed much more variation in data compared to data from neat silicone rings due to nature of complexity involved in making SMORS. However, data from SMORS and ring testing indicated the fixture's inability to capture trends in material property changes if such a change does not fall within sensitivity/resolution bands of the fixture. In order to obtain better resolution in future tests, the fixture was redesigned for automatic data collection so error due to many factors involved in taking measurement can be reduced to an acceptable value.

References:

1. S.J. Clarson and J.A. Semlyen, *Siloxane Polymers*. 1993, New Jersey: Prentice Hall.
2. J.M. Zeigher and F.W.G. Fearon, *Silicon Based Polymer Science: A Comprehensive Resource*. Advances in Chemistry. Vol. 224. 1990, Washington, DC: ACS Press.
3. B. MA, *Silicon in Organic, Organometallic, and Polymer Chemistry*. 2000, New York: Wiley.
4. D.R. Rottach, J.G. Curro, G.S. Grest, and A.P. Thompson, "Effect of Strain History on Stress and Permanent Set in Cross-Linking Networks: A Molecular Dynamics Study," *Macromolecules*, **37**(14), 5468-5473, 2004.
5. R.D. Andrews, A.V. Tobolsky, and E.E. Hanson, "The Theory of Permanent Set at Elevated Temperatures in Natural and Synthetic Rubber," *Journal of Applied Physics*, **17**, 352-361, 1946.
6. R.J. Pazur, J. Bielby, and U. Dinges, "Continuous Compressive Stress Relaxation of Elastomers Used in Engine Sealing Applications," *Rubber World*, **229**(5), 24-29, 2004.
7. N. Nakajima and R.D. DeMarco, "Application of Polyacrylate Rubber for High Performance Automotive Gaskets and Seals," *Journal of Elastomers and Plastics*, **33**(2), 114-120, 2001.
8. D.A. Dillard, S. Guo, M.W. Ellis, J.J. Lesko, J.G. Dillard, J. Sayre, and B. Vijayendra, *Seals and Sealants in Pem Fuel Cell Environments: Material, Design, and Durability Challenges*, in *ASME Second International Conference on Fuel Cell Science Engineering and Technology*. 2004: Rochester, New York. 553-560.
9. B.H. Youn and C.S. Huh, "Surface Degradation of Htv Silicone Rubber and Epdm Used for Outdoor Insulators under Accelerated Ultraviolet Weathering Conditions," *IEEE Transactions on Dielectrics and Electrical Insulation*, **12**(5), 1015-1024, 2005.
10. S. Mitra, A. Ghanbari-Siahkali, P. Kingshott, K. Almdal, H.K. Rehmeier, and A.G. Christensen, "Chemical Degradation of Fluoroelastomer in an Alkaline Environment," *Polymer Degradation and Stability*, **83**(2), 195-206, 2004.
11. J. Tan, Y.J. Chao, J. W. Van Zee, and W.k. Lee, "Degradation of Elastomeric Gasket Materials in Pem Fuel Cells," *Materials Science and Engineering: A*, **445**, 669-675, 2007.

12. J. Tan, Y.J. Chao, J.W.V. Zee, X. Li, X. Wang, and M. Yang, "Assessment of Mechanical Properties of Fluoroelastomer and Epdm in a Simulated Pem Fuel Cell Environment by Microindentation Test," *Material Science and Engineering A*, **In Print**2008.
13. M. Schulze, T. Knori, A. Schneider, and E. Gulzow, "Degradation of Sealings for Pefc Test Cells During Fuel Cell Operation," *Journal of Power Sources*, **127**, 222-229, 2004.
14. J. Tan, Y.J. Chao, X. Li, and J.W.V. Zee, "Degradation of Silicone Rubber under Compression in a Simulated Pem Fuel Cell Environment," *Journal of Power Sources*, **172**, 782-789, 2007.
15. A. Husar, M. Serra, and C. Kunusch, "Description of Gasket Failure in a 7 Cell Pemfc Stack," *Journal of Power Sources*, **169**(1), 85-91, 2007.
16. J. Tan, Y.J. Chao, M. yang, C.T. Williams, and J.W.V. Zee, "Degradation Characteristics of Elastomeric Gasket Materials in a Simulated Pem Fuel Cell Environment," *Journal of Materials Engineering and Performance*, **17**(6), 785-792, 2008.
17. M. Schulze, T. Knori, A. Schneider, and E. Gulzow, "Degradation of Sealings for Pefc Test Cells During Fuel Cell Operation," *Journal of Power Sources*, **127**(1-2), 222-229, 2004.
18. J.G. Curro and P. Pincus, "A Theoretical Basis for Viscoelastic Relaxation of Elastomers in the Long-Term Limit," *Macromolecules*, **16**, 559-562, 1983.
19. X. Wang, H. Zhang, Z. Wang, and B. Jiang, "In Situ Epoxidation of Epdm Rubber by Performic Acid," *Polymer*, **38**, 5407-5410, 1997.
20. S. Mitra, A. Ghanbari-Siahkali, P. Kingshott, H.K. Rehmeier, H. Abildgaard, and K. Almdal, "Chemical Degradation of Crosslinked Epdm Rubber in an Acidic Environment. Part Ii. Effect of Peroxide Crosslinking in the Presence of a Coagent," *Polymer Degradation and Stability*, **91**(1), 81-93, 2006.
21. S. Mitra, S. Ghanbari-Siahkali, P. Kingshott, H.K. Rehmeier, H. Abildgaard, and K. Almdal, "Chemical Degradation of Crosslinked Epdm Rubber in an Acidic Environment. Part I. Effect on Accelerated Sulphur Crosslinks," *Polymer Degradation and Stability*, **91**(1), 69-80, 2006.
22. T. Sugama, "Surface Analyses of Fluoroelastomer Bearings Exposed to Geothermal Environments," *Materials Letters*, **50**(2-3), 66-72, 2001.

23. J. Tan, Y.J. Chao, M. Yang, W.K. Lee, and J.W.V. Zee. in *Proceedings of the 2nd Annual Korea-USA Joint Symposium on Hydrogen & Fuel Cell Technologies*. 2007. Columbia, SC.
24. K.T. Gillen, R. Bernstein, and M.H. Wilson, "Predicting and Confirming the Lifetime of O Rings," *Polymer Degradation and Stability*, **87**, 257-270, 2005.
25. T. Zaharescu, M. Giurginca, and S. Jipa, "Radiochemical Oxidation of Ethylene-Propylene Elastomers in the Presence of Some Phenolic Antioxidants," *Polymer Degradation and Stability*, **63**(2), 245-251, 1999.
26. A.K. Bhowmick, J. Konar, S. Kole, and S. Narayanan, "Surface-Properties of Epdm, Silicone-Rubber, and Their Blend During Aging," *Journal of Applied Polymer Science*, **57**(5), 631-637, 1995.
27. B.H. Youn and C.S. Huh, "Surface Degradation of Htv Silicone Rubber and Epdm Used for Outdoor Insulators under Accelerated Ultraviolet Weathering Condition," *IEEE Transactions on Dielectrics and Electrical Insulation*, **12**(5), 1015-1024, 2005.
28. T. Zaharescu, E. Feraru, and C. Podina, "Thermal Stability of Gamma Irradiated Ethylene-Propylene-Diene Monomer Divinyl Benzene Systems," *Polymer Degradation and Stability*, **87**(1), 11-16, 2005.
29. V. Deniz, B. Karaagac, and N. Ceyhan, "Thermal Stability of Butyl/Epdm/Neoprene Based Rubber Compounds," *Journal of Applied Polymer Science*, **103**(1), 557-563, 2007.
30. L.H. Sperling, *Introduction to Physical Polymer Science*. 4 ed. 2005, New York: Wiley-Interscience.
31. A.V. Tobolsky, *Properties and Structure of Polymers*. 1960, New York: Wiley.
32. A.V. Tobolsky, I.B. Prettyman, and J.H. Dillon, *Journal of Applied Physics*, **15**, 380-387, 1944.
33. K.T. Gillen, M. Celina, R.L. Clough, and J. Wise, "Extrapolation of Accelerated Aging Data - Arrhenius or Erroneous?," *Trends in Polymer Science*, **5**(8), 250-257, 1997.
34. J. Wise, K.T. Gillen, and R.L. Clough, "An Ultrasensitive Technique for Testing the Arrhenius Extrapolation Assumption for Thermally Aged Elastomers," *Polymer Degradation and Stability*, **49**(3), 403-418, 1995.

35. K.T. Gillen, M. Celina, and M.R. Keenan, "Methods for Predicting More Confident Lifetimes of Seals in Air Environments," *Rubber Chemistry and Technology*, **73**(2), 265-283, 2000.
36. K.T. Gillen, M. Celina, and R. Bernstein, "Validation of Improved Methods for Predicting Long-Term Elastomeric Seal Lifetimes from Compression Stress-Relaxation and Oxygen Consumption Techniques," *Polymer Degradation and Stability*, **82**(1), 25-35, 2003.
37. K.T. Gillen, M. Celina, and R. Bernstein. *Review of the Ultrasensitive Oxygen Consumption Method for Making More Reliable Extrapolated Predictions of Polymer Lifetimes*. in *Ann Tech Conf Soc Plast Eng*. 2004.
38. M.P. Burdzy, B.R. Einsla, K.J. Welsh, A.F. Jacobine, J.G. Woods, and S.T. Nakos, *Bonded Fuel Cell Assembly, Methods, Systems, and Sealant Compositions for Producing the Same*, W.I.P. Organization, Editor. 2007: USA.
39. P.R. Hagen, G.E. Mayville, and J.M. Klosowski, "Silicone Performed Joint Seal (Pjs) and Their Applications," *ASTM Special Technology Publication*, **1334**, 129-141, 1999.
40. M.E. Cain and J.I. Cunneen, "Fundamental Approaches to Ageing Problems," *Revue Gen Coautch*, **39**, 1940-1950, 1962.
41. G.R. Hamed and J. Zhao, "Tensile Behavior after Oxidative Aging of Gum and Black-Filled Vulcanizates of Sbr and Nr," *Rubber Chemistry and Technology*, **72**(4), 721-730, 1999.
42. N.J. Morrison and M. Porter, "Temperature Effects on the Stability of Intermediates and Crosslinks in Sulfur Vulcanization," *Rubber Chemistry and Technology*, **57**(1), 63-85, 1984.
43. R. Fan, Y. Zhang, C. Huang, Y. Zhang, Y. Fan, and K. Sun, "Effect of Crosslink Structures on Dynamic Mechanical Properties of Natural Rubber Vulcanizates under Different Aging Conditions," *Journal of Applied Polymer Science*, **81**, 710-718, 2001.
44. A.S. Deuri and A.K. Bhowmick, "Effect of Ageing on Critical Cut Length and Morphology of Fracture Surface in Tensile Rupture of Natural Rubber," *Journal of Materials Science*, **22**(12), 4299-4306, 1987.

45. P. Budrugaec, "Accelerated Thermal Aging of Nbr and Other Materials under Air or Oxygen Pressures and Degradation of Polymers," *Die Angewandte Makromolekulare Chemie*, **247**, 19-30, 1997.
46. K.T. Gillen, R.L. Clough, and J. Wise, "Prediction of Elastomer Lifetimes from Accelerated Thermal-Aging Experiments," *Advances in Chemistry Series*, **249**, 557-576, 1996.
47. M.L. Huy and G. Evrard, "Methodologies for Lifetime Predictions of Rubber Using Arrhenius and Wlf Models," *Die Angewandte Makromolekulare Chemie*, **261**(262), 135-142, 1998.
48. G. Spetz, *Stress Relaxation-Test Methods, Instruments, Test Results and Lifetime Estimation*, in *Lifetime estimation of rubber materials by ageing and stress relaxation tests*. 2000: Boras, Sweden.
49. L.R.G. Treloar, *The Physics of Rubber Elasticity*. 2 ed. 1975, Glasgow: Oxford University Press.
50. W. McKnight, *Introduction to Polymer Viscoelasticity*. Chemical Stress Relaxation, ed. J.J. Aklonis. 1983, New York: Wiley, Interscience.
51. W.L. Hawkins, *Polymer Degradation & Stabilization*. 1984: Springer-Verlag.
52. G. Scott, *Atmospheric Oxidation and Antioxidants*. 1965, Amsterdam: Elsevier.
53. G.R. Hamed, *Materials & Compounds*, in *Engineering with Rubber: How to Design Rubber Components*, A.N. Gent, Editor. 2001, Hanser Gardner Publications: Cincinnati.
54. J.C. Johnson, "Antioxidants: Synthesis and Applications," *Chemical Technology Review* 44:1975.
55. E.B. Magrab, *Integrated Product and Process Design and Development: The Product Realization Process (Environmental and Energy Engineering)*. 1997, Boca Raton, FL: CRC-Press. 320.
56. D. Wright, *Failure of Plastics and Rubber Products: Causes, Effects and Case Studies Involving Degradation*. 2001, Billingham, AZ: Smithers Rapra. 412.

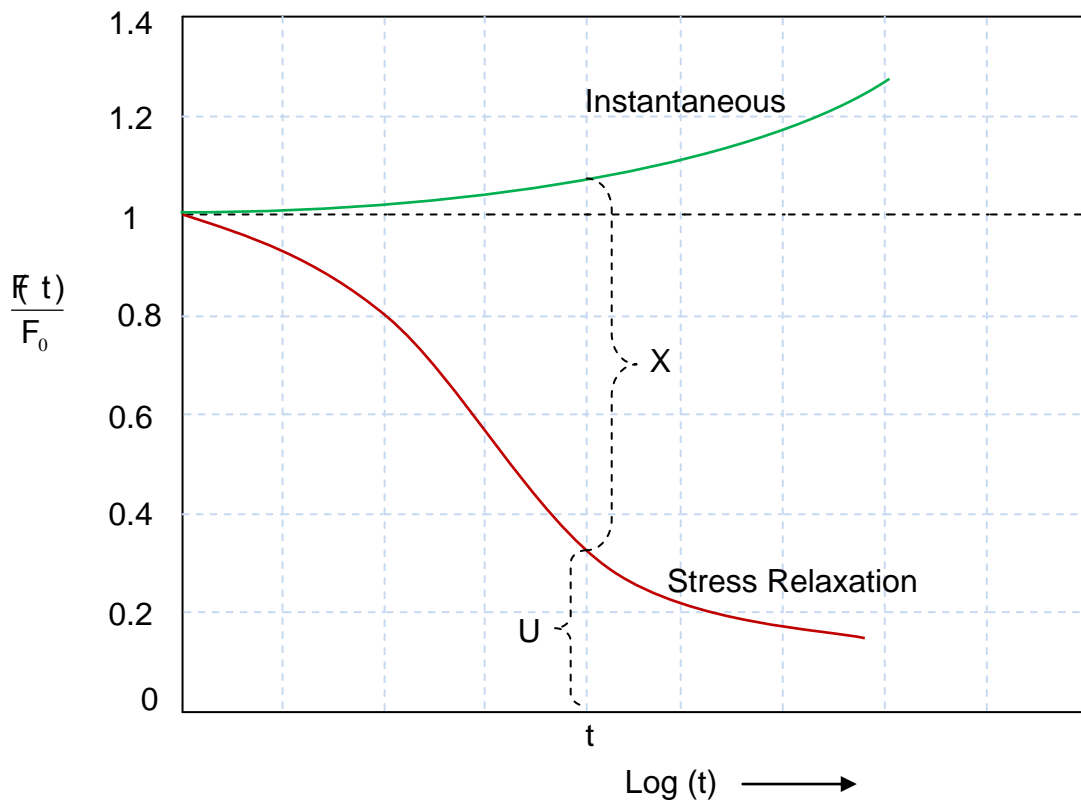
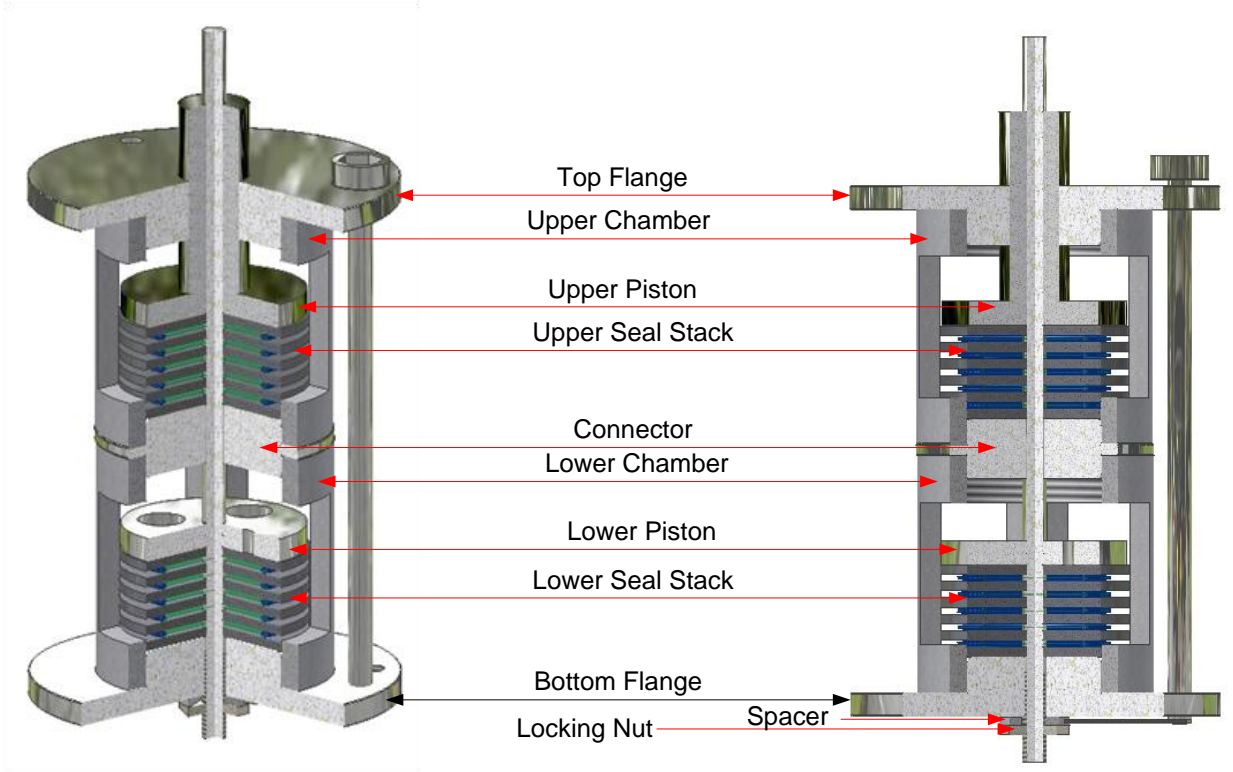


Figure 5.1 Evaluation of U and X from instantaneous and stress relaxation curve. At a given time t , U is the value of the relaxed load and $U + X$ is the load obtained from compressing unstrained samples.



Seals arranged in series to form a stack



Spacer to obtain desired compression of the seals

Figure 5.2 Illustration of quarter-section view of the CSR fixture and other components.

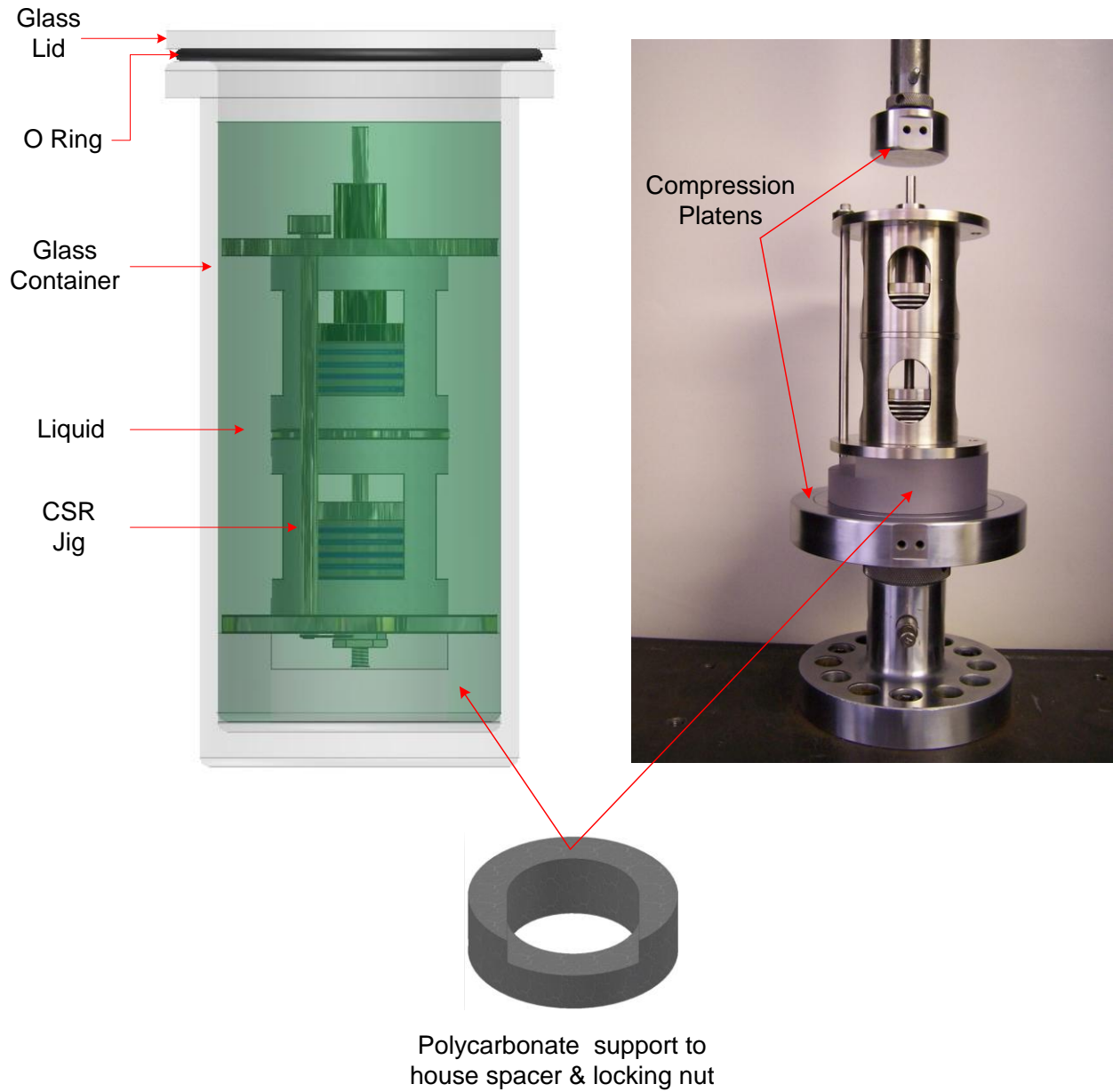


Figure 5.3 Illustration of the fixture placed on a polycarbonate support and immersed in the liquid for aging. Also showing the fixture placed between compression platens in an Instron load frame.

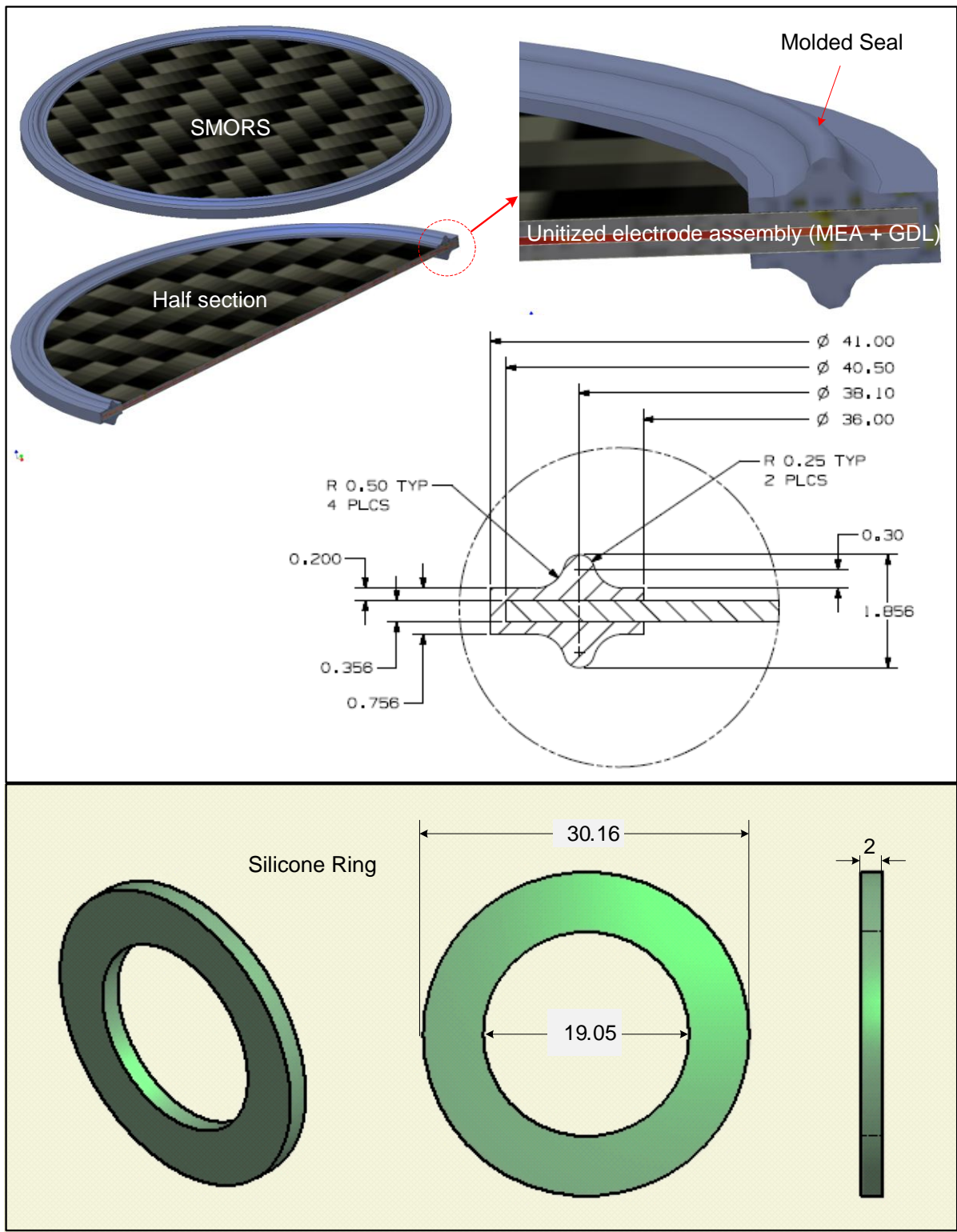


Figure 5.4 Illustration of molded seal (SMORS) and silicone rings with dimensions.

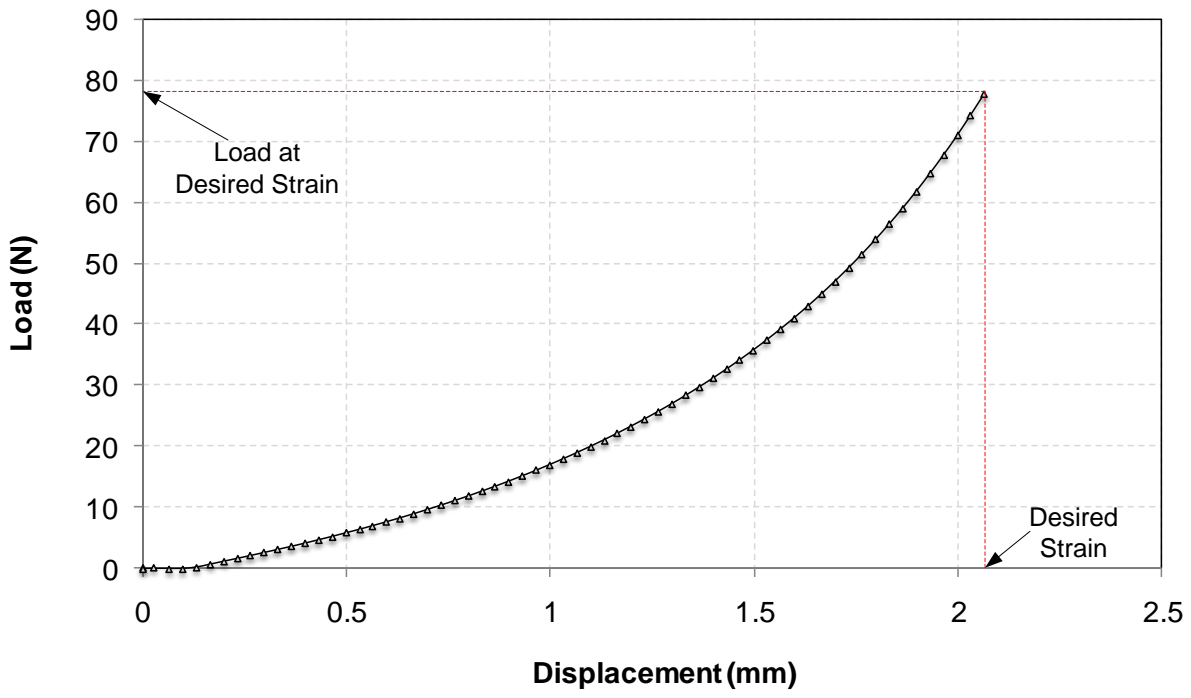


Figure 5.5 Typical load versus displacement behavior of seals obtained from compressing the upper stack.

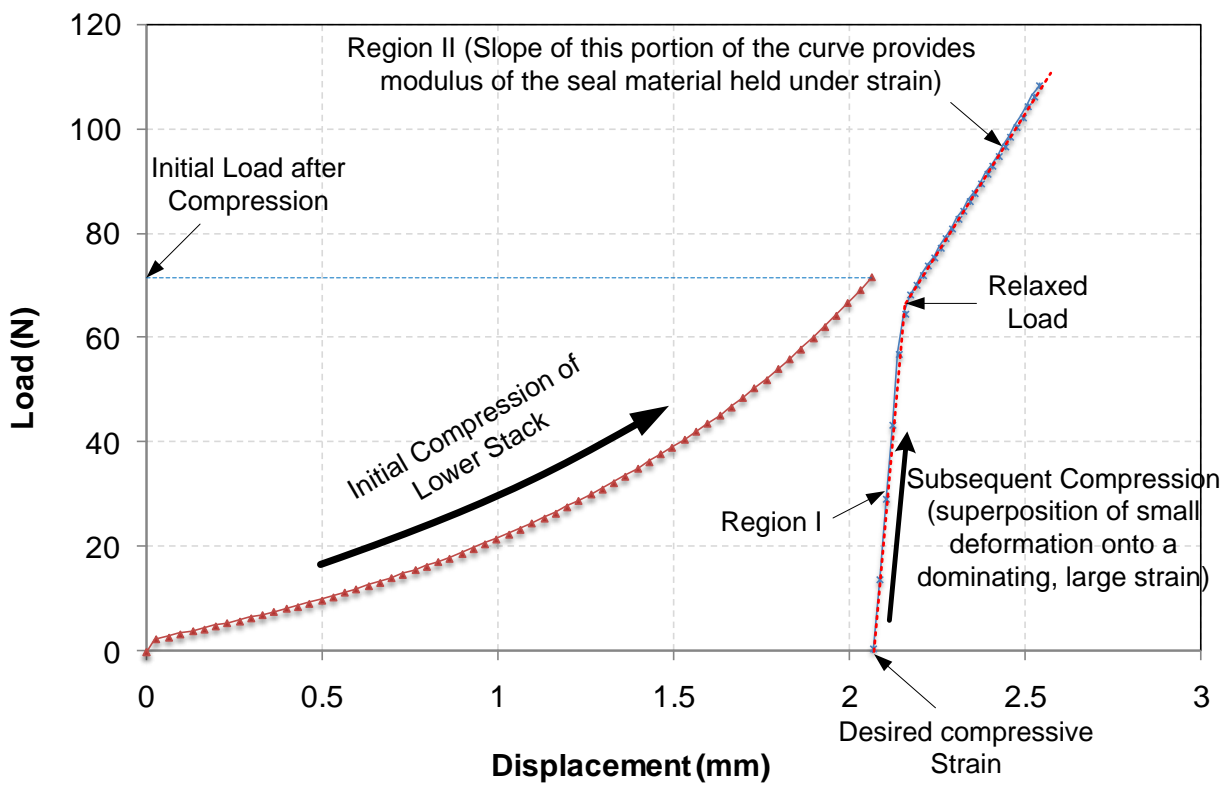


Figure 5.6 Typical load versus displacement behavior of seals obtained from compressing the lower stack. The value of relaxed load, due to stress relaxation, as well momentary properties of the seal can be obtained as a function of time.

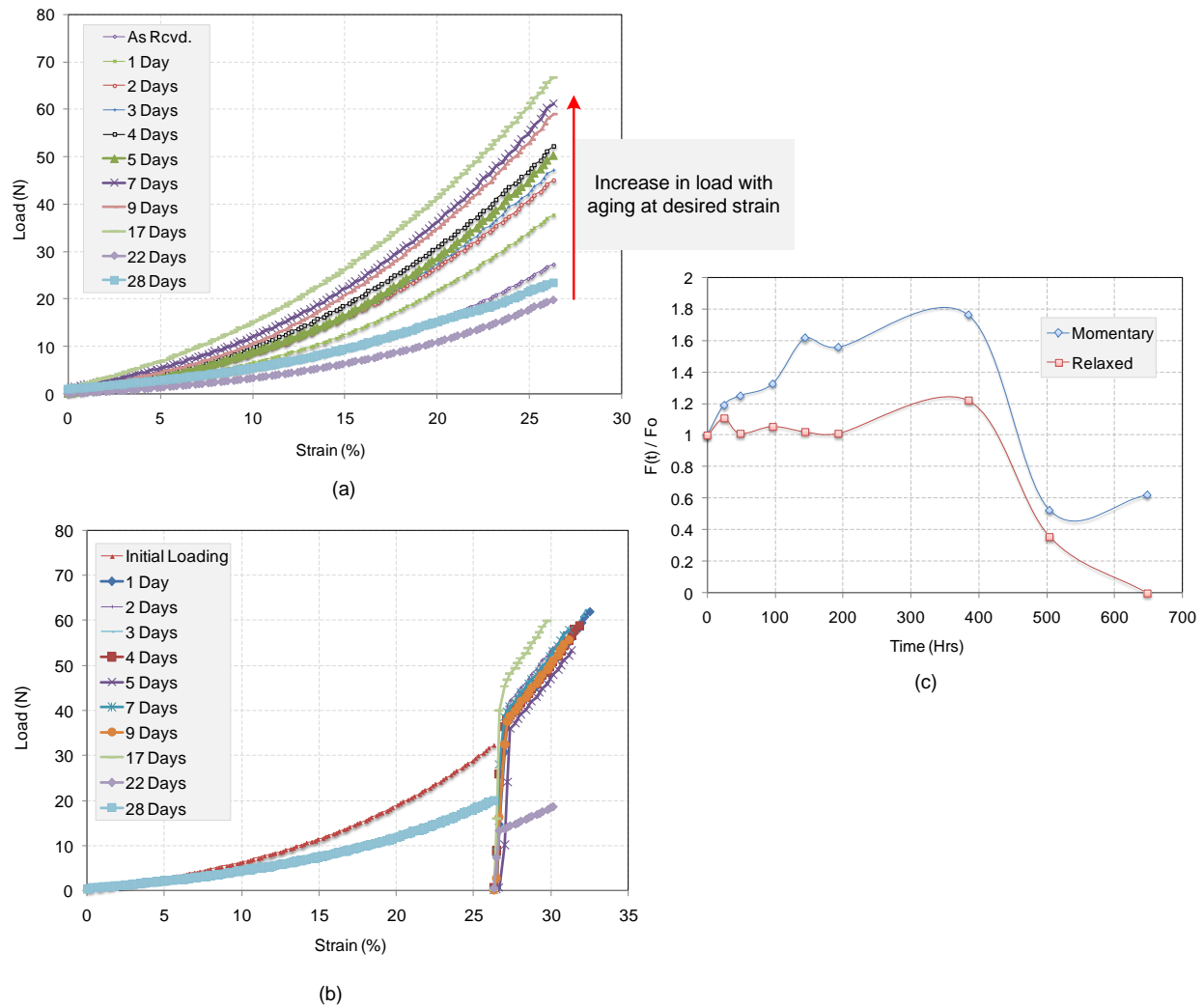
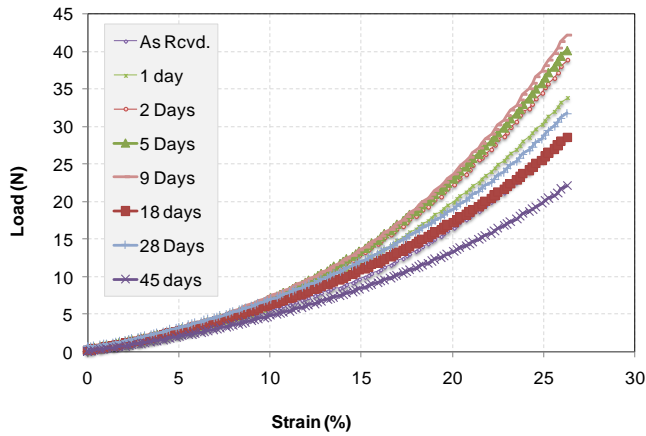
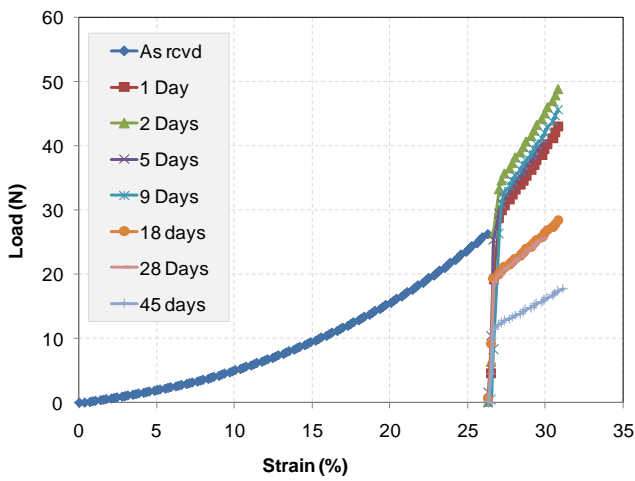


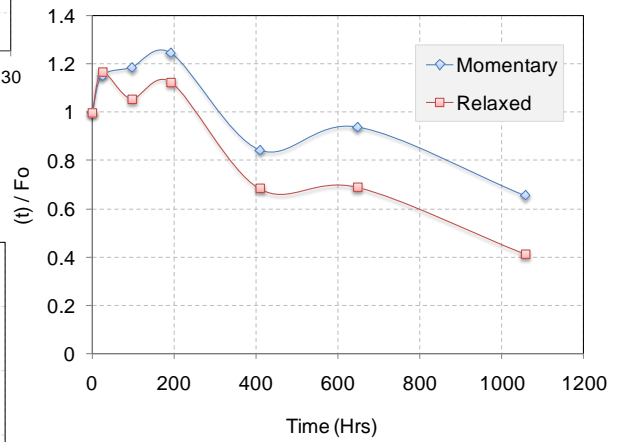
Figure 5.7 Load-displacement data from (a) upper and (b) lower SMORSs stack obtained after different aging times in air at 120°C. Normalized value of momentary and relaxed loads at different aging time is shown in (c).



(a)

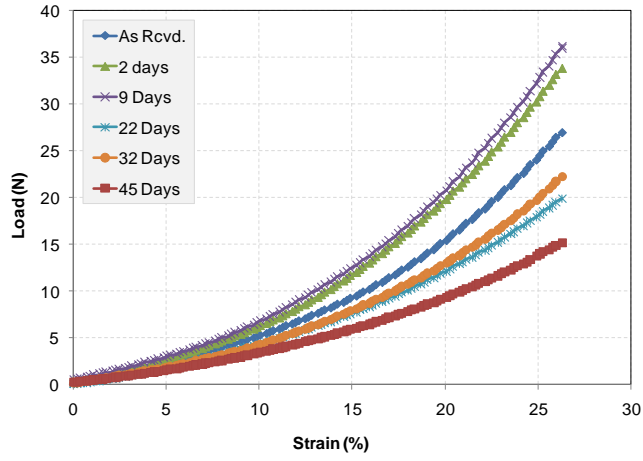


(b)

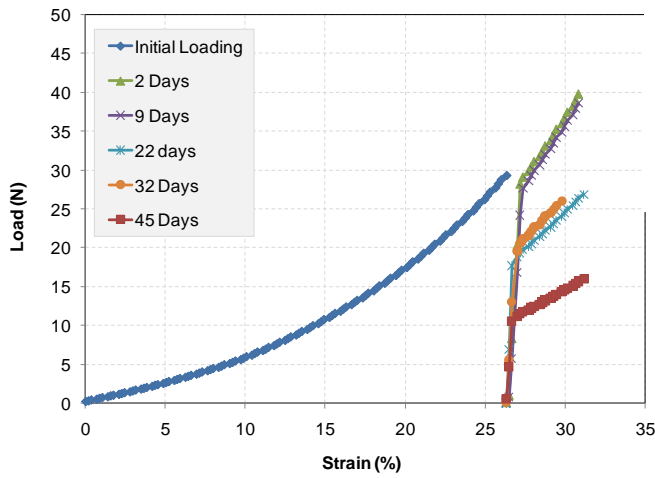


(c)

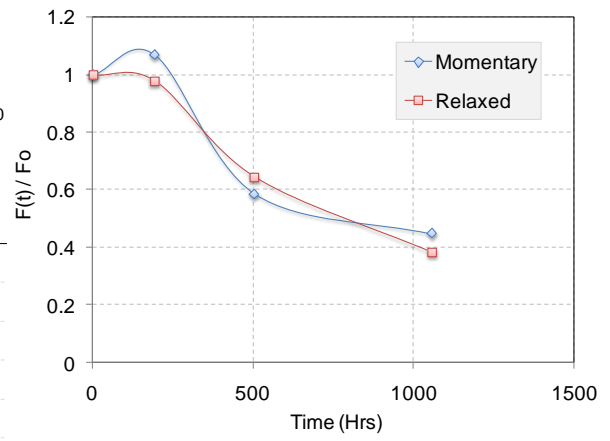
Figure 5.8 Load-displacement data from (a) upper and (b) lower SMORSSs stack obtained after different aging times in air at 90°C. Normalized value of momentary and relaxed loads at different aging time is shown in (c).



(a)

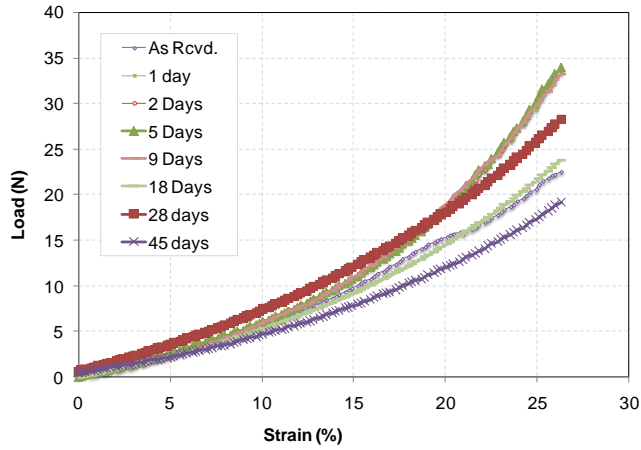


(b)

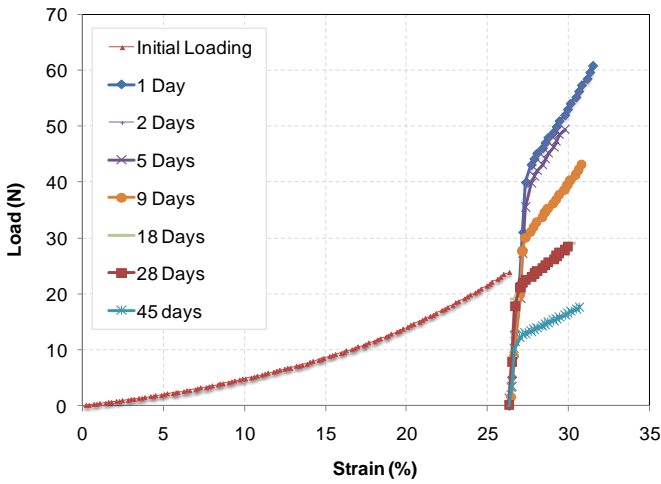


(c)

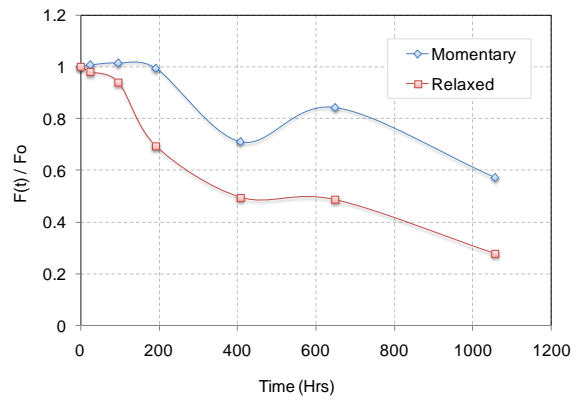
Figure 5.9 Load-displacement data from (a) upper and (b) lower SMORSs stack obtained after different aging times in air at 60°C. Normalized value of momentary and relaxed loads at different aging time is shown in (c).



(a)

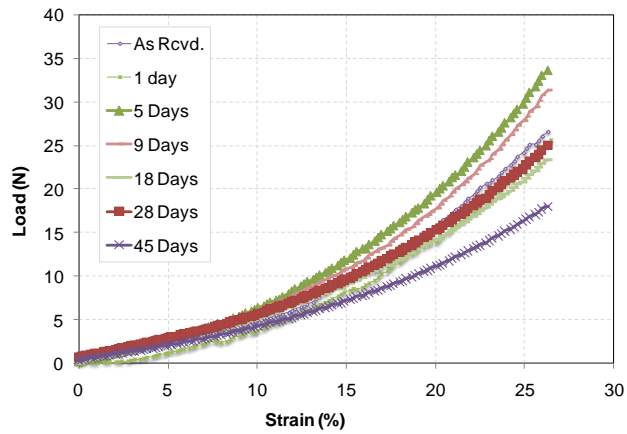


(b)

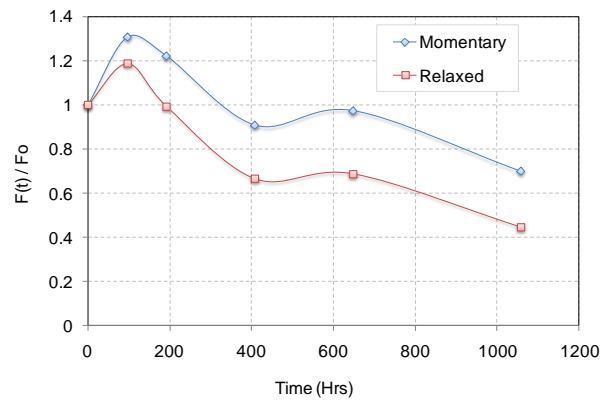


(c)

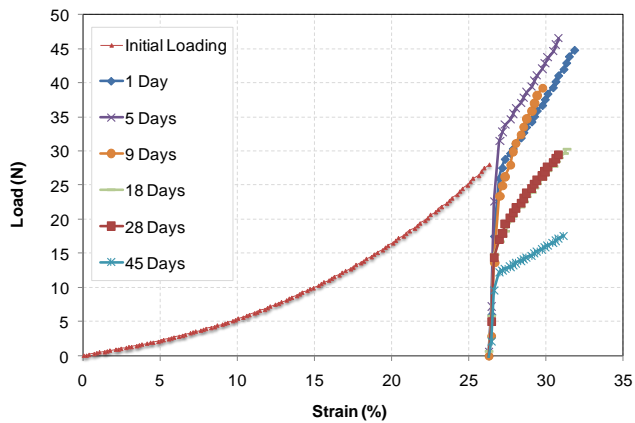
Figure 5.10 Load-displacement data from (a) upper and (b) lower SMORSs stack obtained after different aging times in DI Water at 90°C. Normalized value of momentary and relaxed loads at different aging time is shown in (c).



(a)

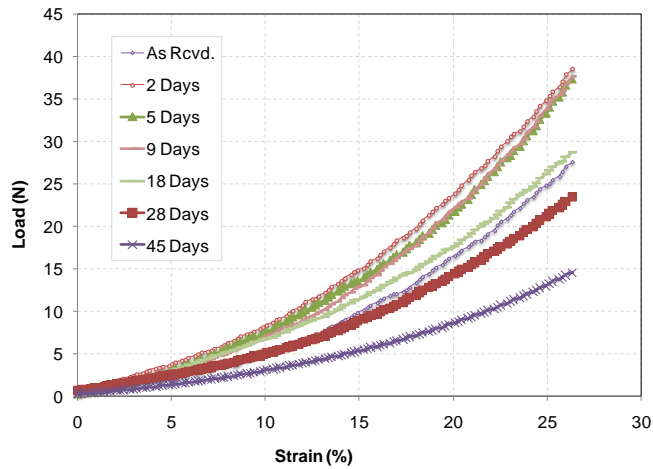


(c)

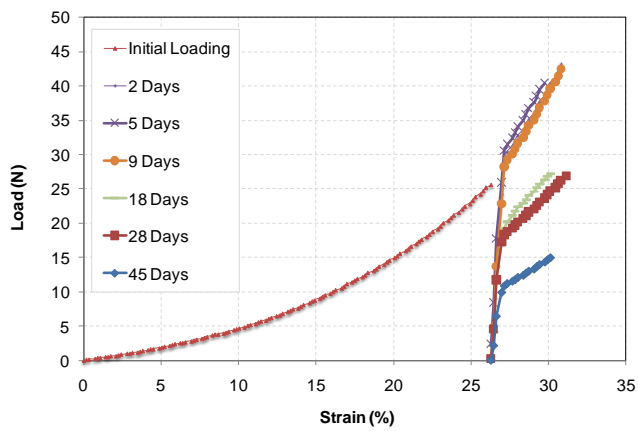


(b)

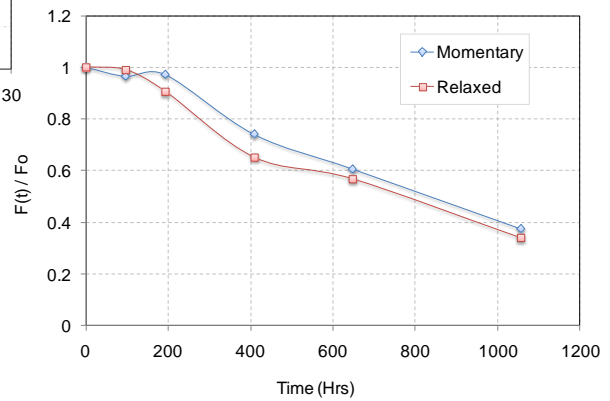
Figure 5.11 Load-displacement data from (a) upper and (b) lower SMORSs stack obtained after different aging times in 50/50 v/v ethylene glycol solution at 90°C. Normalized value of momentary and relaxed loads at different aging time is shown in (c).



(a)



(b)



(c)

Figure 5.12 Load-displacement data from (a) upper and (b) lower SMORSSs stack obtained after different aging times in 0.1M sulfuric acid solution at 90°C. Normalized value of momentary and relaxed loads at different aging time is shown in (c).

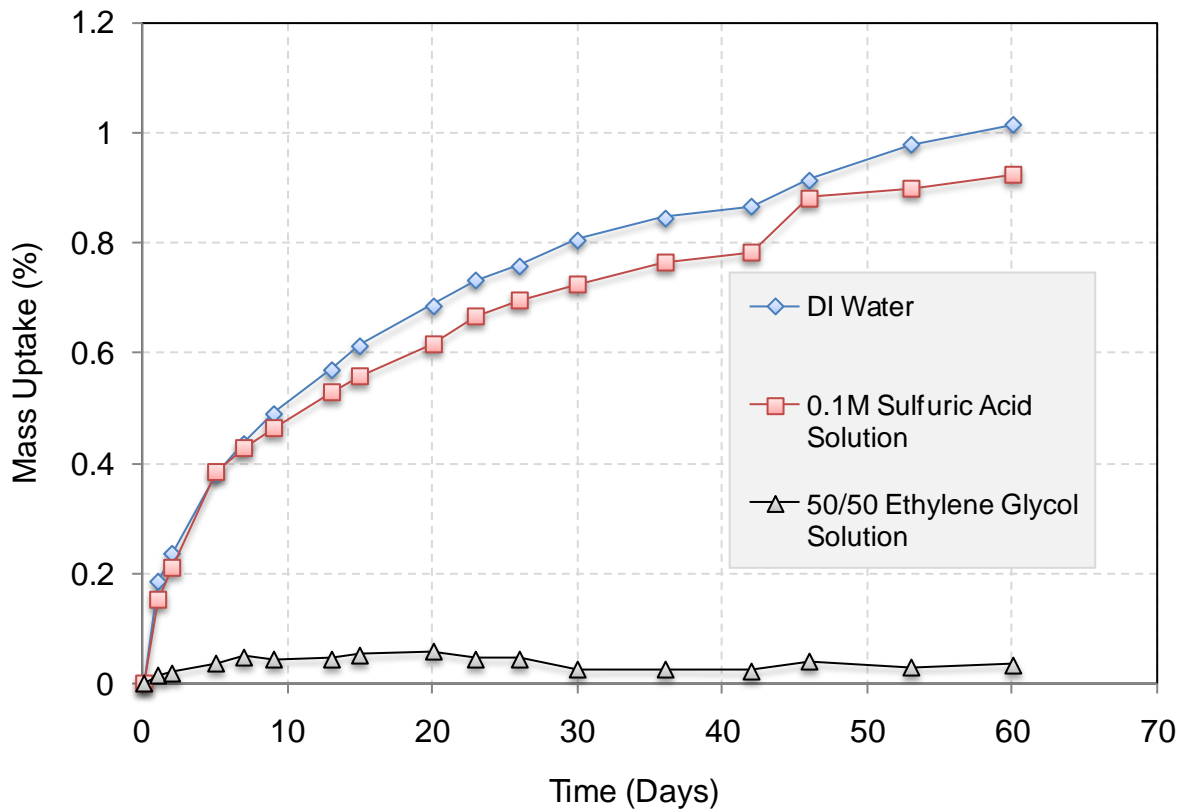
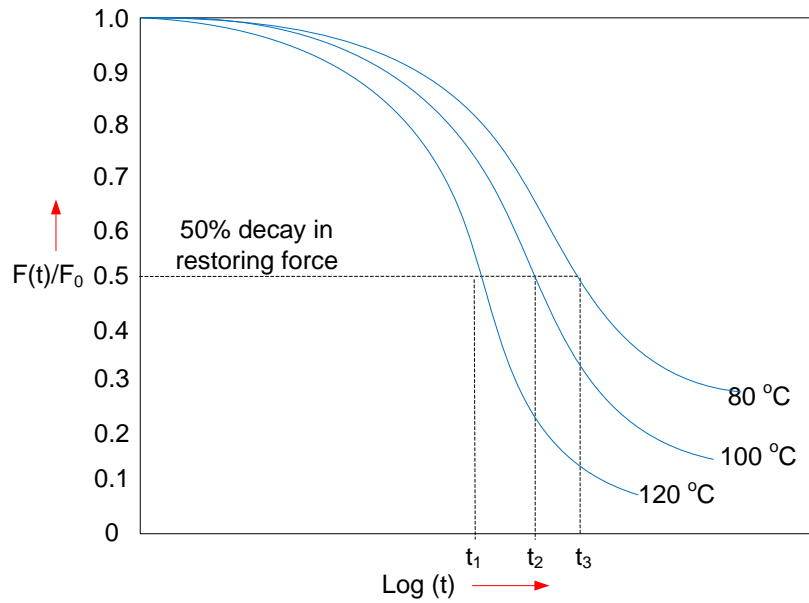
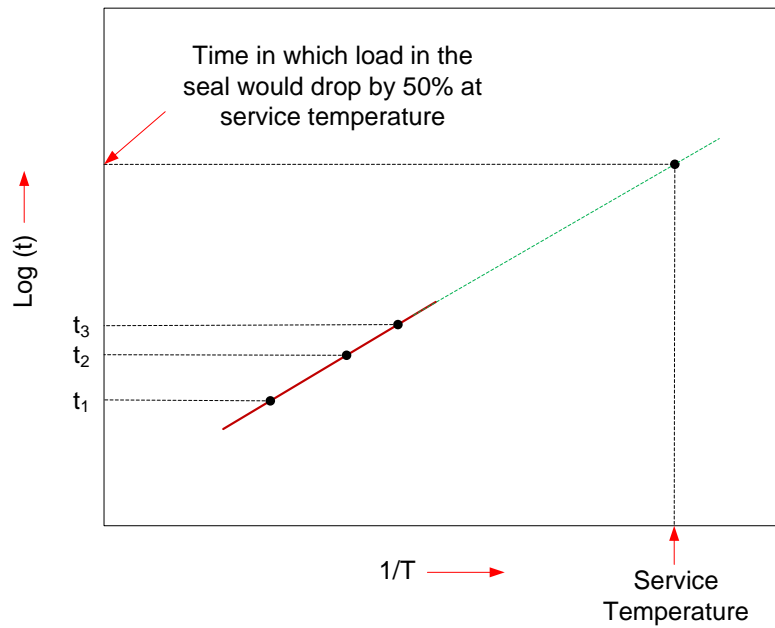


Figure 5.13 Mass uptake results at 90°C for seal material used for SMORS. DI Water and 0.1M sulfuric acid solution show significantly higher mass uptake as compared to ethylene glycol solution.



(a)



(b)

Figure 5.14 (a) Restoring force decay with time at different temperatures, and (b) shows typical Arrhenius approach to predict seal life at a desired temperature for a 50% drop in restoring force.

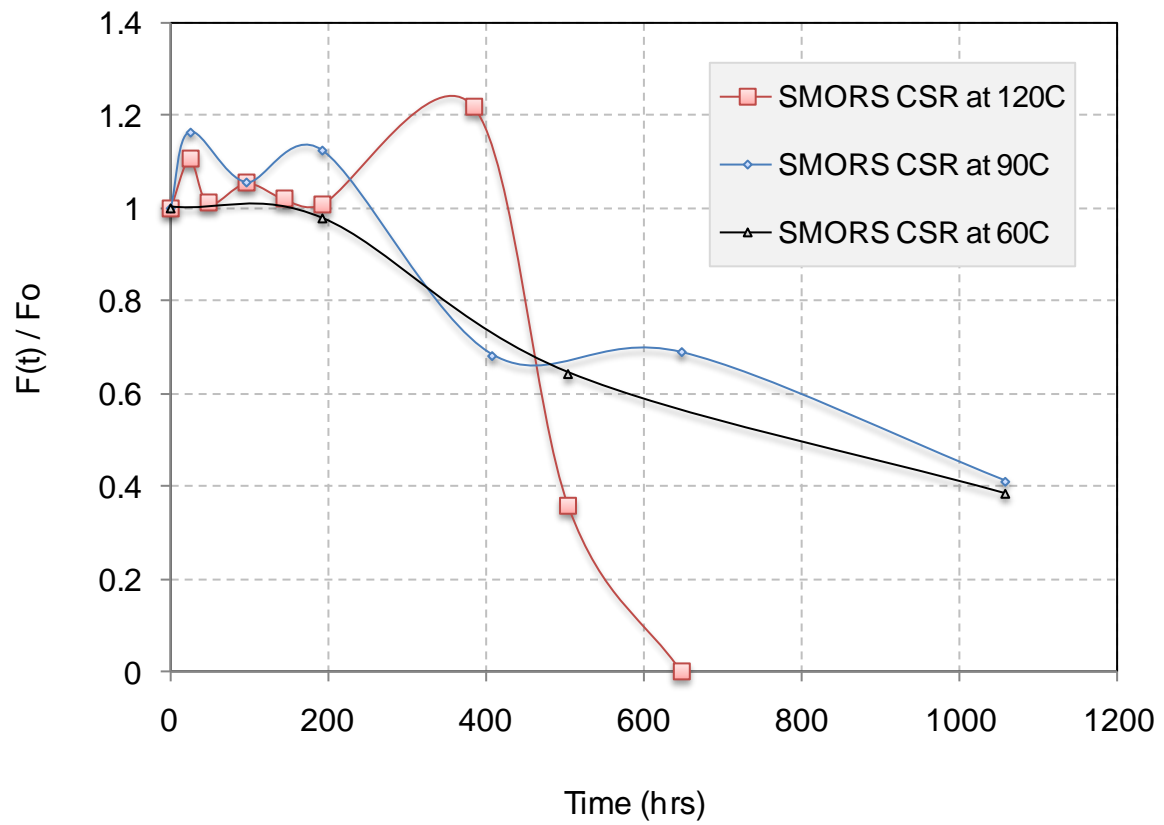
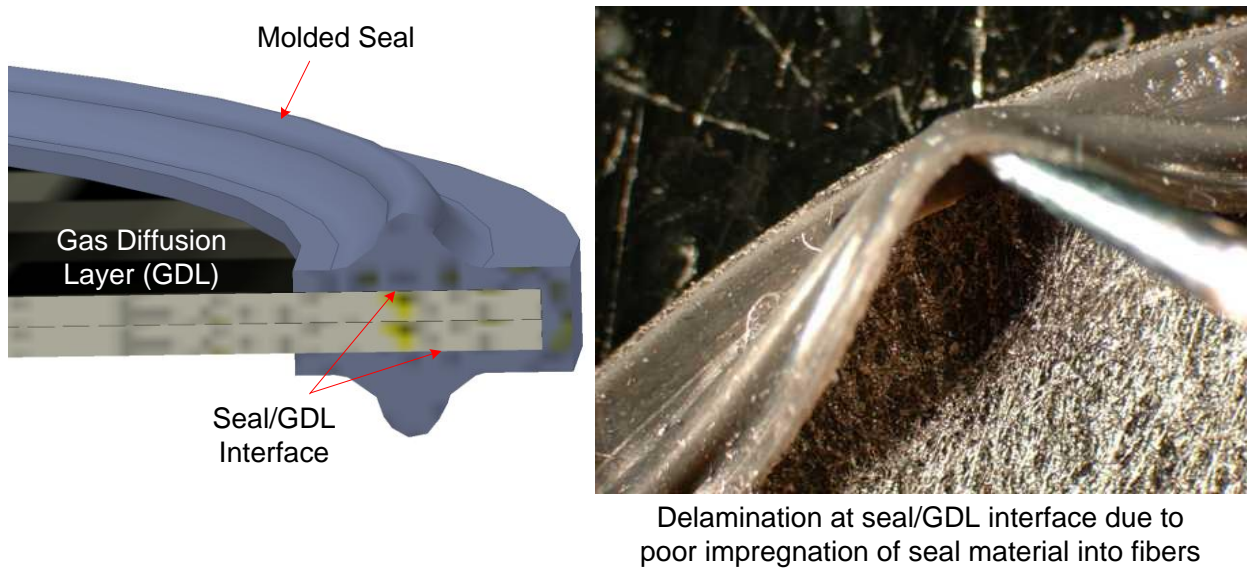


Figure 5.15 Compression stress relaxation behavior of SMORS at 120°C, 90°C and 60°C in air.

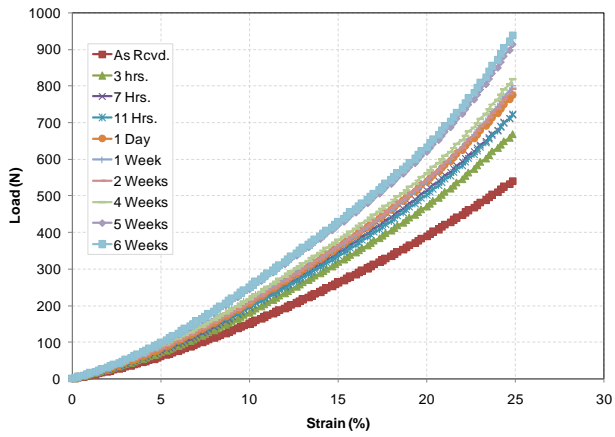


(a)

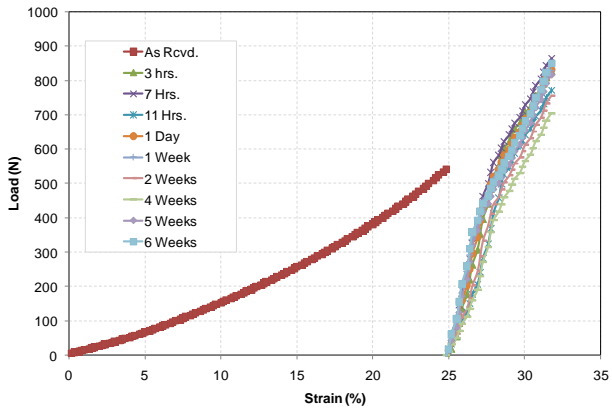


(b)

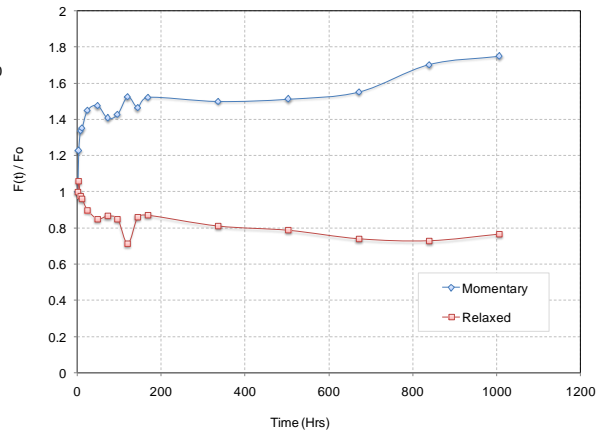
Figure 5.16 Illustration of SMORS failure either due to (a) seal material degradation or (b) poor impregnation of seal material into GDL fibers.



(a)

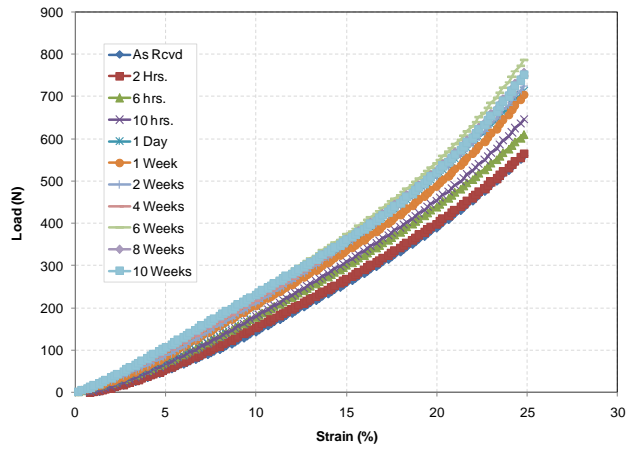


(b)

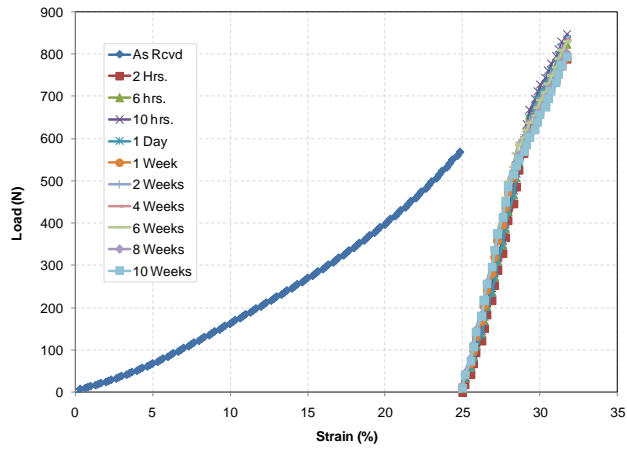


(c)

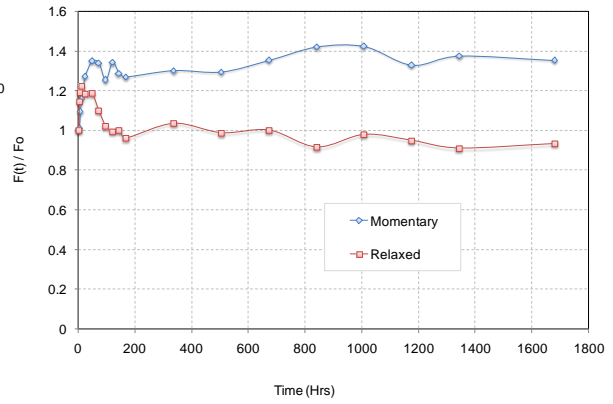
Figure 5.17 Load-displacement data from (a) upper and (b) lower silicone rings stack obtained after different aging times in air at 120°C. Normalized value of momentary and relaxed loads at different aging time is shown in (c).



(a)

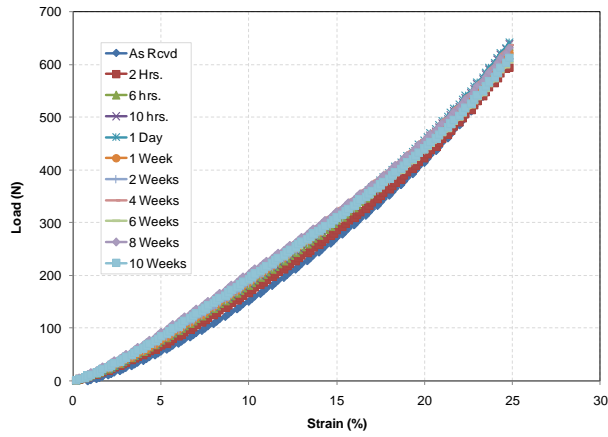


(b)

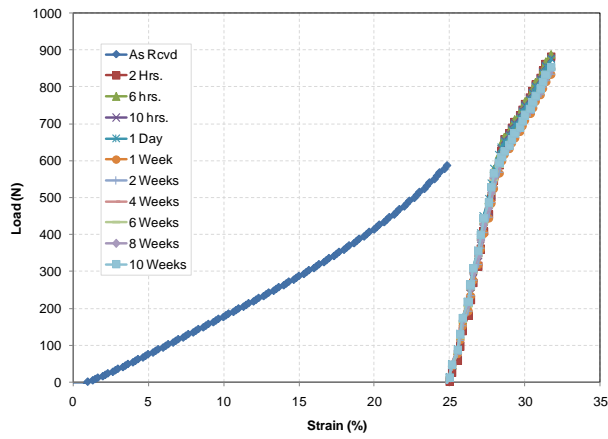


(c)

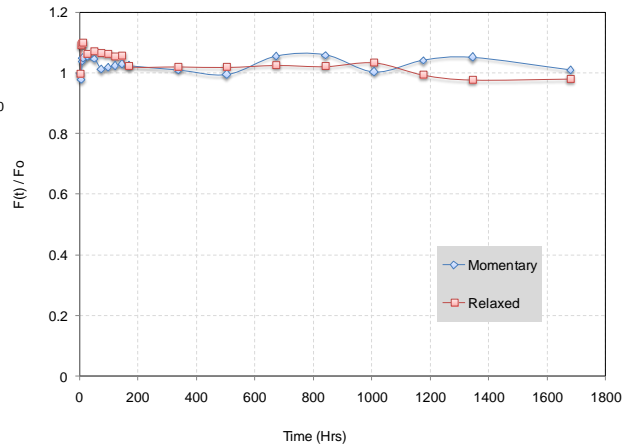
Figure 5.18 Load-displacement data from (a) upper and (b) lower silicone rings stack obtained after different aging times in air at 90°C. Normalized value of momentary and relaxed loads at different aging time is shown in (c).



(a)

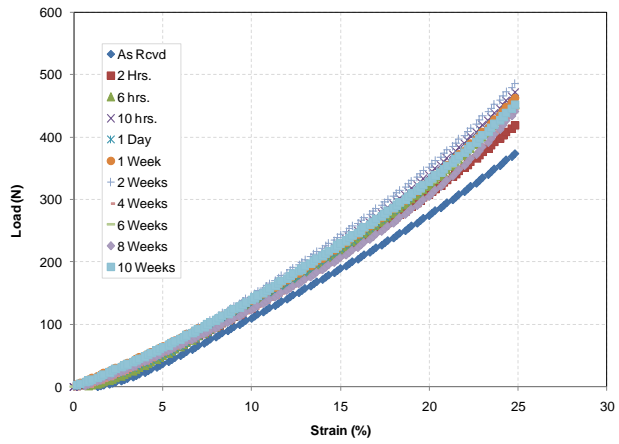


(b)

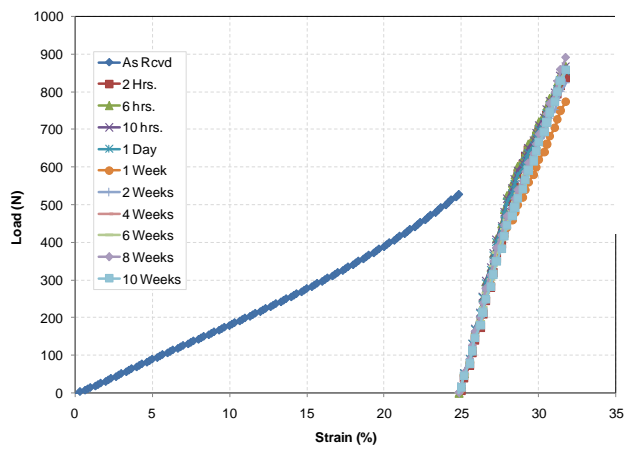


(c)

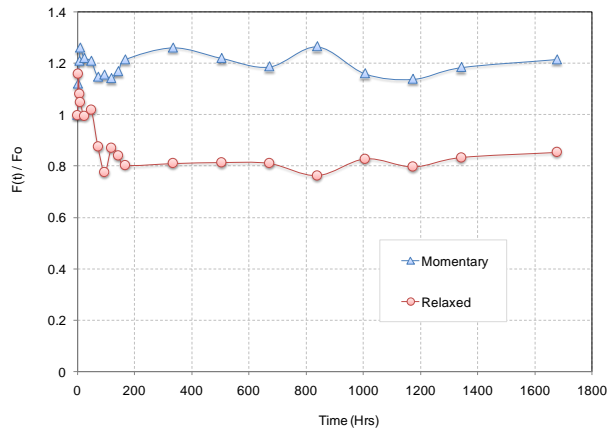
Figure 5.19 Load-displacement data from (a) upper and (b) lower silicone rings stack obtained after different aging times in air at 60°C. Normalized value of momentary and relaxed loads at different aging time is shown in (c).



(a)



(b)



(c)

Figure 5.20 Load-displacement data from (a) upper and (b) lower silicone rings stack obtained after different aging times in DI water at 90°C. Normalized value of momentary and relaxed loads at different aging time is shown in (c).

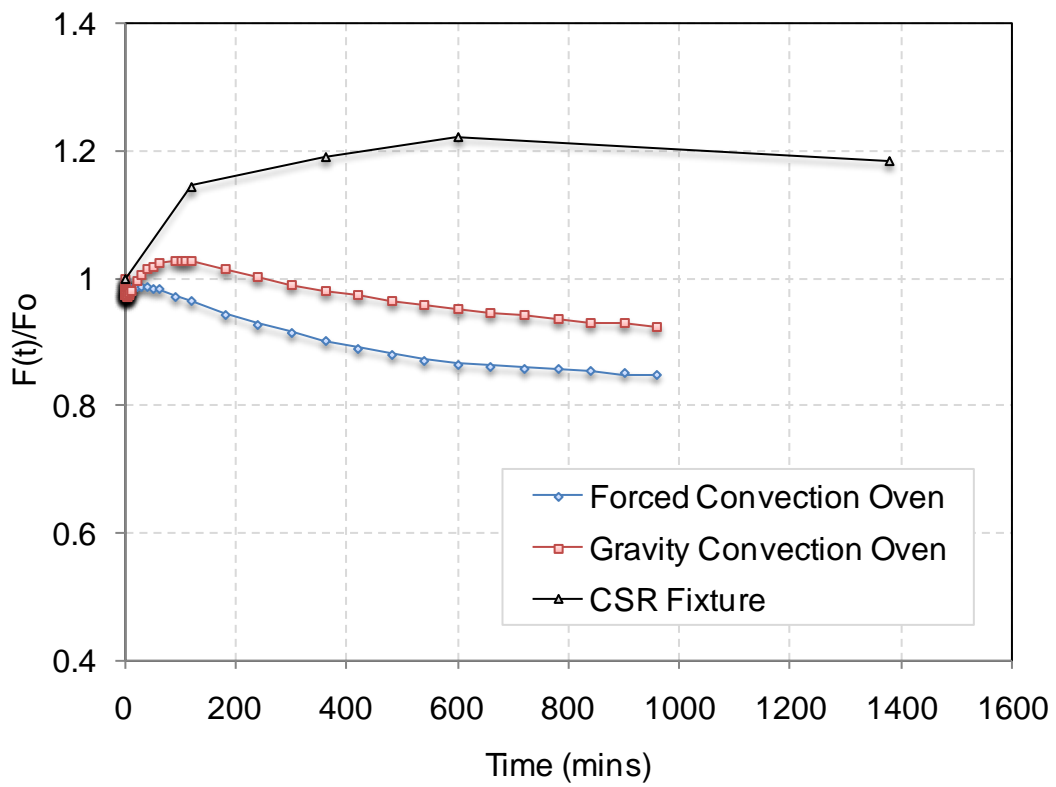


Figure 5.21 Difference in stress relaxation behavior for silicone rings tested in forced and gravity convection ovens at 90°C. Also shown is the result obtained from the CSR fixture tested periodically.

6 Finite Element Characterization of Seal Design

Finite element analysis is widely used to obtain approximate numerical solutions to boundary value problems. Finite element analysis tools, such as ABAQUS, can be used to predict the response of a system when subjected to external loading conditions. Elastomeric seals are used for a variety of applications where they are subjected to compressive loads, static or dynamic in nature, in the presence of environments. The stress-strain and the contact pressure distribution resulting from the seal compression are good indicators of a seal's performance, as well as of its sealing characteristics[1]. During compression of an elastomeric seal, tensile stress in the interior region and on the outside surface of the seal may cause a failure by propagating a pre-existing flaw or crack due to the opening nature of these tensile stresses[2]. A thorough understanding of the local stress state within generic seal profiles may be useful for optimization of the seal design so as to minimize stresses that may lead to seal failure. Results obtained from finite element analysis can be compared with experimental data to check the accuracy of the solution obtained.

6.1 Seal Stress Analysis

To simulate seal compression between two bipolar plates in a fuel cell assembly, a two-dimensional, non-linear, axisymmetric analysis was performed using ABAQUS[3], a commercially available finite element software package. Two seal cross-sections, an O-ring and the SMORS configuration, were considered in the analysis. The seal was meshed with four-node reduced-integration axisymmetric quadrilateral elements, CAX4R, with hybrid formulation. A master-slave relationship was established between the compression platen and seal, respectively to prevent the rigid platen from passing through the seal as it progressively compresses the seal during each computational iteration. Interaction between the compression platens and the seal was established to allow for direct surface-to-surface contact. In order to investigate the effect of

interfacial friction between seal and compression platens on the stress/strain profile, the friction coefficient between compression platen and seal material was assumed to be $\mu = 0$ (frictionless) and 0.3 (rough) (value provided by the sponsor for friction between seal material and bipolar plates). Fixed boundary conditions were used at the lower compression platen while a displacement ramp was given to the top compression platen such that the top platen moves down by a fixed distance in the axial direction, compressing the seal against the bottom platen to achieve the desired strain. Furthermore, a parallel-face boundary condition was established between top and bottom compression platens to prevent any rotation during simulation. A schematic of the applied boundary conditions is also illustrated for O-ring in Figure 6.1. The final deformed shape along with the spatial displacement, stress, strain, contact stress, and contact width distribution, was generated. Table 6.1 outlines the plan for the finite element analysis for various $\frac{R}{r}$ ratios, where R represents the distance of the center of the seal from axis and r is the diameter of seal cross-section, as illustrated for O-ring in Figure 6.1. When a seal bead is laid out on MEA or any substrate, it may follow a path where the bead has varying curvature represented by the ratio $\frac{R}{r}$. Lower the $\frac{R}{r}$ ratio, the higher is the curvature of the seal at a given location which may result in lower value of contact stress where leakage may occur.

In order to characterize seal material response and to satisfy the input requirements of hyperelastic material models in ABAQUS®, stress-strain data from uniaxial tension tests of a hydrocarbon-based fuel cell seal material were used in this study and provided as material input into ABAQUS. Various hyperelastic material models were evaluated in ABAQUS by fitting the material models with the experimental data from uniaxial tensile tests. A least-square fitting procedure was used to determine the coefficients for the selected model. Improper fit between

the model and test data indicates an unsuitable material model. Figure 6.2 shows a plot of experimental data and predicted uniaxial behavior and Figure 6.3 provides information on stability of material models and constants generated from ABAQUS evaluation. It was observed that the two-parameter Ogden model and neo-Hookean models correlate very closely with the uniaxial test data and may also be used for analyzing uniaxial compression up to 50% strain. A two-parameter Ogden model was used in this study to further analyze seal compression between two rigid plates and also to calculate properties such as initial modulus.

6.1.1 O-ring Analysis

Figure 6.5, Figure 6.5, and Figure 6.6 show ABAQUS-generated stress (σ_{11} , σ_{22} , σ_{33}) and strain (ϵ_{11} , ϵ_{22} , ϵ_{33}) profiles from simulation of a frictionless ($\mu = 0$) O-ring under 25% compression for

$\frac{R}{r} = 1, 10 \text{ \& } 100$ respectively. The distribution of the strain, ϵ_{22} , shown in Figures 6.4 (b), 6.5 (b)

& 6.6 (b), is compressive where the plates are touching the O-ring in the deformed state (the region of contact width). Beyond the contact width, b , the strain is tensile in nature. Also interesting to note is the tensile nature of stresses in the 1 and 3 direction, as shown for σ_{11} and σ_{33} . The presence of tensile stresses (or strains) on the outside surface may be detrimental in the presence of temperature and aggressive environments. Stress increases the rate of diffusion in a material, which can lead to a reduction in material strength over a period of time. The presence of tensile stresses may make the situation worse because any minor flaw or crack in the material could propagate under these opening stresses[2]. Also, the stress/strain distribution is more symmetric as expected as the ratio of R/r increases.

The sealing capability of an elastomeric O-ring seal depends on the contact stresses that develop between the O-ring and the surfaces with which it comes into contact. An illustration of

contact stress (σ_c) and contact width (b) is shown in Figure 6.7. It has been suggested in the literature[4] that leakage onset occurs when the the peak contact stress, σ_{cmax} , reduces to a value lower than the pressure differential across the seal, p , (i.e., $\sigma_{cmax} \leq p$). Contact stress profiles (σ_c) were generated for the O-ring for rough surface conditions ($\mu = 0.1$), and nominal compression ranging from 5 to 40%. Contact stress profiles were plotted as the nodal stress component versus the x-coordinates (defined as the horizontal distance from the center of the O-ring cross-section to a node along the perimeter), as shown in Figure 6.8. The information on contact width (b), which is the length of the O-ring that touches the retaining surfaces when viewed from the cross-section (the distance between two points on each profile where the contact stress curve intersects the zero stress line) and peak contact stress (σ_{cmax}) versus $\frac{R}{r}$, was extracted from the contact pressure profiles in Figure 6.8, and results are summarized in Figure 6.9. Results in Figure 6.9 indicate that the values of contact width and peak contact stress do not change significantly as the ratio of R/r increases, i.e. as the cross-section of the O-ring gets farther away from the central axis. This is an important observation and may prove to be helpful when seal bead is laid out in a fuel cell stack, such as shown in Figure [5].

6.1.2 SMORS Analysis

It was observed in Figure 6.9 that increasing the $\frac{R}{r}$ ratio greater than 10 does not lead to significant change in contact stresses and contact width, SMORS compression analysis was also carried out for $\frac{R}{r} = 20$ (also realistic to actual SMORS tested in experiments), according to the plan in Table 6.1, to generate stress, strain, contacts stress, and contact width profiles versus compression strain. In order to simplify the analysis and save computational time, only half a

model of the SMORS was analyzed, where the bottom compression platen was removed and a plane of symmetry at the midplane of GDL was used. Fixed boundary conditions were used at the lower edge of the GDL such that no movement was allowed in the 2-direction but permitted in 1-and-3 direction under the applied displacement conditions. Also, top compression platen was replaced by an analytically rigid line which eliminated the need to model both platens in the analysis. Furthermore, a parallel-face boundary condition was established between the analytically rigid line and GDL in order to prevent any rotation during simulation. A schematic of the applied boundary conditions is illustrated for SMORS in Figure 6.10. A typical stress/strain distribution is shown in Figure 6.11 for 25% nominal compression of the seal; the presence of tensile stresses is evident on the outside surface of the seal, similar to what was observed for the O-ring geometry. Again, the presence of these tensile stresses may be detrimental to a seal, especially if surface flaws are present. Due to hygrothermal fatigue (due to temperature cycling in the presence of moist environment in fuel cell unit), the seal material may degrade over time, resulting in reduced tensile strength/tear strength and eventually leading to surface crack propagation[6]. Any leakage due to seal failure may impede the function of a fuel cell stack. It is therefore critical to design seals so as to minimize the level of tensile stresses on the outside surface. Contact stress profiles were also generated for smooth ($\mu = 0$) and rough surfaces ($\mu = 0.3$) for $R/r = 20$, as shown in Figure 6.12, and information on contact width and stresses were extracted. As shown in Figure 6.13, the contact width, b , and peak value of peak contact stress, σ_{cmax} are not significantly different for frictionless and rough surfaces, indicating that friction does not play a significant role in the distribution of contact stresses and width when a SMORS is compressed.

6.2 Contact Mechanics of Elastomeric Seals

When an elastomeric seal is installed and compressed, the contact configuration is generally regarded as Hertzian contact[7]. In this case, the contact pressure profile along the horizontal direction of a seal's cross-section becomes a parabola, which is the well-known Hertz pressure distribution. By adopting Hertzian contact, Lindley [4, 8] derived an empirical relationship between a compressive force and fractional compression for a bonded rubber block of circular cross-section:

$$F = 2\pi R \cdot 2r \cdot E_c (1.25C^{1.5} + 50C^6) \quad (6.1)$$

where F is the total compressive load, $2R$ and $2r$ are the mean and cross-section diameters, respectively, C ($= x/d$ where x is the diametric compression) is the fractional compression, and E_c is the effective compression modulus. The elastic modulus of the compression platen material was regarded to be infinite when compared with that of the seal. The material of the seal was also regarded as incompressible (i.e., Poisson ratio, $\nu = 0.5$). Using Equation 6.1 and Hertz theory[7], the contact width, b and the peak contact stress (the highest value of the Hertz pressure profile), $\sigma_{c \max}$ can be obtained by:

$$b = d \sqrt{\frac{6}{\pi} g(c)} \quad (6.2)$$

$$\sigma_{c \max} = E_c \left[\frac{16}{6\pi} g(c) \right]^{\frac{1}{2}} \quad (6.3)$$

where $g(c) = 1.25C^{1.5} + 50C^6$. Dragoni and Strozzi [9] analyzed the problem of O-ring compression using finite element analysis method and proposed a modified relationship given as:

$$b = \frac{3}{2} d C^{\frac{2}{3}} \quad (6.4)$$

$$\sigma_{c \max} = E_c \left[\frac{10}{3\pi} \right]^{\frac{1}{2}} C^{\frac{3}{4}} \quad (6.5)$$

For use with equations 6.3 and 6.5, the effective compression modulus, E_c , is given as[10]:

$$E_c = E \cdot (1 + 2K \cdot S^2) \quad (6.6)$$

where $E = \frac{3}{2}(\mu_1 \times \alpha_1)$ is the small-strain tensile modulus calculated from Ogden material coefficients μ_1 and α_1 provided in Figure 6.3 (b), K is the numerical factor depending on the hardness of the seal material and goes from 0.9 for 30 Shore A to 0.5 for 75 Shore A, and S is the shape factor given as:

$$S = \text{loaded Area} / \text{force-free Area} \quad (6.7)$$

and may be defined for the O-ring by an approximate relationship given as:

$$S = \frac{2\pi \cdot R \cdot b}{2 \times \int_{-\frac{\pi}{2}}^{\frac{\pi}{2}} 2\pi(R + r \cdot \text{Cos}\theta) \cdot d\theta} \quad (6.8)$$

where b is the contact width and R is the mean radius of the seal cross-section, as illustrated in Figure 6.14 for various common geometries and O-ring. The seal material used here has a Shore A hardness value of 30 (provided by Henkel Corporation). Therefore a value of $K = 0.9$ was used in Equation 4.2 to calculate E_c .

Hertz theory is valid if the contacting bodies are assumed to be semi-infinite when compared with the contact dimensions; the strains in the contact region must be infinitesimal to apply the

theory of linear elasticity; and the contact surface is frictionless. None of these is valid for the O-ring's contact problem. This has previously been discussed[11], but the results showed that the Hertz theory was applicable until fractional compression of up to 25% [4] or 30% [12]. The contact stress and contact width results obtained from FEA analysis on the O-ring were compared with results obtained by using Lindley's and Dragoni's equations. Figure 6.15 shows the comparison results (also summarized in Table 6.2 along with shape factor and compression modulus values) and a good agreement was found between FEA and analytical approaches proposed by Lindley and Dragoni.

6.3 Theoretical & Experimental Validation of Finite Element Results for SMORS

From experimental testing of SMORS, load versus displacement profiles were obtained, as shown and discussed in chapter 3. Load versus displacement profiles were also generated using Lindley's formula (Equation 6.1) and the FEA method so comparison could be made with experimental data for validation. The total force for a given compression of the seal was calculated from contact width and peak contact pressure profile obtained from FEA, according to the following equation:

$$F_{FEA} = \int_{-\frac{b}{2}}^{\frac{b}{2}} 2\pi(R+x) \cdot \sigma_c(x) \cdot dx \quad (6.9)$$

where is $\sigma(x)$ the parabolic pressure distribution at the contact width given as:

$$\sigma_c(x) = \sigma_{max} \left(1 - \frac{4}{b^2} x^2 \right) \quad (6.10)$$

and illustrated in Figure 6.16. Load values thus obtained from the FEA analysis, the Lindley approach, and the experimental results were plotted against % compression of the seal. Results

provided in Figure 6.17 show a very good agreement between Lindley's approach and the experimental data up to 25% compression, whereas the FEA method shows reasonable agreement with experimental data up to 10% compression of the seal. For more than 10% compression of the seal, the FEA results overestimate the load values. This may be attributed to a number of reasons related to assumptions made during axisymmetric modeling of SMORS in ABAQUS. In order to explain the FEA results in light of the comparison shown in Figure 6.17, it is important to discuss SMORS in detail so that the differences in experimental testing of real geometry and the simplified model analyzed in ABAQUS can be outlined. As discussed earlier, SMORS stands for sub-scale molded o-ring seal where seal material is molded onto two porous gas diffusion layers (GDL) made of graphite fibers (fiber volume fraction approximately 0.3). During molding process, the seal material was required to impregnate the GDL all along the perimeter (area under seal web) so that mechanical interlocking could be established to prevent relative slipping between GDL and seal web. Such an assembly was desired so that conditions for a fuel cell application could be mimicked. In a PEM FC stack, two outer GDL layers would sandwich a cathode-membrane-anode assembly (on which a seal material is molded), an illustration of which is shown in Figure 6.18. In absence of a cathode-membrane-anode assembly, two GDL layers with seal molded outside, illustrated in Figure 6.19 (a), was tested in compression to obtain load versus displacement data. The geometry of the SMORS analyzed in ABAQUS is shown in Figure 6.10 (b), where several assumptions were made to simplify the model and provide stability during analysis. These assumptions are as follows:

6.3.1 No-slippage between seal and GDL

In the ABAQUS modeling, no slippage was assumed at the seal/GDL interface. However, it was found during post-analysis of seals failed during CSR testing that adequate impregnation of GDL

layers was not achieved during molding, as shown in Figure 6.19 (b), which may lead to delamination. Such delaminations at the seal/GDL interface would reduce the load at a given compression during testing. If slippage is allowed at the seal/GDL interface in ABAQUS, significant sliding and lifting of the seal web was observed, as shown in Figure 6.20, resulting in an instability in the model and questionable values of contact pressure and width.

6.3.2 Single GDL with Fixed Boundary Conditions

In ABAQUS modeling, only one GDL layer was assumed as opposed to the two GDL layers present in each SMORS with a very fine gap in between where seal material tends to flow during the molding process. The presence of two GDL layers instead of one, adds one more interface at which sliding may occur, leading to reduced load values measured during experimental testing. Also, fixed boundary conditions were applied to the GDL preventing its movement and rotation in all direction. However, compression of SMORS during the experiment may result in bending, rotation, and crushing of the GDL, as shown in Figure 6.21, which may possibly result in additional sliding at interfaces in a SMORS. Such assumptions in ABAQUS modeling may lead to higher load values than obtained during the experiment.

6.4 Development of Peak Contact Pressure Profile

Due to stress relaxation in the seal compressed between platens, the initial peak contact pressure should decay with time. As illustrated in Figure 6.22, maintaining the peak contact pressure greater than the pressure differential across the seal is important to prevent gas leakage. To develop a long-term peak contact pressure profile and to estimate its value at a given time, time dependent properties, such as modulus decay with time typically obtained from stress relaxation tests, may be used as an input into ABAQUS modeling. When complex seal cross-sections are involved, such as the one studied here, and building a robust finite element model is difficult, an

alternative theoretical approach may be used provided the approach correlates well with experimental results. Based on the results discussed above, it is evident that Lindley's analytical approach showed good correlation with experimental results, and if used in conjunction with compression stress relaxation (CSR) data, may be helpful in developing the long-term pressure profile to predict the decay in peak contact pressure with time. If decay in the modulus of the seal material with time, $E(t)$ versus t , can be obtained from CSR tests in a given environment, decay in peak contact stress with time may be estimated by using Lindley's approach such that:

$$\sigma_{\text{cmax}}(t) = E(t) \left[\frac{16}{6\pi} g(c) \right]^{\frac{1}{2}} \quad (6.11)$$

where modulus E_c in equation 6.3 is replaced by the time-dependent modulus, $E(t)$.

6.5 Conclusion

For the purpose of understanding the deformation behavior of an elastomeric seal and its sealing performance, finite element characterization of representative seal cross-sections was carried out. Uniaxial test data obtained from experiments was used as material property in ABAQUS and several known hyperelastic material models were evaluated. It was found that the two-parameter Ogden or Neo-Hookean models correlated well with experimental results and also exhibited stability in other modes of seal deformation, such as uniaxial compression, shear etc. For simplicity and robustness, the two-parameter Ogden model was selected to carry out seal analysis under compression. The O-ring cross-section was first studied to understand the stress-strain distribution and to develop the contact stress and contact width profiles for a range of compression and how they are affected by the seal's radius of curvature. Symmetric stress/strain distribution and insignificant change in values of contact width and peak contact stress were

observed as the curvature of the seal increases ($\frac{R}{r} \geq 10$). This observation may be helpful when the seal bead is laid out on a substrate for certain application. A simple analysis conducted on an O-ring configuration proved to be helpful prior to analyzing a complex assembly such as SMORS, where several interfaces and boundary conditions are involved. In order to simplify the modeling process for SMORS, a ratio of $\frac{R}{r} \geq 20$ was selected (corresponds to SMORS tested in CSR experiments) and axisymmetric analysis was conducted on simplified SMORS model. Stress/strain profiles were generated to visualize their distributions within the seal cross-section. Frictionless and rough interfacial conditions between seal material and platens were assumed, but their effect on contact width and peak contact pressure was insignificant. Therefore, further analysis was carried out assuming frictionless conditions at the seal/platen interface.

The finite element model developed for seal analysis was validated through comparison with a contact mechanics approach and experimental data. Load versus displacement (or % compression) results from ABAQUS, Lindley's approach, and experiments were compared and it was found that Lindley's equation correlates well with experimental data whereas ABAQUS overestimates the load values at a given compression. Lindley's approach may also be used to develop contact pressure profiles that may help estimate peak contact pressures at a given time so leaking can be avoided. Assumptions made in ABAQUS to provide stability and simplifying the modeling of the complex SMORS assembly resulted in overestimating the load values and better estimates may be obtained if:

1. Improved samples could be developed where slipping at the seal/GDL interfaces in SMORS could be avoided by achieving uniform impregnation of seal material into the GDL. This can be achieved by using a multi-point injection mold rather than single point

injection one, which is currently used. Good impregnation of GDL layers may also eliminate GDL crushing during compression of the seal.

2. One GDL layer is used instead of two.
3. If seal material relaxation behavior is of primary concern, the GDL in SMORS assembly may be replaced by a single rigid substrate that would not crush, bend or rotate and is bonded to the seal under the web. This will not only provide a rigid support to the seal but also prevent slipping at the seal/GDL interface.

Modification of SMORS based on suggestions provided above may provide improved correlation between finite element analysis and experimental data so that future seal designs can be reliably analyzed using robust FEA models prior to manufacturing.

References:

1. F.H. Theyse. *The Inverse Hydrodynamic Theory and Its Application in the Design of Controlled Leakage Seals between Moving Parts*. in *Proceedings of the third international conference on fluid sealing*. 1967. Cambridge, UK: The British Hydromechanics Research Association.
2. T. Ebisu, M. Yamamoto, H. Maekawa, and A. Onodera. *Fundamental Studies on the Performance of O-Ring for Cask*. in *The 7th International Symposium on Packaging and Transportation of Radioactive Materials*. 1983. New Orleans.
3. I. Green and C. English, "Analysis of Elastomeric O-Ring Seals in Compression Using the Finite Element Method," *Society of Tribologists and Lubrication Engineers-Tribology Transactions*, **35**(1), 83-88, 1992.
4. P.B. Lindley, "Compression Characteristics of Laterally Unrestrained Rubber O-Ring," *Journal of International Rubber Institute*, **1**, 202-213, 1967.
5. M.W. Fowler, *Degradation and Reliability Modeling of Pem Fuel Cells*, in *Chemical Engineering*. 2003, Royal Military College of Canada: Kingston, Canada.
6. M.D. Ellul, *Mechanical Fatigue*, in *Engineering with Rubber: How to Design Rubber Components*, A.N. Gent, Editor. 2001, HanserGardner Publications: Cincinnati. 137-175.
7. K.L. Johnson, *Contact Mechanics*. 1985, Cambridge, UK: Cambridge University Press.
8. P.B. Lindley, "Load-Compression Relationships of Rubber Units," *The Journal of Strain Analysis*, **1**(3), 190-195, 1966.
9. E. Dragoni and A. Strozzi, "Analysis of an Unpressurized Laterally Restrained, Elastomeric O-Ring," *Trans. ASME, Journal of Tribology*, **110**(2), 193-199, 1988.
10. A.N. Gent and P.B. Lindley, "The Compression of Bonded Rubber Blocks," *Proceedings of the Institution of Mechanical Engineers*, **173**(3), 111-122, 1959.
11. H. Blok. *Inverse Problem in Hydrodynamic Lubrication and Design Directives for Lubricated Flexible Surfaces*. in *Symposium on Lubrication and Wear*. 1963. Houston, Texas.
12. H. Fessler and E. Ollerton, "Contact Stresses in Toroids under Radial Loads," *Journal of Applied Physics*, **8**, 387-393, 1957.

Table 6.1 Test matrix developed to analyze the seal cross-sections using ABAQUS.

Seal Bead cross-section	Nominal Compression	Distance from Centerline	Coefficient of Friction (μ)	Parameters of Interest
O-Ring	$10\% \leq \frac{\delta}{2r} \leq 40\%$	$\frac{R}{r} = 1, 10 \text{ \& } 100$	$\mu = 0.1$	Stress distribution: $\sigma_{11}, \sigma_{22}, \sigma_{33}$ Strain distribution: $\epsilon_{11}, \epsilon_{22}, \epsilon_{33}$ Contact stress distribution, σ_c Contact width, b
Custom (SMORS)	$10\% \leq \frac{\delta}{2r} \leq 40\%$	$\frac{R}{r} = 20$	$\mu = 0 \text{ \& } 0.3$	

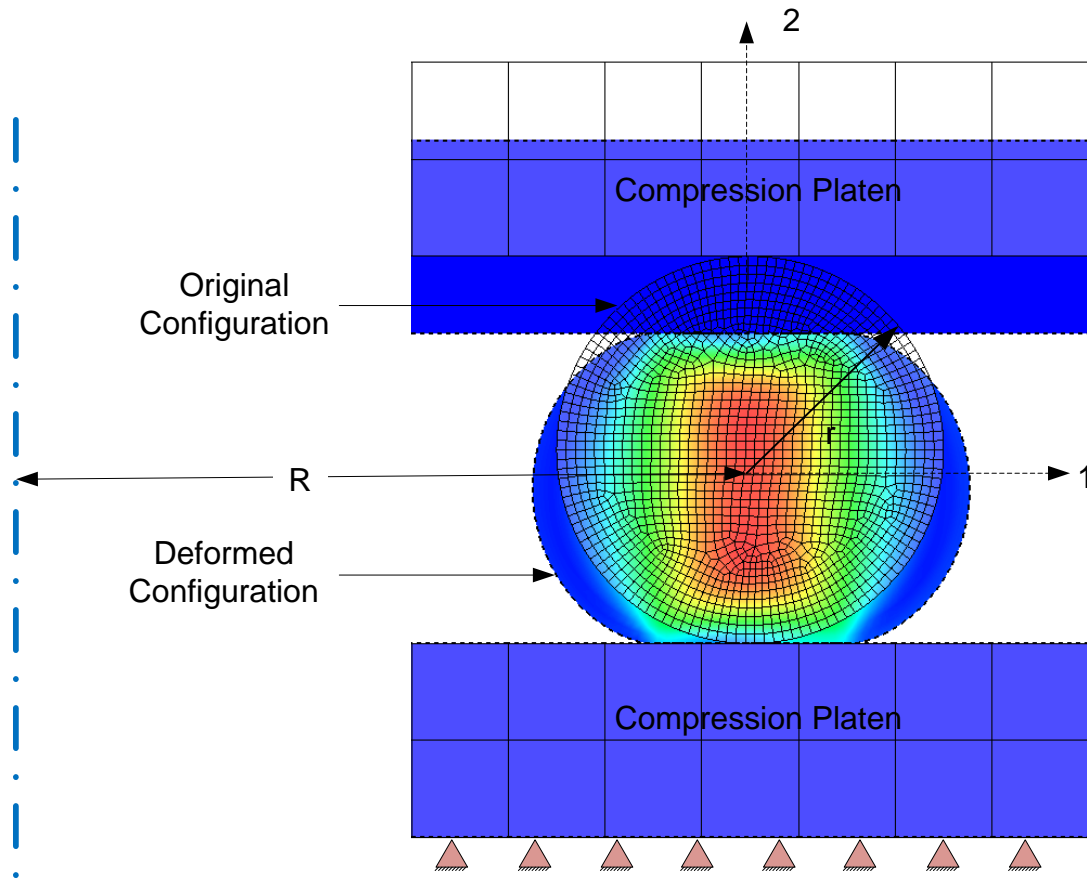


Figure 6.1 Illustration of the O-ring under compression shown with original and deformed configurations in ABAQUS.

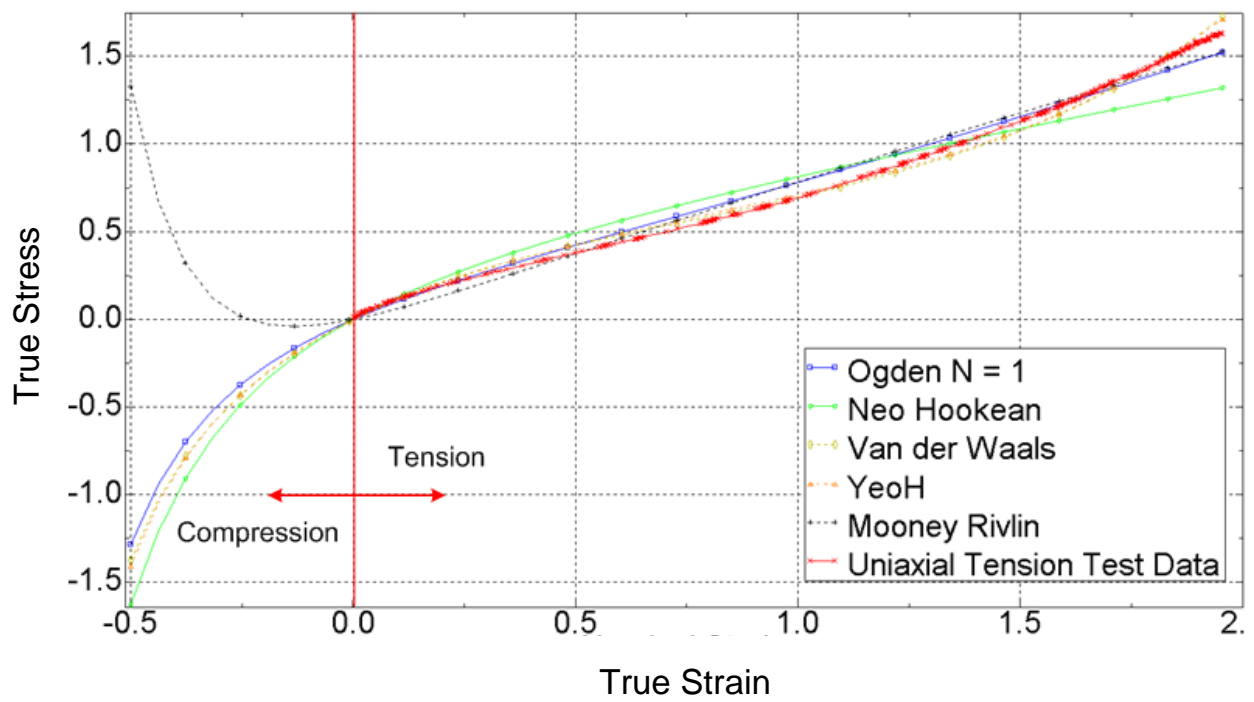


Figure 6.2 Plot of experimental data and predicted uniaxial behavior in tension and compression using various material models.

Material: FCS1																															
Job Name: FCS1_12																															
Polynomial, N = 1 (Mooney-Rivlin)	<p>HYPERELASTICITY - MOONEY-RIVLIN STRAIN ENERGY</p> <table border="1"> <thead> <tr> <th>D1</th> <th>C10</th> <th>C01</th> </tr> </thead> <tbody> <tr> <td>2.327557830E-02</td> <td>0.361766764</td> <td>-0.275782468</td> </tr> </tbody> </table> <p>STABILITY LIMIT INFORMATION</p> <p>WARNING: UNSTABLE HYPERELASTIC MATERIAL</p> <table border="1"> <tbody> <tr> <td>UNIAXIAL TENSION:</td> <td>UNSTABLE AT A NOMINAL STRAIN LARGER THAN</td> <td>0.1500</td> </tr> <tr> <td>UNIAXIAL COMPRESSION:</td> <td>UNSTABLE AT A NOMINAL STRAIN LESS THAN</td> <td>-0.1427</td> </tr> <tr> <td>BIAXIAL TENSION:</td> <td>UNSTABLE AT A NOMINAL STRAIN LARGER THAN</td> <td>0.0800</td> </tr> <tr> <td>BIAXIAL COMPRESSION:</td> <td>UNSTABLE AT A NOMINAL STRAIN LESS THAN</td> <td>-0.0675</td> </tr> <tr> <td>PLANAR TENSION:</td> <td>UNSTABLE AT A NOMINAL STRAIN LARGER THAN</td> <td>0.1300</td> </tr> <tr> <td>PLANAR COMPRESSION:</td> <td>UNSTABLE AT A NOMINAL STRAIN LESS THAN</td> <td>-0.1150</td> </tr> <tr> <td>VOLUMETRIC TENSION:</td> <td>STABLE FOR ALL VOLUME RATIOS</td> <td></td> </tr> <tr> <td>VOLUMETRIC COMPRESSION:</td> <td>STABLE FOR ALL VOLUME RATIOS</td> <td></td> </tr> </tbody> </table>	D1	C10	C01	2.327557830E-02	0.361766764	-0.275782468	UNIAXIAL TENSION:	UNSTABLE AT A NOMINAL STRAIN LARGER THAN	0.1500	UNIAXIAL COMPRESSION:	UNSTABLE AT A NOMINAL STRAIN LESS THAN	-0.1427	BIAXIAL TENSION:	UNSTABLE AT A NOMINAL STRAIN LARGER THAN	0.0800	BIAXIAL COMPRESSION:	UNSTABLE AT A NOMINAL STRAIN LESS THAN	-0.0675	PLANAR TENSION:	UNSTABLE AT A NOMINAL STRAIN LARGER THAN	0.1300	PLANAR COMPRESSION:	UNSTABLE AT A NOMINAL STRAIN LESS THAN	-0.1150	VOLUMETRIC TENSION:	STABLE FOR ALL VOLUME RATIOS		VOLUMETRIC COMPRESSION:	STABLE FOR ALL VOLUME RATIOS	
D1		C10	C01																												
2.327557830E-02		0.361766764	-0.275782468																												
UNIAXIAL TENSION:		UNSTABLE AT A NOMINAL STRAIN LARGER THAN	0.1500																												
UNIAXIAL COMPRESSION:		UNSTABLE AT A NOMINAL STRAIN LESS THAN	-0.1427																												
BIAXIAL TENSION:	UNSTABLE AT A NOMINAL STRAIN LARGER THAN	0.0800																													
BIAXIAL COMPRESSION:	UNSTABLE AT A NOMINAL STRAIN LESS THAN	-0.0675																													
PLANAR TENSION:	UNSTABLE AT A NOMINAL STRAIN LARGER THAN	0.1300																													
PLANAR COMPRESSION:	UNSTABLE AT A NOMINAL STRAIN LESS THAN	-0.1150																													
VOLUMETRIC TENSION:	STABLE FOR ALL VOLUME RATIOS																														
VOLUMETRIC COMPRESSION:	STABLE FOR ALL VOLUME RATIOS																														
Ogden, N = 1																															
Reduced Polynomial, N = 1 (Neo Hooke)																															
Reduced Polynomial, N = 3 (Yeoh)																															
Van Der Waals																															

(a)

Material: FCS1																									
Job Name: FCS1_12																									
Polynomial, N = 1 (Mooney-Rivlin)	<p>HYPERELASTICITY - OGDEN STRAIN ENERGY FUNCTION WITH N = 1</p> <table border="1"> <thead> <tr> <th>I</th> <th>MU_I</th> <th>ALPHA_I</th> <th>D_I</th> </tr> </thead> <tbody> <tr> <td>1</td> <td>0.363497748</td> <td>2.56608450</td> <td>1.101153575E-02</td> </tr> </tbody> </table> <p>STABILITY LIMIT INFORMATION</p> <table border="1"> <tbody> <tr> <td>UNIAXIAL TENSION:</td> <td>STABLE FOR ALL STRAINS</td> </tr> <tr> <td>UNIAXIAL COMPRESSION:</td> <td>STABLE FOR ALL STRAINS</td> </tr> <tr> <td>BIAXIAL TENSION:</td> <td>STABLE FOR ALL STRAINS</td> </tr> <tr> <td>BIAXIAL COMPRESSION:</td> <td>STABLE FOR ALL STRAINS</td> </tr> <tr> <td>PLANAR TENSION:</td> <td>STABLE FOR ALL STRAINS</td> </tr> <tr> <td>PLANAR COMPRESSION:</td> <td>STABLE FOR ALL STRAINS</td> </tr> <tr> <td>VOLUMETRIC TENSION:</td> <td>STABLE FOR ALL VOLUME RATIOS</td> </tr> <tr> <td>VOLUMETRIC COMPRESSION:</td> <td>STABLE FOR ALL VOLUME RATIOS</td> </tr> </tbody> </table>	I	MU_I	ALPHA_I	D_I	1	0.363497748	2.56608450	1.101153575E-02	UNIAXIAL TENSION:	STABLE FOR ALL STRAINS	UNIAXIAL COMPRESSION:	STABLE FOR ALL STRAINS	BIAXIAL TENSION:	STABLE FOR ALL STRAINS	BIAXIAL COMPRESSION:	STABLE FOR ALL STRAINS	PLANAR TENSION:	STABLE FOR ALL STRAINS	PLANAR COMPRESSION:	STABLE FOR ALL STRAINS	VOLUMETRIC TENSION:	STABLE FOR ALL VOLUME RATIOS	VOLUMETRIC COMPRESSION:	STABLE FOR ALL VOLUME RATIOS
I		MU_I	ALPHA_I	D_I																					
1		0.363497748	2.56608450	1.101153575E-02																					
UNIAXIAL TENSION:		STABLE FOR ALL STRAINS																							
UNIAXIAL COMPRESSION:		STABLE FOR ALL STRAINS																							
BIAXIAL TENSION:	STABLE FOR ALL STRAINS																								
BIAXIAL COMPRESSION:	STABLE FOR ALL STRAINS																								
PLANAR TENSION:	STABLE FOR ALL STRAINS																								
PLANAR COMPRESSION:	STABLE FOR ALL STRAINS																								
VOLUMETRIC TENSION:	STABLE FOR ALL VOLUME RATIOS																								
VOLUMETRIC COMPRESSION:	STABLE FOR ALL VOLUME RATIOS																								
Ogden, N = 1																									
Reduced Polynomial, N = 1 (Neo Hooke)																									
Reduced Polynomial, N = 3 (Yeoh)																									
Van Der Waals																									

(b)

Material: FCS1							
Job Name: FCS1_12							
Polynomial, N = 1 (Mooney-Rivlin)	<p>HYPERELASTICITY - NEO-HOOKEAN STRAIN ENERGY</p> <table border="1"> <thead> <tr> <th>D1</th> <th>C10</th> <th>C01</th> </tr> </thead> <tbody> <tr> <td>8.618016485E-03</td> <td>0.232226781</td> <td>0.00000000</td> </tr> </tbody> </table> <p>STABILITY LIMIT INFORMATION</p> <p>UNIAXIAL TENSION: STABLE FOR ALL STRAINS UNIAXIAL COMPRESSION: STABLE FOR ALL STRAINS BIAXIAL TENSION: STABLE FOR ALL STRAINS BIAXIAL COMPRESSION: STABLE FOR ALL STRAINS PLANAR TENSION: STABLE FOR ALL STRAINS PLANAR COMPRESSION: STABLE FOR ALL STRAINS VOLUMETRIC TENSION: STABLE FOR ALL VOLUME RATIOS VOLUMETRIC COMPRESSION: STABLE FOR ALL VOLUME RATIOS</p>	D1	C10	C01	8.618016485E-03	0.232226781	0.00000000
D1		C10	C01				
8.618016485E-03		0.232226781	0.00000000				
Ogden, N = 1							
Reduced Polynomial, N = 1 (Neo Hooke)							
Reduced Polynomial, N = 3 (Yeoh)							
Van Der Waals							

(c)

Material: FCS1																															
Job Name: FCS1_12																															
Polynomial, N = 1 (Mooney-Rivlin)	<p>HYPERELASTICITY - POLYNOMIAL STRAIN ENERGY FUNCTION WITH N = 3</p> <table border="1"> <thead> <tr> <th>D1</th> <th>C10</th> <th>C01</th> <th></th> <th></th> </tr> <tr> <th>D2</th> <th>C20</th> <th>C11</th> <th>C02</th> <th></th> </tr> <tr> <th>D3</th> <th>C30</th> <th>C21</th> <th>C12</th> <th></th> </tr> </thead> <tbody> <tr> <td>9.703500736E-03</td> <td>0.206248680</td> <td>0.00000000</td> <td></td> <td></td> </tr> <tr> <td>0.00000000</td> <td>-4.456420773E-03</td> <td>0.00000000</td> <td>0.00000000</td> <td></td> </tr> <tr> <td>0.00000000</td> <td>1.236736764E-03</td> <td>0.00000000</td> <td>0.00000000</td> <td>0.0</td> </tr> </tbody> </table> <p>STABILITY LIMIT INFORMATION</p> <p>UNIAXIAL TENSION: STABLE FOR ALL STRAINS UNIAXIAL COMPRESSION: STABLE FOR ALL STRAINS BIAXIAL TENSION: STABLE FOR ALL STRAINS BIAXIAL COMPRESSION: STABLE FOR ALL STRAINS PLANAR TENSION: STABLE FOR ALL STRAINS PLANAR COMPRESSION: STABLE FOR ALL STRAINS VOLUMETRIC TENSION: STABLE FOR ALL VOLUME RATIOS VOLUMETRIC COMPRESSION: STABLE FOR ALL VOLUME RATIOS</p>	D1	C10	C01			D2	C20	C11	C02		D3	C30	C21	C12		9.703500736E-03	0.206248680	0.00000000			0.00000000	-4.456420773E-03	0.00000000	0.00000000		0.00000000	1.236736764E-03	0.00000000	0.00000000	0.0
D1		C10	C01																												
D2		C20	C11	C02																											
D3		C30	C21	C12																											
9.703500736E-03		0.206248680	0.00000000																												
0.00000000		-4.456420773E-03	0.00000000	0.00000000																											
0.00000000	1.236736764E-03	0.00000000	0.00000000	0.0																											
Ogden, N = 1																															
Reduced Polynomial, N = 1 (Neo Hooke)																															
Reduced Polynomial, N = 3 (Yeoh)																															
Van Der Waals																															

(d)

Material: FCS1																																			
Job Name: FCS1_12																																			
Polynomial, N = 1 (Mooney-Rivlin)	<p>HYPERELASTICITY - VAN DER WAALS STRAIN ENERGY FUNCTION</p> <table border="0"> <tr> <td>MU</td> <td>LAMBDA_M</td> <td>A</td> <td>BETA</td> <td></td> </tr> <tr> <td>0.449232109</td> <td>4.63078651</td> <td>0.604826135</td> <td>0.00000000</td> <td>8.64</td> </tr> </table> <p>STABILITY LIMIT INFORMATION</p> <table border="0"> <tr> <td>UNIAXIAL TENSION:</td> <td>UNSTABLE AT A NOMINAL STRAIN LARGER THAN</td> <td>3.5900</td> </tr> <tr> <td>UNIAXIAL COMPRESSION:</td> <td>UNSTABLE AT A NOMINAL STRAIN LESS THAN</td> <td>-0.9070</td> </tr> <tr> <td>BIAXIAL TENSION:</td> <td>UNSTABLE AT A NOMINAL STRAIN LARGER THAN</td> <td>2.2800</td> </tr> <tr> <td>BIAXIAL COMPRESSION:</td> <td>UNSTABLE AT A NOMINAL STRAIN LESS THAN</td> <td>-0.5332</td> </tr> <tr> <td>PLANAR TENSION:</td> <td>UNSTABLE AT A NOMINAL STRAIN LARGER THAN</td> <td>3.5200</td> </tr> <tr> <td>PLANAR COMPRESSION:</td> <td>UNSTABLE AT A NOMINAL STRAIN LESS THAN</td> <td>-0.7788</td> </tr> <tr> <td>VOLUMETRIC TENSION:</td> <td>STABLE FOR ALL VOLUME RATIOS</td> <td></td> </tr> <tr> <td>VOLUMETRIC COMPRESSION:</td> <td>STABLE FOR ALL VOLUME RATIOS</td> <td></td> </tr> </table>	MU	LAMBDA_M	A	BETA		0.449232109	4.63078651	0.604826135	0.00000000	8.64	UNIAXIAL TENSION:	UNSTABLE AT A NOMINAL STRAIN LARGER THAN	3.5900	UNIAXIAL COMPRESSION:	UNSTABLE AT A NOMINAL STRAIN LESS THAN	-0.9070	BIAXIAL TENSION:	UNSTABLE AT A NOMINAL STRAIN LARGER THAN	2.2800	BIAXIAL COMPRESSION:	UNSTABLE AT A NOMINAL STRAIN LESS THAN	-0.5332	PLANAR TENSION:	UNSTABLE AT A NOMINAL STRAIN LARGER THAN	3.5200	PLANAR COMPRESSION:	UNSTABLE AT A NOMINAL STRAIN LESS THAN	-0.7788	VOLUMETRIC TENSION:	STABLE FOR ALL VOLUME RATIOS		VOLUMETRIC COMPRESSION:	STABLE FOR ALL VOLUME RATIOS	
MU		LAMBDA_M	A	BETA																															
0.449232109		4.63078651	0.604826135	0.00000000	8.64																														
UNIAXIAL TENSION:		UNSTABLE AT A NOMINAL STRAIN LARGER THAN	3.5900																																
UNIAXIAL COMPRESSION:		UNSTABLE AT A NOMINAL STRAIN LESS THAN	-0.9070																																
BIAXIAL TENSION:	UNSTABLE AT A NOMINAL STRAIN LARGER THAN	2.2800																																	
BIAXIAL COMPRESSION:	UNSTABLE AT A NOMINAL STRAIN LESS THAN	-0.5332																																	
PLANAR TENSION:	UNSTABLE AT A NOMINAL STRAIN LARGER THAN	3.5200																																	
PLANAR COMPRESSION:	UNSTABLE AT A NOMINAL STRAIN LESS THAN	-0.7788																																	
VOLUMETRIC TENSION:	STABLE FOR ALL VOLUME RATIOS																																		
VOLUMETRIC COMPRESSION:	STABLE FOR ALL VOLUME RATIOS																																		
Ogden, N = 1																																			
Reduced Polynomial, N = 1 (Neo Hooke)																																			
Reduced Polynomial, N = 3 (Yeoh)																																			
Van Der Waals																																			

(e)

Figure 6.3 Material Parameters and stability limit information on (a) Mooney Rivlin, (b) two-parameter Ogden, (c) Neo-Hookean, (d) Yeoh, and (e) Van der Waals hyperelastic material models.

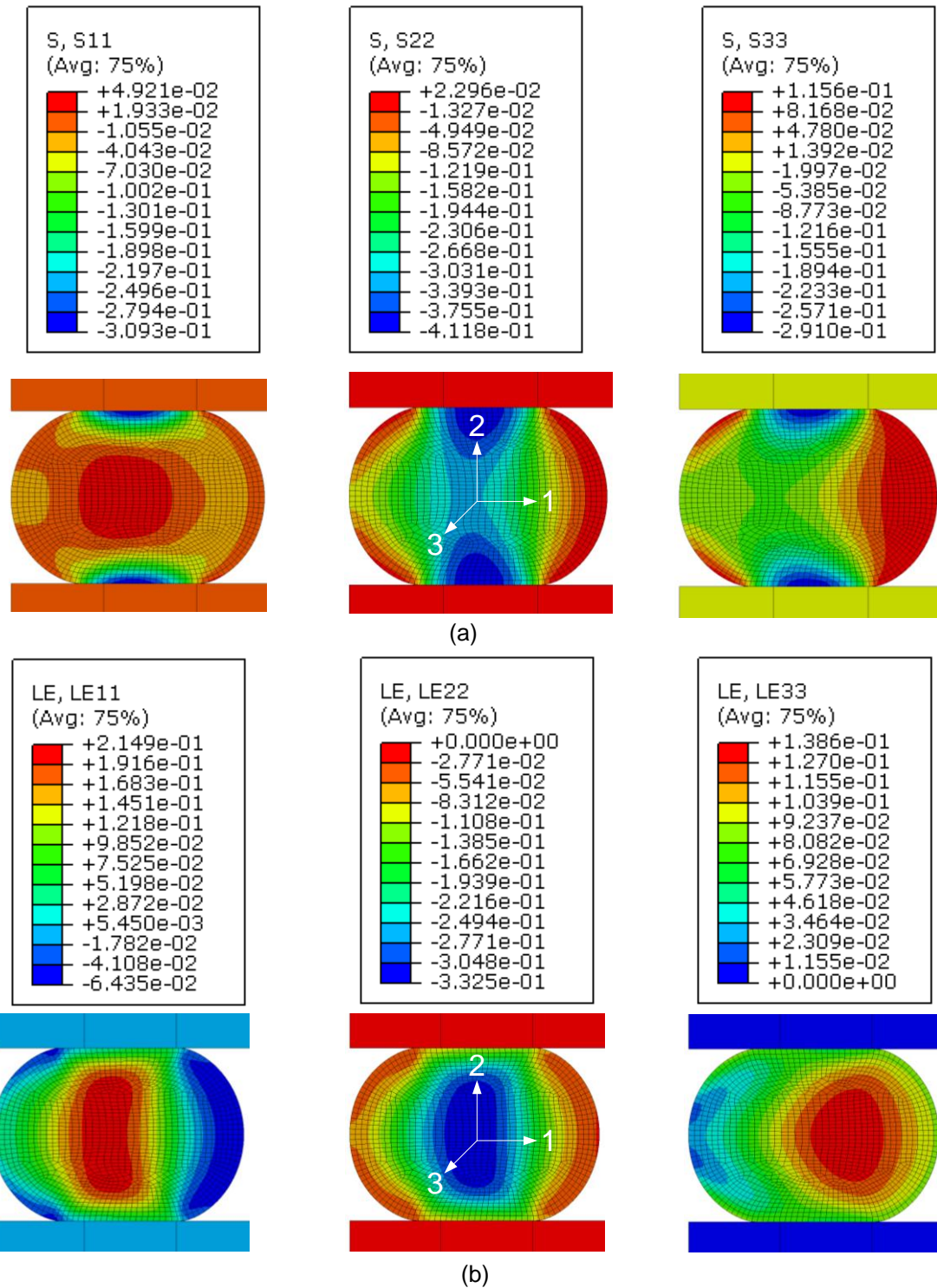
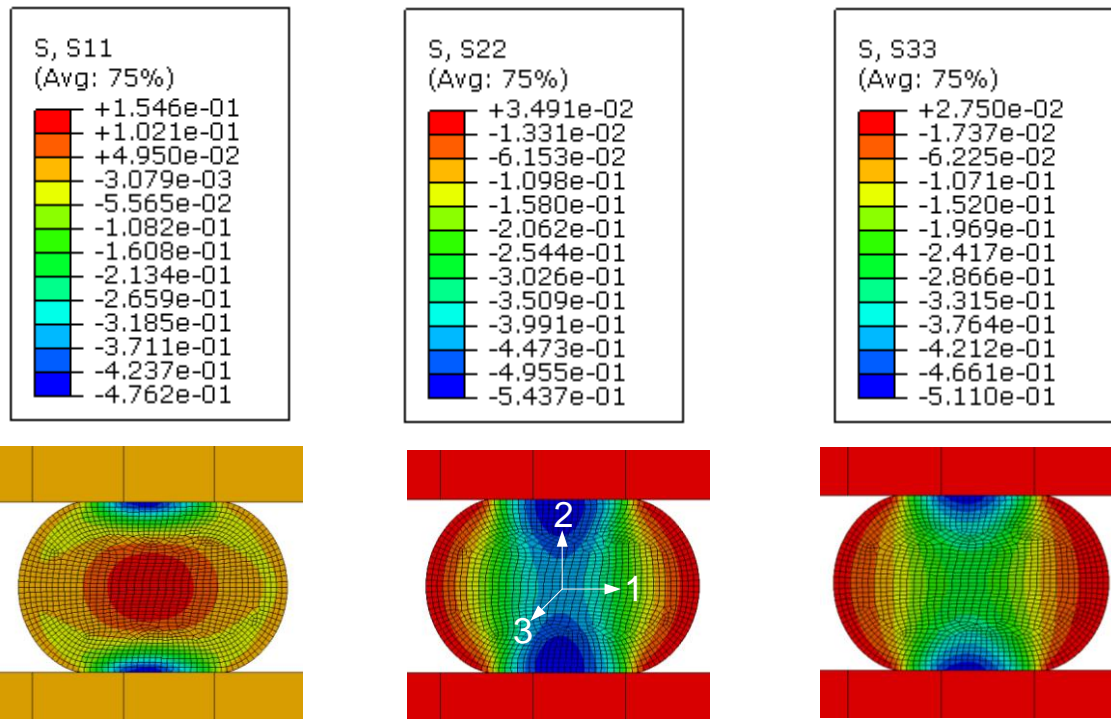
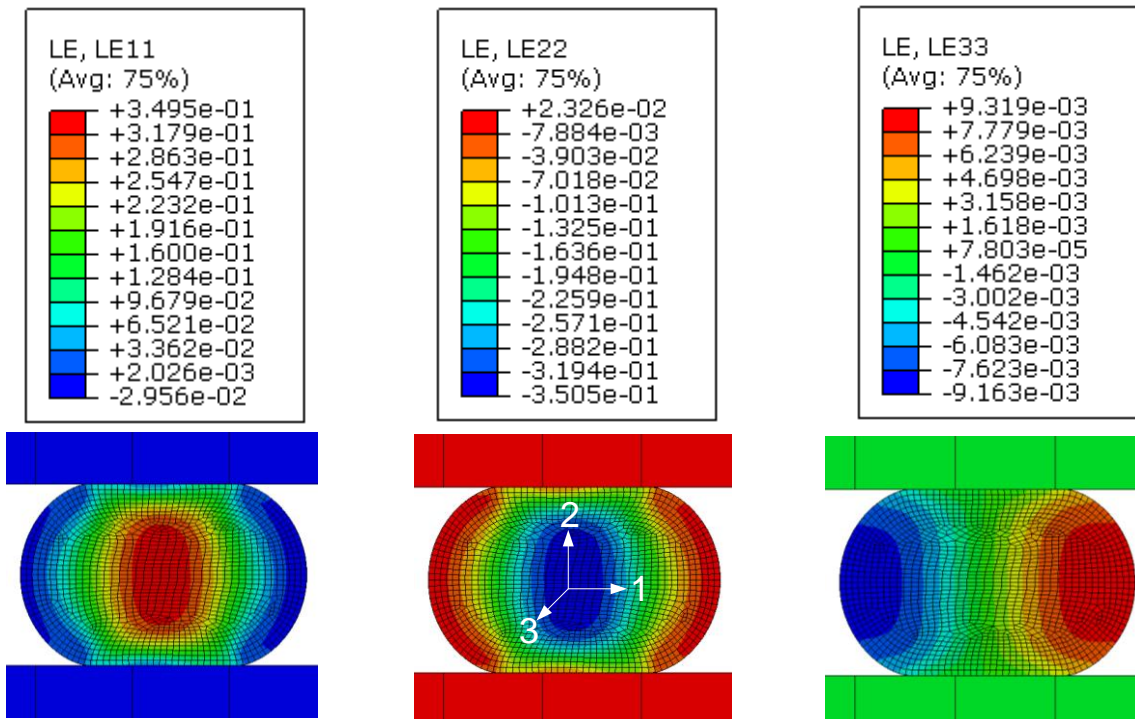


Figure 6.4 FEA simulation of seals subjected to 25% compression for $R/r = 1$. The interfacial friction is given by $\mu = 0.1$. Note the asymmetric nature (with respect to 2-direction) of (a) stresses and (b) strains in 1-2-3 directions for O-ring cross-section.

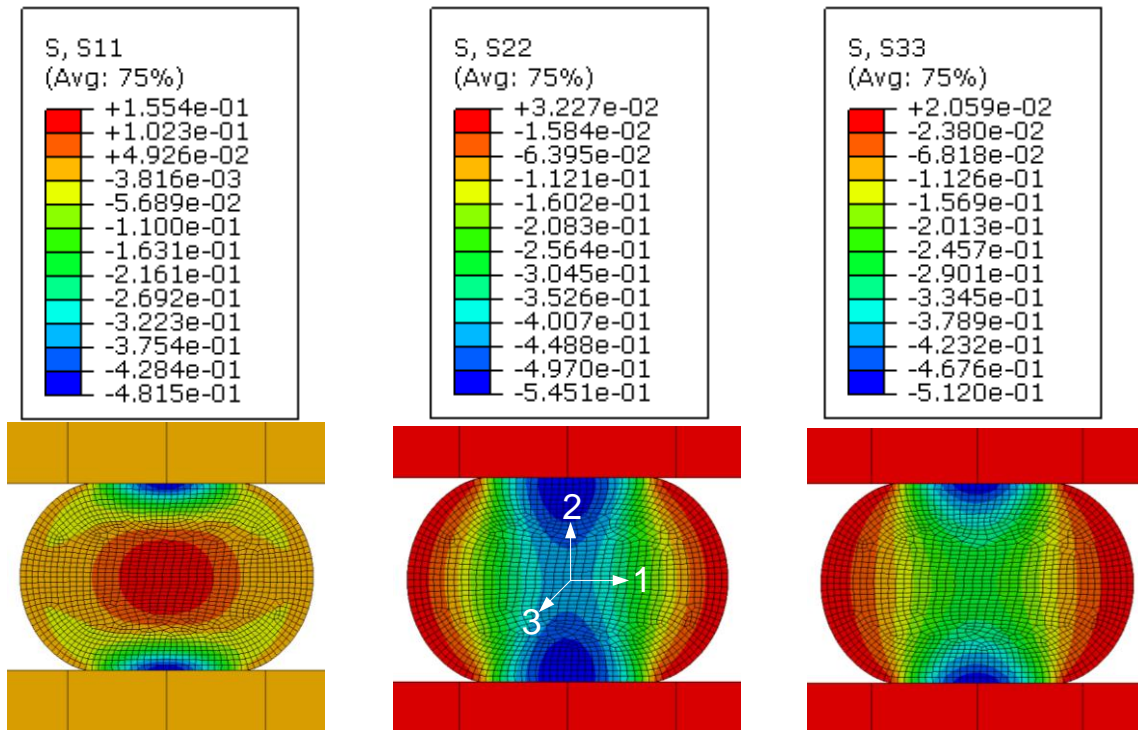


(a)

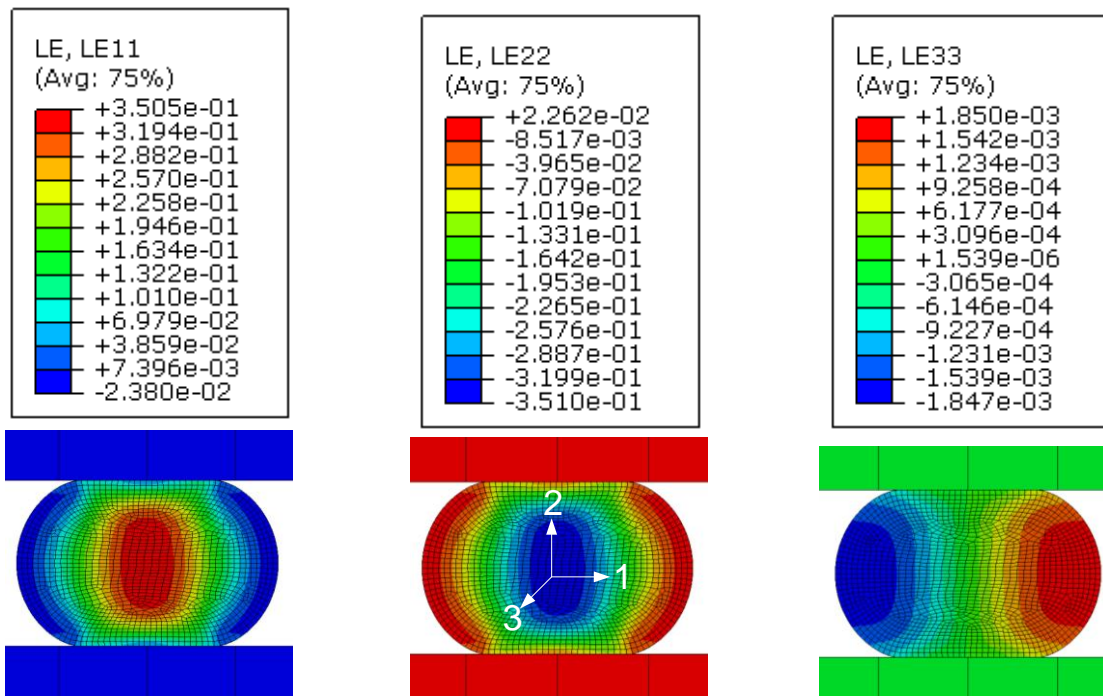


(b)

Figure 6.5 FEA simulation of seals subjected to 25% compression for $R/r = 10$. The interfacial friction is given by $\mu = 0.1$. The stresses (a) and strains (b) are more symmetrically distributed in 1-2-3 directions for O-ring cross-section.



(a)



(b)

Figure 6.6 FEA simulation of seals subjected to 25% compression for $R/r = 100$. The interfacial friction is given by $\mu = 0.1$. The symmetry in stresses (a) and strains (b) is more pronounced in 1-2-3 directions for O-ring cross-section.

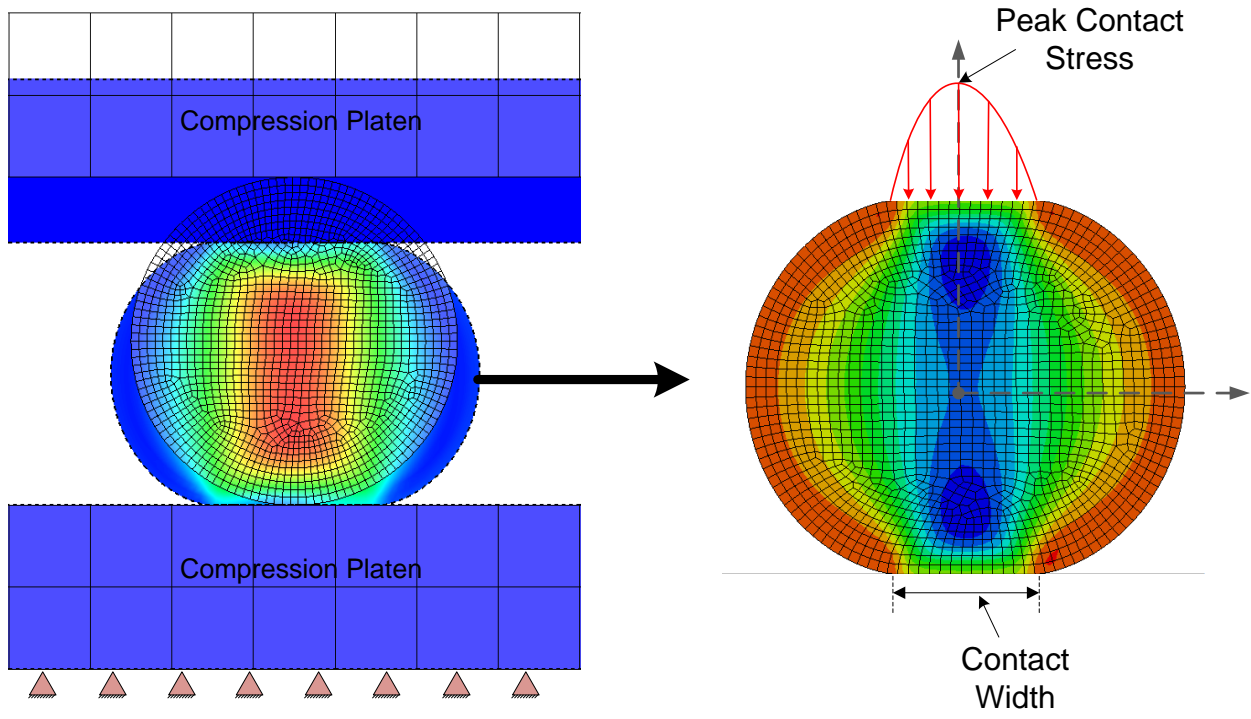
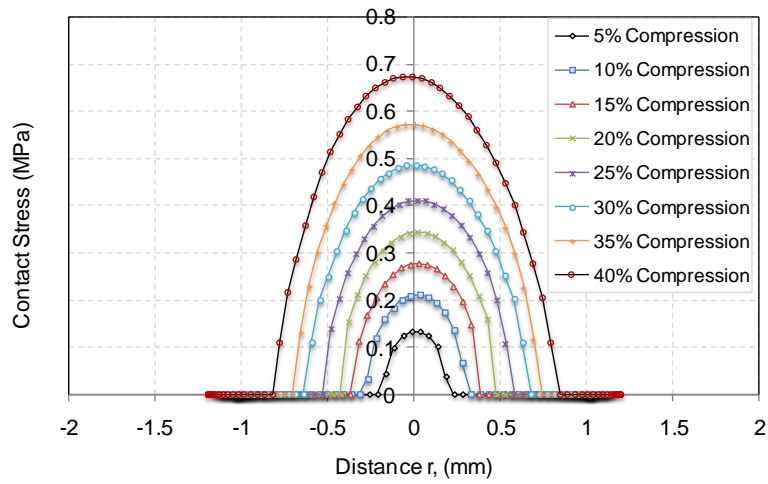
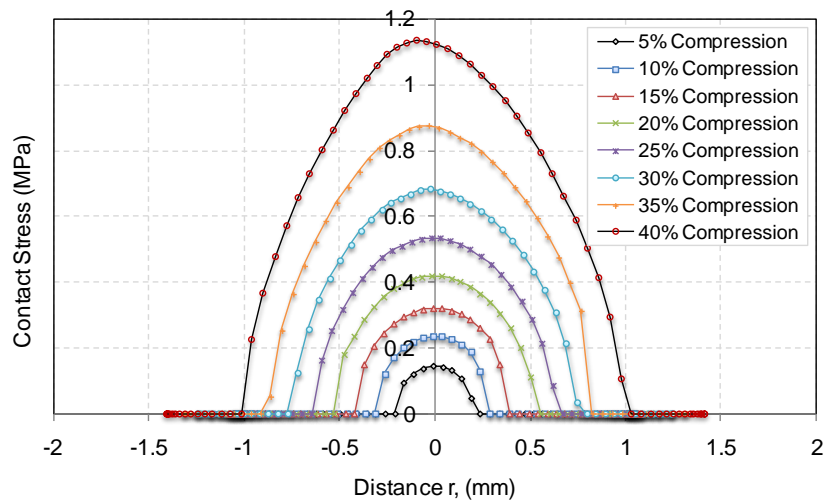


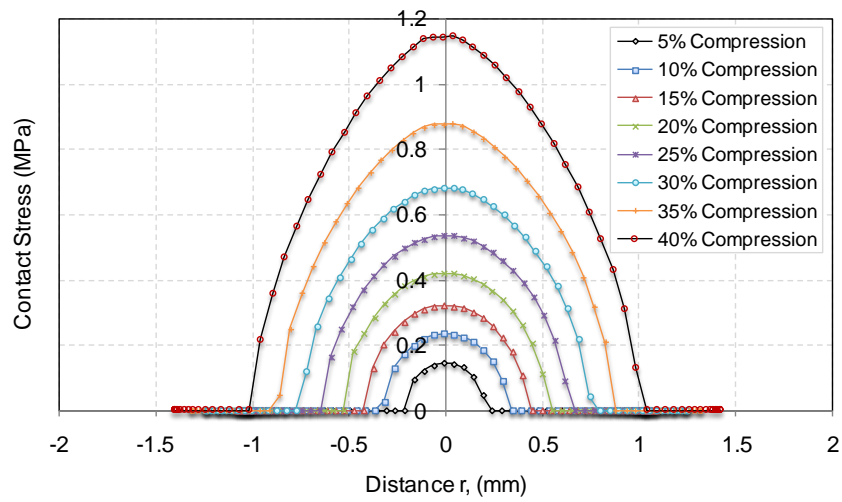
Figure 6.7 Illustration of concept for contact stress and width for O-ring seal.



(a)

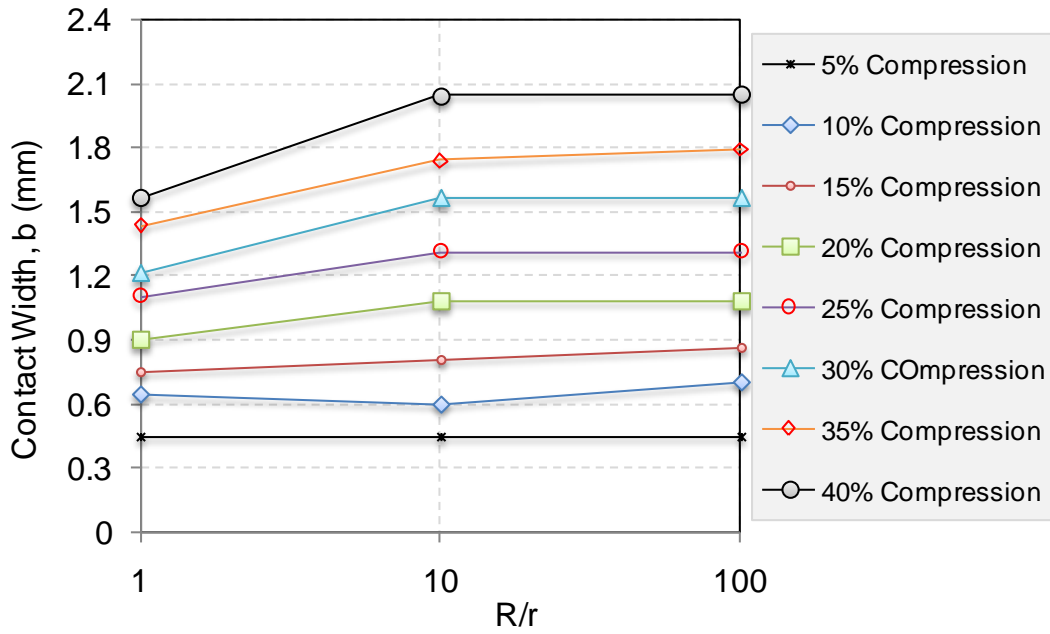


(b)

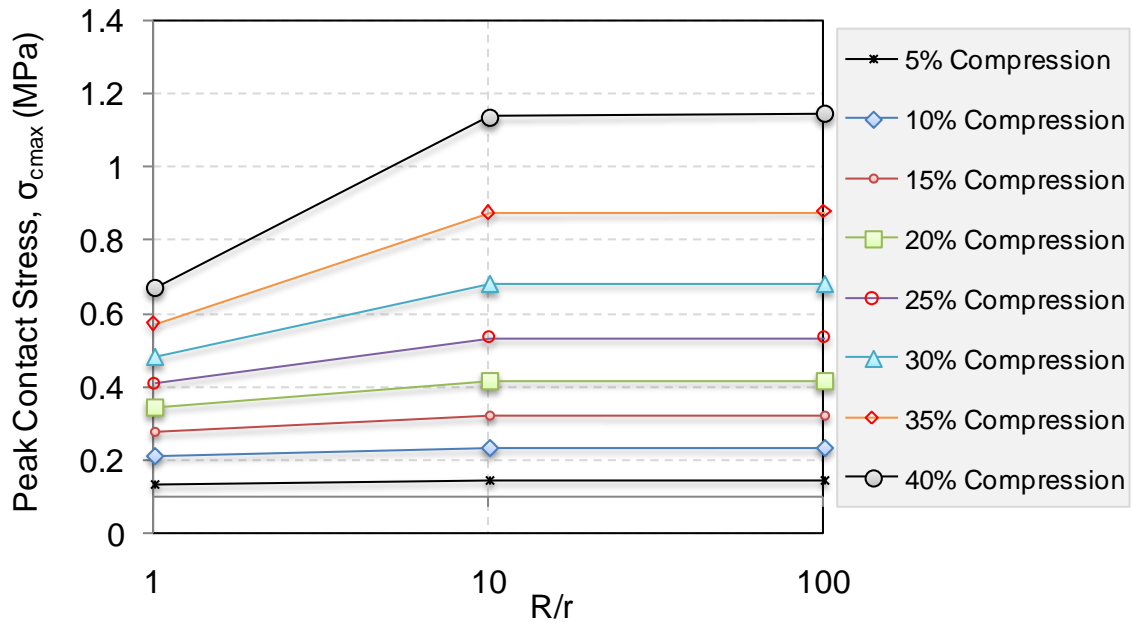


(c)

Figure 6.8 Contact pressure profile for O-ring for (a) $R/r = 1$, (b) $R/r = 10$ & (c) $R/r = 100$ with rough ($\mu = 0.1$) interfacial condition. The symmetry of pressure is more evident as the ratio of R/r increases.



(a)



(b)

Figure 6.9 Contact width and peak contact stress profiles for O-ring under compression for different R/r ratios.

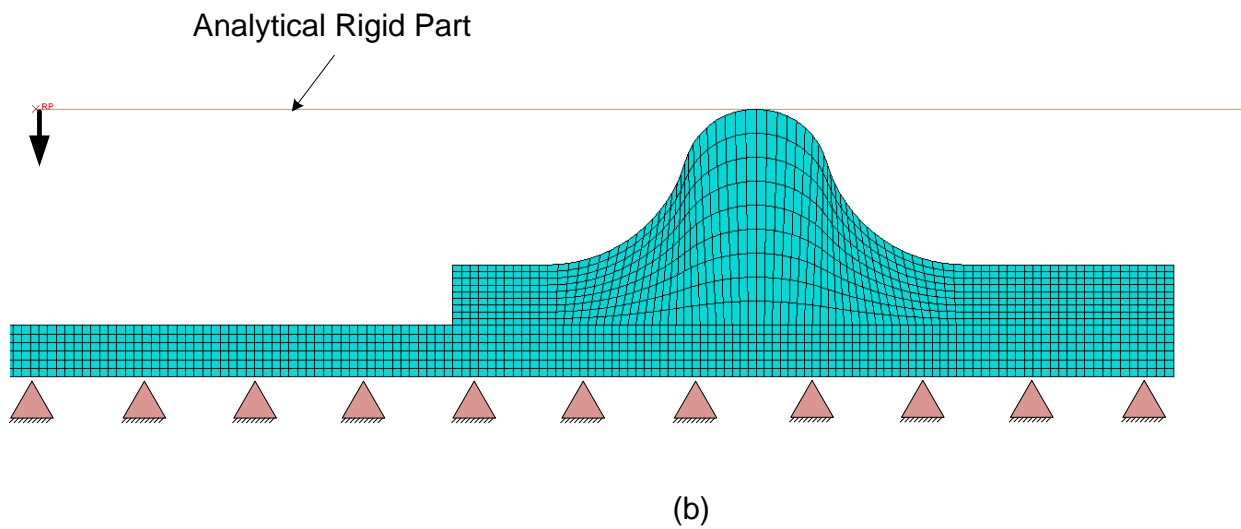
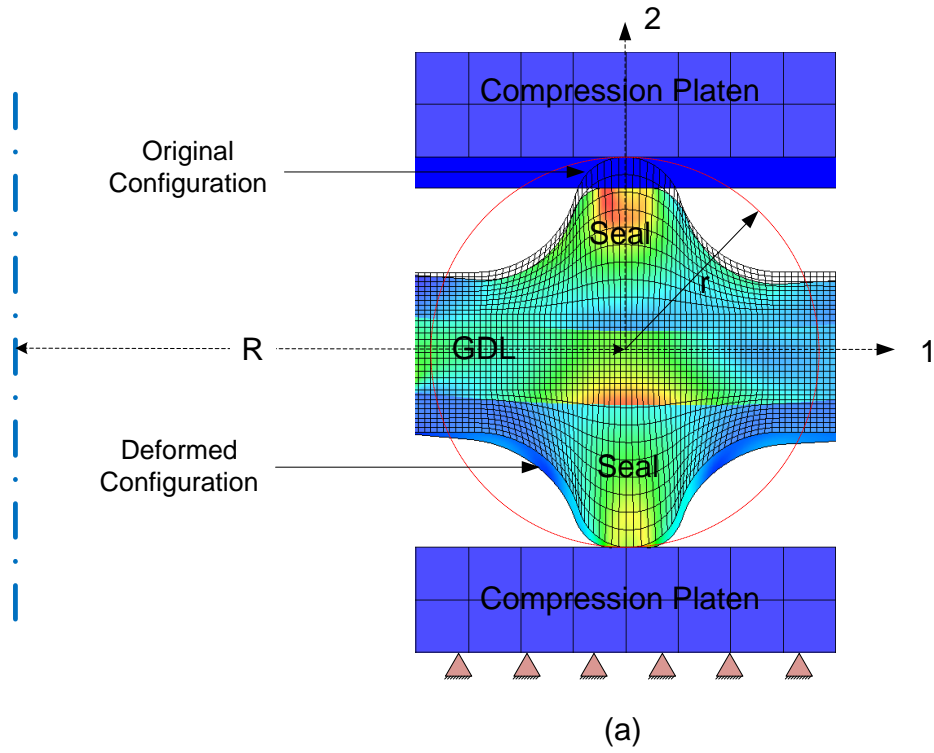


Figure 6.10 Illustration of the SMORS under compression showing (a) full cross-section with original and deformed shape, and (b) half section used for analysis in ABAQUS.

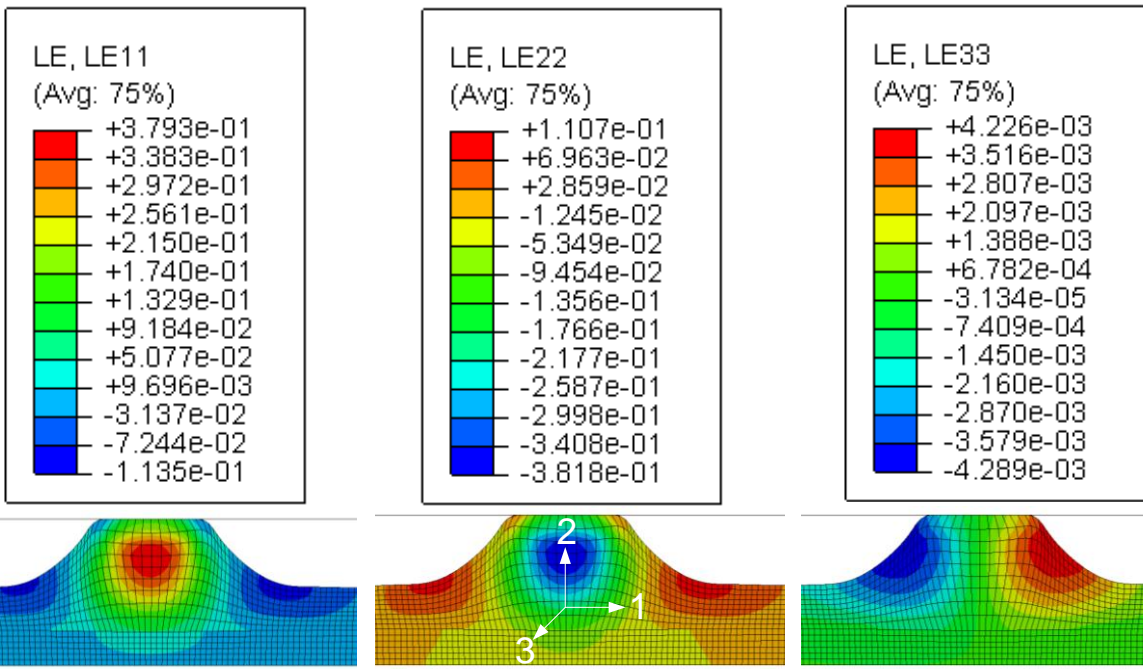
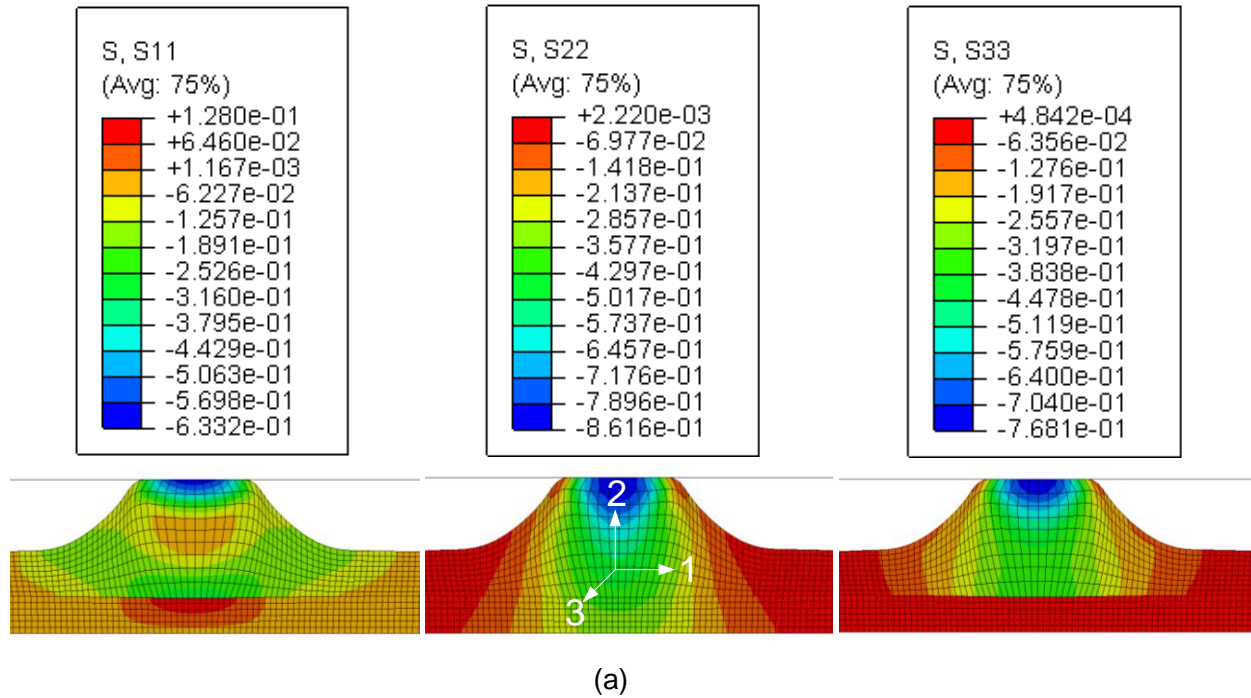


Figure 6.11 FEA simulation of SMORS subjected to 25% compression for $R/r = 20$. The interfacial friction is given by $\mu = 0$. The stresses (a) and strains (b) are symmetrically distributed in 1-2-3 directions for O-ring cross-section.

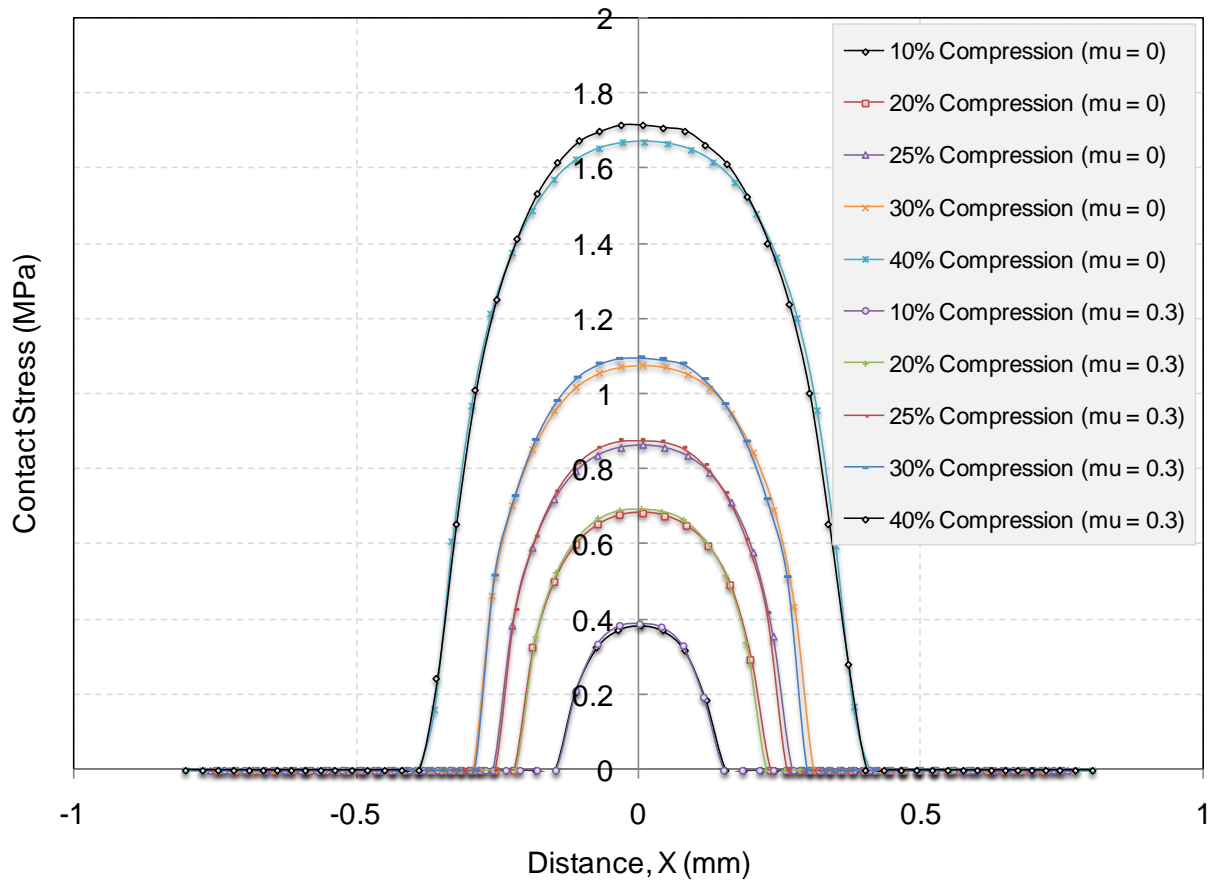
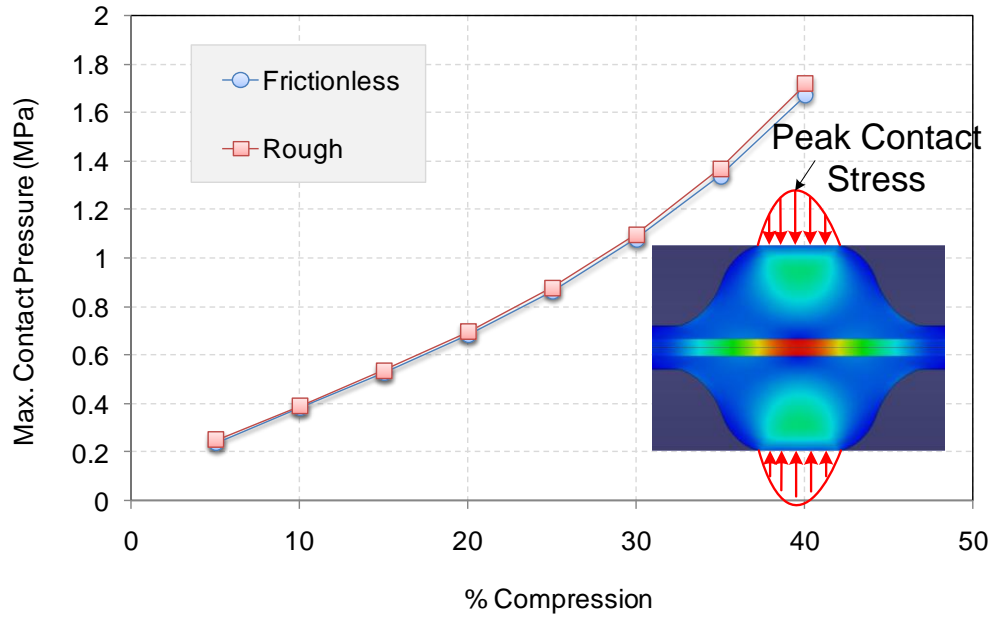
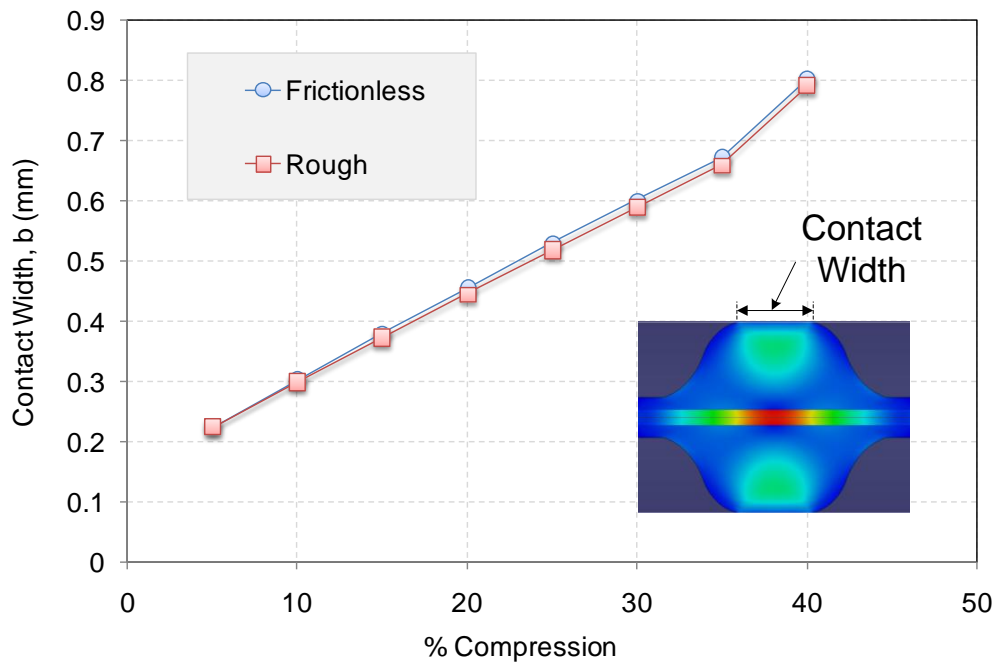


Figure 6.12 Contact stress profile for frictionless and rough conditions from 10 to 40% compression of SMORS. Note the higher peak contact stress for the case where friction is present between seal and compression platen.

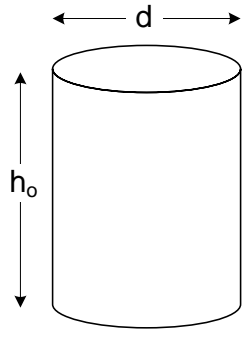


(a)



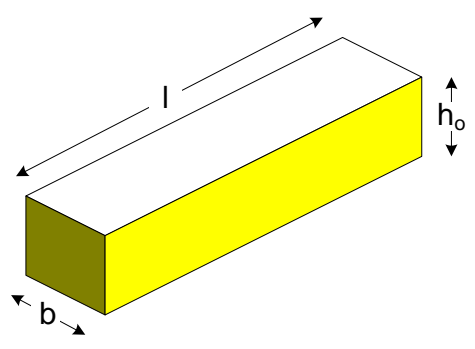
(b)

Figure 6.13 Effect of interfacial friction (frictionless $\mu = 0$ and Rough $\mu = 0.3$) between compression platens and seal on (a) peak contact pressure and (b) contact width.



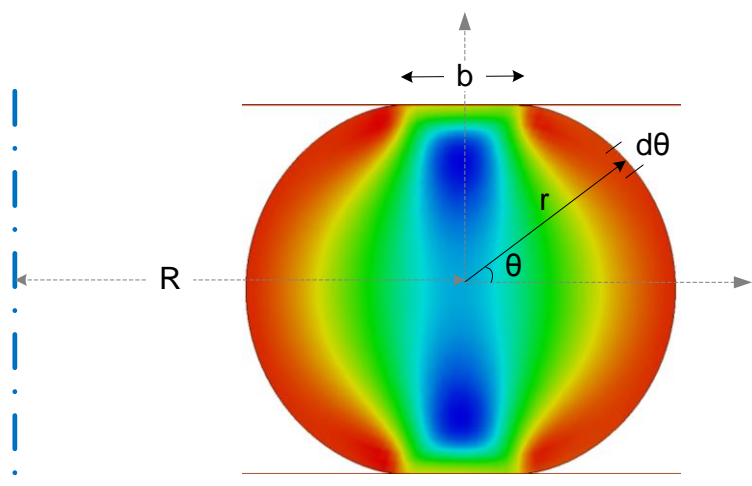
$$S = \frac{\text{loaded}}{\text{force} - \text{free}} = \frac{\pi \cdot d^2 / 4}{\pi \cdot d h_o} = \frac{d}{4 h_o}$$

(a)



$$S = \frac{\text{loaded}}{\text{force} - \text{free}} = \frac{b \cdot l}{2 h_o (b + l)}$$

(b)



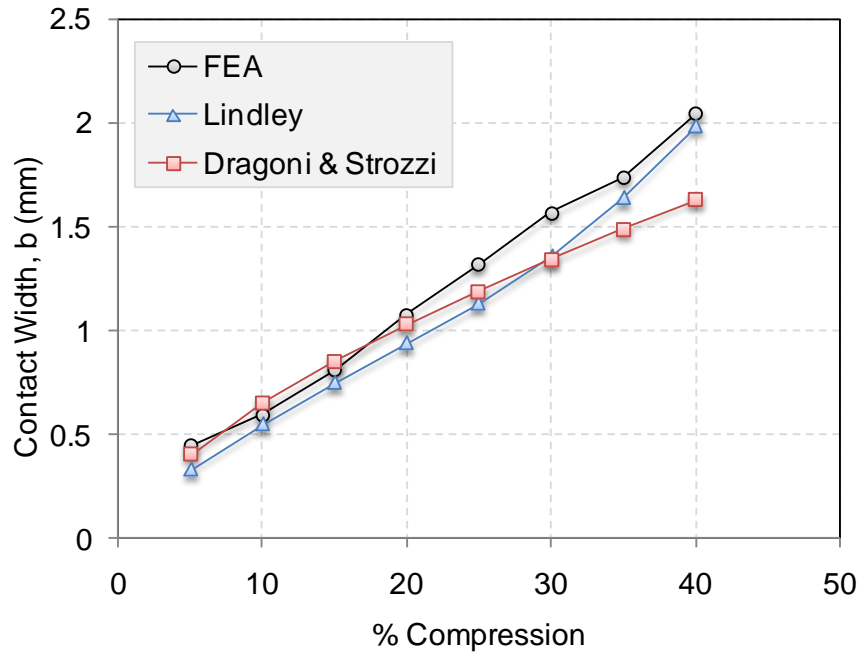
$$S = \frac{2\pi \cdot R \cdot b}{2 \times \int_{-\pi/2}^{\pi/2} 2\pi (R + r \cdot \text{Cos } \theta) \cdot d\theta}$$

(c)

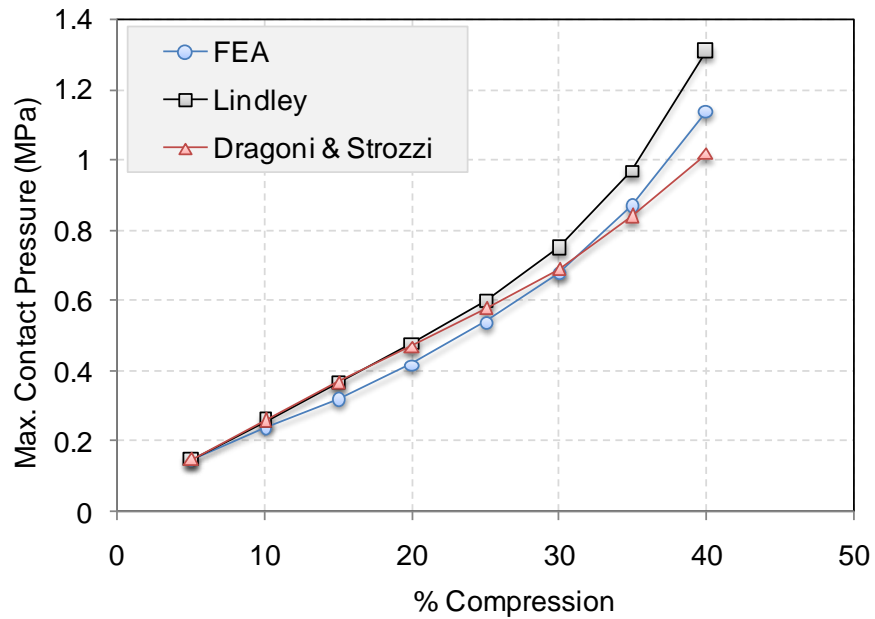
Figure 6.14 Shape factor for some common geometries.

Table 6.2 Contact width and contact pressure data on O-ring obtained from FEA analysis and Lindley and Dragoni approach.

Seal Compression (%)	FEA		Shape Factor, S	Compression modulus (MPa)	Lindley		Dragoni	
	b (mm)	CPRESS (MPa)			b (mm)	CPRESS (MPa)	b (mm)	CPRESS (MPa)
5	0.45	0.15	0.08	1.42	0.33	0.15	0.41	0.15
10	0.6	0.24	0.13	1.44	0.55	0.26	0.65	0.26
15	0.81	0.32	0.18	1.48	0.75	0.37	0.85	0.37
20	1.08	0.42	0.22	1.53	0.94	0.48	1.03	0.47
25	1.32	0.54	0.27	1.58	1.13	0.6	1.19	0.58
30	1.57	0.68	0.32	1.66	1.36	0.75	1.34	0.69
35	1.74	0.87	0.39	1.78	1.64	0.97	1.49	0.84
40	2.05	1.14	0.48	1.97	1.99	1.31	1.63	1.02



(a)



(b)

Figure 6.15 Contact width and contact pressure data on O-ring compression from FEA analysis and Lindley and Dragoni equations.

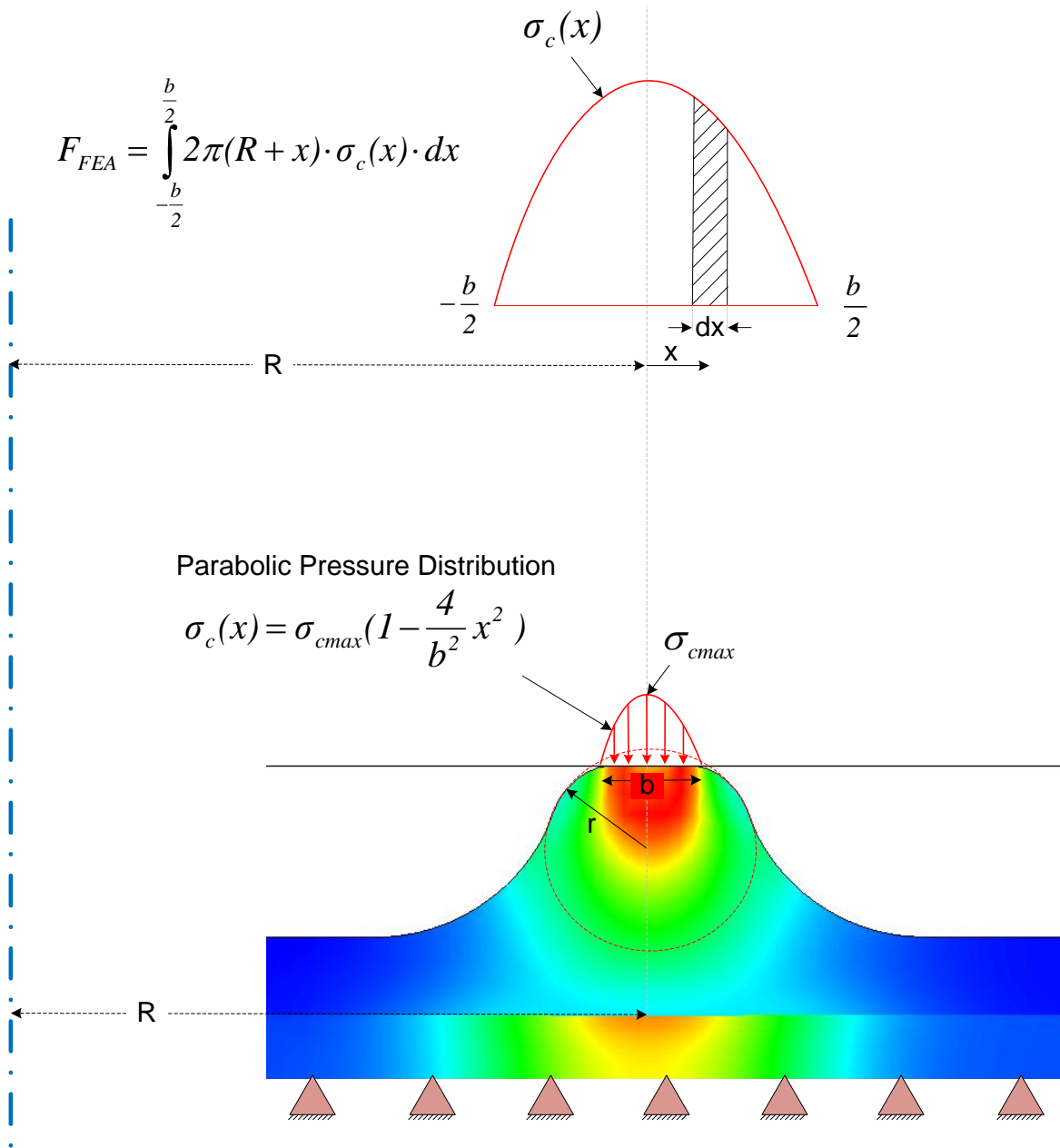


Figure 6.16 Calculation of total load from contact width and contact pressure profile obtained from FEA of SMORS under compression.

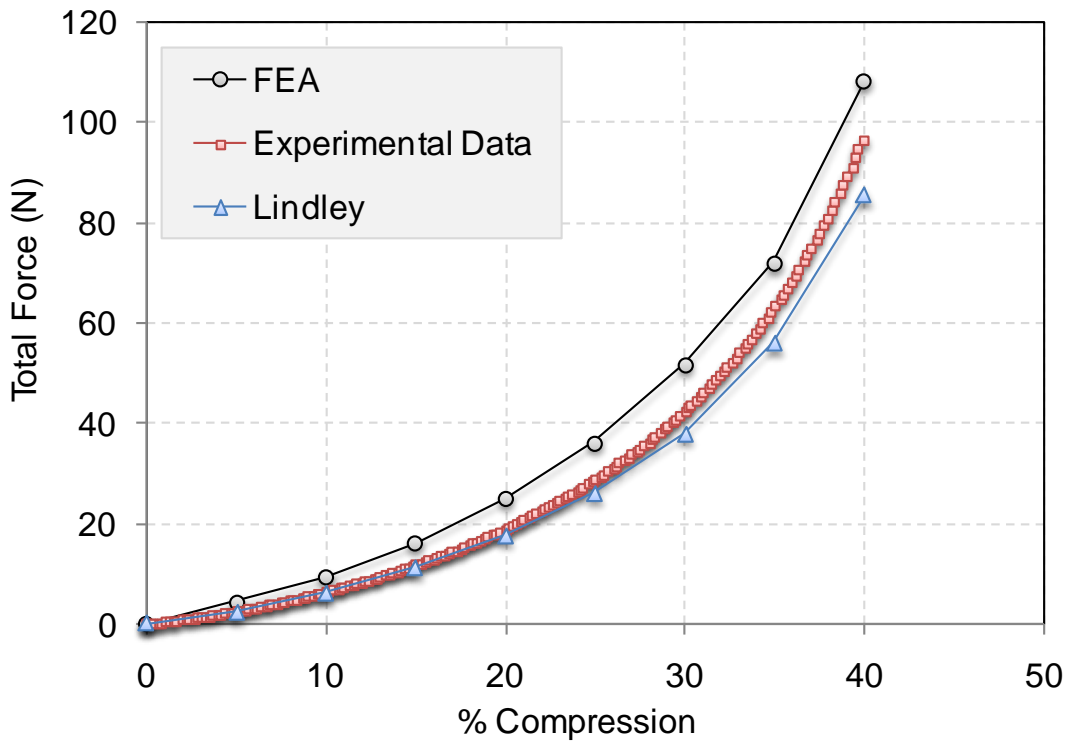


Figure 6.17 Comparison of load versus % compression behavior obtained from finite element analysis in ABAQUS, theoretical approach based on Lindley's empirical relationship and experimental data from SMORS.

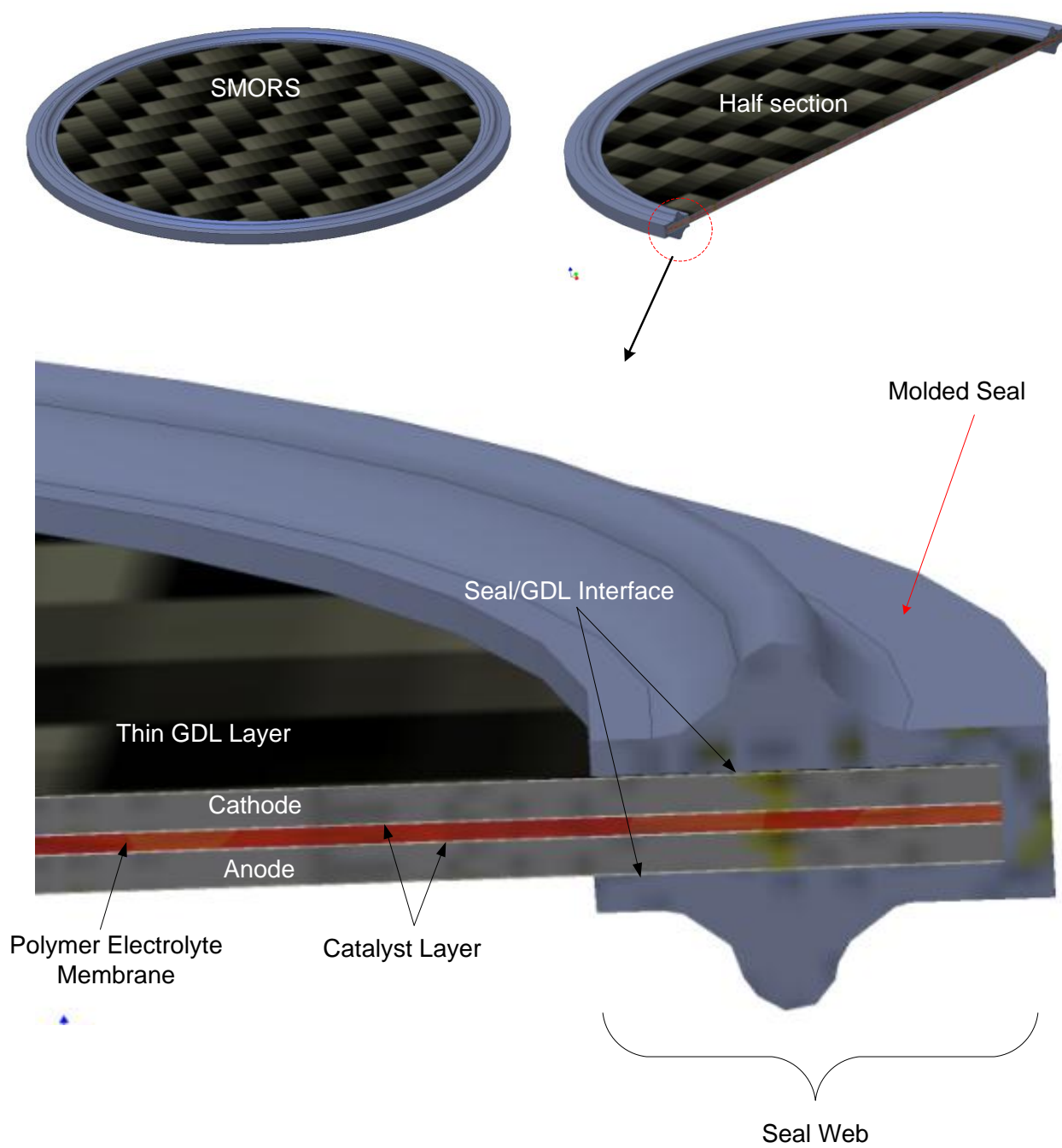
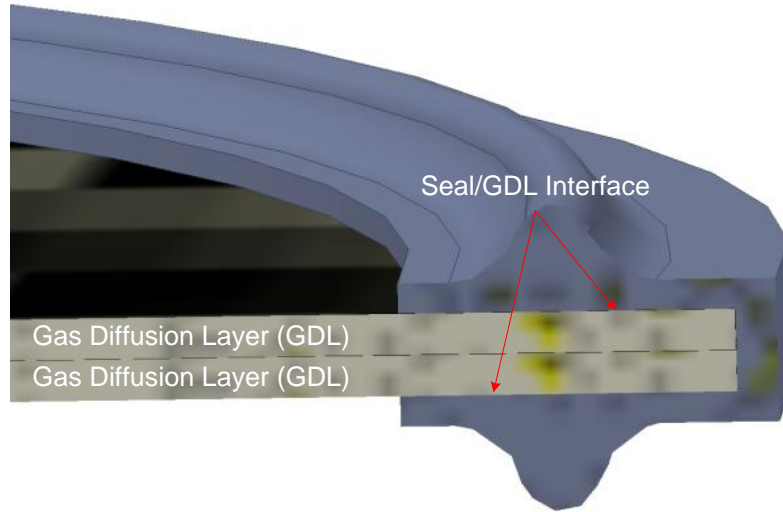


Figure 6.18 Cross-section of SMORS to illustrate various components of a unitized electrode assembly (UEA) (membrane electrode assembly (MEA) consisting of cathode-membrane-anode assembly + two GDL layers).



(a)



(b)

Figure 6.19 (a) Simplified SMORS tested in compression stress relaxation tests, and (b) delamination at seal/GDL interface due to poor impregnation of seal material into fibers (Courtesy of Henkel Corporation).

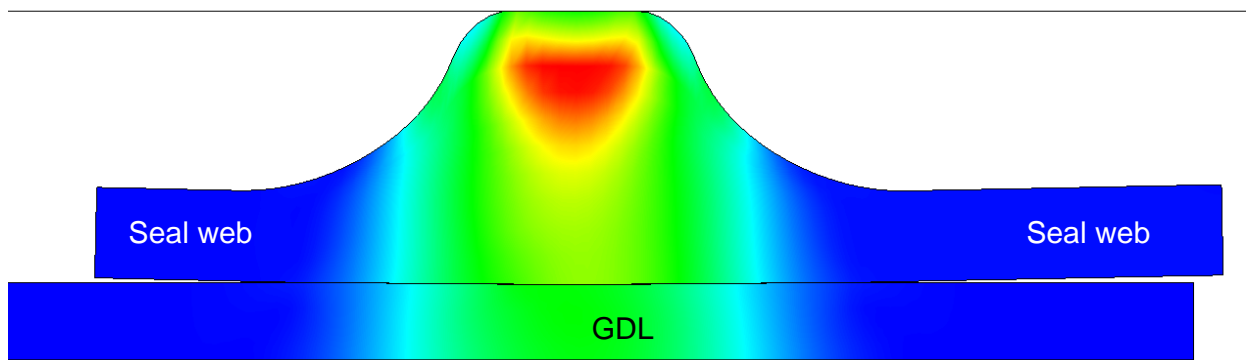


Figure 6.20 Sliding at seal/GDL interface and lifting of seal web observed in ABAQUS.

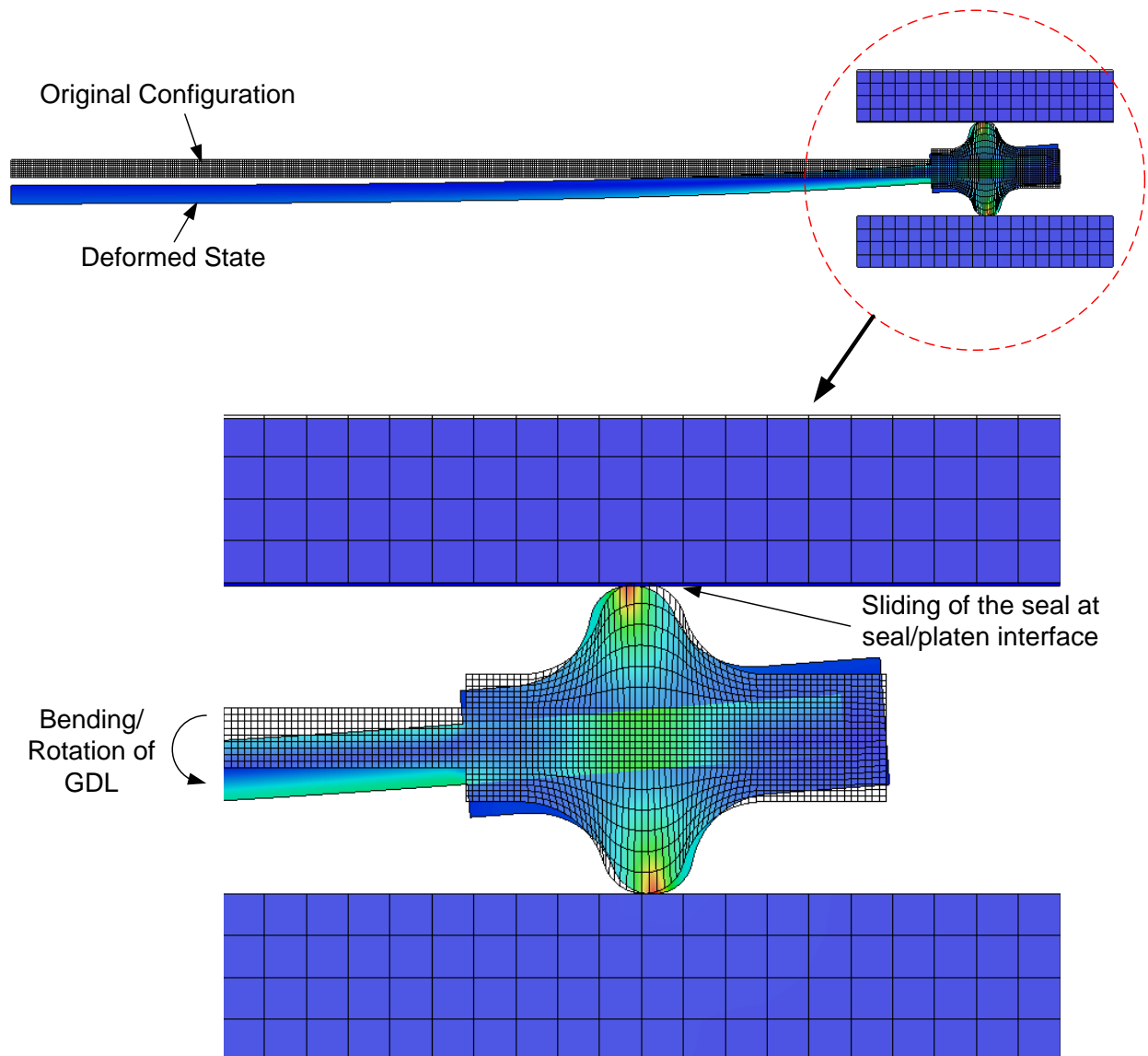
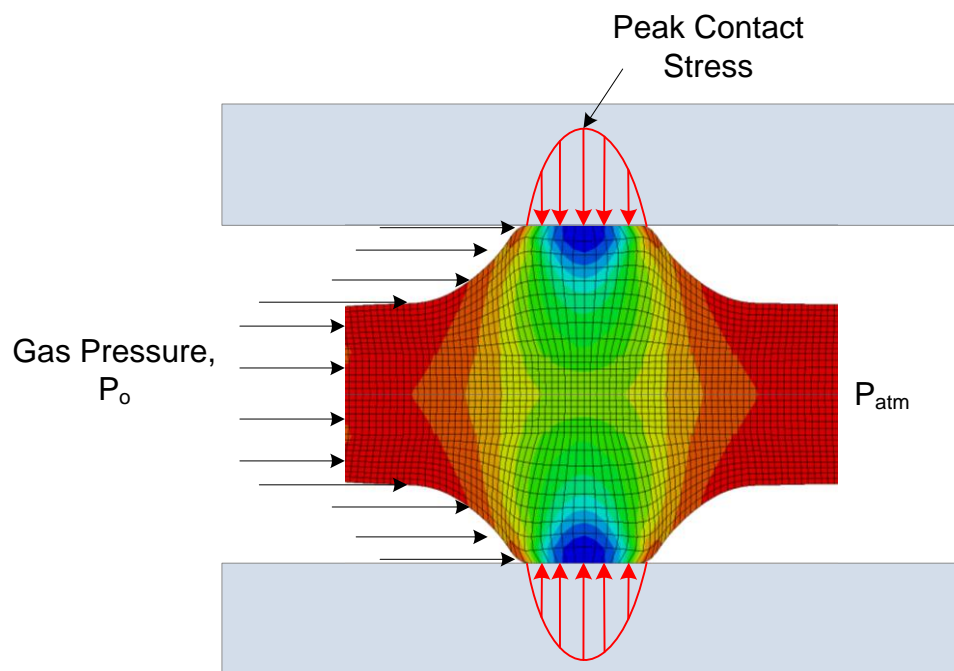


Figure 6.21 Bending & rotation of GDL on compression of SMORS.



$$\sigma_{cmax}(t \rightarrow t_{lifetime}) \geq P_0 - P_{atm}$$

Figure 6.22 Illustration of Lindley's approach used to develop peak contact stress profile to predict seal leakage.

7 Summary

7.1 Observations

The elastomeric seals in PEM fuel cells are exposed to an acidic environment, humid air, and hydrogen, as well as mechanical compressive loads. Due to aging in these environments, the seal material may degrade or fail resulting in the leakage of the reactant gases during operation or standby. Failure of the seal not only affects the overall operation which reduces performance but also poses a safety concern. Since mechanical and viscoelastic properties of elastomeric gasket materials are very important indicators of their level of functionality, long-term mechanical and viscoelastic durability of a seal material are crucial for fuel cell integrity. In this study, mechanical and viscoelastic property degradation of the seal material was investigated by conducting tests such as uniaxial tension, trouser tear, and compression stress relaxation under simulated fuel cell environmental conditions. The objectives of this study were to:

1. Evaluate the mechanical properties (load to break, elongation to break, tensile set, and critical strain energy release rate (SERR)) of a seal material in relevant PEM fuel cell environments.
2. Understand the effect of exposure medium, temperature and stress on the mechanical properties of the materials over time and screen the environments most aggressive to seal material
3. Evaluate the long-term viscoelastic properties (relaxation modulus, sealing force, compression set) of a seal material in relevant PEM fuel cell environments.
4. Develop contact pressure, contact width, and distribution of stress and strains profiles of a custom seal cross-section using finite element analysis techniques along with theoretical and experimental validation of finite element analysis results.

For mechanical property characterization, uniaxial tension and trouser tear tests were conducted. To determine tensile properties and study the long-term effect of combination of stress and environments on these properties, dogbone samples were prepared from a silicone sealant material. Samples were stretched to different levels in a custom-built fixture and aged in environments for two months. It was observed that aging degrades material properties such as tensile strength, strain to break, 100% modulus, crosslink density, and tensile set and the extent of degradation (increase or decrease) depends significantly on the environment as well as the strain level in the specimen. However, depending on the end application of the seal material, attention may be restricted to one or two important properties in an environment most relevant to application. For example, O-rings are typically used for sealing applications and a permanent set is an important parameter in evaluating seal material candidates during screening. Also, observations on change in material properties lead to the conclusion that sulfuric acid is most detrimental to the silicone seal material.

To characterize the fracture behavior and to study the effect of temperature, loading rate, and environment on the tear strength of a seal material, trouser tear tests were conducted on reinforced samples. Stick-slip crack propagation was observed at all temperatures and loading rates, although the behavior was suppressed significantly at low loading rates and high temperatures. Plots relating the crack growth rate with strain energy release rate or tearing energy were obtained at various temperatures. Significant insights into the effect of rate and temperature on the tearing strength of the seal material were obtained. Data obtained from testing at different temperatures were shifted to construct a master curve which may be used in conjunction with strain energy release rate values obtained using J-integral in FEA to predict component lifetime. Tear tests were also conducted in DI water at room temperature (RT) and 90°C and were compared with tear

characteristics in air at the same temperatures. It was observed that the presence of liquid at the crack tip during fracture does not affect the tear strength of the material.

For long-term viscoelastic characterization of a molded seal (SMORS) and a silicone seal, compression stress relaxation tests were conducted by using a novel fixture. The fixture was designed such that the material properties of strained and unstrained samples, relaxed and momentary properties respectively, in a given environment could be obtained. Based on two-network model and rubber elasticity theory, strained and unstrained material properties provided significant scientific insight and understanding of material behavior over a range of environmental conditions. Results obtained from testing on SMORS showed more variation in data as compared to silicone rings due to the complexity associated with various interfaces in the SMORS. Various mechanisms involved in material degradation e.g. chain scission and crosslinking, were discussed and insights were gained into how friction at various interfaces, cure state, and the level of antidegradants dictates the material behavior during testing. Competing mechanisms, such as chain scission, crosslinking, and swelling may affect the relaxation behavior of a material during the first phase of the testing i.e. physical relaxation. Also, testing on SMORS and ring samples indicated the fixture's inability to capture small changes in the relaxed load values and therefore a modified fixture was used for further testing.

For the purpose of understanding the deformation behavior of SMORS when subjected to compression in fuel cell stack and to be able to predict its sealing performance, finite element characterization of O-ring and SMORS cross-section was carried out. Seal material properties in terms of uniaxial stress-strain data was provided as an input to ABAQUS and several hyperelastic material models were evaluated. A two-parameter Ogden model was selected (due to its excellent correlation with experimental uniaxial tension tests data) for compression analysis

of SMORS and the O-ring. Since O-rings are often used for many sealing application and has a simple cross-section to analyze, finite element analysis was carried out to obtain some basic information related to stress-strain, contact pressure, and contact width distribution and how they are affected by seal's radius of curvature. It was observed that as the curvature of the seal increases such that $\frac{R}{r} \geq 10$, the values of contact width and peak contact stress do not change significantly. Information obtained on the effect of seal curvature on maximum contact pressure can be helpful when a seal bead is laid out on a substrate where it may have different curvature in different regions of the substrate. If a pressure differential needs to be maintained across the seal bead, the value of lowest maximum contact pressure (for regions where curvature is smallest i.e. $\frac{R}{r} < 10$) should be used to prevent leakage. Results and insights obtained from O-ring analysis proved to be helpful for analyzing a complex assembly such as SMORS, where several interfaces and boundary conditions are involved. An axisymmetric analysis of SMORS was carried out for $\frac{R}{r} \geq 20$ (more realistic to SMORS tested in CSR experiments). In order to simplify the analysis process and to cut down on computing time, only half-section of the SMORS were analyzed where the top compression platen was replaced with an analytically rigid body. Stress/strain profiles were generated to visualize their distribution and concentration in the seal cross-section. Frictionless and rough interfacial conditions between seal material and the analytically rigid body were assumed and it was found that the effect of friction on contact width and peak contact pressure was insignificant.

Load versus displacement (or % compression) data generated on SMORS with the help of ABAQUS were validated through comparison with a contact mechanics approach (Lindley's

approach) and experimental data. It was observed that Lindley's equation correlates well with experimental data up to 25% strain whereas ABAQUS shows good agreement up to 10% compression of SMORS. For more than 10% compression of SMORS, load values were overestimated by ABAQUS and may possibly be due to assumptions made to simplify the SMORS analysis.

7.2 **Future Work**

Although considerable data was generated from mechanical and viscoelastic characterization of the material which provided a significant insight into the material behavior under various loading configurations in different environments, results were rather inconclusive in terms of lifetime prediction of SMORS when used in fuel cells. In order to address issues related to material testing, approach suggested below may be considered in future.

7.2.1 **Characterization of Bulk Material Properties**

7.2.1.1 *Tensile Properties*

A great deal of information was obtained from conducting tests on silicone dogbone samples stretched to various levels of strains in environments. Similar tests can also be performed on other seal materials so that a comparison can be made between several fuel cell grade seal materials and durability estimates may be obtained. Changes in material property due to aging can be explained based on the chemical analysis of the seal materials before and after aging. Techniques such as X-ray photoelectron spectroscopy (XPS) and Fourier transform infrared spectroscopy (FTIR) spectroscopy can be utilized to study changes in chemical properties. Even though the values of crosslink density obtained from tests may not be accurate, the values may be used as a tool to study trends in material behavior in presence of stress and environments. In

order to obtain a better estimate of crosslink density and also to double-check the values obtained from mechanical tests, samples should be prepared from seal material for swelling experiments and the Flory-Rehner [1] equation used to obtain a measure of the degree of crosslinking.

Using the fixture designed to strain samples in environments, samples should be aged for different aging times, from 1 week up to 24 weeks, and after the desired aging time has been reached, samples should be taken out and studied by chemical and mechanical means. Since strain, rather than temperature, is used as accelerating parameter for material degradation, an approach similar to Arrhenius technique may be useful to predict material property degradation at strain levels at operating conditions.

7.2.1.2 *Tear Properties*

Information on rate-dependent and temperature dependent fracture behavior of the seal material helped obtain master curve which can be used to make prediction for crack growth rate based on strain energy release rate (SERR) values obtained from finite element analysis. Although a threshold value of SERR was not clearly evident in the master curve plot, such a value has been reported by several researchers [2-4]. To estimate a threshold value of SERR for the material studied here, a similar approach may be adopted where trouser tear tests are conducted on samples that were aged in a given environment for a period of time. Alternatively, tests may be conducted at higher temperatures and slower rates to obtain threshold values but caution must be exercised in:

1. Selecting a load cell to accurately read small load values during crack propagation.
2. Preventing the heat transfer to the load cell at high temperatures through load train used for testing.

7.2.2 SMORS Characterization

Compression stress relaxation (CSR) of SMORS in various environments was a major part of this study, the data from which is typically helpful in predicting lifetime of a component. Due to the problems associated with obtaining good quality molded SMORS to obtain repeatable results as well as CSR fixture's resolution to detect small changes in relaxed load values, several modifications were made so that issues related to fixture sensitivity can be addressed. Figure 7.1 shows the modified design of the CSR fixture where the relaxed load in SMORS stacked in the lower chamber is automatically recorded by a load cell connected to the data acquisition system through a custom designed LabVIEW code. A high precision micrometer head attached to the unit provides good results obtained during compression of the seals. Momentary properties of the seals will be obtained separately based on the procedure used with the old fixture design. Figure 7.2 shows three fixtures positioned in a water bath at 90°C collecting stress relaxation data in DI water, a 50v/50v DI water/ethylene glycol, and 0.1M sulfuric acid solutions.

References:

1. P.J. Flory and J. Rehner, "Statistical Mechanics of Cross-Linked Polymer Networks. II. Swelling," *Journal of Chemical Physics*, **11**, 521-526, 1943.
2. A.N. Gent and R.H. Tobias, "Threshold Tear Strength of Elastomers," *Journal of Polymer Science Part B-Polymer Physics*, **20**(11), 2051-2058, 1982.
3. A.K. Bhowmick, C. Neogi, and S.P. Basu, "Threshold Tear Strength of Carbon Black Filled Rubber Vulcanizates," *Journal of Applied Polymer Science*, **41**(5-6), 917-928, 1990.
4. A.N. Gent and J. Jeong, "Tear Strength of Oriented Crystalline Polymers," *Journal of Materials Science*, **21**(1), 355-363, 1986.

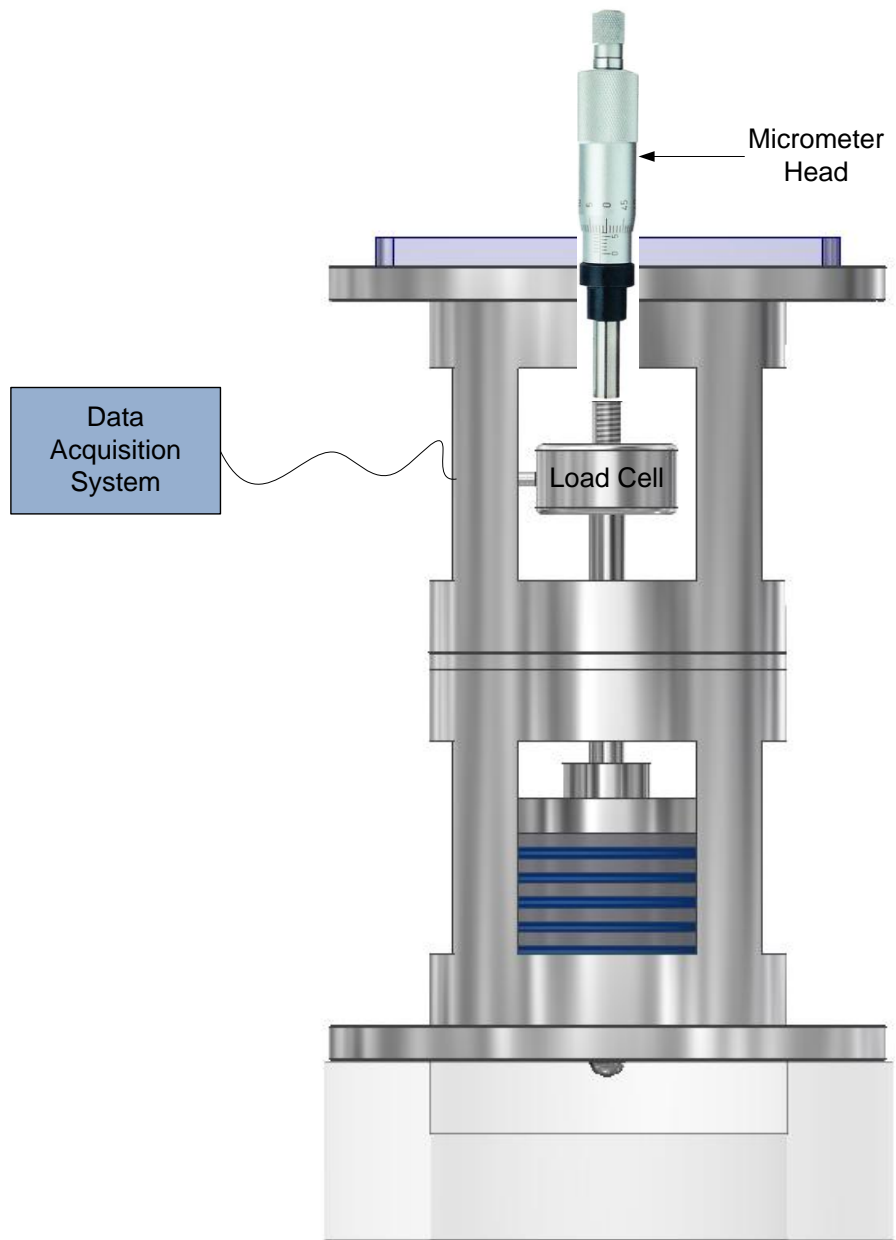
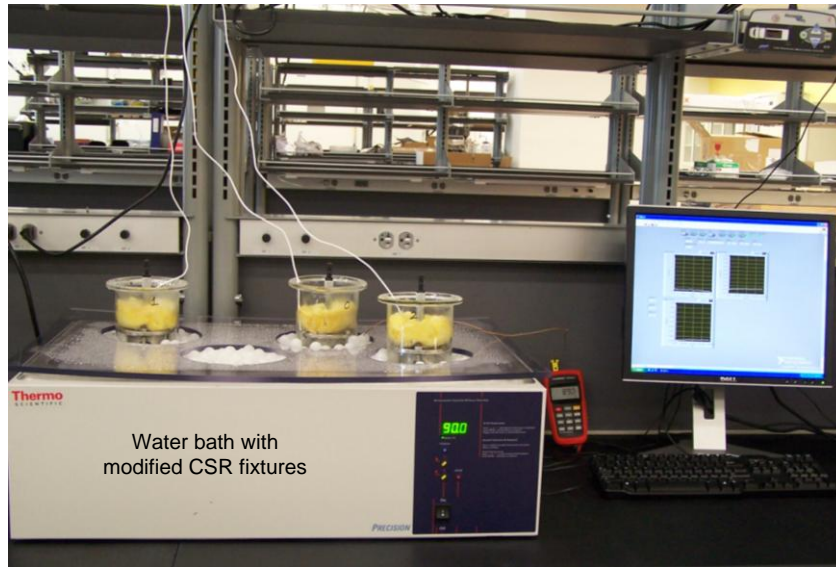
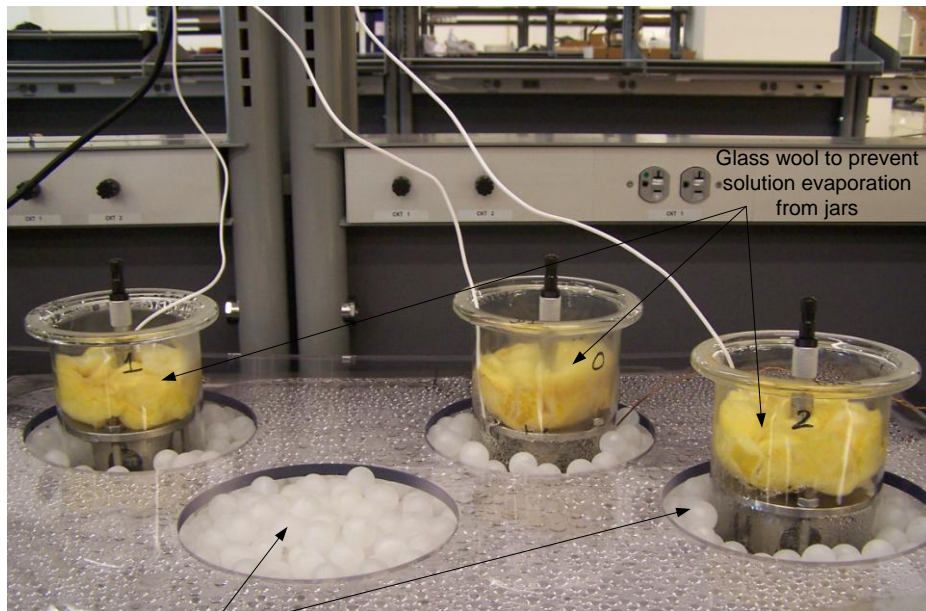


Figure 7.1 New compression stress relaxation fixture design containing a load cell for continuous data collection via a data acquisition system and LabVIEW code.



(a)



Hollow polypropylene balls to reduce water evaporation

(b)

Figure 7.2 Continuous compression stress relaxation test set-up showing (a) fixtures loaded with SMORS in various liquid solutions arranged in the water bath 90°C, (b) close-up of the fixtures showing polypropylene balls and glass wool to minimize liquid evaporation.